A single-cell view on the intra- and inter-population metabolic heterogeneity and ecophysiology of microorganisms at different ecological scales

To the Faculty of Chemistry and Physics (II)
of the Technische Universität Bergakademie Freiberg
approved

THESIS

to attain the academic degree of

Doctor Rerum Naturalium

Dr. rer. nat.

Submitted by

M. Sc. **Federica Calabrese**

born on the 11th January 1988 in Reggio Calabria (Italy)

Reviewers: **Herr Prof. Dr. Michael Schlömann,** TU BA Freiberg

Herr Prof. Dr. Hauke Harms, Leipzig University

Frau Dr. Niculina Musat, UFZ Leipzig

17th September 2021

Table of content

Abbreviations list

Ac	Acetate
AH	**Anabolic Heterogeneity**
At%	Atomic Percent
AMO	Amoxicillin
BFI	Bacterial-Fungal-Interactions
Bz	Benzoate
CARD-FISH	Catalyzed reporter deposition-Fluorescence In Situ Hybridization
CB	Cacodylate Buffer
CDTI	**Cumulative Differentiation Tendency Index**
CIP	Ciprofloxacin
CPD	Critical Point Drying
CSE	Counting Statistics Error
CV	Coefficient of Variation
ddH$_2$O	Distilled and deionized water
DTI	**Differentiation Tendency Index**
DW	Distribution Width
EDX	Energy-Dispersive X-ray spectroscopy
EtOH	Ethanol
FISH	Fluorescence In Situ Hybridization
FoV	Field of View
FSC	Forward Scatter light
GA	Glutaraldehyde
GFP	Green Fluorescent Protein
HC	**Heterogeneity Coefficient**
HGT	Horizontal Gene Transfer
HIM	Helium Ion microscopy
HMDS	HexaMethylDi-Silazane
HPF	High Pressure Freezing

HRP	Horse Radish Peroxidase
IL	Ionic Liquid (1-Butyl-3-Methylimidazolium tetra-fluoroborate)
IRMS	Isotope Ratio Mass Spectrometry
MAD	Median Absolute Deviation
MH	**Metabolic Heterogeneity**
nanoSIMS	**nanoscale Secondary Ion Mass Spectrometry**
OD	Optical Density
OTU	Operational taxonomic unit
PFA	Paraformaldehyde
Pr	Pristine water
QSA	Quasi-Simultaneous Arrival
RoI	Region of Interest
SE	Secondary Electrons
SEM	Scanning Electron Microscopy
SERS	Surface Enhanced Raman Spectroscopy
SIP	Stable Isotopes Probing
SSC	Side Scatter light
ToF-SIMS	Time-of-Flight Secondary Ion Mass Spectrometry
WWTP	Wastewater Treatment Plant
WWT	Wastewater Treatment Plant affected water

Summary

Isogenic microbial populations, even when exposed to homogeneous conditions, display **cell-to-cell differences** in metabolic traits, phenomenon also known as **metabolic heterogeneity (MH)**. The outcome of **MH** can affect the whole function of a population, impacting fitness, metabolic processes, or even the effectiveness of infections treatment. Understanding **cell-to-cell heterogeneity** and its main drivers may thus have huge implications in medical microbiology, concerning antibiotic response and resistance or biofilm formation; in biotechnology with respect to achievement of good performance and high yield in largescale; in environmental microbiology regarding the impact on biodegradation processes and biogeochemical cycles in natural ecosystems. Despite its importance in many fields, a '**unit measure' for heterogeneity** is currently missing; moreover, the triggering factors and its specific ecological role are not yet fully understood.

In the present thesis, the **MH** in microbial populations has been studied at **single-cell level**, to i) understand the influence of **abiotic** and **biotic factors**, and emerging contaminants, i.e. antibiotics, on its occurrence; ii) understand its ecological role at different scales, from model organisms to natural communities. Chemical Imaging with nanoscale Secondary Ion Mass Spectrometry (**nanoSIMS**) was the technology of choice due to the high spatial resolution combined with high precision, which allow for qualitative and quantitative measurements at **single-cell level**.

During my work, I have optimized protocols for the preparation of microbial cells to preserve their morphological and chemical integrity prior to nanoSIMS analysis. This was necessary to reduce as much as possible related artefacts and thus biases on the quantitation of metabolic activity of single cells.

At first, I proposed two methods for **quantitation of MH**: the Heterogeneity Coefficient (**HC**), applicable when populations follow asymmetric, but still unimodal, distribution and the Cumulative Differentiation Tendency Index (**CDTI**) useful for populations following **multimodality**. The developed indices are useful to quantitate heterogeneity in different contexts and with different techniques.

MH in isogenic populations has been shown to increase under nutritional and spatial limitations or fluctuating environments, however little is known on the **MH** of bacteria under favorable and **non-limiting** growth conditions, and its triggering factors. Therefore, using three different model species, I have investigated on the effects of growth substrates, substrates' concentrations, and electron acceptors on their anabolic activity **at single-cell level**. The main finding was that all tested microbial populations did show **MH** under **non-limiting** conditions although none of the tested **abiotic factors** prevailed as a main driver of **MH**.

I subsequently studied the role of **biotic factors** e.g. other microorganisms on the bacterial functional heterogeneity. A synthetic system consisting of hyphal forming pseudo-fungi and two bacterial species, used as reporter system, grown in co-cultures was used. The results showed that bacterial functional heterogeneity in '*horizontal gene transfer*' was observed mainly in the vicinity of hyphal surface, suggesting that such biotic interactions may increase bacterial **MH** in these sites.

In nature, beside **abiotic** and **biotic factors**, microbial communities are exposed to several stressors, even when nutritional conditions are **non-limiting**. As last part of my thesis, I therefore focused on the impact of antibiotics on water samples collected from the river Holtemme (Hartz, Germany) at two different sampling sites. Pristine and wastewater treatment plant-affected waters were treated with two antibiotics, at two different concentrations, and stable isotopes to investigate on the communities' metabolic activity upon 24 hours exposure. Focusing in particular on two specific phylotypes, I found that antibiotics strongly affect the assimilation rates and this corresponded to an increase of bacterial **MH,** which impacted more Carbon than Nitrogen activity.

To conclude, in my thesis I proposed, optimized and successfully applied sample preparation protocols for chemical imaging and electron microscopy. I developed two methods for **quantitation of heterogeneity** that could be exploited by other researchers to investigate not only metabolic but also phenotypic, morphological and functional heterogeneity. I provided evidences for the first time on **MH** occurring under **non-limiting** conditions in isogenic microbial populations, thus shedding light on key factors and its mechanisms. Because the microbial **MH** of different bacterial strains was triggered in a growth-conditions-specific manner, this highlights the necessity to study this phenomenon more deeply to understand its implications in each of the studied processes in the related fields and in nature. Metabolic interactions are constantly taking place in natural environment shaping the functions of the ecosystems. I brought insights on how these microbial interactions can play a role in the functional and **MH** of synthetic and natural systems. Emerging contaminants, such as antibiotics, had a strong impact on the microbial metabolic activities, thus undermining their contribution to the *Carbon* and *Nitrogen cycling* and consequently altering microbial-mediated processes, e.g. remineralization. The targeted phylotypes increased their **MH** but never showed cessation of Carbon or Nitrogen assimilation upon antibiotic exposure, suggesting that **cell-to-cell metabolic diversification** could help microbial populations to better thrive in their environments despite the presence of the stressors.

With my thesis, I provided more insights on the phenomenon of **MH** at different ecological scales, shedding light on its dynamics in microbial populations and its potential ecological role in nature.

Keywords: Metabolic heterogeneity; isogenic populations; non-limiting conditions; abiotic and biotic factors; emerging contaminants; single-cell analysis; nanoSIMS; stable isotope probing (SIP); sample preparation; heterogeneity quantitation; assimilation-rate quantitation.

1. Introduction

1.1 Phenotypic heterogeneity: the origins

In the 1864, Louis Pasteur scientifically proved the existence of microorganisms laying the groundwork for the flourishment of microbiology field as we currently know. Decades later Robert Koch developed a system for growing bacteria on specific media for their characterization, introducing the concept of pure culture. During the Second World War, Jacques Monod started his studies on bacteria growth behavior suggesting the still valid theory of exponential growth and thereafter the diauxic phase growth when microorganisms are feed with two sources of sugar [1,2]. All these discoveries and many others shade light on the physiology and the behavior of microbial populations that were considered as assembly of genetically identical cells originating from a single-common-ancestor cell. Whether growing in agar plate forming single visible colonies or in liquid media forming suspensions, microbiologists usually referred to these as monoclonal or isogenic populations [2,3].

The genetic makeup of a cell, i.e. the set of genes on the chromosome that determines hereditary characters, constitutes its genotype while the visible effects, i.e. the set of characters that the cell manifests, composes the *phenotype*, which depends on the interactions between genotype, epigenetic and external factors [4]. Therefore, the *phenotype* can be considered every observable feature of a cell in its morphology, physiology, function, and behavior. When translating this concept to an isogenic population, it is implied that the offspring or a clonal cell are supposed not only to be genetically identical, i.e. isogenic, but also morphologically, physiologically, and metabolically identical with the ancestor cell.

However, since the early 20th century, many evidences have shown that there is a functional **cell-to-cell variability** within cells belonging to a monoclonal population, phenomenon nowadays knows as **phenotypic heterogeneity**. Benzer was the first one talking about homogeneity referring to the simultaneous response of the cells to a certain stimulus and hence the simultaneous and equal kinetics of a certain enzyme formation [5]. He demonstrated the homogeneous induction of *beta-galactosidase* in a population of *Escherichia coli* under saturated concentration of enzymatic inducer and gratuity conditions, i.e. neither the enzyme itself nor its inducer affect the general cellular metabolism [5]. On the contrary, he noticed that when lactose is used as both carbon source and inducer, the induction of *beta-galactosidase* enzyme resulted heterogeneous among cells within the same population. This observation paved the way to the pioneer work about **cell-to-cell variability** by Novick and Weiner [6]. Always focusing on the induction of *beta-galactosidase* enzyme in *E. coli*, the authors discovered how low inducer concentrations caused the split of the culture in two subpopulations: one expressing enzyme at full rate and the other not expressing it at all. Interestingly, they were already raising the issue on the bias of observing an "average rate" that does not mirror the behavior of individual cells in the culture.

Following this study, Cohn and Horibata showed evidences that the state of the two subpopulations, induced or not induced, was "transmitted" clonally or cytoplasmically inherited to the descendant microbial cells. This "cytoplasmic entity", that today it would probably called translated enzyme (upon induction)

was responsible for the discontinuity in the synthesis of this *beta-galactosidase* enzyme by individual cells. In other words: if the daughter cells received the cytoplasmic entity, the lactose *permease*, these cells were easily induced and produced enzymes always at maximum rate since it was an autoinductive and autocatalytic system; if the daughter cells received just a very small amount or not at all, the cells were insensitive to induction [7]. The authors extended the concept of heterogeneity in autocatalytic systems also to the *galactozymase* of the yeast previously shown by Spiegelman [8].

Another groundwork about **cell-to-cell heterogeneity** regarded *Bacillus subtilis* and the competency, namely the capability to acquire external DNA fragments from the surrounding environment under stressing conditions. The "competent" cells were different from "non-competent" ones in cell density, water permeability and number of chromosomes per cell, but they were able to revert when the conditions became again favorable [9,10]. From then on, just recently in the last few decades a joint and increased research effort began, providing remarkable breakthroughs on this topic with both theoretical understanding and empirical evidences.

Phenotypic heterogeneity is now a common and broad term which indicates **cell-to-cell variation in morphological, physiological, and functional traits among genetically identical cells**. In the following chapters, the most important discoveries in the recent years are discussed, as well as the current challenges and open questions about **phenotypic heterogeneity** and the techniques that allowed for a better understanding and comprehension of this topic.

1.2 *Known sources of phenotypic heterogeneity*

Many decades ago, when the heterogeneity was first observed in the scientific community, single microbial cells were difficult to investigate with the existing methodologies. Therefore, the concept of *individuality* was more challenging to prove. Not all the above-mentioned hypotheses in fact could be experimentally addressed because of the lack of **single-cell techniques**. The problem was partially overcome with genetic engineering which was flourishing at the end of the Nineties [11]. One of the main questions that challenged and still challenges the scientists is: which are the molecular mechanisms behind the occurrence of **phenotypic heterogeneity**?

1.2.1 Cellular noise

Most of the biological processes inside the cells, e.g. gene expression, transcription and translation, are stochastic, that is they do not follow fixed principles or rates but they are rather subjected to randomness and environmental cues [12]. Such **cellular noise** derives from the fact that biochemical reactions depend on a distinct and small number of molecules, meaning that both random encounters of few macromolecules and fluctuations in their transitions or conformational states inside the cell occur in parallel [13]. **The noise** in turn can be distinguished in two sources/occurrences: *"intrinsic"* noise, the inherent stochasticity of biochemical processes, and the *"extrinsic"* noise, fluctuations in the amounts of other cellular components

that indirectly induce variations in the final process [14,15] (Fig. 1). **Cell-to-cell variations** in the expression of a single gene will therefore be the result of both *intrinsic* and *extrinsic* contributions of **noise** [14-16]. However, the first experimental evidence of **noise** in gene expression showed that *intrinsic noise* could be prevalent and most importantly that such **noise** could be t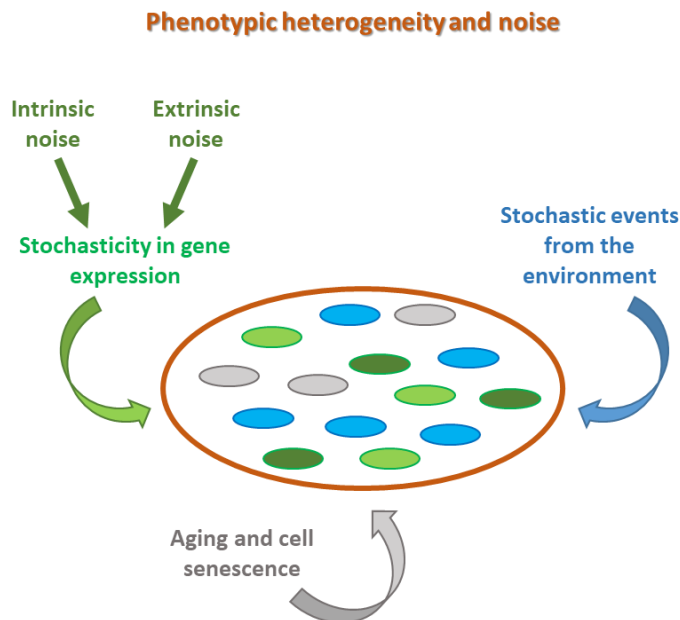he cause of **phenotypic heterogeneity** in isogenic populations [17]. If two genetic elements were introduced into the chromosome of *Escherichia coli* under control of the same promoter, the cyan and the yellow allele of green fluorescent protein (GFP), each cell should express identical and constant levels of the two fluorescent proteins. Instead, different cells showed a pronounced variability in absolute fluorescence levels and the ratio between the two colors [17] (Fig. 2) indicating a strong **cell-to-cell variability**.

Figure 1. A schematic representation of the known sources of stochasticity in the manifestation of **phenotypic heterogeneity**.

A parallel study with an isogenic population of *Bacillus subtilis* investigated the contribution of transcription and translation to the cellular **noise**. The authors used two different methods: an inducible promoter which controlled the expression of a downstream GFP protein for regulating transcriptional efficiency and different point mutations in the ribosome binding site (RBS) and the initiation codon of GFP protein for translational efficiency [18]. The higher the translational efficiency the stronger the variation in gene expression or, in other words, high translation rates induced bigger protein fluctuations and consequently higher *phenotypic variation* within individual cells [18]. Many regulatory proteins control the synthesis of several downstream products and translational **noise** can be a check point to regulate in turn the **noise** in the gene expression cascade. Low transcription but high translation rates produced a fluctuating burst of proteins inside the cell and hence more **noise**. In contrast, high transcription but low translational rates resulted in a constant flood of transcripts that could not be translated, making the translation apparatus the bottleneck of the cycle but overall reducing the **noise** [18,19]. This could explain why most of the promoters upstream of important constitutive genes are less efficient in transcription and translation than other operons [19,20].
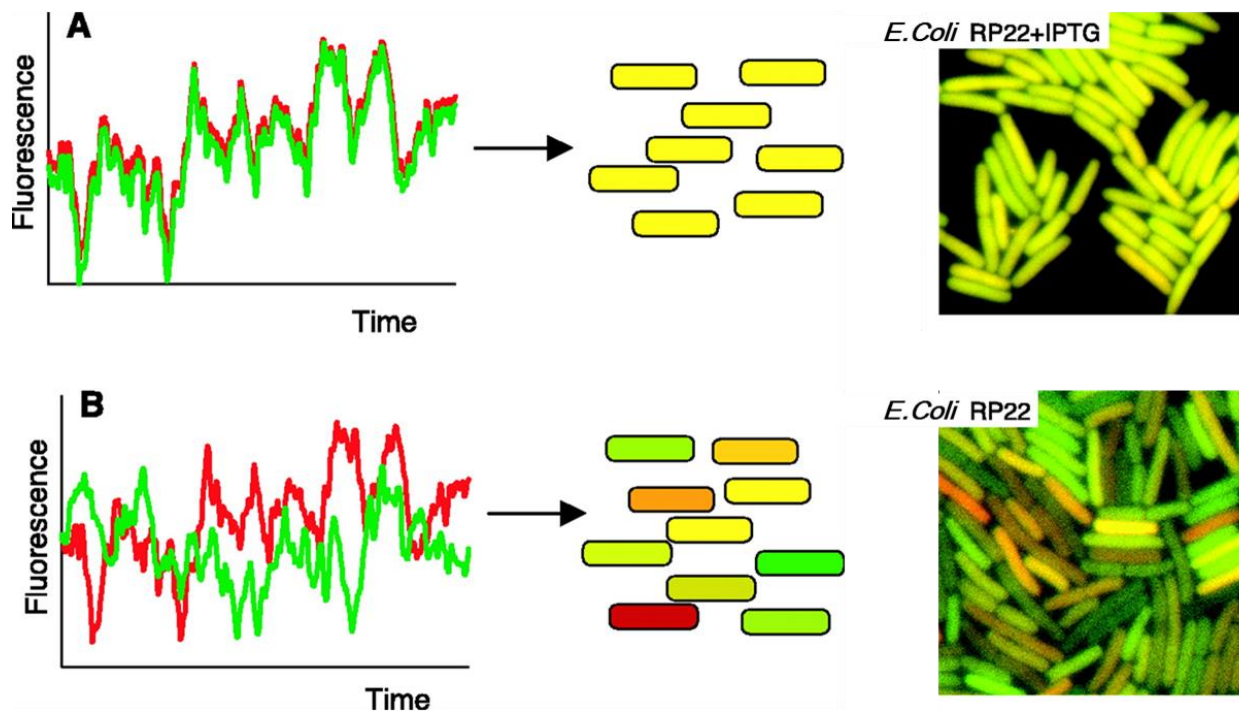
Figure 2. *Intrinsic* and *extrinsic noise* in gene expression. **A)** shows a schematic representation of gene expression in an isogenic population: in the absence of *intrinsic noise* the two fluorescent proteins, under the control of the same regulator, fluctuate in a similar manner and each cell will have the same amount of these proteins (same yellow color), therefore homogeneity. On the contrary, **B)** shows the contribution of *intrinsic noise* which gives rise to **cell-to-cell differences** in the expression of the two fluorescent proteins and therefore heterogeneity (different colors). Right panels show corresponding fluorescent images of *Escherichia coli* strain when the promoter is repressed **A)** or when inducer is added for increasing the *intrinsic noise* **B)**. Pictures are modified from [17].

Regulatory feedbacks can also be responsible of **cellular noise**. In order to limit the entity of fluctuations and **noise**, regulatory mechanisms, amplification and exploitation of **noise** usually interact in the complex cellular networks involving multiple feedback loops [21]. The cells implement auto-regulatory mechanisms, i.e. negative feedback loops in genetic circuits with the aim to bring back the stability into the system [22]. Negative feedbacks regulate and provide homogeneous distribution of transcriptional repressors within the cell, but they are not the only biochemical processes involved in the regulatory mechanisms [22]. Positive feedbacks include, for example, the well-studied phenomenon of quorum sensing or pheromone sensing [23-25], where a series of positive feedback loops are responsible for both input and output of signal transmission.

Moreover, the so-called *Feedback-Based Multistability* can take place, typically involving interconnected positive and/or negative feedbacks. Intuitively, in such case the **cellular noise** increases accordingly due to the many turning points that have to be orchestrated [26]. The *phenotypes* then are responsible for defining the function, structure and physiology of the entire population [27].

These evidences and many others [15,28-31] suggested that **noise** in biochemical networks accounts for one of the main sources of **cell-to-cell variations** (Fig. 1).

1.2.2 Bistability and Multistability

Stochastic fluctuations in the cellular components and **cellular noise** can cause different physiological or functional states, which eventually cause the co-occurrence of two or more distinct *phenotypes*, a phenomenon better known as **Bistability** or **Multistability** respectively [32-35] (Fig. 3).

Under the very same surrounding conditions, the interaction between auto-regulatory and cross-regulatory mechanisms inside the cells can induce either the shift between two states (**Bistability**) or the coexistence of diverse intermediate stable states (**Multistability**) [36].
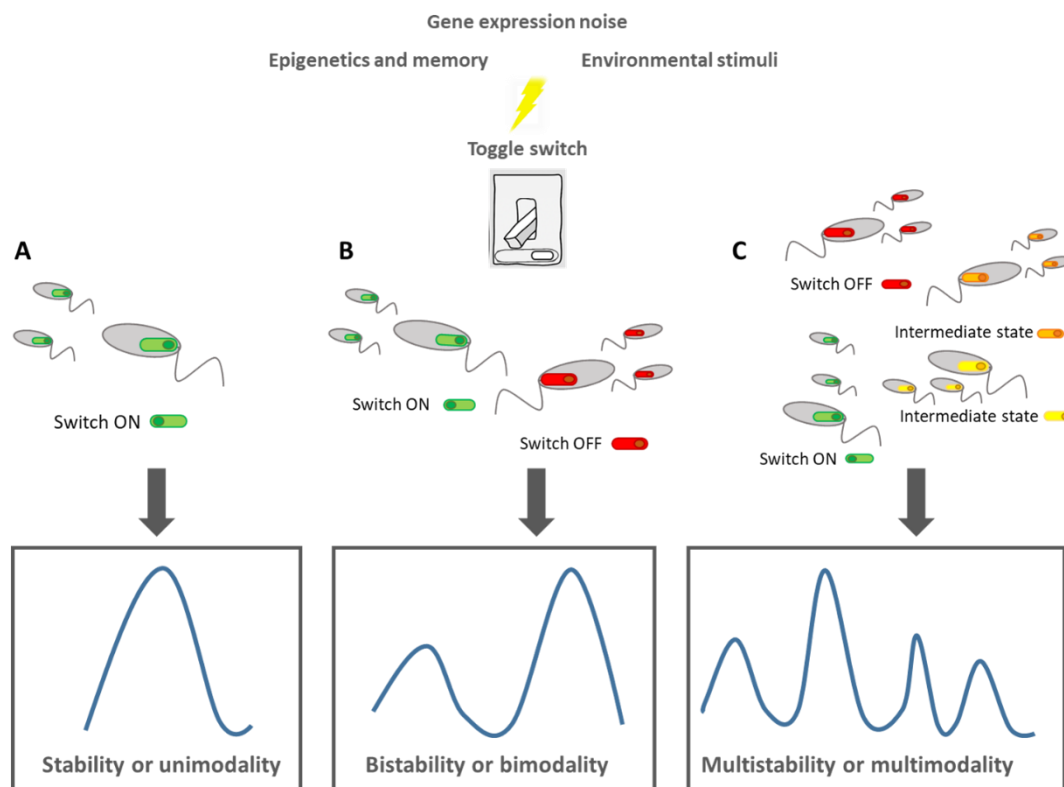
Figure 3. Schematic drawing of the "*toggle switch*" mechanism in gene expression **noise.** Stochasticity in gene expression and **epigenetic** mechanisms together with environmental stimuli can trigger the toggle switch in ON state. This can stay "ON" in a unimodal fashion **A)** for the majority of the cells in the population. However, most of the time, a subpopulation of cells is blocked in "OFF" state generating a **bimodal** distribution **B)** or even in intermediate states that will be revealed as **multimodal** distribution **C).**

Theoretical studies have shown that **Multistability** is favored by the interplay between **noise** amplification and **noise** compensation resulting from balance between auto- and cross-regulation and hence in a series of transient states within the individual cell [37]. These various states are usually called switches or *phenotypic switches* and they are essential for the adaptation of the cells (Fig. 3).

A feature of **bistable** system is the so-called "*toggle switch behavior*" (Fig. 3), which indicates a bi-phase where ON or OFF states are alternating due to the transient nature of the switches [38]. The first example of a **bistable** system in microbial populations was the lactose utilization by *Escherichia coli* via the *lac* operon [6, 39,7]. However, Ozbudak and colleagues have later shown that between the two states of the system, induced and not-induced, there were certain intermediate **multi-states** due to a graded gene expression from low to high values [30].

Very interestingly, the induction of the *lac* system follows a *hysteretic behavior*, meaning that the process response is not equally bidirectional, rather the reverse transition (i.e. uninduction) has to be greater than the forward transition event, (i.e. induction) (Fig. 4). This means that the inducer level must exceed the basal concentration level in order to induce the cells; instead from induction to uniduction, the inducer concentration has to be much lower than the minimum concentration required for induction [30].This behavior is probably responsible of the final ON (induced)/OFF (uninduced) *phenotype*.

Bacillus subtilis model organism also offers several examples of **bistable** systems [34]. One of the best described is the already mentioned competence, which occurs transiently just during stationary phase or stressing conditions [40,41]. Noise in *comK* transcription determined the entry into competency and a **bistable** system determined the reverting process [42,43]. The entry into sporulation is another example of **Bistability** [34]. The activation of *Spo0A*, the main regulator for spore formation was activated under nutrient limitations and followed ON/OFF switch [44]. Likewise, *B. subtilis* displayed a **bistable** mechanism in the flagellar expression for the switch between motile or sessile *phenotype* [45-47].

1.2.3 Epigenetics and phenotypic memory

One of the characteristics of **Bistability** is the *hysteretic behavior* (Fig. 4). This feature is in turn dependent on two mechanisms: **epigenetics**, responsible for the inheritance of the *phenotypic switches*, and **phenotypic memory**, caused by a pool of inherited biomolecules, e.g. intracellular inducers, repressors, enzymatic proteins or mRNA, which carry-over the reminiscence of the cells' past [48-50].

Epigenetics refers to the fact that the *phenotypic* changes do not depend on the mutations in the DNA sequence but rather on the reversible DNA-assembly modifications or cellular biomolecules conformations. **Epigenetic mechanisms** allow the offspring to inherit the *phenotype* for one or even many generations since they are controlled by DNA methylation, protein auto/phosphorylation, prions, phage life cycle shifts, plasmids, transfer of active transcriptional regulators during cell division and protein-protein fold/conformation [51-53].

The methylation of DNA, for example, is responsible for **epigenetic** reversible control of the genetic makeup, being based on the modification of adenosine and cytosine nucleotides in the DNA. This phenomenon, largely known for eukaryotes, has recently attracted attention for prokaryotes studies [51,54,55]. Methylation of DNA in bacteria directly or indirectly regulates a number of important cellular events including DNA repair and replication, cell-cycle progression, gene expression and virulence [54].

Figure 4. Schematic representation of the *hysteretic behavior* of a **bistable** system. The system is stable and uninduced until the level of inducer does not start to increase and overcome a positive threshold (green sphere). After this point, induction is triggered and the system is switched ON, then reaching a stable state with the maximum level of inducer. In order to come back to original uninduced state (switch OFF) the process does not follow the same path. The inducer level inside the cell has to reach a negative threshold (red sphere) and this reverse transition takes longer than the forward one. The difference between the "switch ON" and "switch OFF" represents the "*hysteresis*" and it represents a typical feature of the **bistable** system.
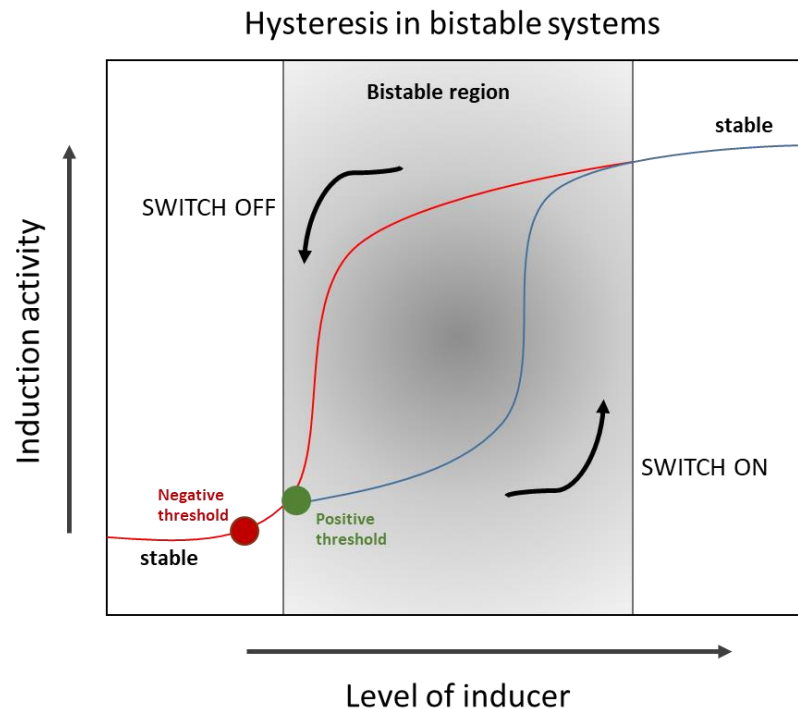
For instance, DNA methylation controls the reversible *switch* of pyelonephritis-associated pili (*pap*) operon responsible for the expression of pili in uro-pathogenic *Escherichia coli* (UPEC); these pila allow the strain to bind epithelial receptors in the bladder. DNA methylation pattern controls the ON/OFF expression state of *pap* operon. The methylation of the proximal site of the promoter activates the transcription of pilin as well as the positive feedback between regulatory proteins (*PapI* and *Lrp*) and the transcription of *pap* operon (switch ON), while methylation of the distal site of the promoter inhibits the process (switch OFF) (Fig. 5-A). The methylation pattern of the operon is imposed by alternating binding and unbinding of regulatory proteins to the specific binding site of *Dam* methylase; hence, this inherited pattern is responsible for the *phenotypic switch* and for the heritable transcription state ON or OFF in UPEC strains [56-58] (Fig. 5-A).

The expression of several operons in *Escherichia coli* is regulated by a mechanism called chromosome superhelicity, supercoils forming DNA-superhelixes. It has been proposed that the coordination between chromosomal modifications, energetic levels, and environment signals finely tunes the basal expression of many operons in *Escherichia coli*. Both the chromosomal constraint, imposed by DNA superhelicity and the proteins responsible for supercoils can be inherited from the daughter cells that will "receive" the same type of regulation [59].
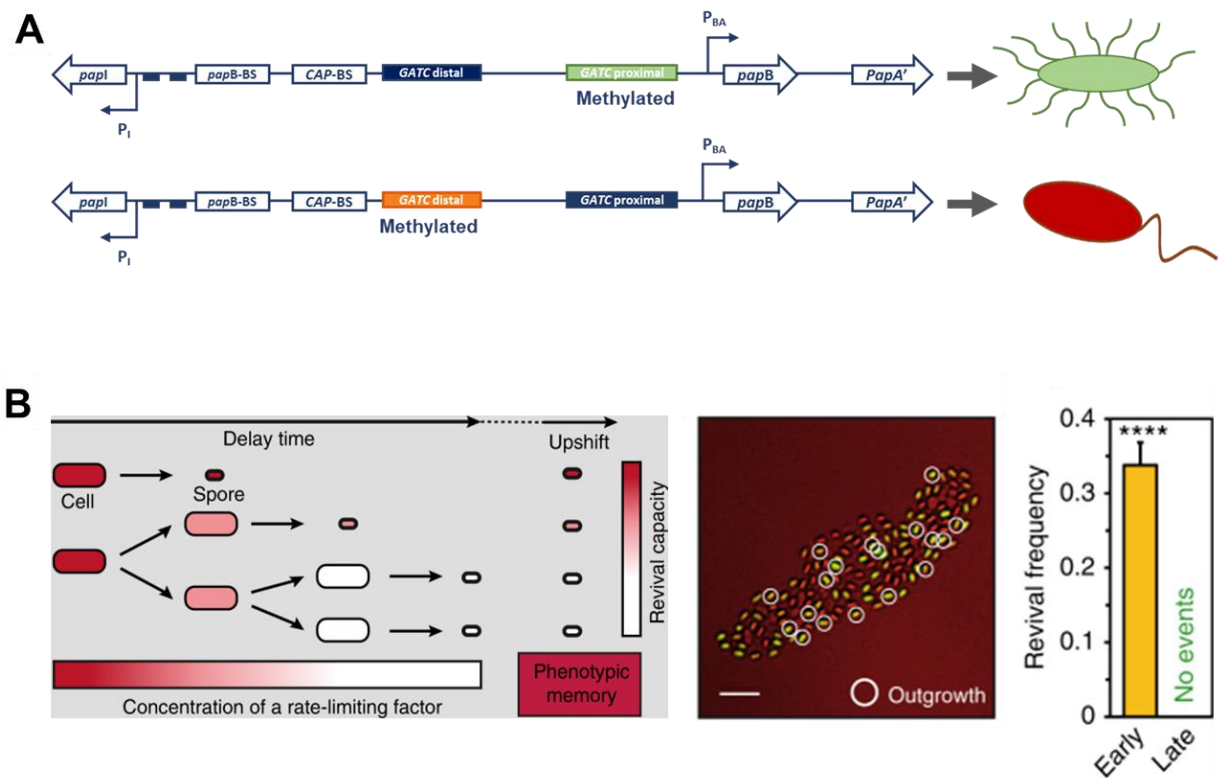
Figure 5. Example of **phenotypic heterogeneity** due to **A) epigenetics** or **B) phenotypic memory**. **A)** is a schematic representation of *pap* operon in *Escherichia coli* UPEC and its **epigenetic** transmission to the daughter cells. **B)** Example of **phenotypic memory** in *Bacillus subtilis* for the sporulation entry. Figure **B)** readapted from [60].

Phenotypic memory instead results from a transfer, or carry-over, of cellular components from mother to daughter cells, which in turn determines the *phenotype* of the offspring. In such way the cells passively acquire the knowledge of the previous environment and the cost of frequent regulatory switches will be mitigated [48]. An example of this mechanism is the so called "non-inherited resistance", referred to a transient invulnerability of cells to antibiotics purely conferred by a *phenotypic switch*. This differs from the non-(vertically) inherited resistance resulting from transposons, horizontally transferred genes or plasmids and mutations in existing genes [61].

In bacterial populations of *Escherichia coli* and *Campylobacter jejuni* subtle changes in gene expression, e.g. phage receptors, were thought to be responsible for the *phenotype* that conferred phage-resistance, "deciding" about the lysis or non-lysis fate of the entire culture. This *phenotypic resistance* rendered phages unable to kill bacterial cells; these latter were virtually sensitive to the phage infection but because of a low transient receptors' expression, phage adsorption was hindered and the cells were not lysed [62].

Bacillus subtilis is able to switch between a proliferative vegetative state and a dormant state when nutrients availability become limiting into the environment. It was recently shown that *B. subtilis* displayed **phenotypic memory** by remembering the state expressed before entering dormancy [60]. The timing of sporulation was different at individual level and the population was constituted of early- and late-sporulating cells. During cell division, the late-sporulating cells "diluted" the amount of metabolic enzymes

(in this study *alanine dehydrogenase* was used as proof of concept) before becoming spores while the early-sporulating did not (because they form spores before dividing). When the conditions became favorable again, early-sporulating cells were able to reinitiate growth already after a weak nutrient up-shift thanks to the carry-over of the pool of *alanine dehydrogenase*, necessary to promptly reinitiate the metabolism and growth. On the contrary, late-sporulating cells needed a strong nutrient up-shift because of the lack of such pool and the necessity of enzymatic induction (Fig. 5-B). The authors named this process as "first in–first out" and they speculated that this behavior could be widespread among other bacterial spore formers [60].

Phenotypic memory was shown for *Escherichia coli* grown in microfluidic chambers under cyclical glucose/lactose nutritional environment; cells were able to remember the previous metabolic adaptation reducing significantly the lag phase between the diauxic shifts [50]. The *lac* operon was shown to be under control of two different types of memory: 1) a **phenotypic memory**, i.e. the "transmitted" cellular concentration of lactose, allolactose, *lac* operon-mRNA and *lac* proteins; 2) a *response memory*, i.e. the ability of the regulatory network to respond even when the inducing signal is removed. The first type was supposed to help maintaining an adapted state for multiple generations when longer shifts in carbon sources occurred, the second type took place upon rapidly changing conditions. These two different types of physiological memories were suggested to allow for the adaptation of *E. coli* to a wide range of fluctuations depending on their timescale occurrence [50].

Interestingly, a recently published work has speculated that both mechanisms, **epigenetics** and **phenotypic memory** can happen in parallel within isogenic populations of *E. coli* and *B. subtilis* [63]. Each of the parental DNA strands is associated to so-called "strand-specific hyperstructures"; these **epigenetic structures** are segregated to different positions during the replication of the chromosome upon cell division. The inheritance of one of the parental DNA generated a strand-specific *phenotype* and it was supposed to be responsible for **cell-to-cell differences** in growth rate; one subpopulation inherited the hyperstructures which led to a slow-growing *phenotype* while the other inherited the hyperstructures imposing fast-growing *phenotype*. In conjunction with this **epigenetic** transmission, **phenotypic memory** could occur because during cell division there is a partition of RNA polymerases, ribosomes, transcription/translation regulators, and DNA-binding proteins. This unequal carry-over of these biomolecules in the daughter cells was supposed to contribute to the observed *phenotypic switch* in growth rate [63].

Although the occurrence of a certain genetic variability cannot be excluded, especially considering the speed of bacterial replication and growth, it has to be considered that genetic mutations will not be really beneficial for the population as a whole. Indeed, if a mutation is fixed in the DNA and is transmitted to the offspring, the new mutants will scarcely adapt to the environment as soon as sudden fluctuations occur again. In such scenario, non-genetic variability would be preferred: while cells keep bearing the original genetic makeup, their *phenotypes* will adapt faster and concurrently to the external conditions. On the other hand, the genetic variability could become beneficial when the environmental changes last for long periods; in this case, the new *phenotype* will be better adapted to a permanent change.

1.3 Phenotypic heterogeneity in metabolic traits: metabolic heterogeneity

The stochastic nature of biochemical processes affects the metabolic activity within isogenic populations [15,17,29,64,65]. **Cell-to-cell variability** in metabolic traits is usually referred to as **metabolic heterogeneity (MH)** [66,67] since the observed *phenotype* in this case would be a specific metabolic function. Metabolic pathways are controlled by cascades of molecular events, in turn tuned by few key regulator factors; stochastic fluctuations of these factors were supposed to be responsible for the outcome of subpopulations, which will perform metabolically differently [15,19]. Theoretical models have shown that asymmetric partitioning of metabolic enzymes or large enzyme complexes may cause immediate metabolic differences in daughter cells upon division, being both gene expression and genome duplication random processes [68]. The environment surrounding the cells strongly influences the metabolic behavior of the population but which factors are mainly responsible for the display of **MH** is still an open question.

So far, it has been suggested that the major environmental driver of **MH** is nutrients limitation, especially when occurring together with temporal and spatial fluctuations [67]. In clonal populations subjected to scarcity of nutrients, electron donors or electron acceptors, **MH** increased [69-71]; fluctuations of such resources such as nutrient up-shift after long starvation were responsible for the outcome of subpopulations with distinct growth *phenotypes* and metabolic activities [72]. Spatial limitation was also shown to be a driver of **MH**. *E. coli* cells grown on microfluidic chambers created nutrient gradients alongside the channels with the subsequent formation of two distinct subpopulations that cross-feed each other [73]; this spatial distribution created heterogeneous microenvironments which caused the generation of subpopulations with different growth- and gene-expression rates. Such differences were suggested to allow the subpopulations to become stress resilient during alternating substrate injection [73] and antibiotic exposure [74]. Besides the special distribution and differentiation within biofilm [75], fluctuations in space and time favored the metabolic codependence, i.e. peripheral and internal cells alternated cyclically metabolic phases with a reciprocal benefit, on one side preventing the starvation of the inner biofilm and on the other side allowing for colony growth toward the periphery [76].

Nutrients shifts from glucose to the gluconeogenic substrates induced the emerging of two cellular subpopulations: one growing and one non-growing, indicating heterogeneous adaptation occurring just after the shift [64]. Such responsive diversification was suggested to reside at the core of central metabolism and strongly depended on the metabolic fluxes within each individual cell. The occurrence of two distinct growth *phenotypes* underlaid a **bistable** control: if the flux inside the cells was below a certain watershed, cells chose the non-growing *phenotype* entering the dormant state, otherwise cells continued to grow quickly switching to gluconeogenic substrates [64].

Single cells are challenged for the optimization of their fitness in temporally and spatially fluctuating environments. Displaying **cell-to-cell variations** has functional consequences because it allows the whole population to benefit in fitness or survival even if one or more subpopulations will succumb [77]. Besides stochasticity, isogenic microbial populations have evolved two main strategies to display **phenotypic** and

MH heterogeneity, which reflect different response mechanisms to fluctuating and ever-changing environments: **bet-hedging** [78] and **division of labor** [79] (Fig. 6) [31,32,77,80-82].

The **bet-hedging** strategy, literally counterbalancing the wager, does not require a real interaction or communication within different members of the population but it requires a certain investment from the cells. This risk-spreading strategy pays back because when the fluctuation is gone the population as whole will survive, in spite of the subpopulation that will not [83-85].

When facing a diauxic shift from glucose to a less-preferable carbon source like cellobiose, isogenic populations of *Lactococcus lactis* differentiated in two subpopulations, one dividing and continuing growing on the new substrate and the other stopping growing [86]. The cellobiose consumption from individual cells strongly depended on the stringent response, a negative control of catabolism for minimizing energy use, and the carbon catabolite repression, a regulatory system which determines the order and the cell preference of multiple sugar sources. The interplay between these two mechanisms generated the alternation of metabolic states, presumably as result of **bet-hedging** strategy. Interestingly, the non-growing *phenotype* on cellobiose was able to resume growth on another source much faster than cellobiose-specialized cells; the promptness of individual cells to adapt to fluctuations in the environment further suggested the evolutionary advantage of **MH** [86].
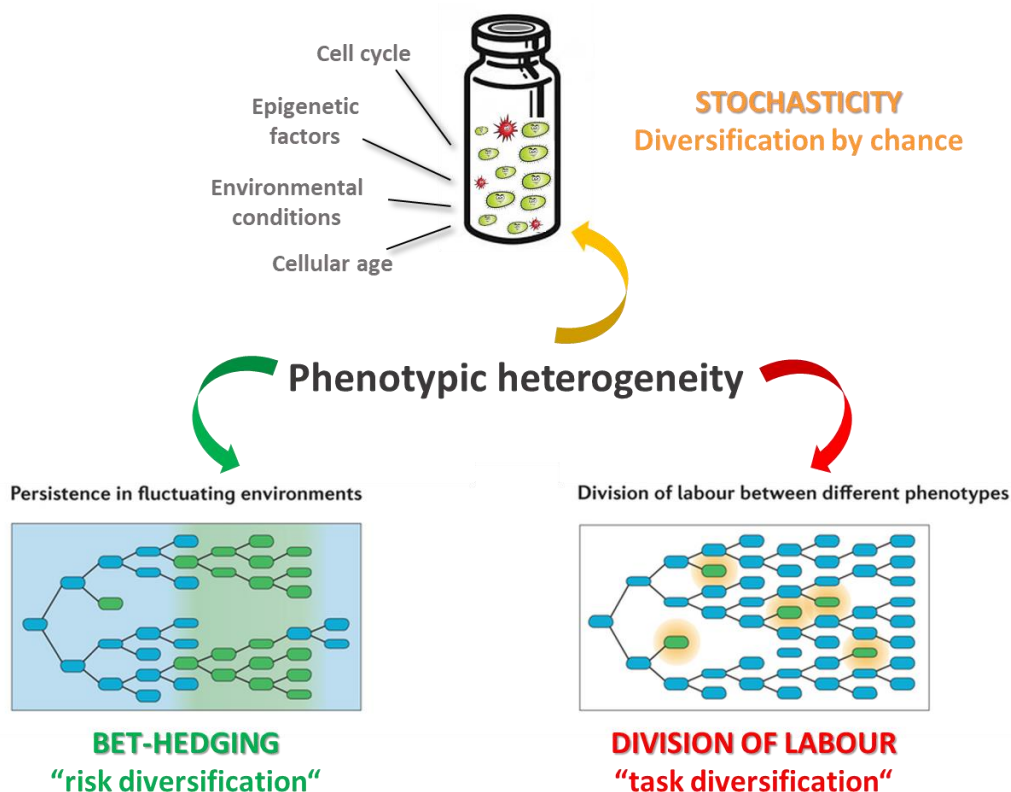

Figure 6. Different ways of displaying heterogeneity in microbial populations. Stochasticity is a constitutive feature of biological systems. **Bet-hedging** and **division of labor** are different strategies used by microorganisms to take advantage from the diversification within the population and increase its survival under changing environmental conditions. Image modified from [77].

The **division of labor** strategy consists in the formation of two or more subpopulations, each having a different task in a shared pathway, for the common benefit of the population. The **division of labor** involves interactions between cells or subpopulations and is based on a collective behavior rather than a selfish and competitive one as for the **bet-hedging**. Environmental fluctuations over time, such as shifts in temperature or from oxic to anoxic conditions, boosted **MH** of *Candidatus* Microtrhix parvicella [87]. Within the same filament, individual *Ca*. M. parvicella cells differed a lot in substrate uptake providing an example of **division of labor**. The high activity of some cells in the same filament was suggested to support the low or non-activity of the rest, enabling the whole population to better cope with the ever-changing environment inside biological wastewater treatment plants [87]. Microfluidic experiments with *B. subtilis* showed that bacteria engage in **division of labor** when growing on two carbon sources [88]. Co-consumption of glucose and malate usually causes the accumulation and secretion of high levels of acetate, which in turn may be toxic for the cells [89]. However, under these conditions two different subpopulations emerged: one growing on glucose and malate and secreting high level of acetate and the other specialized on the conversion of acetate to acetoin, which was nontoxic for the cells. This subpopulation appeared just when acetate started to accumulate in the medium, showing the advantage of such metabolic specialization for the benefit of the whole population [88].

Interestingly in some case **division of labor** strategy can be the consequence of a **bet-hedging** scheme in which bacteria engage, as for example in various biodegradation pathways. *Pseudomonas putida* mt-2 isogenic populations degrade aromatic compounds via the *TOL* plasmid [90]. The *TOL* transcriptional network encompasses two operons that encode for i) the upper pathway, which serves to process m-xylene or toluene and ii) the lower pathway, which encodes for meta-enzymes for the conversion of intermediates such as benzoate or 3-methyl benzoate in central metabolic intermediates, i.e. pyruvate and acetaldehyde. In the presence of m-xylene and succinate, the *TOL* network followed **bimodal** activation, resulting in a subpopulation able to grow on m-xylene and a subpopulation growing just on succinate [91]. Besides this **bet-hedging** strategy, it has been shown that the cells using the *TOL* plasmid engaged in different segments of m-xylene catabolic pathway, i.e. one subpopulation activated just the upper pathway, providing intermediates to the other subpopulation, which activated just the lower pathway [92]. This metabolic specialization of *P. putida* mt-2 was suggested to be an example of **division of labor** as strategy used to balance the cost-benefit of an energy-demanding biodegradation process [93].

There is a growing body of evidences supporting the phenomenon of **MH** and nowadays it is receiving a lot of interest because of its implications in many fields especially medicine and biotechnology [66,94-99]. The reason resides in the fact that striking and insightful examples of physiological and **metabolic cell-to-cell variations** have been possible just with the emerging of **single-cell techniques**, which are able to provide information at individual-cell level. The concept of *individuality* allowed for understanding the importance of features and behaviors of single cells and will be discussed in the next section.

1.4 *Single-cell techniques for studying heterogeneity*

The field of single-cell approaches is rapidly growing, shading light on the physiology of individual cells within a population [100,101]. The implementation of **single-cell techniques** has indeed brought to the understanding that the behavior of an individual bacterium often differs from the average of its own population. Therefore, **single-cell techniques** became essential for studying phenotypic and **MH** since they are able to give insights on many levels of information: intracellular components or genetic circuits regulation, individual-cell dynamics in space and time, morphological and physiological states and cell-to-cell interactions in a population or a group [102-105]. However, our understanding is still limited and the further development of single-cell analyses and techniques will continue to be indispensable [106]. Several **single-cell techniques** are applied for studying heterogeneity. As a very general principle, it is possible to divide them in *high-throughput* and *low-throughput*. While *low-throughput* methods provide for spatially resolved information on the isolated cells, this is usually not possible with *high-throughput* methods. The choice of one of these two categories usually depends on the research question behind. In this section, the focus will largely be on the technique used for my PhD work and to a lesser extent on the other **single-cell techniques**, which will be just briefly presented.

1.4.1 Nanoscale Secondary Ion Mass Spectrometry (nanoSIMS)

Methods for microbeam analysis characterize the elemental composition of a sample, giving both qualitative and quantitative insights at **single-cell level** resolution with high sensitivity [100,106,107]. A very powerful microbeam technique is nanoscale Secondary Ion Mass Spectrometry (nanoSIMS) for isotopic and trace elements analysis at high spatial and mass resolution, and high sensitivity, qualities that render this instrument unique (Fig. 7-A). A primary ion beam bombards the sample surface, triggering a collision cascade and causing the production of secondary ions; the latter are ejected from the sample surface and transferred to a mass spectrometer, where they are separated according to their *mass-to-charge ratio* (*m/z*) [108-110]. Thus, secondary ions are collected for each individual pixel while scanning a precise area (raster), usually no larger than 100×100 μm^2. The isotopic and elemental distribution maps of the analyzed sample are given by the secondary ion counts per pixel per unit time and the chemical mapping (i.e. imaging) is possible for up to 7 masses simultaneously. Using specific software, such as WinImage (from CAMECA), OpenMIMS [111], L'Image (developed by Nittler L. R., Carnegie Institution of Washington), Look@NanoSIMS - LANS [112] (a review on the different software tools is given by [113]), it is possible to correct for detector dead-time, quasi-simultaneous ion arrival (QSA) and lateral drift as well as to calculate isotope and elemental ratios.

In combination with *Stable Isotopes Probing* (SIP), i.e. using isotope-labeled compounds as tracers, SIP-nanoSIMS technique allows for the quantitation of assimilated elements into the cell biomass from the changes in isotopic composition upon uptake of each single cell, due to its high lateral resolution, down to

35 nm, and a mass resolving power M/ΔM > 8000 [104,111,114-117]. For this reason, SIP-nanoSIMS technique was recently applied in several studies analyzing **MH** of microbial populations [69-71,87,118,119].

The use of nanoSIMS has many applications in the analysis of different biological samples, particularly microorganisms which require high spatial resolution [114,120-122], and allows alone or in combination with other techniques to track microbial intra- and inter-species interactions as well as symbioses [104,116,117].
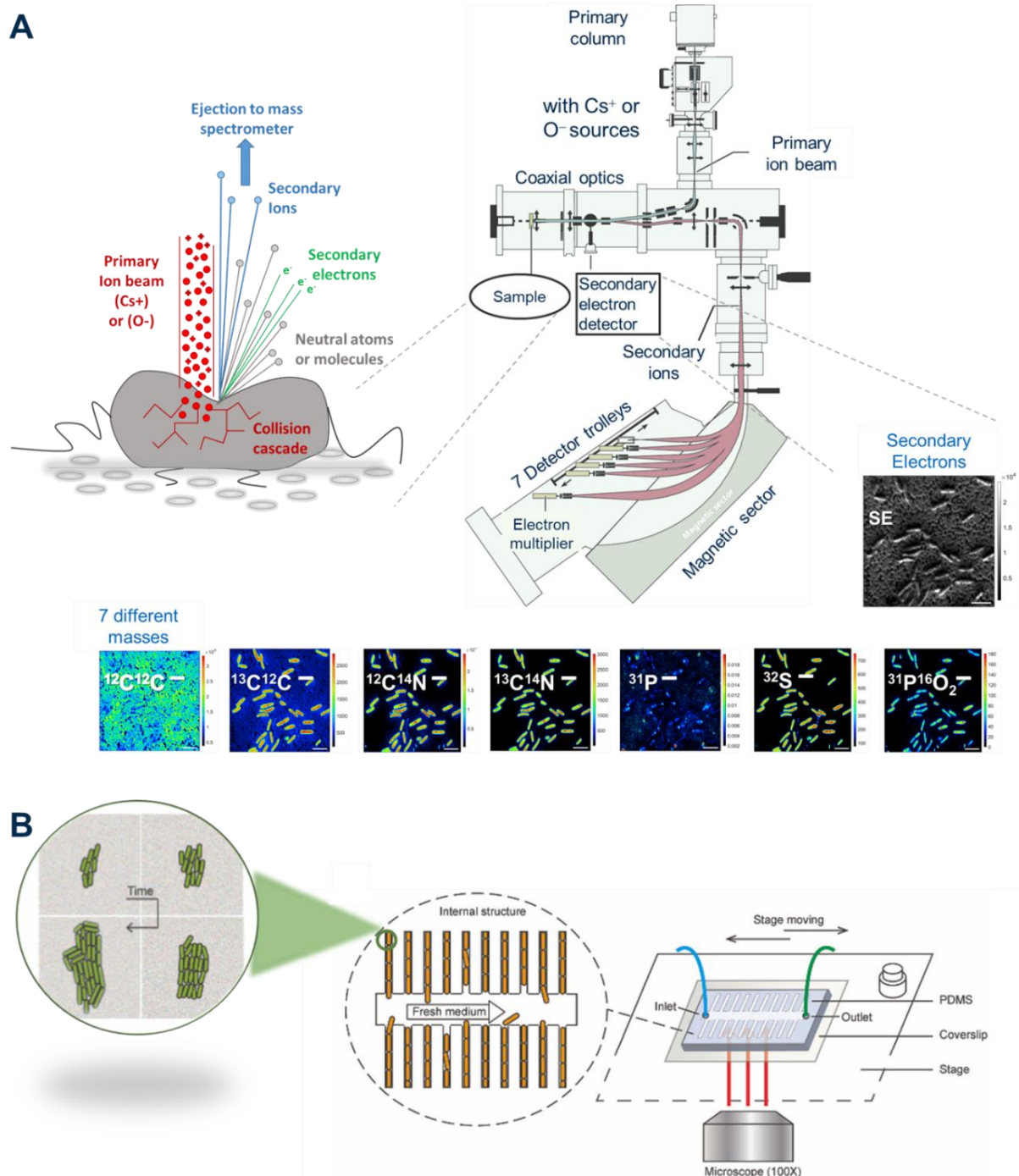

Figure 7. Example of the two main **single-cell techniques** used for **metabolic** and **phenotypic heterogeneity** studies. **A)** nanoSIMS technique, mainly used in my project. **B)** Time-lapse in microfluidic devices with fluorescence microscopy. Figure 7-**B)** modified from[101].

A very powerful approach with the nanoSIMS is the possibility to combine such technique with Fluorescence In Situ Hybridization (FISH, [123]) and Catalyzed reporter deposition-FISH also known as tyramide signal amplification (CARD-FISH, [124]) for linking cells' identity with their metabolic activity in complex microbial populations. FISH and CARD-FISH give information on the phylogenetic identity of single cells, being based on a specific probe which targets the ribosomal RNA. For FISH applications, the probe has a fluorescent dye directly attached on it at the 5'-end (Fig. 8). For CARD-FISH a Horse Radish Peroxidase (HRP) is attached to the 5´of the probe and in a second step the cells are treated with tyramide coupled with a fluorophore; many tyramide molecules will react in the vicinity of HRP-probe, and will be deposited in the vicinity of HRP binding site, in the presence of the H_2O_2, allowing for an amplification of the fluorescence signal (Fig. 8).
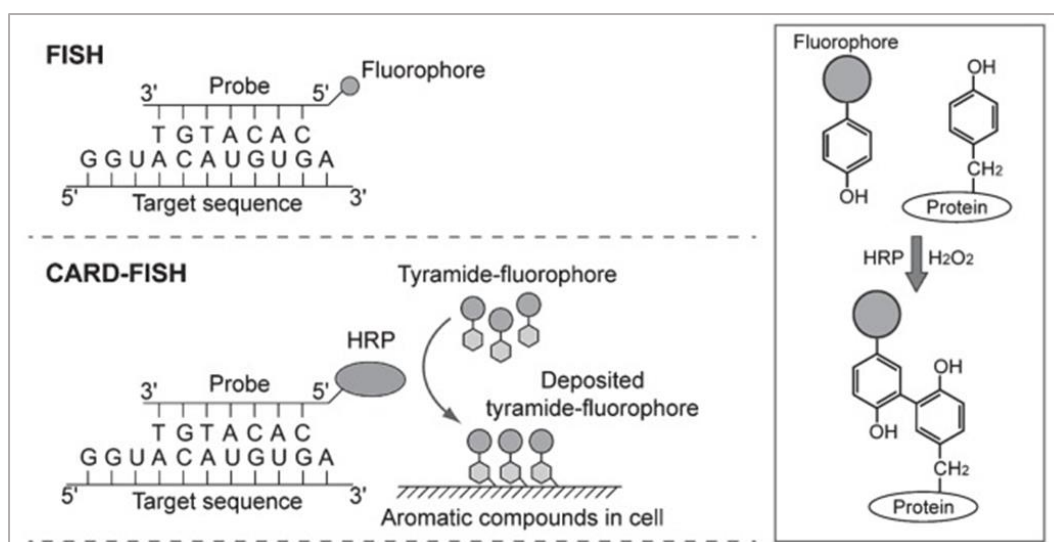
Figure 8. Schematic depiction of FISH and CARD-FISH adapted from[125].

Cell identification for both FISH and CARD-FISH is done using a florescence microscope equipped with filters corresponding to the excitation/emission of the fluorescent dyes used to label the probes or the tyramides [125]. While FISH or CARD-FISH are used to identify the cells phylogenetically, the nanoSIMS analysis gives insight on the elemental and isotopic composition and distribution at sub-cellular level as well as on the metabolic activity of the cells [126]. Moreover, in complex microbial communities, co-cultures or consortia it is possible to study the mutualistic metabolic pathway and syntrophic interactions [127] and [128,129](see appendix).

1.4.2 Microfluidic techniques

Microfluidic techniques allow for the manipulation of reduced amount of fluid, incorporating both sorting and analysis of small biological samples, such as microorganisms and molecules into a small-scale system working with a laminar flow. Usually, the cells flow inside micro-channels, which can be very tiny,

and can be afterword collected for further analysis. An interesting application of microfluidic system is the droplet microfluidic which allows separating single cells inside small droplets; the latter will be further processed with other techniques or used for cell growth assays and cell-to-cell interactions studies. Compartmentalization in droplets can be useful as a method for linking *phenotype* to genotype of each single cell, for instance specific responses after drug treatment, virus infection and antigenicity [130].

Another application always combined with microfluidic is time-lapse microscopy, the recording of sequential microscopic images from which a movie with the population history can be extracted. Combining the monitoring of cells on micro-spatial scales in microfluidic channels with the fluorescence observation made possible to measure cellular properties, intracellular dynamics, gene expression, protein transcription and single-cell response to environmental cues [101]. The monitoring of spatiotemporal dynamic with microfluidics and time-lapse microscopy (Fig. 7-B) allowed to unravel some of the mechanisms responsible for **phenotypic heterogeneity** in stress response of *Mycobacterium tuberculosis* [131] and **MH** in response to antibiotics treatment, spatial and nutritional limitations [73,74,132]. The power of microfluidic lies in the possibility to control and change the chemical composition of growth medium by continuous perfusion, while observing the behavior of single cells in temporal and spatial scale. However, the perfusion itself may be also a disadvantage when studying, for instance, cell-to-cell-interactions, environmental signals, or protein secretions, since these molecules cannot accumulate but are continuously washed away [133].

1.4.3 Spectroscopic techniques

Spectroscopic methods can provide biochemical information on the molecular composition of single cells at different levels of lateral resolution. Raman spectroscopy and Surface Enhanced Raman spectroscopy (SERS) techniques are probably the most exploited for microbial studies [134]. Raman spectroscopy exploits the inelastic scattering of a very small number of photons, the so called Raman scatter, which depends on the chemical structure of the analyzed samples [135]. As a result, a Raman spectrum is obtained which encompasses a number of peaks, showing the intensity and wavelength position of the Raman scattered light, each providing information on the types of chemical bonds and on the molecular conformation within the cell. Single-cell Raman spectrometry often coupled with laser tweezers, is a non-invasive technique, which has been applied for investigating the biochemical and morphological heterogeneity of microbial populations [136,137]. Laser tweezers and other optical tweezers techniques are essential for single-cell isolation, a prerequisite for analyzing individual cell and hence study cell heterogeneity [138]. Confocal Raman micro-spectroscopy has been largely applied in biology [139] even in combination with SIP [140]. However, the main drawback for the application of Raman-SIP in the study of **cell-to-cell MH**, is the relatively high enrichment in heavy isotopes that cells have to incorporate in order to achieve a good peak resolution (sensitivity), e.g. for ^{13}C a minimum of 10at% (atomic percent) is required [140]. Additionally, the interpretation of metabolic pathways and the quantitative contribution of isotope-labelled-compounds incorporation into microbial biomass with Raman-SIP is difficult and the

method is undoubtedly less sensitive than SIP-NanoSIMS approach [140]. The lateral resolution achieved by Raman is primarily defined by the combination of laser wavelength and microscope objective, ranging from 250 nm up to 1 μm, while the depth resolution can span from ~1 to 6 μm [141-143]. Moreover, this technique has other downsides, such as auto-fluorescence of certain samples that interferes with Raman signal, low sensitivity (signals are weak especially at single-cell level), relatively slow acquisition time and time-consuming data processing [139,142]. These last features indeed make even the Raman a *low-throughput* technique but less sensitive in comparison with nanoSIMS.

1.4.4 Flow cytometry

One of the most applied single-cell *high-throughput* techniques is flow cytometry. This technique rapidly analyses single cells while "flowing" alongside channel, giving both quantitative and qualitative insights [144,145]. This includes, for example, the use of fluorescent activated cell sorting (FACS) approaches to sort, count and recover cells of a specific size and with specific florescence, which in turn indicates specific functions or even the presence of photosynthetic pigments [146]. Cytometry combined with cell sorting has been extensively used for detection of heterogeneity within isogenic populations [98,147-149] since each individual cell is analyzed for both fluorescence and visible light scatter. The latter can be measured as Forward Scatter light (FSC), which give insights about cell size and Side Scatter light (SSC), which further provides information on the cell complexity or granularity according to the light refraction [150].

The applicability of flow cytometry in single-cell studies is further exploited by its linking to other *high-throughput* techniques such as transcriptomic, genomic, metagenomics approaches, i.e. the recovery of RNA, DNA from single cells obtained from laboratory cultures or directly from the environmental samples [151-153]. Once the cells are sorted and segregated, they can further undergo genomic [154], proteomic and metabolomic analyses, applied for the study of physiological single-cell heterogeneity [101]. However, the dynamism of the single-cell metabolism and the quick turnover of most of the intracellular proteins cannot be captured by these techniques [155]. Moreover, most of the single-cell "omics" approaches have the limitation to require a high amount of material for a reliable and sensitive analysis, which sometimes might be difficult to obtain [156], especially for microorganisms. This is a current challenge that scientists have to tackle, giving the raise of multiomics approaches application and the contextual need for a better understanding of the dynamics of intracellular pathways and the mechanisms responsible for heterogeneity.

It is important to remark that each method delivers a different type of information. None of the above is able to measure the isotopic composition of individual cells with a combination of high precision and high lateral resolution, features that make nanoSIMS unique for the investigation **of metabolic activity at single-cell level**. The other techniques can offer important information on physiological, metabolic, or *phenotypic traits*, but missing the quantitative precision, e.g. assimilation of isotope-labelled substrates per cell, that it is very valuable when studying **MH**.

2. Knowledge gaps

The advent of **single-cell techniques** has facilitated the study of individual cells revealing that each population is composed of *phenotypically* distinct subpopulations, although genetically identical. In fact, the possibility to investigate each individual cell within an isogenic population is extremely valuable in combination with bulk analyses and omics methods. Thanks to the single-cell approaches, it is possible to increase our understanding of many biological phenomena, especially regarding the physiology and the metabolism of microbial populations. Despite the huge plethora of insightful studies about **phenotypic** and **metabolic heterogeneity (MH)**, there are still many unsolved questions regarding this phenomenon.

The main scope of this work was to investigate the influence of various factors on the **MH** of microbial populations, to provide a broader understanding of this phenomenon in model organisms and synthetic systems and then to extend its significance in natural microbial communities. In this perspective, the whole doctoral project was divided in the following specific objectives:

1. Optimization of sample preparation for cell-integrity preservation and reliable measure of cellular isotopic content.

2. Method validation for: a) quantitation of assimilation rates and b) quantitation of **MH**.

3. Assessing the influence of abiotic factors such as C-source concentrations, different growth substrates, and electron acceptors on the display of **MH** in three model microbial strains.

4. Assessing the influence of microbial interactions such as Bacterial-Fungal-Interactions (BFI) on bacterial **MH**.

5. Assessing the influence of emerging contaminants, such as antibiotics, on the ecophysiology and the **MH** of natural microbial communities.

3. Results and discussion

To study metabolic heterogeneity (**MH**) and the factors that may be responsible for this phenomenon, SIP-nanoSIMS approach was used in the present work. However, in order to achieve accurate information on the extent of **MH**, a series of upstream measurements and calculations are necessary, which, if not considered properly, may lead to errors. For instance, it is pivotal to preserve the integrity of the cells during sample preparation prior to nanoSIMS, in order to avoid massive loss of cytoplasmic content and therefore strongly underestimate the cellular elemental content. Then, it is essential to have a common way to measure assimilation rates after nanoSIMS analysis to compare reliably the metabolic activities between single cells. Finally, it is fundamental to have a parameter for the quantitation of the degree of **MH** **displayed** under different environmental conditions. To date, such comprehensive approach is still missing but urgently needed for the **quantitation of heterogeneity**.

3.1 Optimization of sample preparation

A suitable protocol for nanoSIMS analysis usually has to fulfill few main requirements: 1) usage of a relatively low number of chemicals, 2) low exposure times to chemicals, 3) usage of chemicals that are less damaging to cells, in order to preserve cell integrity and native chemical composition, 4) complete dehydration of the specimens to stand high vacuum, 5) samples have to be either conductive or deposited on a conductive substrate. In general, the first step of sample preparation requires the concentration of liquid cell suspensions on porous polycarbonate filters coated with thin conductive layer. But filters and samples need to be as flat as possible in order to be efficiently ionized upon nanoSIMS analysis and avoid the so-called topography effect. In fact, the samples topography is responsible for aberrations and shadow effects (Fig. 9) [113,157], and influences the ionization trajectories of secondary ions into the spectrometer, thus impacting the imaging, the pixel by pixel-ion mapping and the ions quantification (Fig. 9) [113,158].
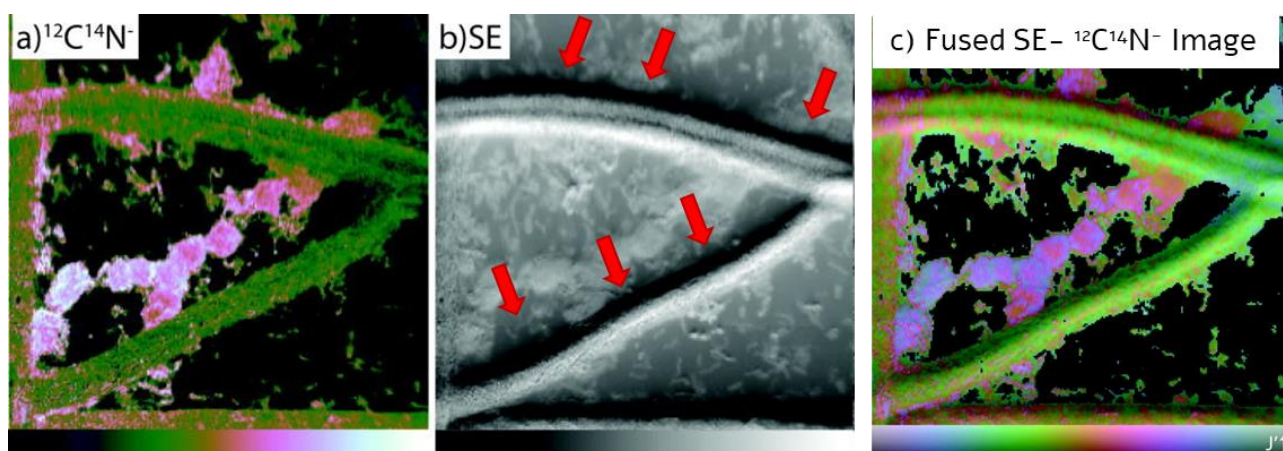
Figure 9. Example of distortion due to topography and ions-distribution effects within a single image. **a)** $^{12}C^{14}N^{-}$ secondary ions and **b)** secondary electrons (SE) nanoSIMS images of a cyanobacterial microbial consortium; **c)** represents the merged image of **a)** and **b)** with a scale intensity realized with special python's cubehelix software [113]. Shadow effects are shown with red arrows, which distort the signal in **c)**. Figure panels are modified from [113].

In principle, a sample preparation that is suitable for Scanning Electron Microscopy (SEM) imaging works also for SIMS imaging [159]. However, one has always to test the preexisting protocols and validate the suitability for specific samples, since different organisms may require different protocol adaptations. Moreover, while SEM analysis provides morphological information about the specimen, nanoSIMS analysis additionally provides chemical information at nanoscale resolution; therefore, it is essential to preserve cells shape, to consequently preserve their isotopic and elemental content. Because the quality of the samples will strongly influence the quality of the measurements, it was necessary to invest a lot of effort in the sample preparation protocols prior to chemical imaging analysis.

Classical protocol

The classical protocol usually includes a first step of chemical fixation with either Paraformaldehyde (PFA) or Glutaraldehyde (GA) followed by washing steps to remove excess of fixative and afterwards a post-fixation procedure that increases the preservation of the cellular morphology [160-163]. Fixation cross-links mainly proteins while post-fixation is done with oxidizing agents for keeping the cells-structural information as well as achieving a better contrast during SEM imaging [162,164] (Sketch 1). The post-fixatives mostly used are osmium tetroxide (OsO_4) or potassium permanganate ($KMnO_4$), which are strong oxidative and staining agents [165,166]. After these steps, the cell walls usually become stiffer but their cytoplasmic content is still liquid [167].

Water has a high surface tension to air, meaning that the cohesive bonds of water molecules to one another form a strong barrier between the atmosphere and the water. When cells are immersed into the aqueous solutions and they are left to air-dry, the surface tension of the water exerts a huge force on the cells, pressing on their surface and causing damages to the cell walls [168]. Therefore, a water-substitution step is necessary to facilitate dehydration while preserving the cells structure. The commonly used techniques for water substitution are: HexaMethylDi-Silazane (HMDS); 1-Butyl-3-Methylimidazolium tetra-fluoroborate (Ionic Liquid, IL); Acetone or Ethanol (EtOH). The principle is the same for all: slow and gradual substitution of the water content inside the cells with the above-mentioned fluids, which create less surface tension and evaporate with minor effects on the cells shape [168] [167,169]. In the case of IL, after immersion in a solution of 4% IL dissolved in distilled deionized water (ddH_2O), the samples are air-dried [170]; for HMDS, water is first substituted with EtOH, then EtOH is substituted with HMDS and finally samples are air-dried [171,172]; for acetone, methanol or EtOH, a series of gradually increasing concentration is used to substitute water inside the cells while the alcohols are then dried with a critical point drying (CPD). The latter exploits the critical point of CO_2, in which EtOH can mix acting as inert fluid. At a certain temperature and pressure, CO_2 can be found at the liquid and gaseous phases together and when its critical point is reached, the transition from liquid to gas will be possible without any disruption of the cells [167]. EtOH is usually preferred for bacterial preparation, since acetone has a lower viscosity and induces a more rapid dehydration process; additionally, acetone is more hygroscopic and may lead to incomplete dehydration with the resulting disruption of cell integrity [161].
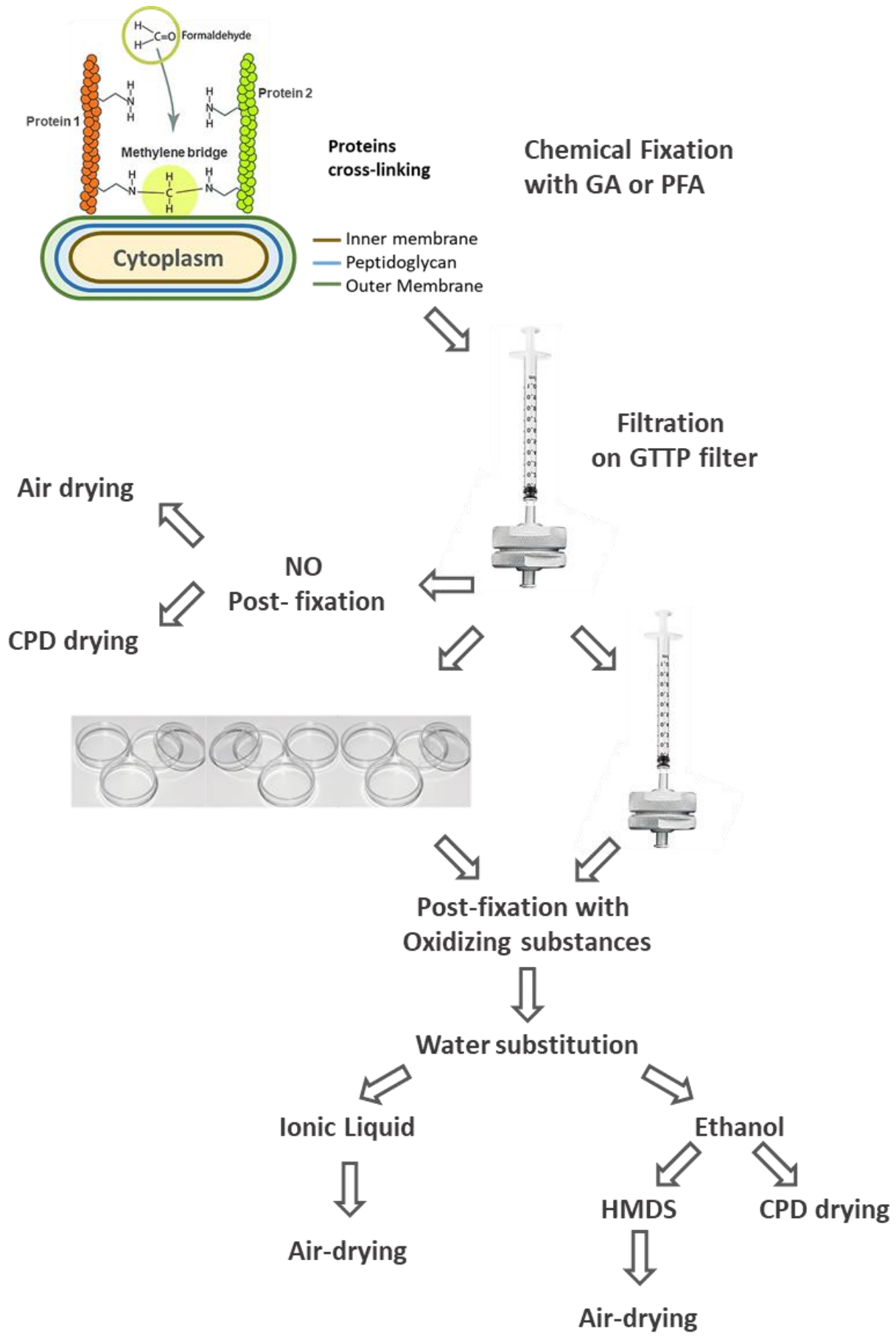
Sketch 1. Protocols applied for sample preparation prior to SEM observation.

Protocol optimization

The sample preparation optimization was done for i) single bacterial species and ii) bacteria and pseudo-fungi co-cultures.

Maintaining cells' morphological and chemical integrity for single bacterial species

i) The first part of sample preparation optimization was done with *Pseudomonas putida* mt-2 KT2440 as model organism.

Cells were fixed with either 4% PFA or 3% GA in cacodylate buffer (CB) (0.2 M, pH 7.4, EM Science, Hatfield, Pennsylvania) overnight at 4°C. After fixation, cells were filtered and distributed onto Gold Palladium (Au/Pd)-coated filters (GTTP type, 0.22 μm pore size, 25 mm, Merck). Pieces of filter were used to apply different post-fixation agents after each of the fixative: KMnO4, OsO_4 or H_2O_2 1% v/v in ddH_2O or no post-fixation. Water substitution was performed with EtOH (30, 50, 70, 80, 90, 96 and 100%; 3 min each), HMDS in EtOH (50 and 100%, 5 min each), 4% v/v IL in ddH_2O, and drying either with CPD or air (Sketch 1). Samples were observed with SEM to check the cells' integrity and the quality of the sample preparation.

The first preparations were done using PFA or GA as fixatives, $KMnO_4$ or OsO_4 for post-fixation and the 3 above-mentioned methods for water substitution (Figs. 10, 11). The best results were achieved with OsO_4 followed by CPD drying with both fixatives. The protocol with OsO_4 is strongly recommended when the main aim is keeping the surface structural information for imaging with SEM or Helium Ion microscopy (HIM), e.g. to visualize the interactions between predator-prey and study their life cycle [173] or within microbial co-cultures able to oxidize ethane [128] (see appendix). OsO_4 was largely used as staining in protocols for electron microscopy due to its property to penetrate the cells and react with lipids [174].

However, the introduction of this oxidant may change the chemical composition as well as the nature of chemical bonds, influencing the ionization under the primary ion beam during nanoSIMS analysis [113] and thus the chemical imaging.

Hydrogen peroxide (H_2O_2) was successfully applied as method for oxidized-protein labeling in mass-spectrometry (MS)-based proteomics. Oxidizing specific chemical groups of the proteins made them easier to be detected, separated and quantified with MS [175]. We aimed to use the oxidative principle of H_2O_2 for the post-fixation, because it is less penetrant and cause mostly *in situ* oxidation [175] in comparison with OsO_4 and $KMnO_4$. Therefore, in a further attempt, bacterial cells were post-fixed using 1% H_2O_2 in ddH_2O, or trying with no post-fixation at all. In parallel, different concentrations of GA were also tested to evaluate the possibility to decrease the concentration of fixative as well (Fig. 12). No post-fixation followed by CPD-drying resulted in the formation of holes in the membranes, and presumably loss of cytoplasmic content (Fig. 12); no post-fixation in combination with air-drying resulted in the collapse and the disruption of cell morphology (Fig. 12).
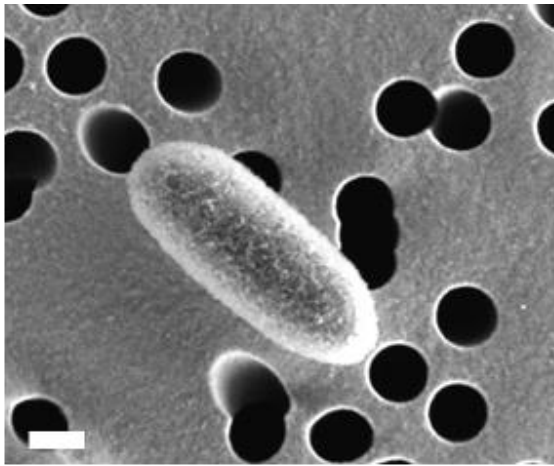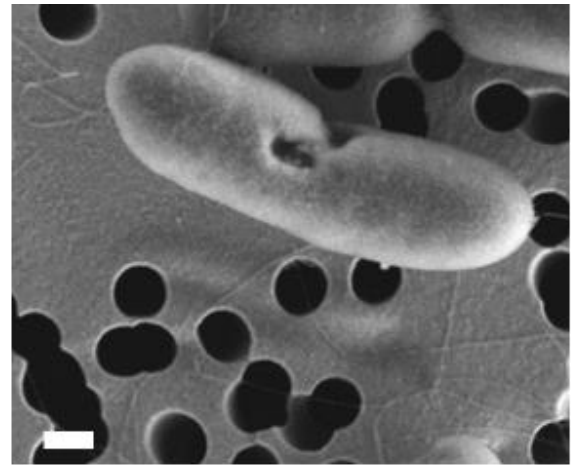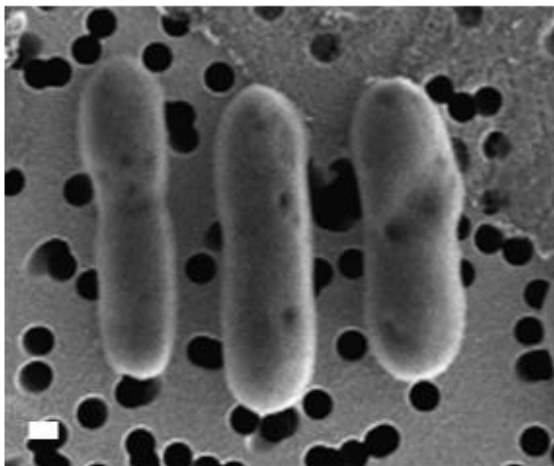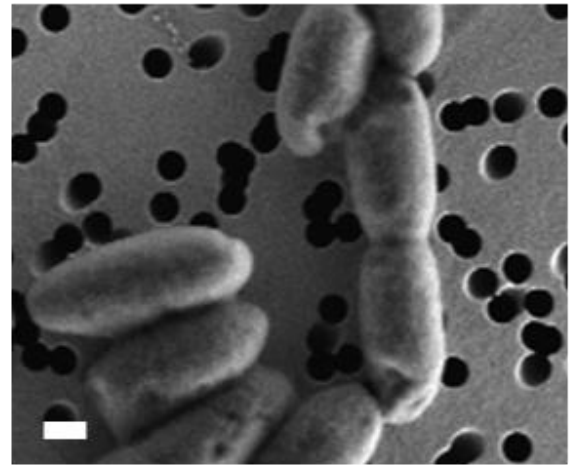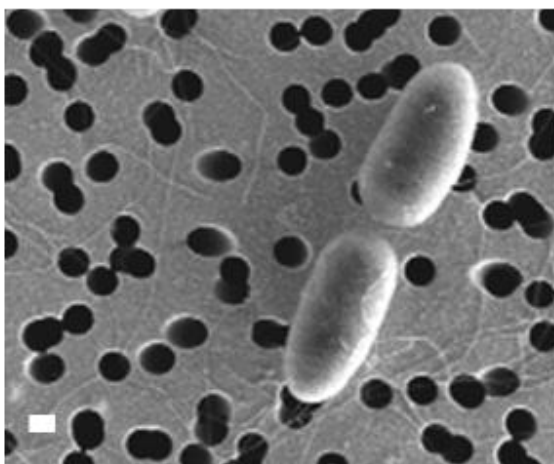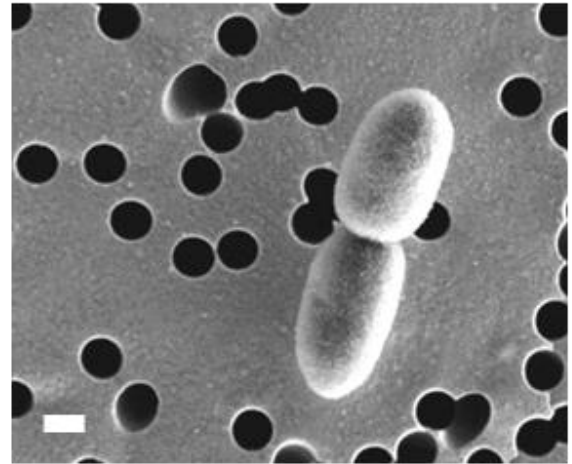
Figure 10. *P. putida* cells prepared with different protocols after PFA fixation. White bars correspond to 200 nm.
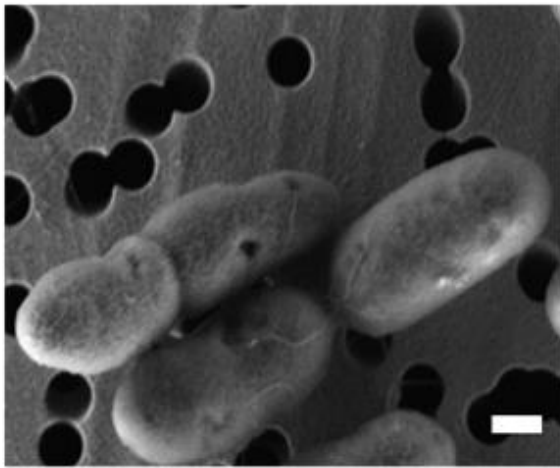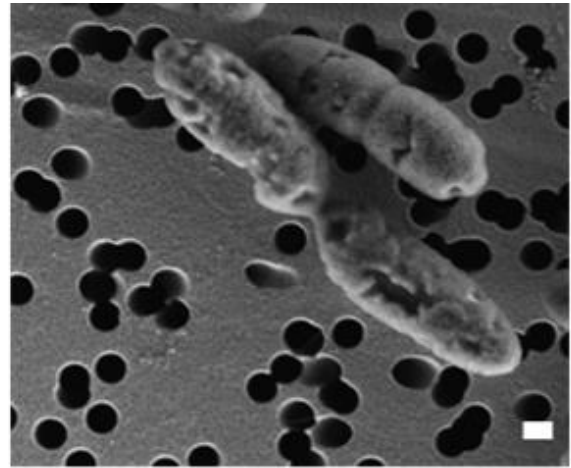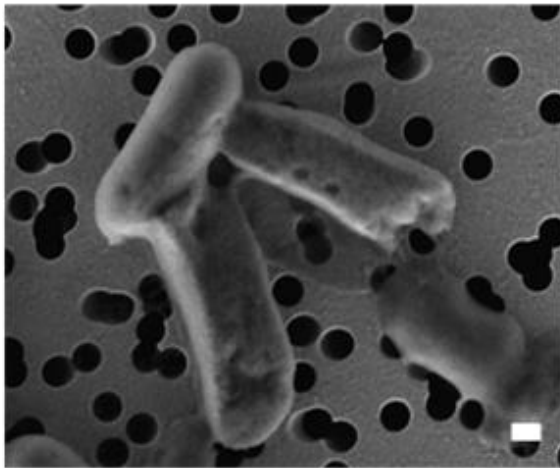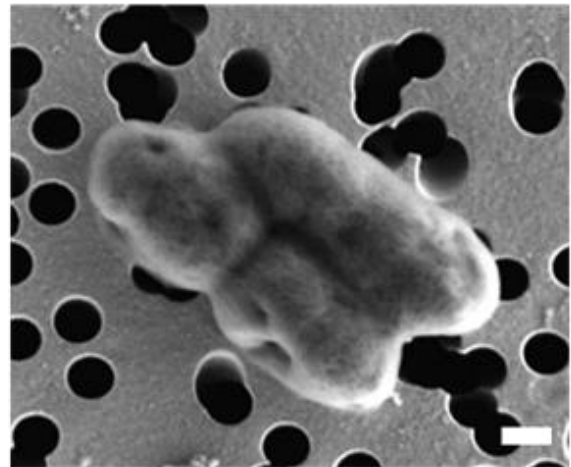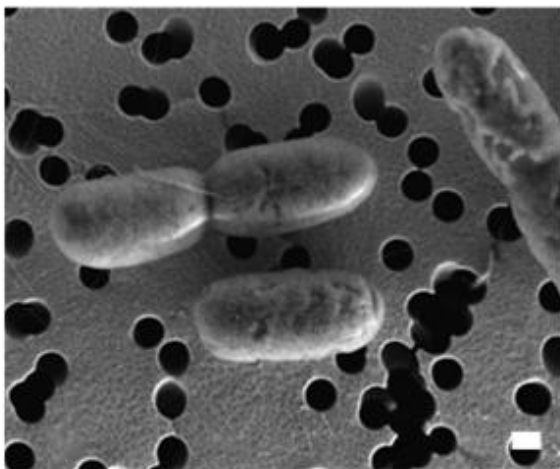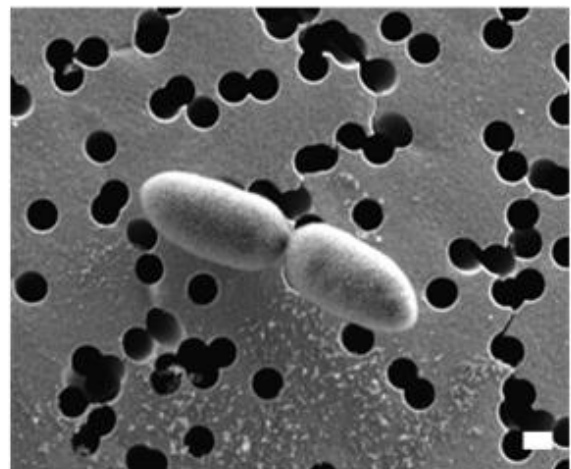
Figure 11. *P. putida* cells prepared with different protocols after GA fixation. White bars correspond to 200 nm.
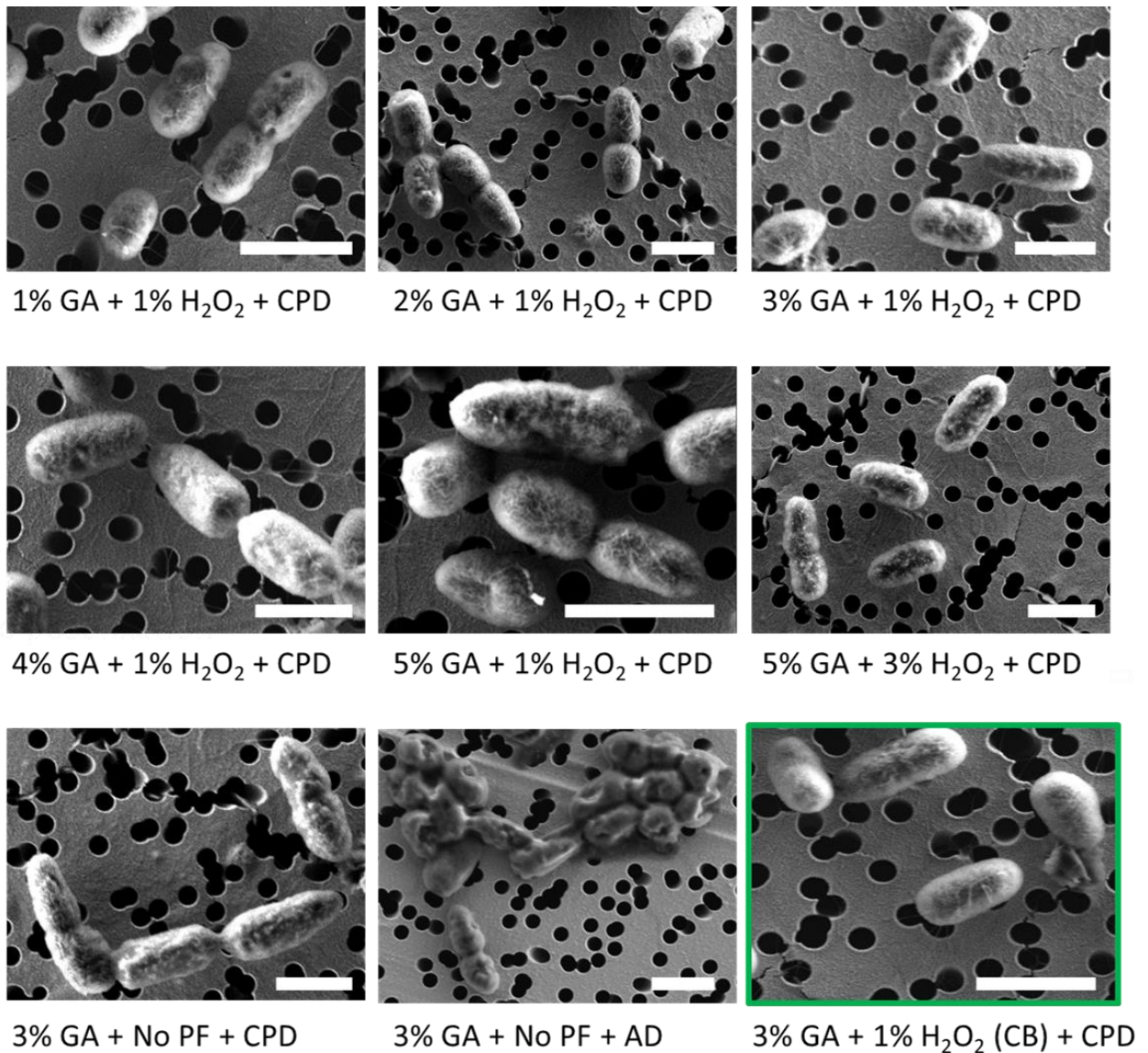
Figure 12. *P. putida* cells prepared after GA fixation. Different concentrations of GA have been tested and two concentrations of H_2O_2 or no post-fixation (No PF). Dehydration was done with CDP or air-drying (AD). Green-framed picture shows the result after all steps in CB. White bars correspond to 1 μm.

Instead, *fixation with 3% GA, post-fixation with 1% H_2O_2 and CPD* gave the best result (Fig. 12), but still the surface of bacteria was slightly "fury" and sometimes irregular (Fig. 12). An increase of H_2O_2 concentration to 3% did not improve bacterial shapes, suggesting that 1% H_2O_2 was enough to preserve their structure (Fig. 12). In the previous protocol, after both fixation (in CB) and post-fixation (in ddH_2O), one washing step in CB and two washes in ddH_2O were performed. Assuming that such alternation of buffer and water might cause osmotic stress to the cells, all steps were performed in CB, from fixation until water substitution. SEM observations confirmed that the cellular shape was better preserved (Fig. 12, green framed picture), hence I chose this protocol as the most suited one for *P. putida* cells (Fig. 13-A).
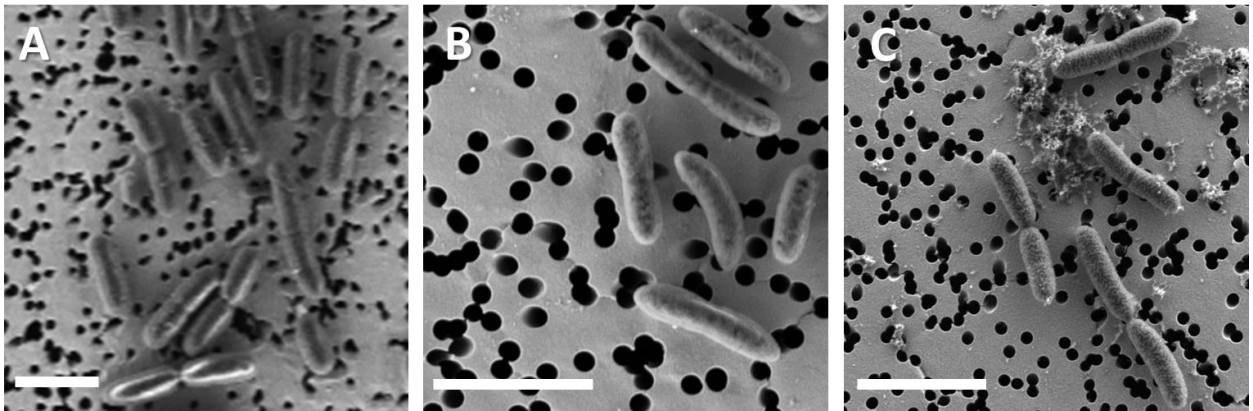
Figure 13. Sample preparation with the optimized protocol for **A)** *P. putida*, **B)** *P. stutzeri* and **C)** *T. aromatica*. Scale bars correspond to 2 μm.

Different microorganisms may require different sample preparations because of the different cell-wall composition [162,171,176,177]. However, as general principle, bacteria with similar cell-wall composition, e.g. gram negatives, should give similar results with the same preparation. Thus, the chosen protocol was tested with *T. aromatica* and *P. stutzeri*, to validate the suitability for the other strains involved in my study. The cell shape was likewise preserved for these species (Fig. 13-B, C).

The samples prepared with different post-fixatives were analyzed with Energy-Dispersive X-ray spectroscopy (EDX) coupled with SEM. High levels of Osmium (coming from OsO_4) and Manganese (from $KMnO_4$) were found on top of bacterial cell membranes (Fig. 14). Instead, H_2O_2 does not accumulate as compound per se, because it either forms radicals oxidizing the molecules *in loco* or it self-decomposes by forming water and oxygen [178].
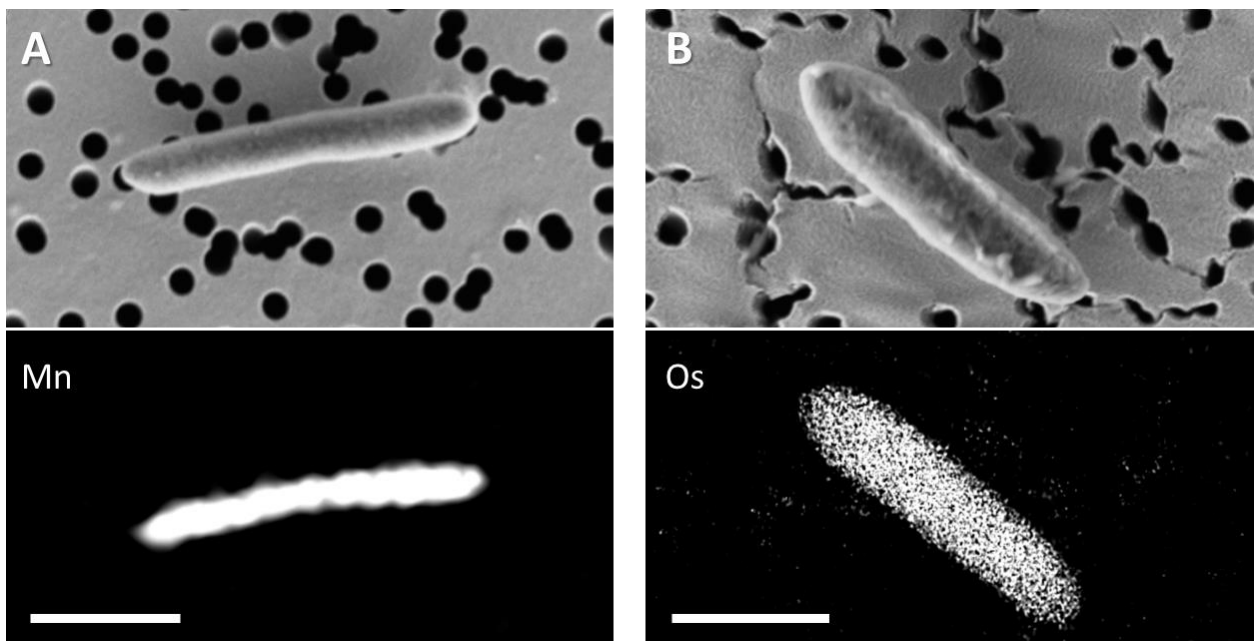
Figure 14. SEM-EDX analysis on *P. putida* cells after sample preparation with the **A)** $KMnO_4$ and **B)** OsO_4 as post-fixation agents.

NanoSIMS is a chemical imaging technique and each chemical modification in the samples will alter the ionization efficiency when bombarding by the primary ion beam, hence resulting in strong changes of signal intensity up to many orders of magnitude [113].

The incorporation into the cell membranes of Osmium (Os) or Manganese (Mn) could thus change the molecules ionization. For this reason, and due to the well-preserved cell integrity (Fig 13), the protocol with 1% H_2O_2 as post-fixative was preferred for the subsequent sample preparations prior to nanoSIMS in my work. The sample preparation development described here is intended as peer-reviewed publication and is currently in preparation (see appendix).

Maintaining cells' morphological and chemical integrity for bacteria and pseudo-fungi cocultures

ii) The second part of sample preparation optimization was done with co-cultures of the pseudo-fungus *Pythium ultimum* and the bacteria *Pseudomonas putida*. This required particular attention, due to the necessity to keep the spatial context and potential trophic interactions between the partners.

As part of my PhD project, I studied the role played by associated microorganisms on the bacterial heterogeneity in a laboratory-controlled system, using *Pythium ultimum* as hyphae forming pseudo-fungus and the engineered strain *Pseudomonas putida* KT2442::dsRed-*lacI*^{q}(pWW0::P$_{lac}$-*gfp*) with the wild type strain *Pseudomonas putida* KT2440 as reporter system [230] (see chapter 3.4 for further details). In such case, the whole protocol was adapted to maintain the morphological integrity of both partners and consequently the integrity of their potential interactions.

Prior to nanoSIMS analysis, samples need to be fixed and then dehydrated as explained above but it becomes challenging to keep the spatial distribution of bacteria and hyphae unaltered, particularly when sample-preparation steps require immersion in various liquid solutions (Sketch 1).

First, fixation in vapor was considered for this set-up in order to avoid i) sudden dryness of the microorganisms and especially ii) soaking into fixative, thus disturbing the spatial distribution of the whole system. Samples were fixed under vapor with a mixture of 10% PFA (in ddH$_2$O) and 37% EtOH at 35°C. The water was removed from the samples while fixing and substituting it with EtOH vapor to reduce the tension on the cell surfaces. Then vapor was released very slowly and sample air-dried overnight. However, bacteria cells were flattened and hyphae resulted transparent under SEM observation (Fig. 15-A, B).

Other 4 subsequent tries were performed with this method gradually decreasing the content of water in the fixative mixture (53, 40, 25, 0% water respectively). The principle was to avoid "new" introduction of water and to facilitate the fixative-vapor/air exchange for a slower dehydration (EtOH boiling point is lower than water). Nevertheless, these tries resulted again in a bad morphology of bacteria, which were buried underneath the collapsed hyphae (Fig. 15-C). Moreover, at higher magnification, many impurities remained on the hyphal surface, probably salts and other organic residues (Fig. 15-D); in fact, no washing steps were performed with such protocol. Air-drying without any fixation also resulted in transparent or uneven hyphae surface, flattened and distorted bacteria shapes, and many inorganic and organic residues on the hyphal surface (yellow arrow-heads, Fig. 16).
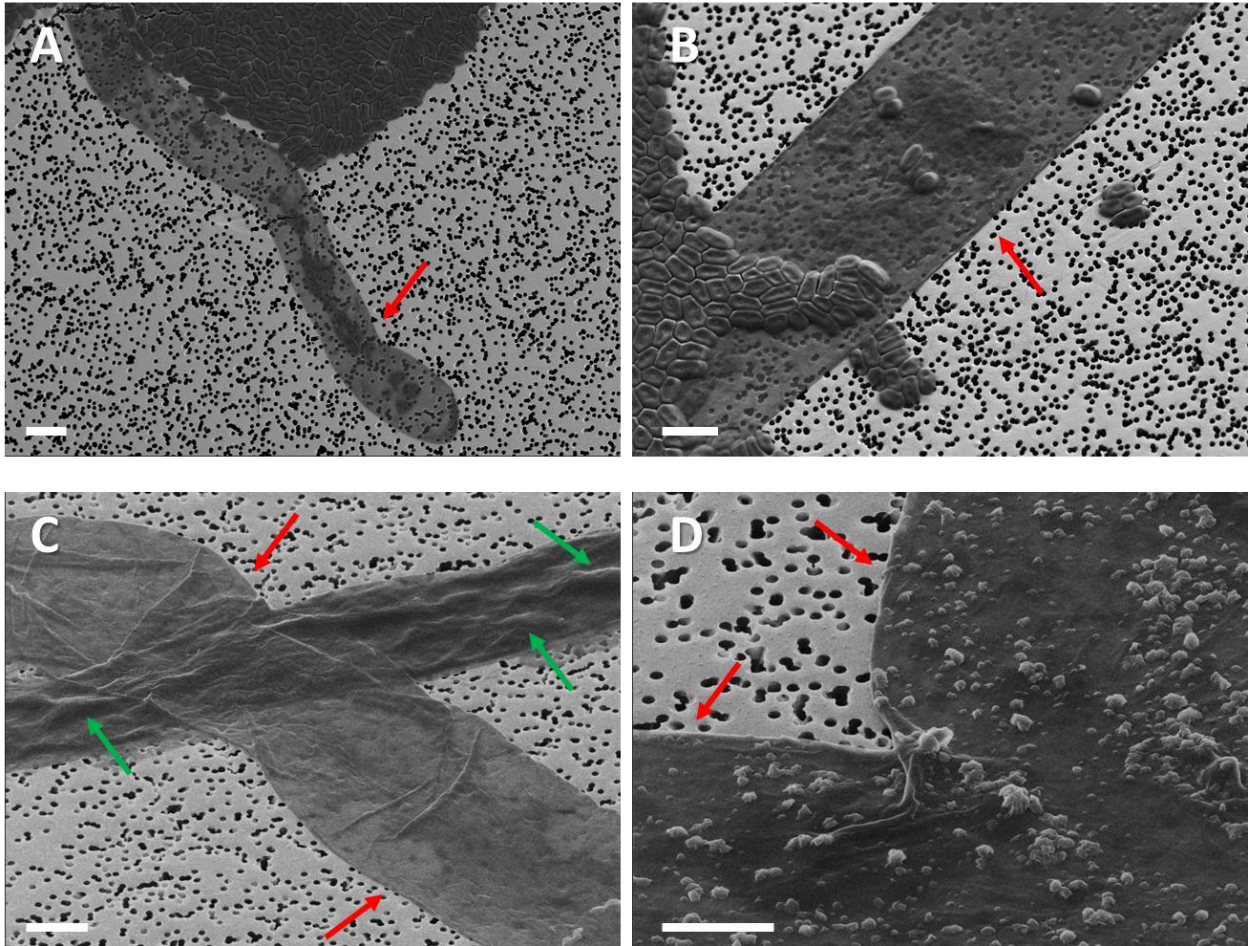
Figure 15. Sample preparation of pseudo-fungi and bacteria set-up with vapor fixation. **A)** and **B)** show the first try with vapor-fixation. Hyphal surface is completely transparent (red arrows) and bacteria cells are flattened and almost melted to each other. Observations were done with SEM. **C)** and **D)** show a subsequent try resulting again in **C)** flattened hyphae (red arrows) with bacteria buried underneath (green arrows) and **D)** many impurities on the hyphal surface. Observations were done with HIM. Scale bar is 2 μm.
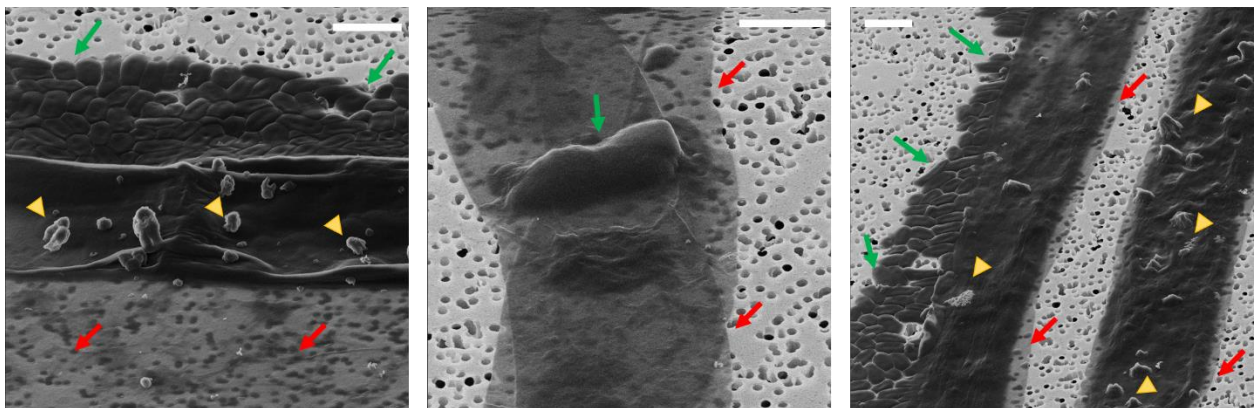
Figure 16. Air-drying of pseudo-fungi and bacteria set-up. Hyphae are transparent (red arrows), bacteria shape is aberrant and sometimes cells are fused with the close ones (green arrows). Many impurities are present alongside the hyphae (yellow arrow-heads). Observations were done with HIM.

From these results, I concluded that fixative-vapor/air exchange was not optimal to substitute water inside the bacterial cells and the hyphae. Therefore, I tried with the protocol optimized for *P. putida* (previous section), although it was in liquid, aiming to a better shape of hyphae and bacteria. I developed a method where all these sample preparation steps were performed inside a single well of a 12-wells-plate (2 cm of diameter). Using a small piece of gaze underneath the filter and keeping the filter on the opposite side of the pipetting spot, I aimed to reduce the disturbance of the spatial distribution.

HIM observations confirmed that hyphal and bacterial morphologies were much better preserved (Fig 17-A). Surprisingly their physical interactions were likewise maintained, making even possible to observe the migration of bacteria on the "hyphal highway" [179] (Fig. 17-B). Thus, I was able to prepare samples suitable for high-vacuum conditions, while contemporarily preserving spatial arrangements of the co-cultures.
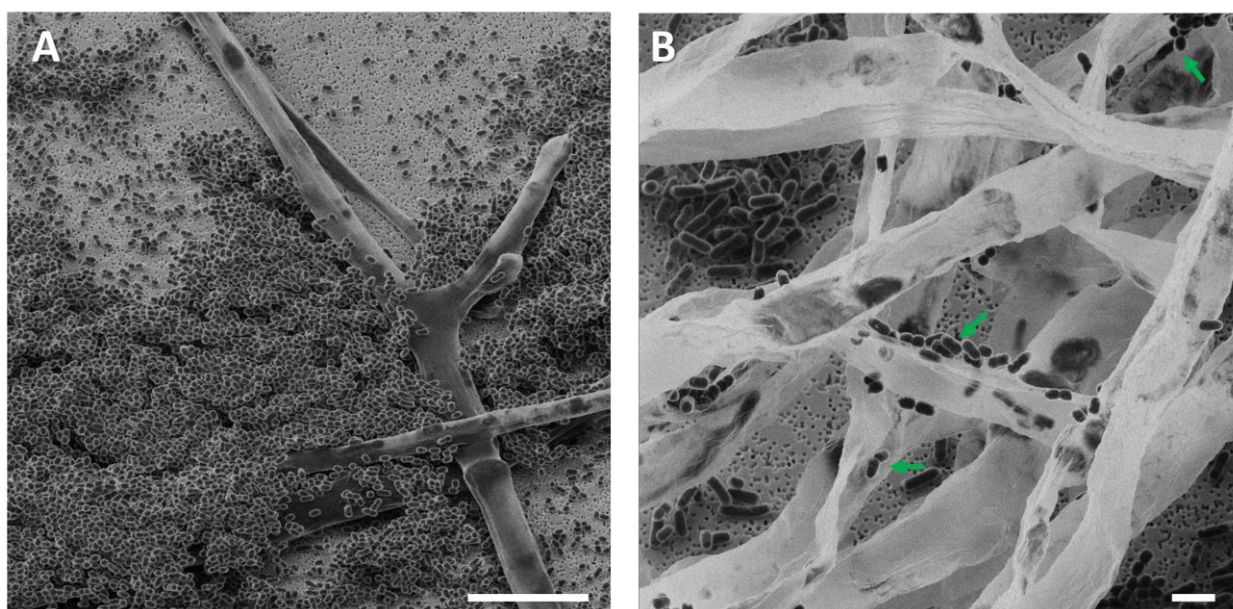
Figure 17. Sample preparation in "liquid" of pseudo-fungi and bacteria set-up. **A)** Hyphal and bacterial morphologies are well preserved. **B)** Bacteria along their journey on "hyphal highway" (green arrows) in a different area with higher magnification. Pictures were acquired with HIM.

Further preparation improvements

Improvement of cell distribution and density

Cell density and homogenous distribution on the filter/support are other prerequisites for single-cell analysis by nanoSIMS, not always easy to achieve. This issue is mostly faced when preparing cell suspensions, especially when samples come from natural environments with a relatively low cell number, or in general when it is not possible to yield higher cell density. Moreover, the numerous washing and dehydration steps upon sample preparation can strongly contribute to a reduction in the initial cell numbers

on the filter area, which may result in a non-homogenous distribution. The classical protocol in fact involves several washing steps in small petri dishes containing the chemicals (Sketch 1), implying a strong loss of cells throughout the procedure. This may result in few tens of cells per Field of View (FoV) during SEM observation (Figure 18-A). To overcome this issue, I develop a method, in which all the preparation steps were performed inside a stainless-steel syringe filter holder (Sartorius, Model 16214), a filtration device custom-made for a single 25 mm Ø filter (Sketch 1). After fixation overnight into 2-ml tubes, the suspensions were withdrawn with 1 ml syringe, filtered, and concentrated inside this holder; then the successive steps, such as washing of fixative, post-fixation and post-fixation-washing, water substitution, were performed, never removing the filter from the inside. In this way, it was not only possible to concentrate the cells but also to reduce the quantity of chemicals used; 1 ml of solution was enough for each step to prepare the samples in a proper way. Filters were removed from the holder just before undergoing CPD, resulting in a very low dilution in cell numbers per surface area (Fig. 18-B).
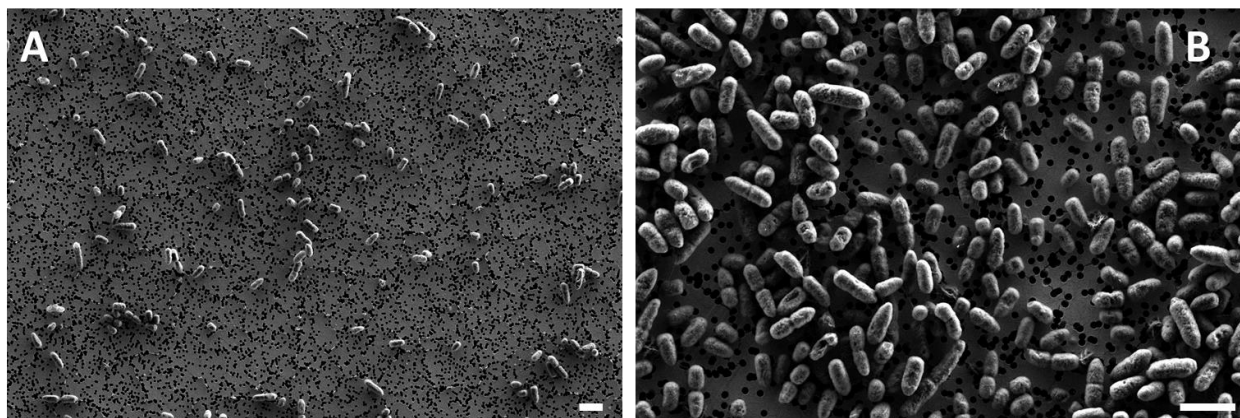
Figure 18. Sample preparation of *P. putida* cells for the optimization of cell density. All the steps were performed in **A)** petri dishes and **B)** entirely in the filter device. Scale bars correspond to 2 μm.

Improvement of the sample carrier

All the attempts for sample preparation mentioned above have been performed using as support polycarbonate filters, which were coated with a thin (30 nm) layer of Au/Pd to be conductive. One of the disadvantages of these filters however can be the introduction of topography effects because the filters are easily bending during the numerous sample preparation steps. Still, their utilization is necessary for cell concentration during filtration, particularly important for environmental samples [69,70,126,180].

We recently proposed a way to overcome the challenges of filters topography and cell density mentioned above for sample preparation. It consists of a silicon wafer (Si-wafer) covered with a special polymer layer used as a specimen support for high-resolution imaging. We called it carrier since it can be subsequently used for different preparation steps and with many techniques such SEM, HIM, Fluorescence

Microscopy and Time-of-Flight-Secondary Ion Mass Spectrometry (ToF-SIMS)[181] (Fig. 19-A). The polymer was inert, solvent resistant and most importantly it acted as a sponge for liquid suspensions due to its hydrophilicity.
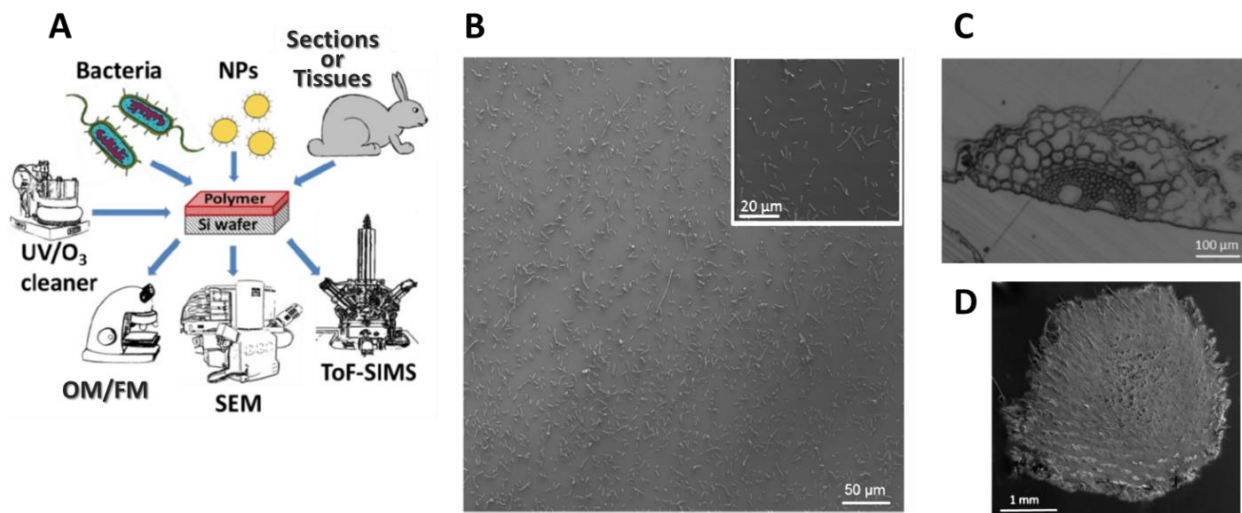
Figure 19. A) The polymer-coated silicon wafer after treatment with UV/O$_3$ cleaner and its applicability to many analytical techniques, such as Optical and Fluorescence Microscope (OM/FM), Scanning Electron Microscopy (SEM) and Time-of-Flight Secondary Ion Mass Spectrometry (ToF-SIMS) and several specimens, i.e. bacteria, sections, tissues and nanoparticles (NPs). **B)** High-resolution microscopy observations of *Pseudomonas putida* with Helium Ion Microscopy. **C).** Optical microscope observation of thin section of plant root embedded in resin. **D)** High-resolution SEM images of frozen rabbit skin sections deposited onto polymer-coated carrier, modified from [181].

These features allowed for i) a reduction in sample preparation steps (a single carrier can be used from the beginning until the end of the protocol) ii) diminution of chemicals volume used (everything is done on the carrier that is usually 1×1cm^2), and especially iii) homogeneous distribution of the samples on the filter while preserving the sample integrity, as revealed by SEM observation [181] (see appendix and Fig. 19-B, D).

SEM and nanoSIMS imaging usually require a conductive support for the sample's analyses. The polymer layer was not acting as a full insulator, thus providing enough conductivity with low-current beam and charge compensation upon SEM observations (the latter to avoid the so called "charging effect" on the samples). However, it was not conductive enough for the analysis with nanoSIMS. The lack of conductivity could be circumvented in the future by coating the carrier after sample preparation, but this requires further optimizations, since it can introduce some bias, e.g. topography effects or localized surface potential [182]. This emphasizes the necessity for further improvements of sample preparation supports and carriers suitable for comparative high-resolution imaging and complementary analyses which reduce the effort of preparing samples individually for each single technique.

In conclusion, the choice of a sample preparation protocol strongly depends on the subsequent downstream analysis that one has to perform. In my case, the preservation of the cellular morphology and the native chemical composition was necessary in order to avoid bias that could have disturbed the chemical imaging with nanoSIMS later on. Artifacts from sample preparation may indeed hinder the quantification of the cellular elemental composition and hence compromise the evaluation of **cell-to-cell differences** and **MH**. The effort to optimize the protocol thus served the scope to find the best trade-off between making the sample suitable for high-vacuum conditions of the NanoSIMS and preserving the native chemical composition as much as possible.

3.2 *Validation of quantitation methods*

3.2.1. *Common quantitation method for nutrient assimilation by single cells*

The application of SIP-nanoSIMS approach allowed for the quantitation of metabolic activity in microbial communities. However, to date, a widespread and common way to assess the metabolic activity is missing. Many attempts have been done to quantify the elemental assimilation and most of the time in an empirical way [69,70,119,183]. The analysis with nanoSIMS allows calculating and quantifying the enrichment of the heavy isotope, for instance ^{13}C versus ^{12}C or ^{15}N versus ^{14}N at the initial and final states of the incubation using isotope-labelled compounds. The uptake of ^{13}C or ^{15}N into the cell biomass is measured as isotopic ratios and used for showing the activity of bacteria in the samples [184]. For a correct quantitation, the sample preparation effects, physiological state of the cells and potential errors propagation from all parameters have to be considered in the calculations. Besides the already-known dilution effect on the final isotopic enrichment [185,186], there are other factors to consider, such as cultivation parameters and analytical errors. For this reason, I was involved in a work aiming to quantitate single-cells assimilation when SIP-nanoSIMS approach is employed [187] (see appendix).

Dilution effect and errors

Using the nanoSIMS-50L (CAMECA, France), we analyzed *Pseudomonas putida* mt-2 KT2440 cells grown on ^{13}C-glucose and calculated the changes in heavy isotopes ratios, D_f, such as $^{13}C/^{12}C$ or $^{12}C^{15}N/^{12}C^{14}N$. For the calculation of the assimilated elements over certain times of incubation, we considered the following parameters: i) dilution effect due to the sample preparation including [185], ii) cultivation conditions, iii) isotope fractionation effects, volume and element-specific-density, i.e. mass of an element (e.g. C or N) per volume (fg · μm^{-3}) of the cells considered for the analysis.

For the restoration of single-cell isotopic composition we considered the dilution effect while taking into account the fraction of heavy isotope in chemicals (D_{ch}) and the calculated fraction of C introduced upon a specific preparation method, (K) [185]. The fraction of heavy isotope of the growth substrates, D_{gs}, in the culture medium as well as the isotope fractionation effects, α, were also considered in the calculation. The latter refers to the preferential uptake/processing of lighter isotopes in comparison with heavier during biochemical reactions [188]; this "preference" may bring to a reduced assimilation rate for the heavy isotope. The propagation of errors in all these factors was considered in the expression of the K_A error (dK_A value) [187].

The K_A value accounts for the *fraction of an assimilated element*, e.g. C or N, relative to its initial content in the cell. Starting from this value, we were able to calculate the **rate of assimilation** of an element. To do so, it is important to provide the cell volume and the element-specific cellar density. The cell volume can be calculated for a single cell with optical microscopy or SEM [189] or alternatively can be calculated as Region of Interest (RoI)-confined cellular volume from nanoSIMS data (each RoI corresponding to a single cell). In the last case, a certain bias will be included considering that RoI definition is usually performed manually and therefore is more prone to errors. Indeed, when estimating

the error of assimilation rate calculated from RoI-confined volume or per volume (μm^3), errors are much higher in the first case (Fig. 20). However, especially in mixed and/or natural community is not always possible to calculate the "real" biovolume for each single cell, then it becomes useful to quantify the assimilation rate using RoI-confined volume (see chapter 3.5). Despite the consideration of volume, in both cases, the element-specific-density has to be given in input for a correct expression of the assimilation rate. In this way, it is possible to approximate the initial elemental content, e.g. C or N, per cell or per volume.
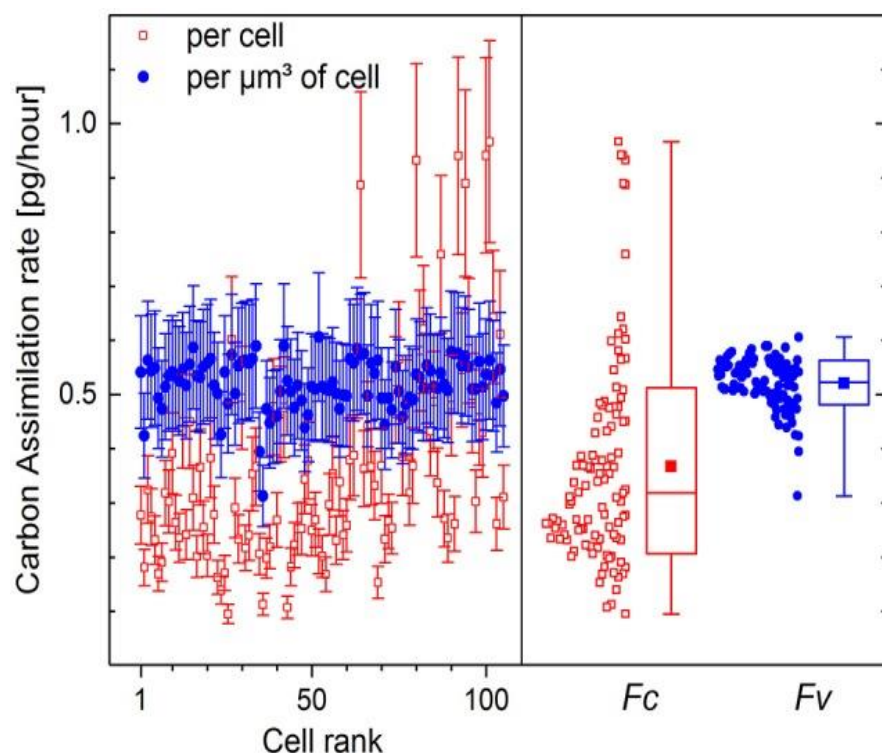
Figure 20. Carbon assimilation rates calculated for *P. putida* incubated in ^{13}C-glucose medium. In the left frame, assimilation rates per single cell, F_c (hollow red rectangles, $pg \cdot cell^{-1} \cdot h^{-1}$), and per volume, F_V (filled blue circles, $pg \cdot \mu m^{-3} \cdot h^{-1}$), are shown with mean value and standard deviation for each of the 105 single cells analyzed.
In the right frame, the distributions of cell-specific (F_c) and volume-specific (F_V) assimilation rates are shown as box plots. Boxes represent Q_{16}–Q_{84} interpercentile range; Min-Max values, median values (horizontal lines) and mean values (rectangles) are also shown. Picture from [187].

By knowing the elemental composition of that specific cell before and after nanoSIMS measurement, it is possible to reconstruct back the total assimilation rate. If the single-cell volume is reconstructed from the RoI-confined volume, Fc will be calculated corresponding to pg or $fg \cdot cell^{-1} \cdot h^{-1}$ of an element; otherwise Fv can be calculated, i.e. pg or $fg \cdot \mu m^{-3} \cdot h^{-1}$ of that element (Fig. 20). In few words, K_A represents the quantity of assimilated elements, e.g. C or N, relatively to their initial abundance in the cells, and from this value it is possible to reconstruct the assimilation rates per single cell (Fc) or per volume (Fv) giving as input the element-specific density [187] (see appendix).

Lateral dilution effect

Another interesting finding was that the quantification of the heavy isotope based on counts acquired with nanoSIMS is different between monoatomic carbon (i.e. [13]C− and [12]C− ions) and molecular carbon (i.e. [13]C[14]N− and [12]C[15]N− ions)[187] (Fig. 21). When the volume was calculated from the RoI definition, cell

size derived from monoatomic carbon ion maps was smaller (Fig. 21-B) in comparison with the cell size calculated from molecular carbon ion maps (Fig. 21-D), probably due to the high contribution of $^{12}C-$ counts from the polycarbonate filter used as substrate (while contribution of $^{13}C^{14}N-$ from the filter is very low) (Fig. 21 A, C).
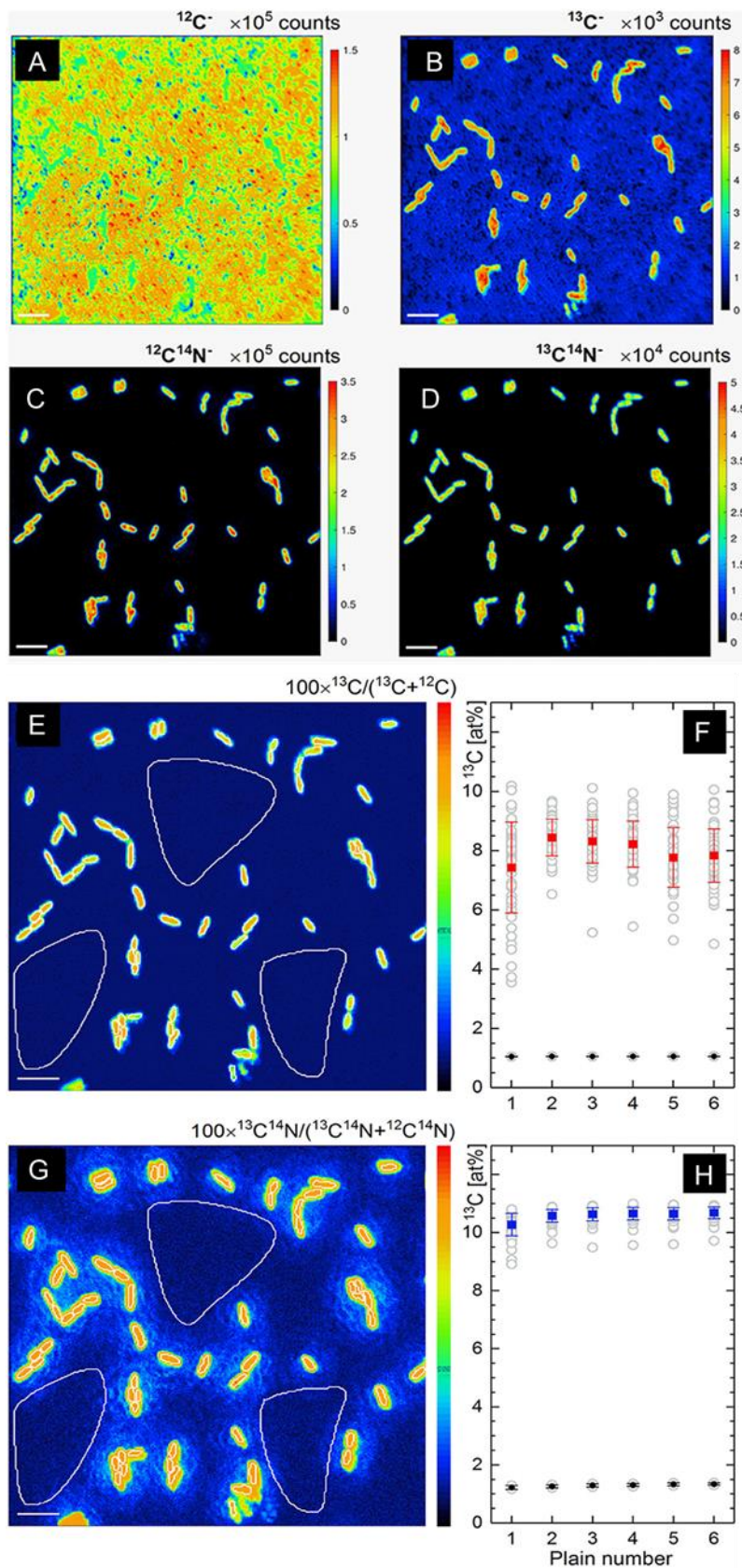
Figure 21. *P. putida* cells measured by nanoSIMS. Lateral distribution maps of monoatomic ions **A)** $^{12}C-$ and **B)** $^{13}C-$ counts and **E)** their fraction; molecular ions **C)** $^{12}C^{14}N-$, **D)** $^{13}C^{14}N-$ and **G)** their fraction derived in at%. **E)** and **G)** show RoIs definition around bacteria and filter areas drawn on LANS software (white line confined). **F)** and **H)** show the depth profiles of the respective ^{13}C fractions (gray circles) for all defined RoIs. The mean values of ^{13}C fraction with standard deviation are shown for cells (red and blue rectangles) and filter areas (black circles) in each scanned plain. Scale bar length is 4 μm. Figure readapted from [186].

Moreover, two main outcomes were visible when the fraction of heavy isotopes was calculated after definition of RoIs: i) the final fraction achieved from monoatomic counts was smaller than the fraction from molecular counts (Fig. 21-E, G); ii) the standard deviation was bigger for monoatomic counts than for molecular counts (8.003± 0.378at% vs. 10.585 ± 0.153at% Fig. 21-F, H). Such differences were probably due to the fact that secondary CN− ions originates in higher amount from proteins and nucleic acid belonging to the cells, while the filter contains just low molecular mass compounds escaped during sample preparation or remained from growth-substrate leftover. Therefore, the total contribution of CN− ions was much higher (Fig. 21).

It becomes important to consider this lateral dilution effect when deciding for the masses to measure with the nanoSIMS on the one hand and when defining RoIs (and consequently doing quantitation) on the other hand. For instance, when RoIs are drawn on the monoatomic C− maps, it is important to exclude completely the filter area, rich in ^{12}C−, confining each cell within the inner side, rich in ^{13}C−. This may lead to imprecision, in fact when considering RoI-confined volume, the error in the assimilation rate was much higher (Fig. 20). However, also these errors were included in the calculation of the K_A value [187] (see appendix).

K_A as metabolic activity index

The majority of studies using SIP-nanoSIMS derived the assimilation or metabolic activity from i) the isotopic ratios [114]; ii) the isotope enrichment values in delta notation or atomic percent (at%) [180,190-195]; iii) the normalization of nanoSIMS-derived isotope ratios to either bulk rates, unlabeled cells, cell volume or standards [71,126,196-199]. The most common way [69-71,119,200] to quantify the assimilated elements into the biomass is to calculate the final fraction of ^{13}C taken up by the cells, D_f. However, we showed that the dependency of K_A on D_f was not linear [201] (dotted line in Fig. 22).

Let's assume that one wants to measure the single-cell C assimilation from the D_f alone; upon incubation with isotope-labelled substrates the cells will become gradually enriched. If we consider a cellular ^{13}C enrichment from 1 to 3 at% or from 7 to 10 at% (Fig. 22, X-axis), the final assimilated quantity will correspond to the difference between the two values (and it will be 3 at% in both cases). With this assumption, one can consider that the extent in cell assimilation from 1-3 at% is exactly the same as from 7-10 at%. Let's now assume that K_A, calculated from the same cells, is considered for activity quantitation instead. In this case, we need to consider the right Y-axis in Fig. 22. When D_f values go from 1 to 3 at% enrichment (Fig.22, X-axis), the corresponding K_A values go from 0 to 0.125 (Fig. 22, right Y-axis), meaning that cells assimilated 12.5% of the total carbon. However, if we consider D_f from 7 to 10 at%, the corresponding K_A values go from 0.45 to 0.90 (Fig. 22-A, right Y-axis), meaning that in this case the cells have to assimilate 45% of the total carbon, that is twice as much, to achieve that level of enrichment. Such discrepancy can be explained by the fact that D_f value considers just the final ^{13}C enrichment and with this assumption the cells make the same "metabolic effort" despite the initial amount of carbon upon the incubation time; instead, K_A considers both ^{12}C and ^{13}C and thus it assumes that the more carbon cells

have to accumulate in the biomass the higher effort/engagement they have to make. The K_A value thus can better quantify the "real" metabolic activity since it takes into account the total carbon assimilation relative to the initial quantity upon cells incubation.

Additionally, the K_A value has its own error that comes from the propagation and consideration of all the uncertainties related to the input parameters (error in ions counts consideration, e.g. $C-$ vs. $CN-$, error in volume or in carbon density), making it even more precise. Because of so many different ways to calculate and express assimilation and metabolic activity from nanoSIMS-measured isotopic ratios, so far, a universal parameter would serve two scopes: 1) a better accuracy in the quantitation of elemental assimilation or rates; 2) the possibility to compare reliably different studies from different laboratories with a certain consistency. The calculation of K_A values was further used for the quantitation of single-cell relative assimilation from the further SIP-nanoSIMS experiments performed in my work.
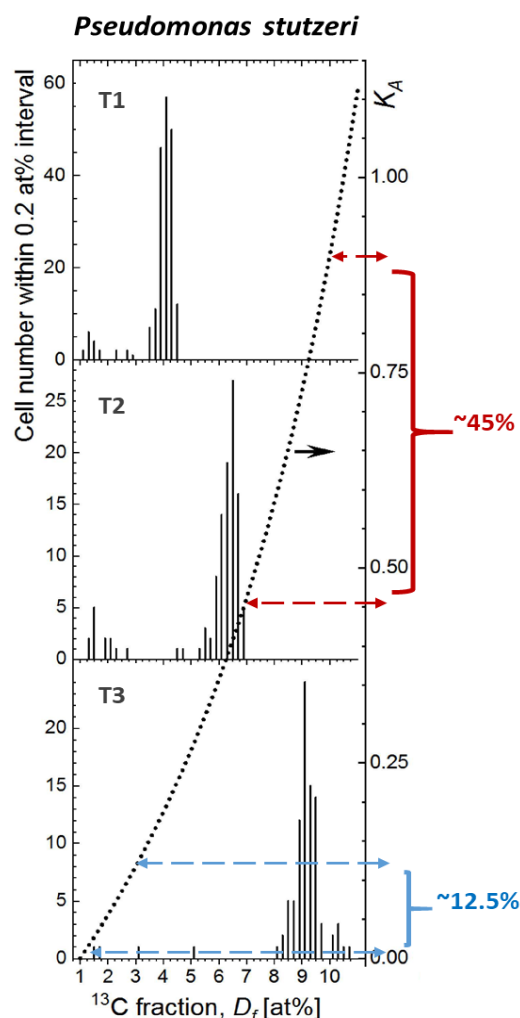
Figure 22. Histograms of *P. stutzeri FC01* cells in their ^{13}C fraction (D_f) plotted at three different time points of incubation with ^{13}C-labeled substrate. Right Y-axis represents the relative carbon assimilation (K_A) values. The dependence of K_A on D_f is shown with the dotted line representing the trend of K_A in comparison with D_f.

3.2.2. Quantitation of heterogeneity

Phenotypic or **MH** is a spread phenomenon shown by many microbial species and with several analytical approaches [77,80,202]. In many studies, the occurrence of **cell-to-cell differences** was an obvious and visible outcome, e.g. two different fluorescent proteins, two different sizes, two evident *phenotypes*, clear **bimodal** distribution, ON-OFF *switches* [34]. These qualitative types of observation did not necessarily require a quantitation, since the outcome was already informative. In other cases, however, the extent of **cell-to-cell heterogeneity** was not clear; it was measured indirectly via comparing growth rates, nutrients

assimilation [70,118,119], normalizing for averaged measurements or standards [69,71] or with the Coefficient of Variation (CV), the ratio of the standard deviation over the arithmetic mean value of the population considered [69,118,119,203 and many others].

The downside of the CV as a **measure of heterogeneity** is that it implies a normal distribution of single cells in their activity or function. This means that when plotting the cells on a probability distribution function or a histogram, their distribution will follow the bell-shape or Gaussian curve, with the mean (μ) corresponding roughly to the peak of the distribution (Fig. 23-A). Such distribution is often called ´normal´. When isogenic populations display heterogeneity, instead, the single cells follow either asymmetrical distribution (meaning that the shape presents a tail with outliers) or a typical **bi-** or **multimodal** distribution (meaning two or more peaks as shown in Fig. 23-B). In few words, cells in a heterogeneous population do not follow Gaussian distribution, and in such case the μ of the population would not be representative (Fig. 23-B dotted lines); hence the CV cannot take into account the **bi-** or **multimodality**, that is one of the main features of heterogeneity.
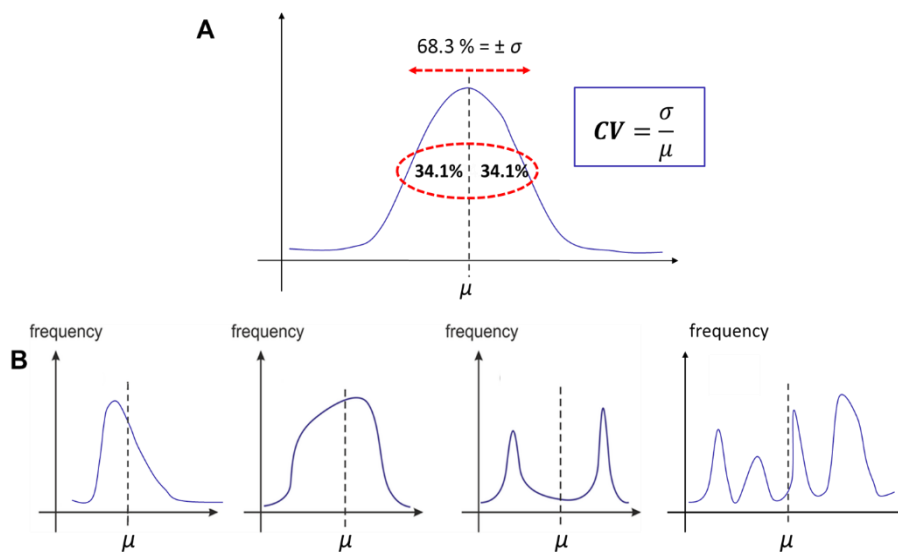
Figure 23. Different distributions of single cells. **A)** Normal distribution and Coefficient of Variation (CV), calculated from the ratio between the standard deviation (σ) and the mean (μ).
B) Asymmetric, bi- and multi-modal distributions, meaning that the single cells are spread out in different ways. The μ values represented as dotted lines cannot be representative of the real data dispersion. Figure **B)** is modified from www.ck12.org/c/statistics/measures-of-spreaddispersion/.

In fact, a universal parameter to **quantitate heterogeneity** is currently missing. This is becoming urgent because while a growing body of evidences is demonstrating **phenotypic** or **MH** occurrence, it is not possible to compare different conditions or studies in a reliable and unbiased way. To understand the importance of a **measure unit for heterogeneity**, one can consider the length of a certain object. Although everybody can measure with ´its own thumb´ and deliver a "proper and subjective measure", a scientifically recognized quantity would be given in ´inch´ or ´meter´, officially part of the International System of Units.

For this reason, I was aiming to develop measuring parameters for **quantitation** and **comparison of MH** (Sketch 2) between different experimental conditions, potentially exploitable with the use of other techniques.
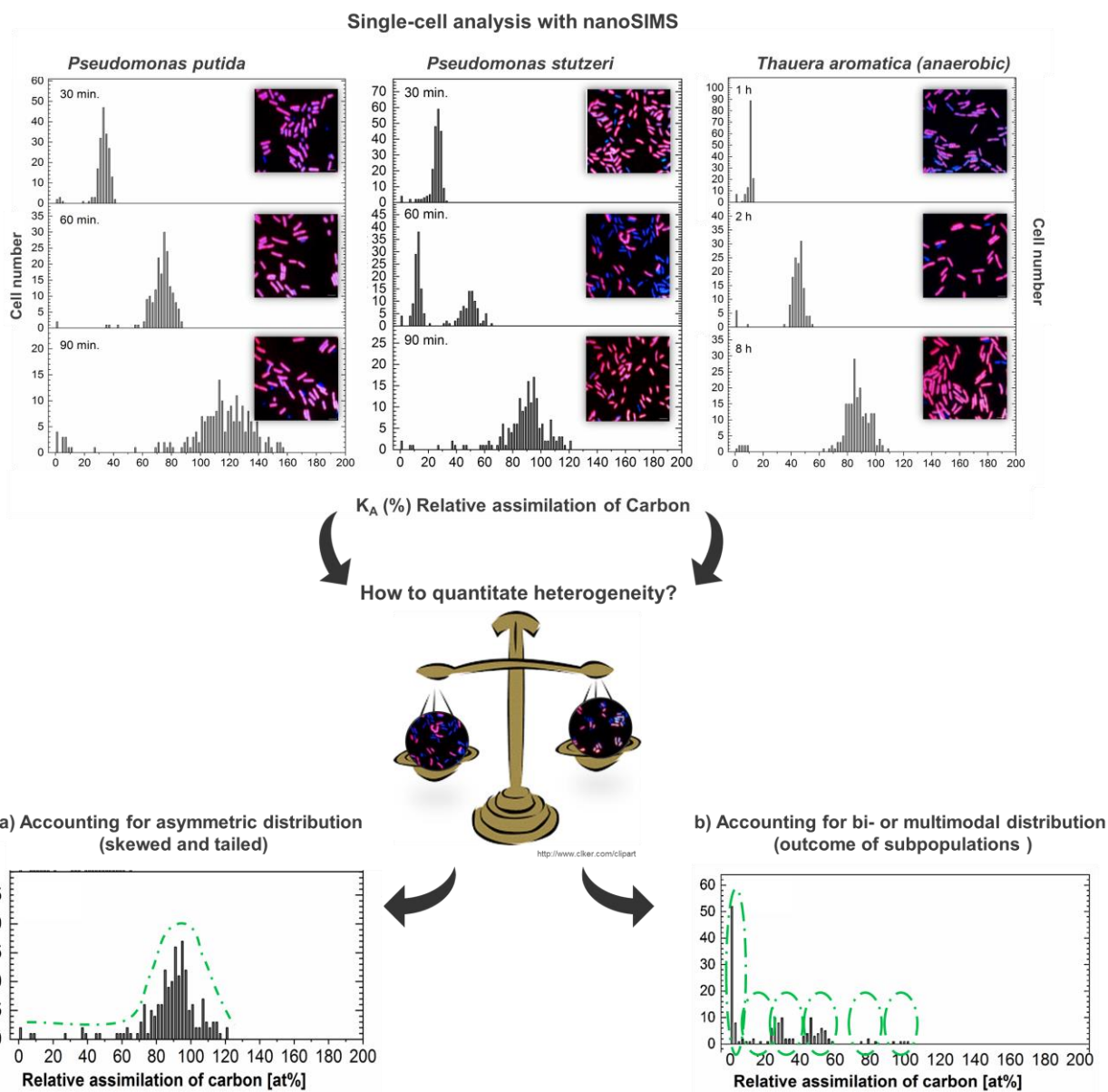
Sketch 2. Approaches used for quantitation of **MH**. After nanoSIMS analysis, single-cell metabolic activity is calculated as K_A and the distributions of single-cells values are plotted as histograms; chemical maps acquired with nanoSIMS [RGB overlay of $^{13}C^{14}N-/^{12}C^{14}N-$ (red), $^{31}P^{16}O_2-$ (green), and $^{12}C^{14}N-$ (blue)] are shown as insets. Two approaches were developed for **quantitation of MH**, depending on the distribution of the populations**: a)** asymmetric (skewed) distribution, **b) bi-** or **multimodal** distribution.

Precision of cellular isotopic composition measurements with nanoSIMS

As first step, it was necessary to achieve good precision (agreement between repeated measurements under the same conditions) of the single-cell isotopic composition measured with nanoSIMS. With the aim to reduce as much as possible **cell-to-cell variability** coming from analytical and technical errors, *Pseudomonas stutzeri* FC01 cells were grown with unlabeled-acetate substrate, thus detecting natural abundance of ^{13}C isotope, which is an already known reference value. NanoSIMS measurement parameters, such as the current of the primary ion beam, raster size (in pixel) and area (in μm^2) were optimized[201] (see appendix and Fig. 24-A).

The best single-cell precision was achieved with a primary ion current beam of 4 pA, a raster size of 512×512 pixels and a raster area of 20×20 μm^2. Slightly compromising the focus of the picture (Fig. 24-B), we were able to optimize the parameters and achieve two main goals: 1) enhancement of the counting statistics (number of secondary ions counted per each analysis) and 2) reduction of analytical errors (precision) coming from the measurement parameters (Fig. 24).
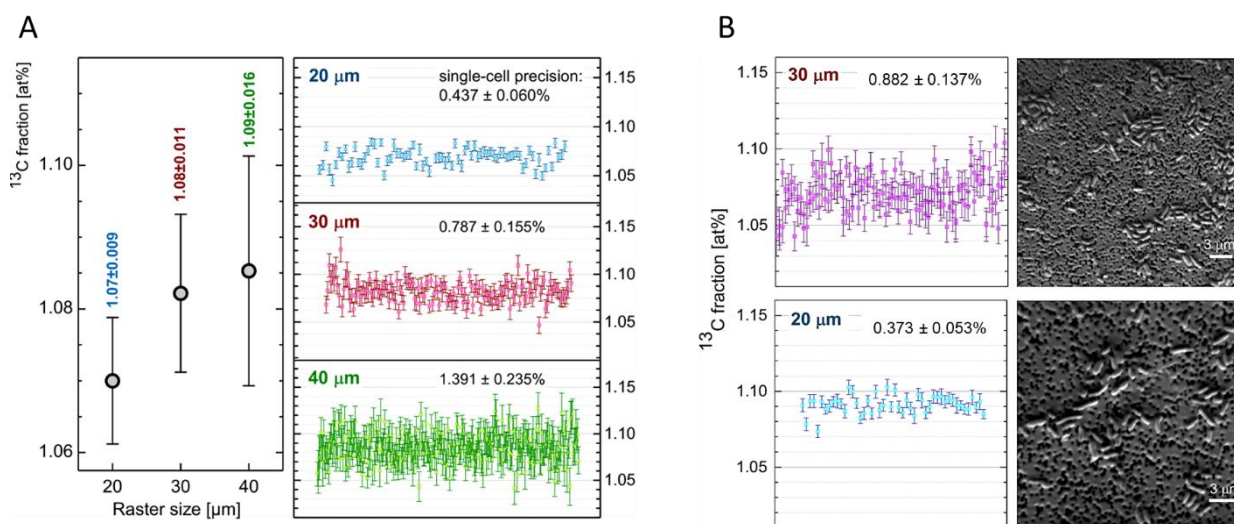
Figure 24. Optimization of nanoSIMS measurement parameters on *P. stutzeri* cells. **A)** On the left panel the mean values ± SD of ^{13}C fraction achieved with three different raster sizes analyzed with 2 pA primary ion current are shown. On the right panels, each dot represents single-cell ^{13}C fraction value [at%] and its error (± SD, error bar). **B)** On the left panel single-cell ^{13}C fraction values achieved with two different raster sizes analyzed with 4 pA primary ion beam. On the right panel Secondary-electrons pictures acquired upon nanoSIMS analysis are shown. Single-cell precision values are indicated in the insets for each condition.

Labeling experiments and evaluation of metabolic heterogeneity (MH)

Isotope-labelling experiments were performed with *Pseudomonas putida* mt-2 KT2440 and *P. stutzeri* FC01 (isolated from environmental samples during this work) grown in a mineral salts medium, supplemented with $NaHCO_3$ (30 ml/L) and 10% CO_2 in the headspace as buffer system, with addition of

5 mM acetate, of which 20% was ^{13}C-labeled. Cells were withdrawn at three time points of their exponential growth phase and prepared for nanoSIMS analysis. Each sample was analyzed with the optimized parameters mentioned above and the acquired data were treated with the software Look@NanoSIMS (LANS) [112] for planes accumulation, drift correction and RoIs definition. Each RoI was drawn around each single cell using the ^{12}C^{14}N$^-$ ions map, as proxy for biomass distribution, ^{31}P^{16}O$_2^-$ ions map, as indicator for DNA and RNA molecules within the cells, and Secondary Electrons (SE) images, as indicator of cellular morphology. Ratios values from the LANS software were used as input for the calculation of the K_A values on the excel file provided with [187](see appendix). K_A values from the excel sheet were further exported, plotted and statistically analyzed with Origin software package (version 2019). Single cells belonging to each time point and to each condition were plotted as histograms for the evaluation of the single-cells distribution (Fig. 25, Sketch 2). Both histograms and nanoSIMS-acquired chemical maps revealed the occurrence of different extent of **MH** in all samples. While in some cases the distribution was skewed, in others was clearly **multimodal** with many cells, especially for *P. putida* strain, showing very low assimilation even after 2 hours of incubation with the ^{13}C-labeled-acetate (Fig. 25). For this reason, two different approaches were developed for **quantitation of heterogeneity** under one or the other occurrence (Sketch 2).
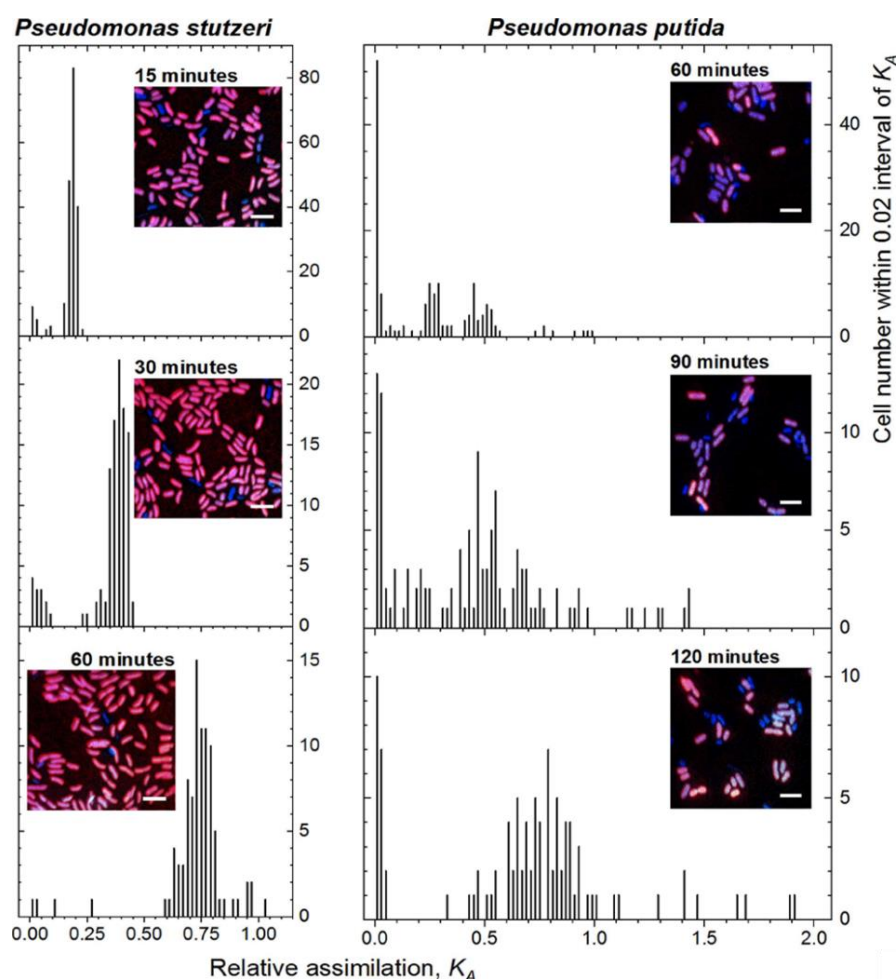
Figure 25. The histograms of *P. stutzeri* and *P. putida* cells distribution in their relative assimilation K_A. The insets show the RGB overlay of ^{13}C^{14}N$^-$/^{12}C^{14}N$^-$ (Red), ^{31}P^{16}O$_2^-$ (Green), and ^{12}C^{14}N$^-$ (Blue) acquired with nanoSIMS at each time point for the respective strains.

Heterogeneity Coefficient (HC)

Previous studies measured **phenotypic** or **MH** with the Coefficient of Variation (CV). As mentioned before, the CV as **a measure of heterogeneity** implies a normal distribution of single cells in their activity or function (Fig. 23-A). However, no bacterial populations tested in my work followed normal (Gaussian) distribution, rendering the CV not applicable to my samples. Thus, by extending the concept of CV, the expression of the **heterogeneity coefficient** (HC) was developed (Fig. 26), which additionally involved the correction for the Counting Statistics Error (CSE) as source of bias coming from the nanoSIMS analysis, that we called **HC**$_{corr}$ [201](Fig. 27-A, B).
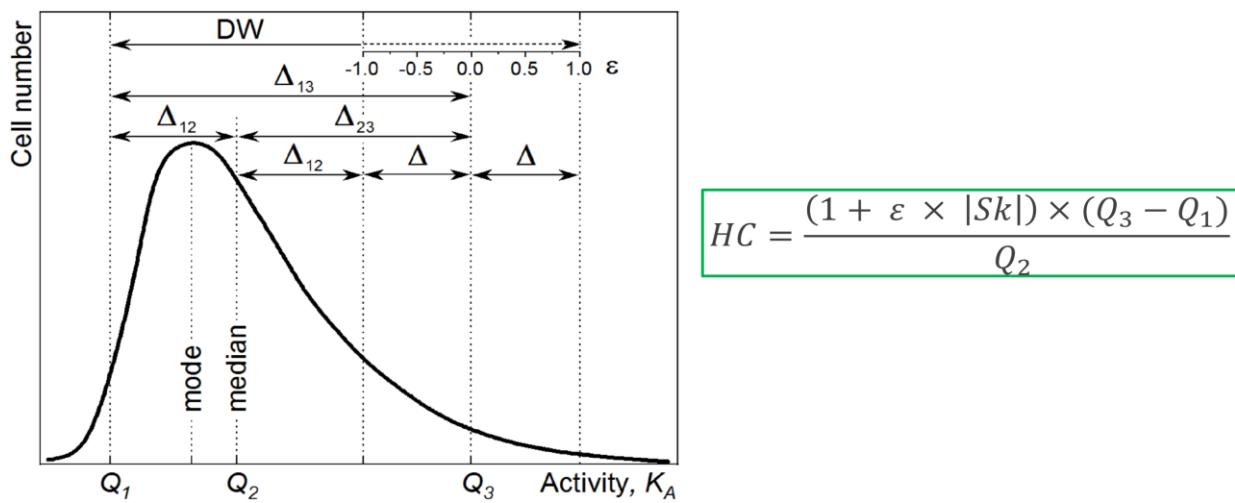
Figure 26. Representative illustration of a skewed distribution and derivation of the distribution width (DW). $Q_3 - Q_1$ corresponds to interquantile range $\Delta_{13} = Q_{84} - Q_{16}$. The ε factor represents the sensitivity to the skew for the consideration of DW. The full equation of **HC** is shown as inset with green frame.

$$HC = \frac{(1 + \varepsilon \times |Sk|) \times (Q_3 - Q_1)}{Q_2}$$

The CV considers ~68% of the cells distributed around the mean value, the distribution width (DW) (Fig. 23), while **HC** considers the 68% around the median (Fig. 26). Since median corresponds to Q_2 or Q_{50}, this range corresponds to the interquantile range $Q_3 - Q_1 = Q_{84} - Q_{16}$ (Fig. 26). In order to provide a tool for tuning the sensitivity to the distribution asymmetry, i.e. the skew, we introduced the *ε factor* into the **HC** expression (Fig. 26). With this *ε*, it was possible to include in the DW range the cells from the extremes of the distribution (outliers) that are usually excluded from statistical analysis of the variance. Nonetheless, the presence of such outlier-cells at the two extremes of the distributions was often observed in my experiments (Fig. 25). In fact, by changing the *ε factor,* the resulting **HC**$_{corr}$ values were very different, especially for *P. putida* that was much more heterogeneous than *P. stutzeri* (Fig. 27-A, B).
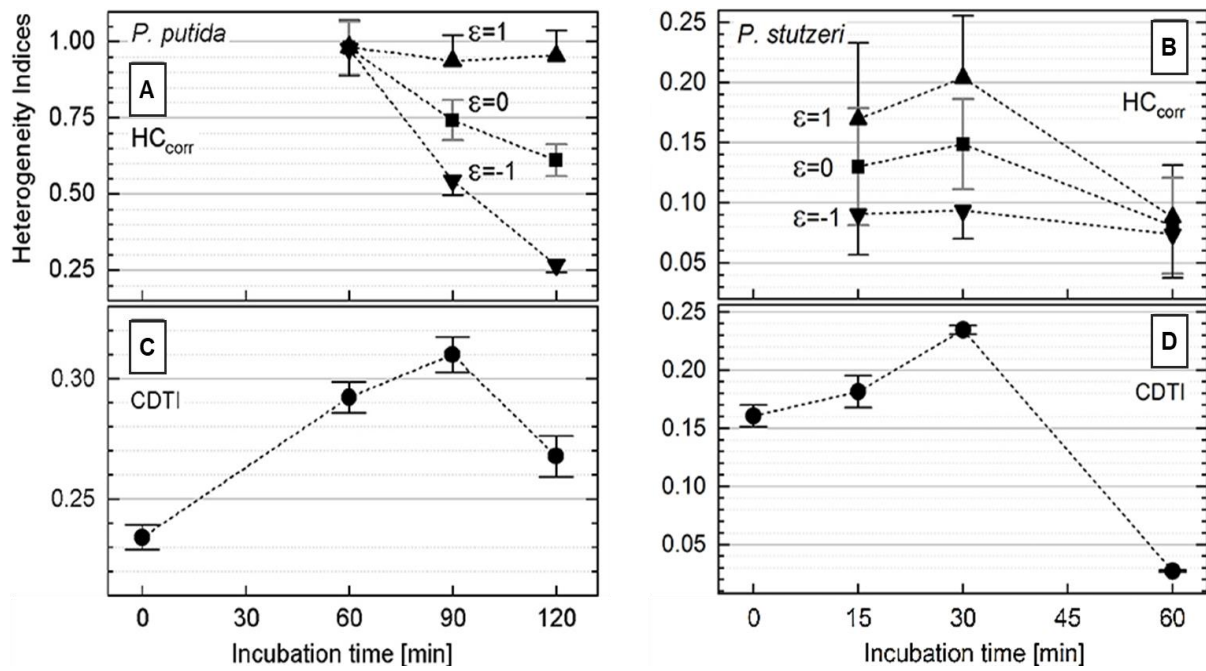
Figure 27. Heterogeneity indices. **A)** *P. putida* and **B)** *P. stutzeri* show the comparison of HC_{corr} values at different incubation times calculated with different ε values; error bars represent the correction for CSE, ΔHC_{corr}. **C)** and **D)** show the trend over time of the Cumulated Differentiation Tendency Index (CDTI) represented as $S \pm \Delta S$.

Importantly, the **HC** expression returned the same value of CV if applied on datasets with normal (Gaussian) distribution, since both skew and ε *factor* would equal zero. However, neither the CV nor the **HC** could account for one of the features of **MH**, that is the outcome of subpopulations. In this latter case, cells were no longer distributed into a skewed distribution, but rather into two or several peaks (Fig. 23-B), namely **bi-** or **multimodal** distribution.

Cumulative/Differentiation Tendency Index (C/DTI)

For tackling the challenge to **quantitate heterogeneity** under **bi-** or **multimodality**, we used a modification of Lavallette's power function describing the empirical *Zipf's law* [204], previously used to describe the rank–frequency distribution of words in literary texts [205] and applied it to the rank-activity distribution of bacterial cells [201](see appendix). Instead of showing the cells activity distribution with histograms (Fig. 25), we first represented them in double logarithmic scale, putting the rank on X-axis and cell activity, expressed in K_A, on Y-axis (Fig. 28). With this representation, it was easier to see the occurrence of many steps alongside the distribution of single cells, corresponding to each subpopulation within the same bacterial population (grey arrows, Fig. 28). When plotting the cells as histogram it was not possible to appreciate this net subdivision (histogram on the Y-axis, Fig. 28). Once having the rank-activity plot, each population of cells was then approximated with the modified Lavallette's function by fitting its parameters (q, s, N) using Origin2019 software; with this approximation it was possible to obtain a "fitting curve" with one slope (s), which indicated the **differentiation tendency index** (DTI) of the population.

We found that when *s* was equal or close to zero, the slope was horizontal and the population followed unimodality; in fact, this corresponded to having many cells with similar K_A values (e.g. up-left subpopulation in Fig. 28).
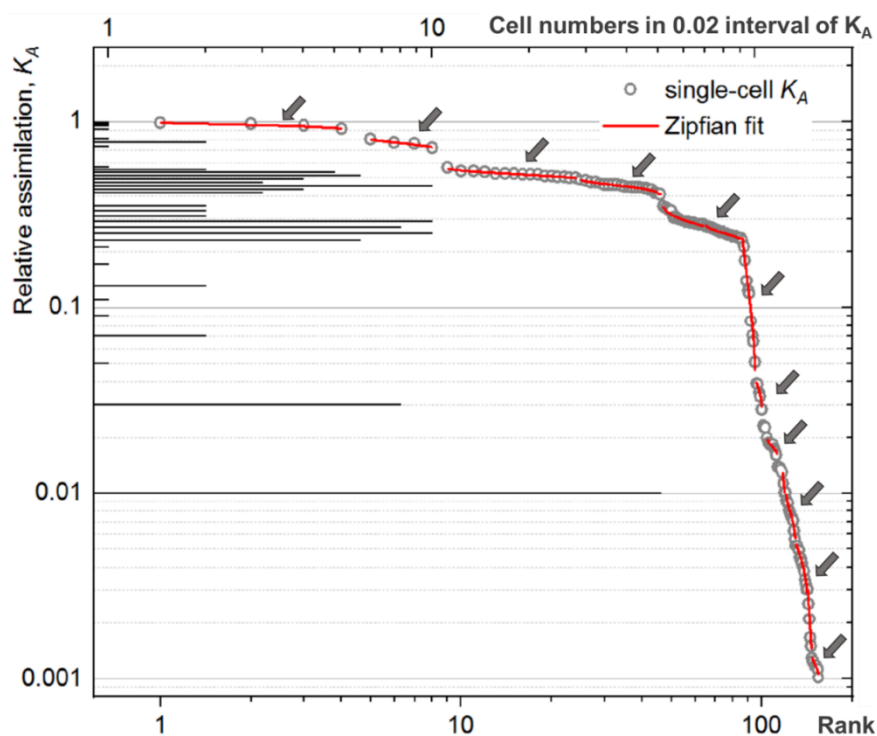
Figure 28. Rank–activity (K_A) distribution of *P. putida* single cells after 60 min of incubation with ^{13}C-acetate. Grey hollow circles represent the relative C assimilation (K_A) of each single cell. Dark grey arrows represent subpopulations. On the Y-axis, the histogram representing the distribution of the same cells overlaid for comparison. Red lines represent the fitting with modified Lavallette's Zipfian law.

When single-cell-K_A values differentiated a lot to each other, the resulting slope after fitting was more and more steep, meaning that the higher the *s* values the more the heterogeneity within the population increases (e.g. down-right subpopulation in Fig. 28).

In few words, when the population followed normal (Gaussian) distribution, it was possible to fit all the cells with one single **DTI** (Fig. 29). Instead, when it followed **bi-** or **multimodal** distribution, one single **DTI** did not fit anymore the whole population, resulting in a very large error ($s \pm \Delta s$, inset in the Fig. 30). In such case, it was necessary to derive one **DTI** for each subpopulation (red lines and grey arrows, Fig. 28). Because we wanted to obtain a unique parameter to measure **MH**, the **Cumulative Differentiation Tendency Index (CDTI)** was derived, which "cumulates" each **DTI**, while accounting for the number of subpopulations and the number of cells in each subpopulation. We called such method multi-component *Zipfian approximation*, due to the necessity to fit each single component first and derive the cumulative value thereafter [201] (see appendix).

We thus calculated **CDTI** for the two *Pseudomonas* strains at each time point (Fig. 27-C, D). *P. putida* was much more heterogeneous than *P. stutzeri* at each incubation time considered.
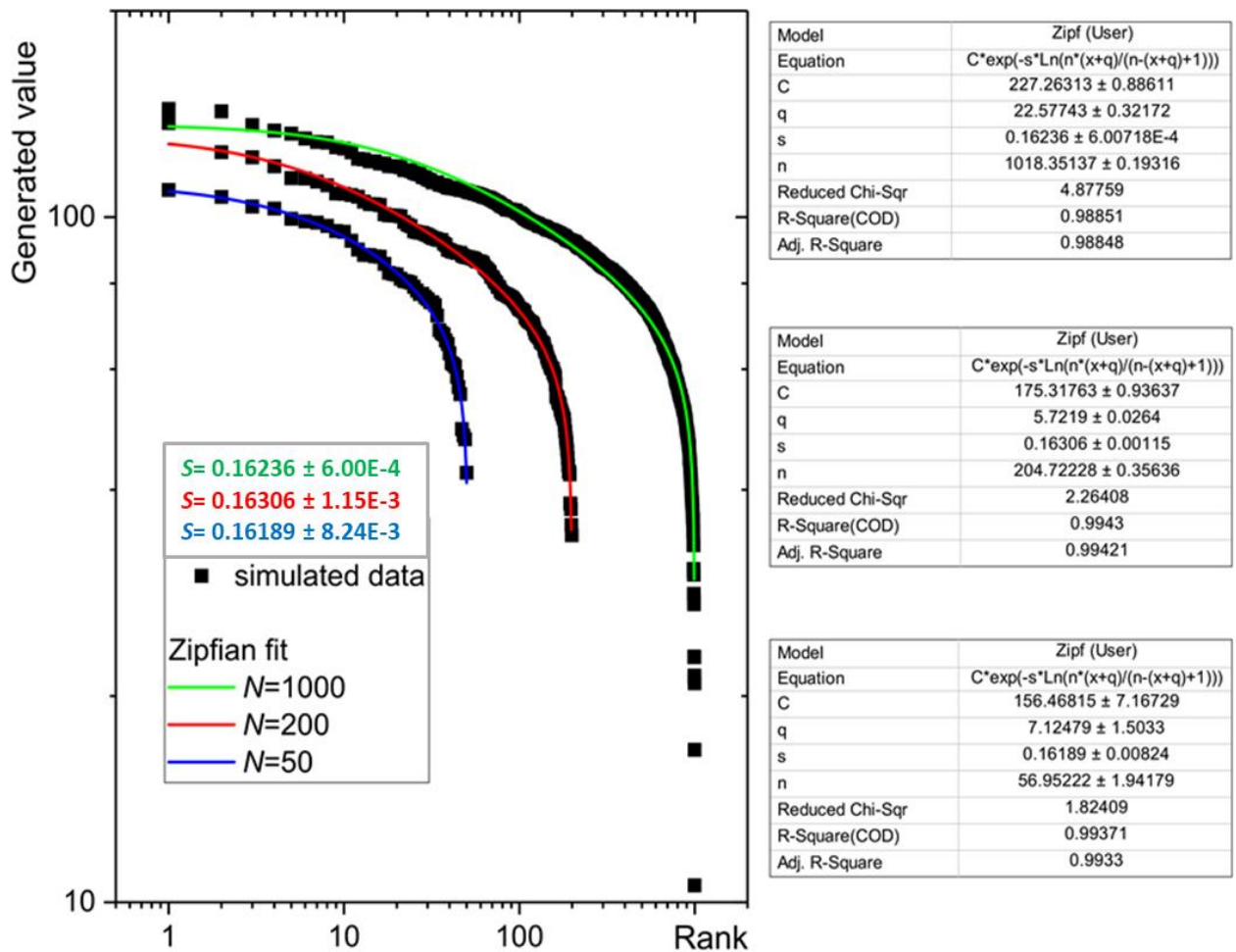
Figure 29. Simulated unimodal distributions of different population sizes plotted as rank-cellular activity and fitted with modified Zipfian law. Different colors show different cell numbers (N). DTI (s) values are provided as inset in the plot. On the right panels, the outcome of Zipfian approximations is shown as it is provided by Origin software.

Indeed, the **CDTI** trend over time for *P. putida* resulted completely different from the trend in **HC_{corr}** (Fig. 27-A, C); this was because the distribution of the population was clearly **multimodal** and **CDTI** could appreciate and account for the contribution of the subpopulations (Fig. 27-C). For *P. stutzeri* instead, the **CDTI** trend was more similar to the **HC_{corr}** calculated with the *ε factor=1*, i.e. more sensitivity to the outliers (Fig. 27-D). *P. stutzeri* showed less **MH**, resulting in a **bimodal** distribution just at time 30 minutes (Fig. 25), which indeed corresponded to an increase of **CDTI** (and of **HC*corr*** just when calculated with *ε factor=1*)(Fig. 27-B, D) [201](see appendix).
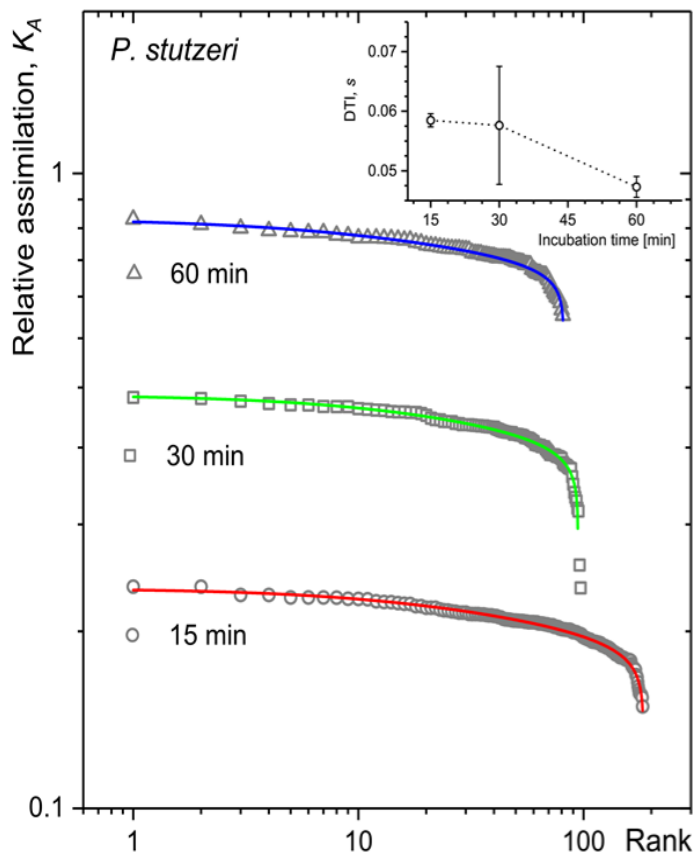
Figure 30. Rank-activity in K_A plots and single-component Zipfian approximation for *P. stutzeri* at three different time points. The inset shows the s±Δs obtained with the fit. Time point 30 minutes showed a huge error of fitting because of the non-unimodal distribution.

Besides CV, so far, few other attempts have been done to calculate heterogeneity in microbial populations. *Saccharomyces cerevisiae* and *Escherichia coli* grown aerobically in glucose-limited chemostats showed **phenotypic heterogeneity** depending on applied dilution rates and glucose pulses in the media [206]. Simulating fluctuations in substrate concentration normally happening at industrial scale, the heterogeneity was quantified based on the shape of the distribution of single-cell fluorescence values obtained with flow cytometry [206]. In particular, a combination of parameters such as the slope of the distribution function, peak width, CV and skewness have been used; the latter was calculated as difference between mean and mode, and considered as index for measuring asymmetry. The slope of the distribution in turn indicated the distribution width: the higher the slope the narrower the distribution and therefore the lower the population heterogeneity. On the contrary, an increase of heterogeneity was displayed as lower slope, higher peak-width, and higher CV values. In comparison with our approach, this approach presents two limitations: it does not provide a unique value of heterogeneity (it is actually the combination of more parameters) and it is less sensitive and powerful in the case of the occurrence of subpopulations, especially when unimodal distribution is hiding a potential **Bimodality** or when the distribution is clearly **multimodal** [206].

Another application focused on the dynamics of heterogeneity overtime, using a segregostat, a particular chemostat able to monitor *phenotypic diversification* of microbial populations with online analysis. A special pattern of subpopulations of *Pseudomonas putida* and *Escherichia coli* grown with

glucose pulses could be observed and the heterogeneity was measured based on subpopulations ratios [207]. Such approach did not consider heterogeneity under unimodal distribution. Moreover, it did not take into account the contribution of each subpopulation, i.e. cell numbers, within the whole population. Indeed, the focus of the study was on the heterogeneity dynamics, rather than **heterogeneity quantitation**, upon induction of the outcome of subpopulations via glucose pulses [207].

A further attempt was done to quantitate and compare **MH** on photosynthetic pico-eukaryotes, *Prochlorococcus* and *Synechococcus* species sampled from two different locations [208]. Coupling flow cytometry with nanoSIMS, the authors could reveal heterogeneity in metabolic activity when different inorganic C- or N-sources or urea were administered to the cells. The heterogeneity was measured always as CV, although a correction factor for the analytical error coming from the Poisson distribution of the counts detected with nanoSIMS was introduced. The correction was done using counts average from isotope fraction, Poisson distribution model and assimilation based on the normalization with bulk method, omitting the statistical error (CSE) upon ions counting in each single cell, the duration of cell incubation and the initial isotopic abundance, thus possibly introducing other bias in the heterogeneity measurement [208].

HC and DTI/CDTI as universal parameters

The **DTI** is independent of the population size (Fig. 29), normalization procedures, and measure units, making its use general and universal. To prove this last point, we applied the **HC** and **DTI/CDTI** indexes for **quantitation of heterogeneity** measured with other techniques.

Flow cytometry

P. putida cells grown in M9-leucine medium supplemented with 1 g/L of acetate were sampled at 8 time points upon cultivation in batch for 26 h, stained with DAPI (4′,6-Diamidin-2-phenylindol) and analyzed with flow cytometry (Fig. 31). During the cell cycle, cells duplicate their DNA and expand, but not always, their volume; additionally many chromosomes may co-exist before cell division within each cell [209]. DAPI stains the DNA, thus labelling the chromosome inside each individual cell, so that with flow cytometry it is possible to measure DAPI fluorescence intensity on the one side and the cellular Forward Scattered signals (FSC) on the other [209]. Cells can thus be sorted based on their size (FSC) and their DNA content (DAPI) and the resulting dot plots allow for the identification of subpopulations based on the chromosome numbers (Fig. 31-A). **Multimodal** distributions (outcome of subpopulations) were clearly evident from the dot plots and further confirmed from the histograms (Fig. 31-B). Single cells represented as dot plots of FCS (X-axis) vs. DAPI intensity (Y-axis) (obtained from data transformation with dedicate flow cytometry software) (Fig. 31-A) were compared with the same cells represented as histograms (Fig. 31-B) and as rank-DAPI intensity plot (Fig. 31-C). Therefore, using flow-cytometry-raw data and plotting them in the rank-DAPI intensity distribution, **CDTI** was calculated with *multicomponent Zipfian approximation* (Fig. 31-C, E) for each of the time points analyzed. The measured **CDTI** values were able

to reproduce the changes in subpopulations' number, and additionally **quantitate heterogeneity** within and between the bacterial populations at each time point (Fig. 31-E). Considering all the subpopulations (G_1-G_x), the **CDTI** patterns nicely described the dynamics of the population heterogeneity: at the T0 it was very high, then decreased at 2 h to steeply increase at 6 h; at 24h it returned back to a very similar value with the initial one (Fig. 31-E). This pattern similarity further supported the applicability of the **CDTI** for measuring heterogeneity with different data sets, due to its ability to resolve the subpopulations contribution. **HC** was also calculated on these data, but it failed to reproduce the same heterogeneity dynamics, proving once more its unsuitability for **quantitating heterogeneity** when populations follow **multimodality** (Fig. 31-D).
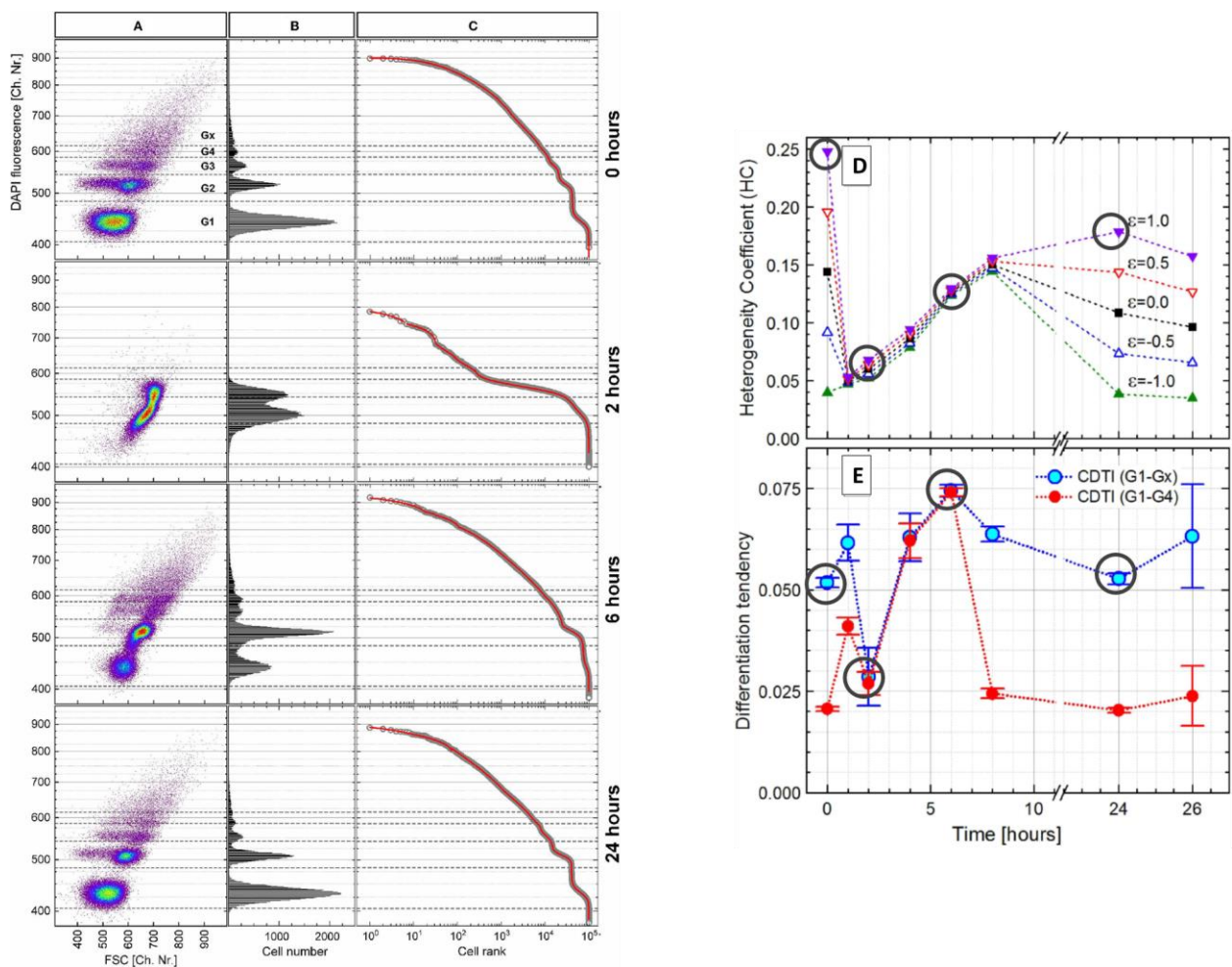
Figure 31. Flow cytometry data of *P. putida* cells and heterogeneity dynamics during growth over 26 h. **A)** Representative dot plots corresponding to 0, 2, 6, and 24 h samples showing DAPI fluorescence intensity (related to DNA content) vs. forward scatter (FSC) intensity (related to cell size). **B)** Histograms of DAPI fluorescence intensity distribution used to define the boundaries between the subpopulations G1–Gx, which correspond to the chromosomes number in the cells. **C)** Rank-DAPI intensity plots with the *multicomponent Zipfian fit* (solid red line). **D)** Derived **HC** and **E)** **CDTI** values after *multicomponent Zipfian approximation*. The corresponding time points are highlighted with black open circles.

Microscopy

We further proved the applicability of our method using an already published dataset where the cell length was measured with microscopy [119]. In this work, the metabolic specialization of *E. coli* under feeding or co-feeding with two C-sources, glucose (Glc) and arabinose (Ara), was studied.

Measuring heterogeneity with CV, the authors found the highest heterogeneity during co-feeding under C-limitations conditions (Fig. 32-C); instead, growth on one single C-source, even under nitrogen limitation, caused less heterogeneity. The bacterial populations showed unimodality under all tested conditions, never showing **bimodality** even upon co-feeding [119]. We further tested these results while applying **HC** and **DTI** for **heterogeneity quantitation**. The **HC** values calculated with *ε factor=0*, or *=−1* (Fig. 26) followed the CV trend (Fig. 32-C, D), as expected for unimodal distribution. **HC** with *ε factor=1* was higher for the condition 10 μM Glc + 10 μM Ara (Fig. 32-D), reflecting indeed the slight skew of this distribution (Fig. 32-A). Then, we plotted the cell populations as rank–length distributions (Fig. 32-B) and approximated with **DTI** (Fig. 32-E). Two observations could be done: i) heterogeneity between 3 μM Ara + 3 μM Glc and 10 μM Glc + 10 μM Ara was almost the same although this was not revealed by the CV values (Figure 32-C). Moreover, the condition 3 μM Ara + 3 μM Glc showed a higher **DTI** error reflecting the larger distribution width of this population (Fig. 32-E). ii) We could approximate all conditions with one single **DTI** and high goodness of fit (Fig. 32-E). Indeed, both **HC** and **DTI** indices confirmed the unimodal distribution of all populations, in agreement with what was reported by Nikolic and coauthors[119].

These results showed the usefulness and applicability of our method on a large variety of datasets and different techniques. While accounting for unimodal and asymmetric distribution on one side and **bi-** or **multimodal** distribution on the other, we provided two universal indices as **heterogeneity units measure**. When applied on nanoSIMS data, the correction for CSE was implemented to account for the error in **HC** coming from the experimental conditions. To the best of our knowledge, no studies have shown this before. Understanding the entity of CSE helps to estimate how much ion counts need to be acquired per cell in order to minimize the heterogeneity caused by counting statistics [201]. The developed indices are suitable for measuring not only metabolic but also physiological, morphological and **phenotypic heterogeneity**. Most importantly, both **HC** and **DTI/CDTI** provide unique values, with their errors, that can be used reliably to compare different conditions to each other. For this reason, such indices were successfully applied for **quantitation** and **comparison** of **MH** under different experimental conditions in the next section of my work.
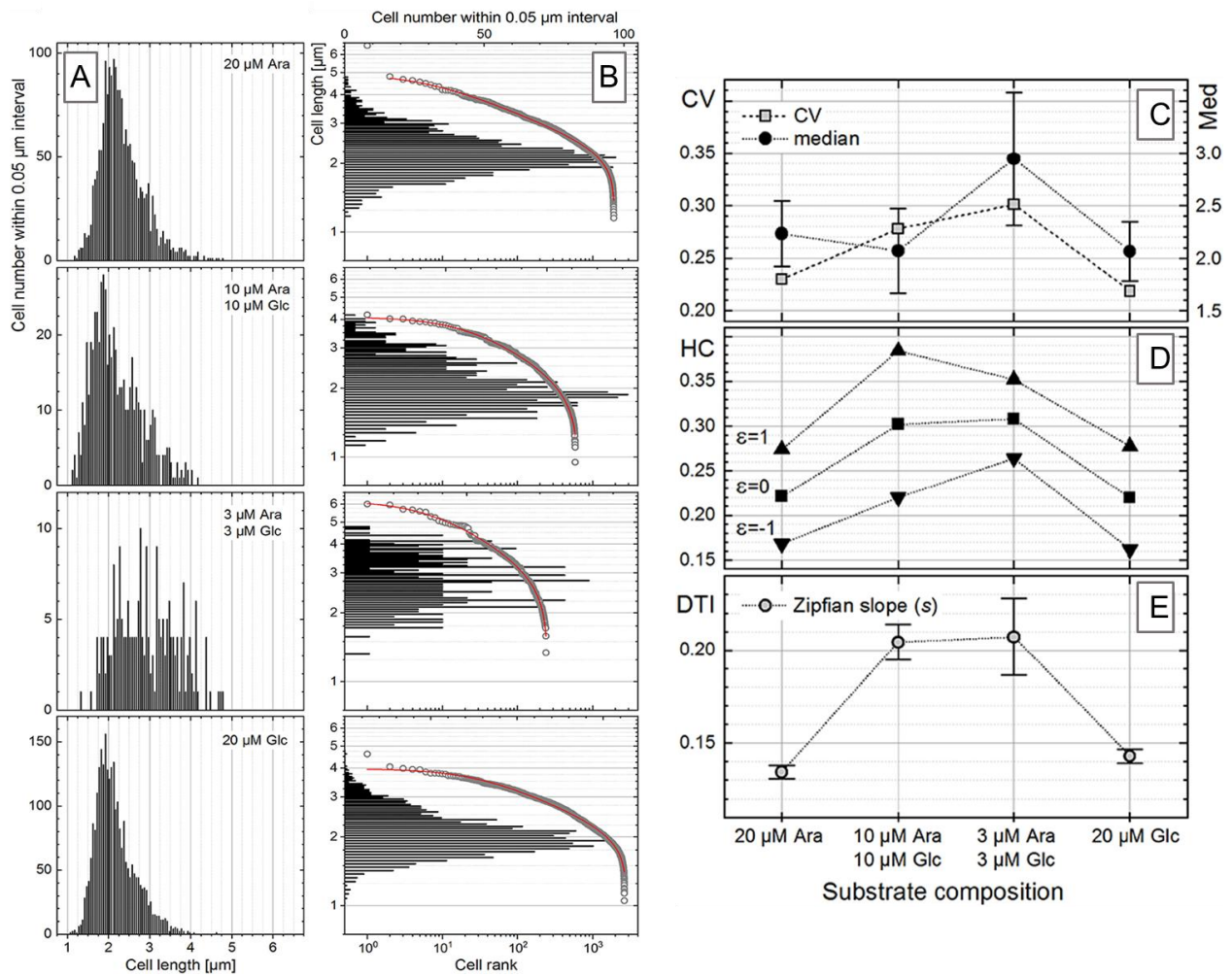
Figure 32. The distribution of *Escherichia coli* single cells in their length upon growth under different conditions as reported in [119] represented as **A)** histograms and **B)** rank–length plots of the respective histograms. Single-cell length heterogeneity derived as **C)** Coefficient of variation (CV) together with the median cell length and its error [± median absolute deviation (MAD) interval]; **D)** Heterogeneity Coefficient (HC) calculated with different ε values; **E)** Differentiation Tendency Index [DTI, *s*, Zipfian slope] of the rank–length distributions as $s \pm \Delta s$ (error bars are shown as $\pm \Delta s \times 100$ to be magnified).

3.3 *Abiotic factors shaping metabolic heterogeneity in bacterial populations*

A quantitative understanding of each single-cell contribution to metabolic activity of the whole population could help to explain **cell-to cell variability** in response to different factors. **Phenotypic** and **MH** have been shown so far mostly under unfavorable conditions, such as nutrients limitations, oxidative and thermal stresses, spatial restriction, or antibiotics exposure. However, little is still known about **MH**, if and how can be displayed by microbial populations under physiological or **non-limiting conditions** and particularly which **abiotic factors** influence mostly its outcome. Under limiting conditions, different species behave in the same way upon equal modality of limitation. For example, **MH** in N_2 fixation of *Klebsiella oxytoca* [69] and *Chlorobium phaeobacteroides* [72] populations increase in a similar way under NH_4 limitation, although the species are phylogenetically distant. There are no studies currently investigating on how the same **abiotic factors** can influence the outcome of heterogeneity in the same or diverse microbial genera under physiological conditions.

Non-limiting conditions

I aimed to investigate the **MH** of three bacterial strains under **non-limiting conditions** considering the influence of **abiotic factors** such as carbon sources (C-sources) and their concentrations as well as two electron acceptors, namely oxygen and nitrate (Sketch 3-A). During the semi-logarithmic phase of their growth, bacteria do not experience any limitations in growth substrate and electron acceptors, which at this phase should be not yet depleted. To test this hypothesis, three different species were cultivated in batch: *Pseudomonas putida* mt-KT440, *Thauera aromatica* K172 and *Pseudomonas stutzeri* FC01. For the two *Pseudomonas* species a mineral salts medium was used, supplemented with $NaHCO_3$ (30 ml/L) as buffer system, with addition of 10% CO_2 in the headspace (9 ml) and 1 ml inoculum. For *T. aromatica* a phosphate-buffered DSM 586 medium [210] was used because of the strain preference for this buffer instead of $NaHCO_3$. For aerobic cultivation, medium was prepared with the omission of nitrate; for anaerobic one the complete DSM 586 medium was prepared following the procedures for anoxic media preparation [211]. All bacterial suspensions were prepared in sealed 140-ml serum bottles containing 29 ml of medium and 1 ml inoculum and grown at 30°C with orbital shaking (100 rpm). The three strains were grown with two distinct C-sources, acetate and benzoate, at two concentrations, 0.5 and 5 mM or 0.1 and 1 mM, respectively. *T. aromatica* was grown using either oxygen or nitrate as electron acceptors (Sketch 3-A).

Bacteria were cultivated for several passages under each of the above-mentioned condition, after which growth kinetics (optical density at $\lambda = 600\ nm$, OD_{600}) and substrate consumption (Ionic-exchange Liquid Chromatography for acetate and High-Pressure Liquid Chromatography for benzoate) were measured over time in duplicate for each condition (Sketch 3-B). This was necessary to establish the sampling time corresponding to the phase in which bacteria are growing exponentially while still having more than half than initial substrates and electron acceptors (mid-log phase). From now on, I will refer to such conditions as **non-limiting.**
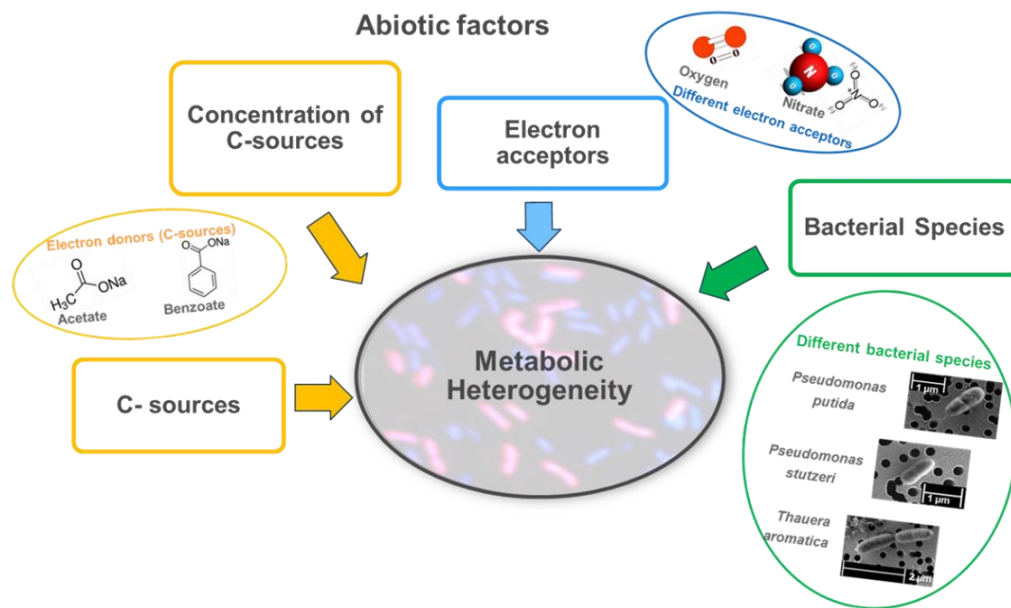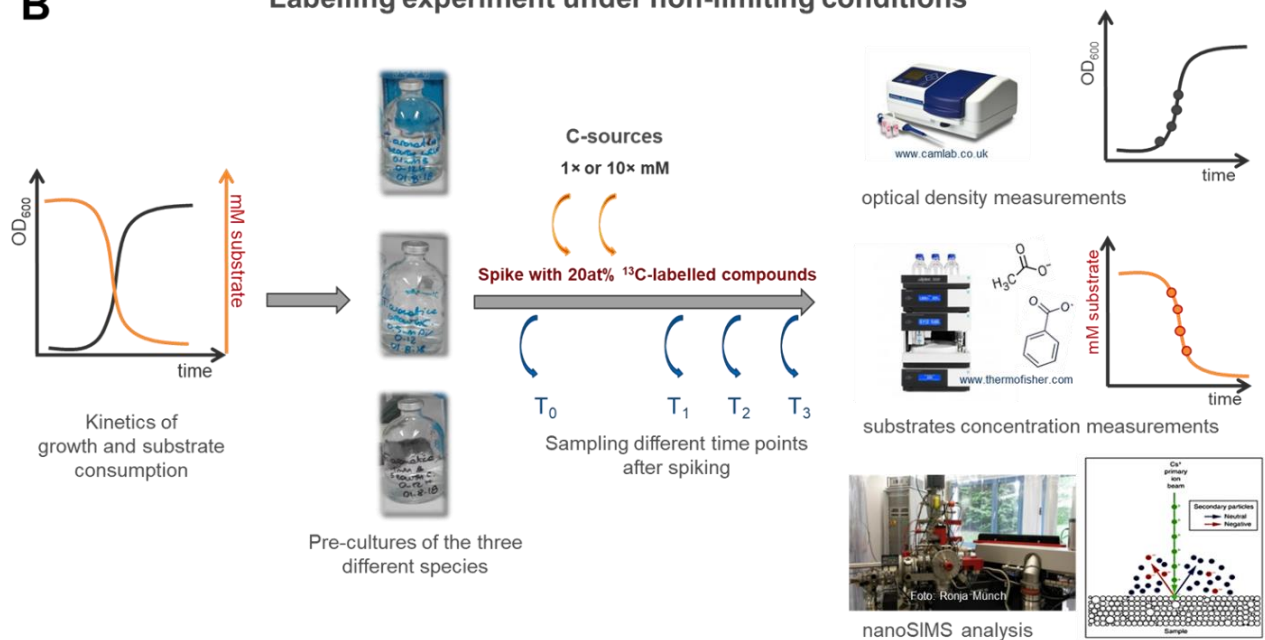
Sketch 3. Investigation of factors shaping **MH** in three bacterial populations **A) Abiotic factors** tested to investigate their influence on **MH**. **B**) Schematic of the labelling experiments workflow: growth kinetics evaluation in batch cultures, labelling experiments, sampling at different time points and downstream analysis, such as growth evaluation with optical density, substrates concentration measurement and nanoSIMS analysis.

Afterwards, isotope-labeling experiments were performed. The cultures were grown with each combination of C-sources and concentrations and, for *T. aromatica,* electron acceptors. Each culture was incubated with unlabeled substrates for the span of the lag-phase, determined from the growth curve, and

then spiked with ^{13}C-acetate (Ac) or ^{13}C-benzoate (Bz), corresponding to 20 at% of the initial concentration, just after the beginning of the exponential phase (Sketch 3-B).

Cells were withdrawn before the addition of label, called T0, and for three subsequent time points until the mid-exponential phase, depending on the growth kinetic of each strain under different growth conditions. Then, samples were split in three aliquots to test: bacteria growth (OD$_{600}$), substrate concentrations, and anabolic activity (nanoSIMS analysis) (Sketch 3-B). This was done to confirm that cells were still under **non-limiting conditions**, so that we could measure their activity and investigate on their **MH**. Each sample was analyzed with nanoSIMS instrument with the optimized parameters discussed above (see paragraph "Precision of cellular isotopic composition measurements with nanoSIMS"); 7 masses (secondary ions) were collected in parallel: $^{12}C_2-$, $^{13}C^{12}C-$, $^{12}C^{14}N-$, $^{13}C^{14}N-$, $^{31}P-$, $^{32}S-$, and $^{31}P^{16}O_2-$ in negative extraction mode. The data treatment, the calculation of K_A values and **heterogeneity quantitation** were performed as mentioned in the previous chapters. In total, 10443 cells were analyzed, corresponding to 3 to 5 randomly picked FoVs per each condition and time point (Table 1).

Single-cell Carbon assimilation

Before isotope-labels addition, at T0, cells showed $^{13}C^{14}N-/^{12}C^{14}N-$ ratios ranging from 0.0103 to 0.0118, values very close to the natural abundance (^{13}C =0.0109). Following the addition of 20 at% labelled substrate, cells collected from each set-up showed a gradual enrichment in the ^{13}C content over time, further revealed by their relative C-assimilation measured as K_A (Fig. 33).

Single cells of *P. putida* showed a similar distribution in their carbon assimilation at both Ac concentrations, 0.5 vs. 5 mM (Fig. 33-A), with relatively similar K_A median values. A substantial fraction, i.e. 14 to 35% of analyzed cells, showed no or little assimilation of carbon (K_A<10%) at both substrate concentrations and all time points, except for T3 of the culture growing with 0.5 mM Ac (Fig. 33-A, B). Instead, *P. putida* cells showed distinct carbon assimilation trends with Bz, with significantly higher K_A observed for 1 mM vs. 0.1 mM initial substrate concentrations (Fig. 33-B); even the distribution of single cells in their carbon assimilation was different: with 0.1 mM Bz it was always scattered around the median at all T points, while with 1 mM it was initially more compact at the beginning to become more scattered at T3 (Fig. 33-B).

Single cells of *P. stutzeri* showed higher C-assimilation with the higher initial substrate concentrations for both substrates; in fact, at T3 the median K_A was about 6.2-fold higher for both conditions (Fig. 27-C, D). The cells distribution in C-assimilation is less scattered around the median K_A values for the higher concentration in comparison with a much scattered for 0.5 mM Ac and 0.1 mM Bz. Interestingly, T2 of both 5 mM Ac and 1 mM Bz assays showed a marked **bimodal** distribution, where 4.5 and 56% of the cells respectively showed K_A values below 25% (Fig. 33-D); this was also the reason why the K_A median values were small despite the highly active cells, especially for 1 mM Bz (Fig. 33-D, Table 1).
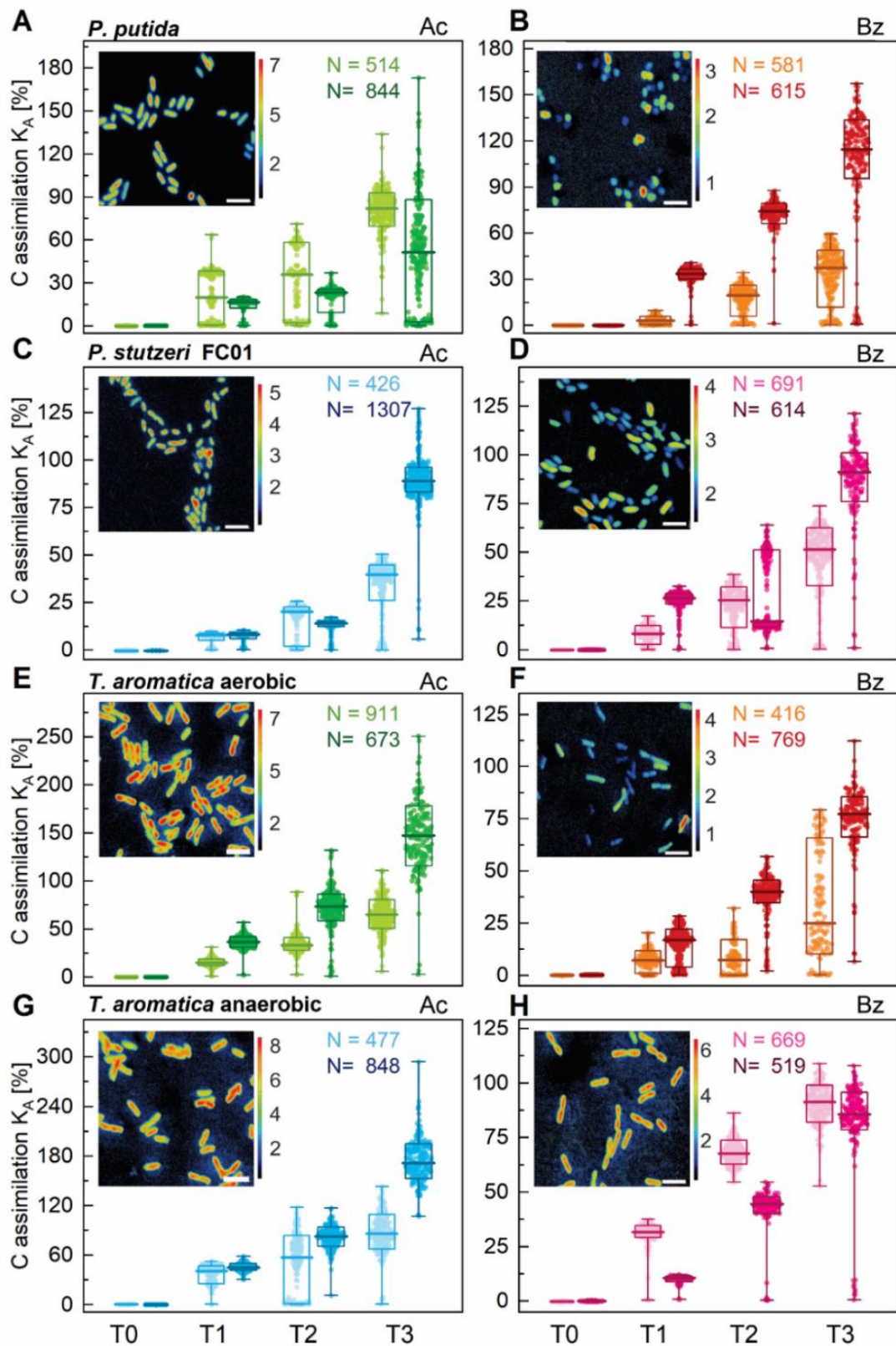
Figure 33. Single-cell assimilation over time. Each row represents a different strain with the two C-sources used: acetate (Ac - A, C, E, G) and benzoate (Bz - B, D, F, H). *P. putida* **(A, B),** *P. stutzeri* **(C, D)** and *T. aromatica* under aerobic **(E, F)** vs anaerobic conditions **(G, H)** are shown. For each substrate, the panel shows single-cell carbon assimilation values (K_A) with the low concentration (lighter color) and the high one (darker color) distributed in box plots (boxes include the 16–84 percentile range, whiskers and Min or Max values the rest of the distribution); horizontal lines represent median values. Examples of $^{13}C^{14}N^-/^{12}C^{14}N^-$ ion maps acquired with nanoSIMS, corresponding to the low substrate concentration assays, are shown as insets. Scales of micrographs is 2 μm.

Table 1. Number of cells analyzed with nanoSIMS at each time point for all the tested conditions. Carbon assimilation (median K_A) in percentage, growth rate calculated from OD_{600} (bulk) and calculated from K_A (single cells) are provided.

STRAIN	Growth substrate and initial concentration	Sampling time (h)	Number of cells analyzed	Carbon assimilation (Median K_A, %)	Bulk growth rate (v, h^{-1})
Pseudomonas putida	Acetate, 0.5 mM	0	66	0.22	0.640 ± 0.19
		1	137	21.16	
		1.5	128	36.77	
		2	183	83.99	
	Acetate, 5 mM	0	143	0.159	0.776 ± 0.07
		0.5	236	16.61	
		1	190	23.34	
		2	275	54.04	
	Benzoate, 0.1 mM	0	58	0.14	0.926 ± 0.06
	Benzoate, 1 mM	0	58	0.14	0.757 ± 0.03
		0.5	220	33.65	
		1	166	74.62	
		1.5	187	38.77	
Pseudomonas sp. FC01	Acetate, 0.5 mM	0	64	0.18	0.658 ± 0.02
		0.25	114	7.99	
		0.5	105	20.30	
		1	143	40.58	
	Acetate, 5 mM	0	62	0.18	1.057 ± 0.03
		0.25	167	8.40	
		0.5	246	14.12	
		1.5	406	89.19	
	Benzoate, 0.1 mM	0	39	0.21	1.113 ± 0.00
	Benzoate, 1 mM	0	51	0.22	0.856 ± 0.03
		0.5	209	26.45	
		1	191	14.63	
		1.5	163	51.69	
Thauera aromatica, Aerobic	Acetate, 0.5 mM	0	122	0.16	0.155 ± 0.08
		2	265	15.10	
		4	247	33.31	
		8	277	64.99	
	Acetate, 5 mM	0	122	0.16	0.067 ± 0.03
		2	181	36.47	
		4	206	73.30	
		8	164	147.33	
	Benzoate, 0.1 mM	0	28	0.35	0.050 ± 0.02
	Benzoate, 1 mM	0	101	0.25	0.094 ± 0.06
		2	296	16.92	
		4	207	40.11	
		6	139	7.66	
		8	130	25.46	
Thauera aromatica, Anaerobic	Acetate, 0.5 mM	0	27	0.34	0.113 ± 0.03
		2	149	40.80	
		4	154	57.20	
		6	133	7.12	
		8	147	86.01	
	Acetate, 5 mM	0	128	0.44	0.278 ± 0.00
		2	299	45.25	
		4	221	82.84	
		6	242	67.75	
		8	200	171.80	
	Benzoate, 0.1 mM	0	103	0.18	0.280 ± 0.00
	Benzoate, 1 mM	0	44	0.1	0.223 ± 0.12
		1	138	10.92	
		2	136	44.54	
		8	201	85.69	

T. aromatica cells under aerobic conditions showed a similar behavior to that of *P. stutzeri* (Fig. 33-E, F). C-assimilation was higher for the higher concentration of both substrates. Moreover, the cells distributions from incubations with 5 mM Ac and 1 mM Bz were less scattered around the K_A median values for all time points, except T3 (Fig. 33-E). On the contrary, incubations with lower substrate concentration showed more scattered distributions, particularly the 0.1 mM Bz assay that showed **bi- or multimodality** (Fig. 33-F).

Instead, most of *T. aromatica* cells grown under anaerobic conditions (nitrate as electron acceptor) showed high C-assimilation, with none or few cells showing low K_A values. Again, the distribution of cells was less scattered around the median for high substrate concentration assays in comparison with low concentrations; cells from T1 grown with 5 mM Ac showed even unimodal, though skewed, distribution (Fig. 27-G). For 1 mM Bz instead there was always a percentage of low-active cells, 21%, 5% and 4% for T1, T2 and T3 respectively, which made the distribution very tailed. For Ac, median K_A values were always higher at high concentration (Fig. 33-G; Table 1) while for Bz the opposite was observed (Fig. 33-H; Table 1).

From the analysis of the single-cell distributions in relative C-assimilation, it was obvious that in almost all the cases bacterial populations were not following unimodality but rather **bi-** or **multimodality**. However, the distribution per se was uninformative about the heterogeneity within each bacterial population, so the single-cell K_A values were exported to the Origin software (package version 2019) and further used for **quantitation of heterogeneity** (Sketch 2). Because the distribution was never unimodal, the cumulative differentiation tendency index (**CDTI**) was calculated as a quantitative measure of the **MH.**

With SIP-nanoSIMS approach, isotope-labeled compounds are used as tracers to quantify assimilated elements into the cell biomass, thanks to their biosynthetic activity (anabolism); for this reason, **cell-to-cell differences** shown with nanoSIMS analysis are considered as anabolic heterogeneity (**AH**)[118]. The higher the **CDTI** value, the higher **AH** displayed by the population.

To study the dynamics of heterogeneity over time, we calculated **CDTI** values for the T1 – T3 samples and linked them to the actual substrate concentration (consumed upon labeling experiments) and the relative C-assimilation, namely K_A median values (Fig. 34). At T0, the ^{13}C fraction in the growth substrate corresponded to the natural abundance, thus offering a different resolution degree (from 0.0103 to 0.0118) in comparison with the ^{13}C-enichemnt in T1–T3 samples (from 0.0103 to 0.1711 in all other T points) for the evaluation of **AH** heterogeneity.

Dynamics of the anabolic heterogeneity (AH)

In general, the addition of isotope-labeled substrates (Fig. 34, red arrows) brought to a temporary increase in the substrate concentrations. The only exception was *P. putida* with 0.5 mM Ac, where the concentration at T1 was lower than T0, probably because of the rapid substrate consumption within the 1 h sampling interval (Fig. 34-A, Table 1). Upon growth on labels, while Ac and Bz concentrations were decreasing, the single-cell C-assimilation was increasing as shown by K_A values at each incubation condition (Fig. 33). The only exceptions to that were *P. stutzeri* with 1 mM Bz and *T. aromatica* aerobic

with 0.1 mM Bz assays, which showed a nonlinear increase of K_A median values over time; this was probably the effect of the clear **bimodal** distribution of these populations at T2, as shown before (Fig. 33-D, 33-F).

For *P. putida*, the **CDTI** values decreased with increasing median K_A and decreasing substrate concentrations for all tested conditions. The extent of **AH** was generally higher for Ac vs. Bz (Fig. 34-A, D). While Ac assays showed similar initial **CDTI** (T1) for both concentrations, with a decrease over time more prominent for the 0.5 mM Ac initial (Fig. 34-A, B), Bz assays showed **CDTI** values inversely correlated with the concentration: 0.1 mM Bz resulted in **CDTI** index more than 2-fold higher than 1 mM Bz concentration (Fig. 34-C, D).

For *P. stutzeri*, the **CDTI** values also showed a decreasing trend with increasing median K_A, except for cells grown with 0.5 mM Ac which showed a relatively low **AH**, with low and similar **CDTI** values over time (Fig. 34-E, H). The 5 mM Ac assay was more heterogeneous than 0.5 mM Ac with a decreasing trend over time. On the contrary, the **CDTI** dynamics for Bz assays was clearly inverse with substrate concentration (Fig. 34-E, F). The 0.1 mM Bz assay showed the highest heterogeneity, especially at T1 and T2, among all tested conditions. Although decreasing from almost 1 to 0.6 at T3, the **CDTI** values remained high over time. Instead, the heterogeneity of 1 mM Bz assay stayed relatively low over time, with slightly decreasing **CDTI** from 0.2 to less than 0.1 at T3 (Fig. 34-G, H).

For *T. aromatica* differences in anabolic activity were observed not only within but also between the bacterial populations grown under aerobic or anaerobic conditions (Fig. 34-I to P). With oxygen as electron acceptor, **CDTI** trend over time slightly decreased for 0.5 mM Ac but steeply increased for 5 mM Ac initial concentration (Fig. 34-I, J); when nitrate was used instead, the opposite trend was observed: **CDTI** trend steeply increasing for 0.5 mM Ac, and slightly decreasing, though having very low values, for 5 mM Ac assay (Fig. 34-M, N).

A different scenario was observed for Bz. **CDTI** values were relatively constant over time at 0.1 mM Bz concentration, although overall **AH** was higher for aerobic vs. anaerobic conditions (Fig. 34-M, N). For the 1 mM Bz assays, **CDTI** trend steeply decreased following the steep decrease of substrate concentration under aerobic conditions (Fig. 34-L), while it just decreased from T1 to T2 and remained constant at T3 under anaerobic conditions (Fig. 34-P). In the latter case, the substrate consumption was not as evident as for aerobic counterpart, probably influencing the **AH** of the bacteria population (Fig. 34-P).

The heterogeneity dynamics of each single condition was necessary to understand how each species react to different **abiotic factors**. However, we wanted to determine which factor/s influenced the most **AH** among substrate type and concentration, strain type, and electron acceptor. Plotting the actual concentrations (values measured with liquid chromatography) vs. the respective **CDTI** showed no obvious correlation (Fig. 35-A).
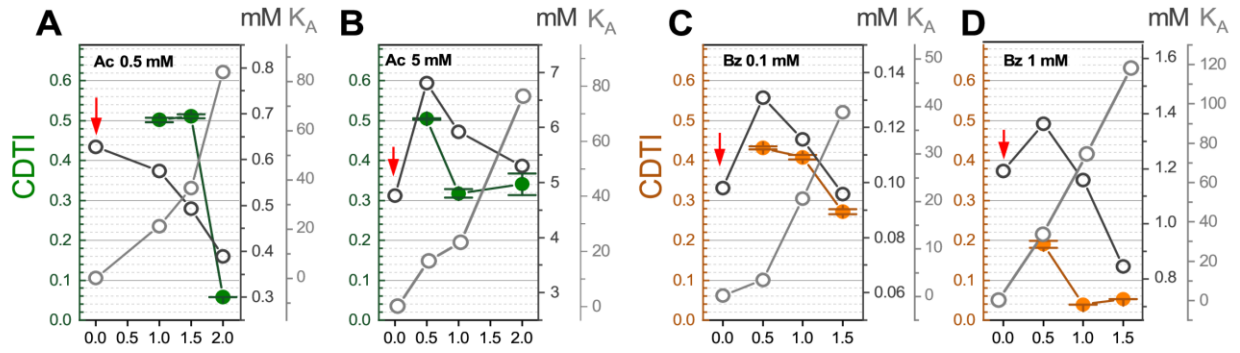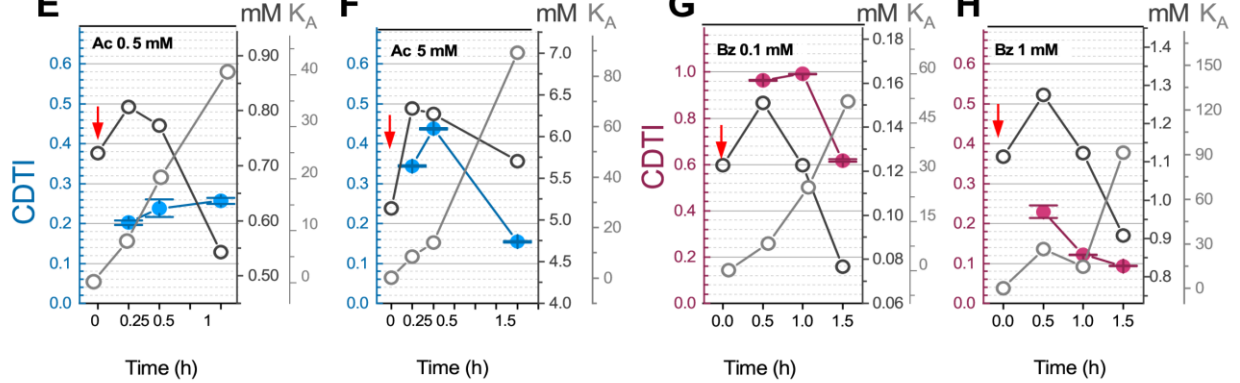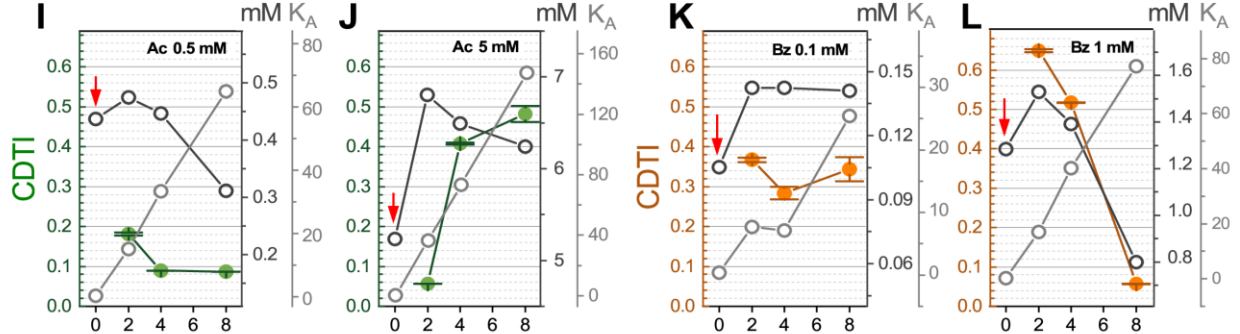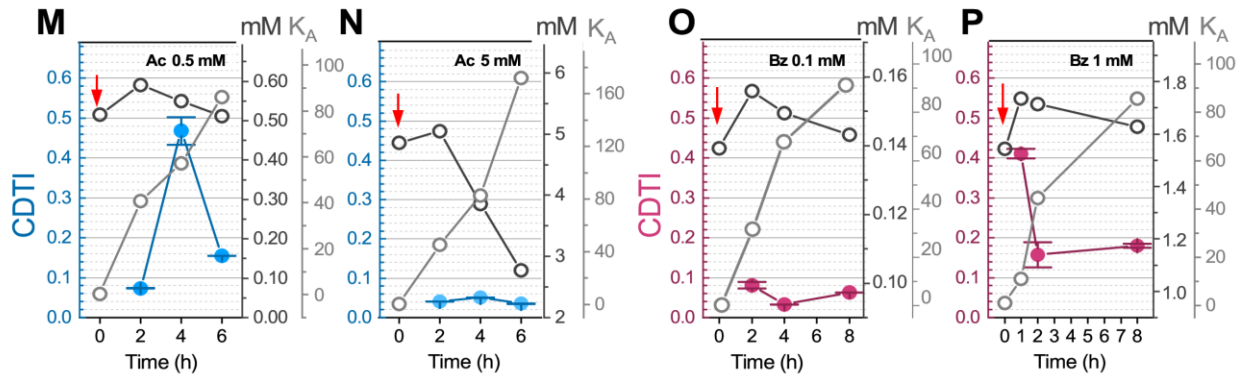
Figure 34. Heterogeneity, carbon assimilation and substrate concentration over time. Carbon assimilation (as median K_A) and substrate concentration over time before (red arrow) and after label addition. Colored filled circles show the trend of the CDTI index; hollow gray circles represent the median K_A; hollow black circles correspond to substrate concentration for assays of *P. putida* (panels A-D); *P. stutzeri* FC01 (panel E-H); *T. aromatica* under aerobic (panels I-L) or anaerobic (panel M-P) conditions. Note the different CDTI scale for *P. stutzeri* with 0.1 mM benzoate vs. all other CDTI plots, and the different scaling for the concentrations and K_A axes.

We also performed Mann-Whitney-U paired test as a statistical non-parametric test to study the differences between the treatments on the **CDTI**. When paired-compared, neither the concentration (Fig. 35-B) nor the other factors (Fig. 35-C) showed a statistical significance, indicating no influence on **CDTI**, thus on **AH.** To verify if some of the treatments were following a common **CDTI** trend over time, **CDT**I values were plotted as hierarchical clustering. However, also in this case no obvious clustering was visible, indicating that the **AH** dynamics over time were not influenced by the **abiotic factors** tested (Fig. 35-D). As final step, we calculated growth rates at both bulk level (from OD_{600}) and single-cell level (from K_A values) to test if there was at least a correlation of **CDT**I values with the growth rates (Table 1). The growth rates at single-cell level differed from the bulk growth rate (Table 1), due to the fact that OD measurement cannot distinguish between less and highly-active cells (while K_A does resolve **cell-to-cell differences** [187]). However, none of the growth rates showed any correlation with **CDTI** values.

Previous experiments with SIP-nanoSIMS approach showed higher **MH** in continuous cultures in comparison with batch [71,118,119]. Different dilution rates in chemostat possibly induce single cells or small subpopulations to differentiate, changing their metabolic activity and their growth rates as a strategy for optimization of resources [118]. To reduce as much as possible additional sources of heterogeneity, we thus chose batch cultivation to investigate if substrate types, concentrations and electron acceptors, influence the **AH** of three different bacterial populations. However, growing bacteria under **non-limiting conditions** brought to two very surprising results: i) microbial populations display **AH** even in batch cultures under **non-limiting conditions**, in the absence of apparent stressors; ii) almost in all conditions the decrease in substrate concentration corresponded to a decreasing trend of **AH** (Fig. 34). On the contrary, we would have expected that while approaching limiting conditions (low Ac or Bz in the growth medium) heterogeneity would increase [67,69].

In general, some common trends were found in almost all conditions. For example, the substrates were never depleted in any of the conditions (Fig. 34). Even when the substrates were 50% of the initial concentration, namely for *T. aromatica* with 1 mM Bz (aerobic) and *T. aromatica* with 5 mM Ac (anaerobic), the corresponding **CDTI** values were close to zero, i.e. very little heterogeneity. This was a further proof that bacteria were not facing yet nutritional limitations.

Moreover, the median K_A values showed in almost all conditions a linear increase in C-assimilation over time, indicating that the cells were still actively engaging in anabolic activities (Fig. 33 and Fig. 34). The only exceptions were *P. stutzeri* with 1 mM Bz and *T. aromatica* grown aerobically with 0.1 mM Bz, but this was rather the effect of a **bimodal** distribution that strongly decreased the median, than an evidence of an overall decrease in population activity (Fig. 33-D and 33-F).

However, statistical analyses showed that **CDTI** values are not influenced by any of the **abiotic factors** tested (Fig. 35-B, C). Nor a common heterogeneity pattern over time could be identified (Fig. 35-D), probably due species-specific dynamics of metabolic interactions and regulations over the growth phase. These results brought to the consideration that stochasticity was the driving force for the display of **AH** in bacterial cultures. Gene expression noise and extrinsic noise could be part of the causes, as it has been well documented *for Escherichia coli* [14,17,19,212].
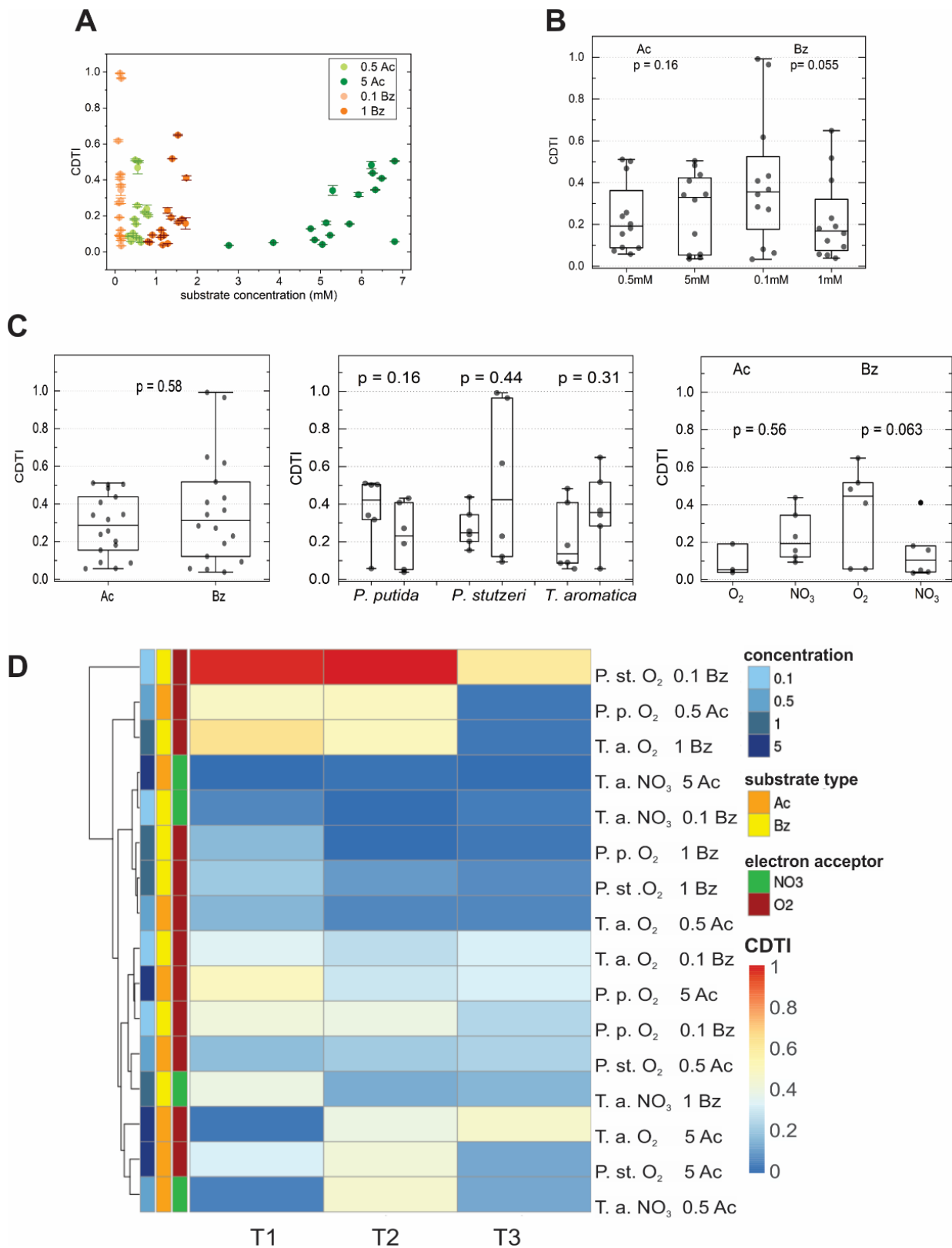
Figure 35. Factors influencing **anabolic heterogeneity. A)** Scatter plot of CDTI vs. substrate concentration. **B)** and **C)** show the results of Mann-Whitney-U paired test comparing **B)** substrate concentration **C)** substrate type, species and electron acceptor. Box plots of CDTI from all treatments grouped by the tested variables; lines in the box represent median values. **D.** CDTI represented as a heatmap with the different conditions ordered by hierarchical clustering as shown by the dendrogram. Clustering was computed with the CDTI values from all treatments to reveal patterns of heterogeneity over time. Color gradient represents a scale from 0 to 1, with the highest values in red (high CDTI) and the lowest in blue (low CDTI).

The transport and metabolic pathways of C-sources into the cells are key regulation points [213] and can be also subjected to noise, since in turn, they depend on promoter activity, ribosomal RNA and cytoplasmic content of proteins and enzymes involved in that pathway [214]. For instance, benzoate degradation pathway is either encoded by chromosomal or plasmid-borne operons [215] and their induction is often subjected to phenotypic **Bistability** [6,7,30,91]. Last but not least, **phenotypic memory** can also be responsible for **cell-to-cell differences** caused by inherited concentration of inducers, mRNA transcripts or proteins from mother to daughter cells [50].

Using SIP-nanoSIMS approach, we could demonstrate how the stochasticity can be reflected quantitatively in the cellular anabolic activity, and additionally we could follow the dynamic over time. The nanoSIMS analysis offers a snapshot of a microbial population, allowing for quantification and visualization of the labels' incorporation into the single cells in that specific time [216]. In previous experiments using SIP-nanoSIMS approach, the dynamics component, i.e. trend over time was missing, because the focus was the study of heterogeneity under limitation of C- or N-sources [69,70,119] or electron donors [70,71]. Instead, we could also provide qualitative and quantitative information on anabolic activity in a temporal dimension over the span of their mid-exponential growth. After each passage, the cultures would bear a certain "*memory*" of the past conditions. Such memories are coming both from the environmental conditions and biochemical, structural and genetic information; phenomenon also known as **phenotypic memory** [48]. Assuming that at the beginning of each "new" growth phase bacteria carry already this heterogeneity, after the addition of isotope-labelled compounds, the initial heterogeneity can be "magnified", via tracking the ^{13}C-incorporation and thus single-cell anabolic activity. This means that if a cell at the T1 is enriched in ^{13}C, that same cell can never go back to ^{13}C-natural abundance: instead, the cell will have two "choices": i) to stop the label uptake (thus remaining with the same ^{13}C-enrichment value overtime), or ii) to increase the uptake, thus resulting in higher ^{13}C-enrichment at T3.

Consequently, the cells with very low K_A values, i.e. very low C-assimilation, found at T3, would be the very same cells that since the beginning "decided" not to engage in substrate uptake probably as a result of a **bet-hedging** strategy.

Ecological significance

In this perspective, our findings have a potential importance in environmental microbiology and biogeochemistry studies focused on *in situ* metabolic activity of natural populations with the use of SIP-nanoSIMS approach. While very useful to study the impact of uncultured microbial populations, or the mechanisms of trophic interactions in natural or synthetic systems [217-220] and [129](see appendix), such studies often revealed heterogeneous populations with respect to isotopic enrichment or substrate assimilation. So far, heterogeneity has been interpreted as resources limitations [69-71], reduced substrates availability [221] or potential differences in metabolic pathways [120]. According to our results, we suggested that the low-enriched cells should not be interpreted as dormant or poorly active per se, but rather as the results of **cell-to-cell metabolic diversification** in response to environmental conditions, or as a '*memory effect*' of their

past conditions [48,50]. *T. aromatica* growing with 0.5 mM Ac (aerobic) and with 0.1 mM Bz (anaerobic) showed high C-assimilation while having and keeping a very low **AH** over time. Likewise, one would expect that environmental limitations, such as low nutrients or growth-substrates concentrations, should not necessarily bring to an increase of **cell-to-cell heterogeneity**.

Future studies will be necessary to investigate if the display of low or high **AH** over time ensures the survival and the success of microbial populations in their natural environments.

Understanding the mechanisms taking place under physiological conditions will also help to understand the role and the evolution of **MH** between cells belonging to the same population. In turn, this can help to exploit the heterogeneity in a positive way if the factors that are boosting or reducing its occurrence are known. These insights can be especially important for biotechnological applications as well as bioprocesses, where bacteria have to perform a constant activity to achieve the highest possible yield starting with high concentration of substrates. Moreover, microbial populations could face abundance of nutrients even under environmental conditions, e.g. during biodegradation processes, in the vicinity of eutrophic areas or heavily contaminated environments.

3.4 *Influence of biotic factors in shaping heterogeneity*

Several evidences proved **cell-to-cell heterogeneity** in microbial populations both in model strains and in isolates from natural environments. Very little however is known about this phenomenon upon interactions of more than one species. Especially in soil, fungi and bacteria are important functional groups, where they shape new ecological niches. Bacteria-Fungal-Interactions (BFI) play an important role in element cycling and compounds turnover [222-225]. Fungal hyphae can act as a dispersal networks for bacteria, allowing for important ecological processes such as biodegradation, that otherwise would be limited or hindered because of physically distant substrates [179,226-228]. The hyphosphere is the spatially and physiologically defined habitat formed and affected by hyphae [229]. Such habitat has been described as a location of increased Horizontal Gene Transfer (HGT) [230] between bacterial strains. However, how this directly influences the **MH** of the bacteria is still an open question. HGT may depend on physiological status of the bacteria and may not take place if bacteria are under nutrients limitations. In turn, the physiology of bacteria can be influenced by the physical and metabolic interactions with hyphae. The latter may influence metabolic activity, e.g. by promoting HGT between bacteria or the exchange of nutrients, and thus be a driver of bacterial **MH.**

Optimization of the experimental set-up

In order to study the BFI, I created a laboratory controlled ecosystem, using a bacterial reporter system consisting of two strains: *Pseudomonas putida* KT2442::*dsRed-lacI^q(pWW0::P$_{lac}$-gfp)* as plasmid donor, (by the simultaneous expression of *LacI^q*, this bacteria express *DsRed* while repressing the plasmid-encoded GFP), and *Pseudomonas putida* KT2440 wild type (Sketch 4).

When the transconjugation takes place, i.e. the plasmid uptake, the recipient will be able to express GFP, thus fluorescing in green and making possible to track it with fluorescence microscope (Sketch 4). The species of oomycete *Pythium ultimum,* a pseudo-fungus, was used as model of hyphae-forming organism as described earlier [230]. The rationale was to study and visualize HGT between bacteria and to correlate later on with their metabolic activity (i.e. uptake of isotope-labeled substrates) with SIP-nanoSIMS approach. To do so, it was first necessary to validate a suitable set-up able to preserve the spatial distribution between hyphae and bacteria but also suitable for high-vacuum-compatible sample preparation. In a previous paper [117], a set-up was built, consisting of two plugs of agar and a Si-wafer in between (Fig. 36-A): the pseudo-fungus was inoculated on one side and allowed to grow over the Si-wafer before reaching the second agar plug (Fig. 36-B). However, in [117] hyphae grew over a bare Si-wafer mainly in dry conditions (to test the resuscitation of bacterial spores).

On the contrary, for my experiments, a humid environment was required because both organisms needed to be alive and the water film around the hyphae was necessary for the movement of the bacteria alongside [179, 230]. Exploiting the same principle, a slightly different set-up was used (Fig. 36-C), simply substituting the Si-wafer with a third agar plug in the middle, inside a 3-well chamber glass slide (ibidi®, Germany).
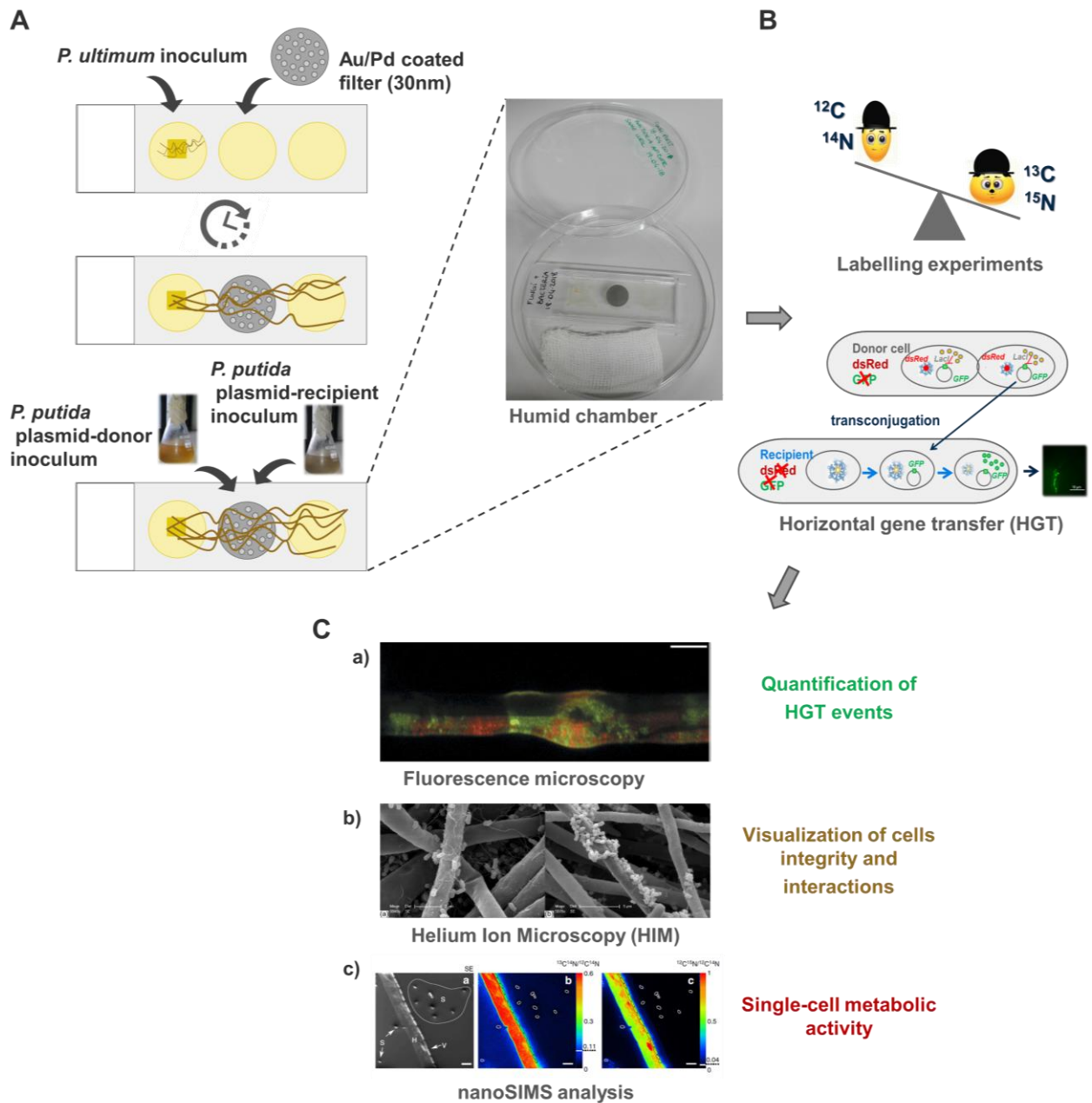
Sketch 4. Workflow to study **biotic factors** influencing **MH**. **A)** Optimization of the experimental set-up. **B** Performing in parallel labelling experiments and letting bacteria to engage in Horizontal Gene transfer (HGT). After incubation the bacteria-pseudo-fungi interactions are observed with a) fluorescence microscope to quantify the trans-conjugants; b) HIM microscopy to verify the cells structures preservation and the physical interactions; c) nanoSIMS to quantify the metabolic activity at single-cell level. **C)** Pictures taken from **a)** [230]; **b)** [231]; **c)** [117].

Classical chemical fixation and dehydration, that are usually performed under soaking conditions (Sketch 1), applied to the agar resulted in the formation of clumps that disturb the topography and in turn the subsequent observations (Fig. 37-A). High Pressure Freezing (HPF) coupled with Freeze-Substitution [232] could be a good alternative to visualize co-cultures and study the BFI. Samples are usually prepared in special support with a height of 200 µm. So, a very thin agar layer was placed in the middle of the set-up, to verify the growth of the hyphae. However, *P. ultimum* did not grow well over the agar when

the thickness was below 1 mm (Fig. 38-C) and the agar tended to dehydrate very soon even at room temperature. Double pseudo-fungi inoculum in either the opposite agar wells (Fig. 38-A) or the same well (Fig. 38-B) did not show hyphal growth after 72 hours (h) as well (Fig. 38).
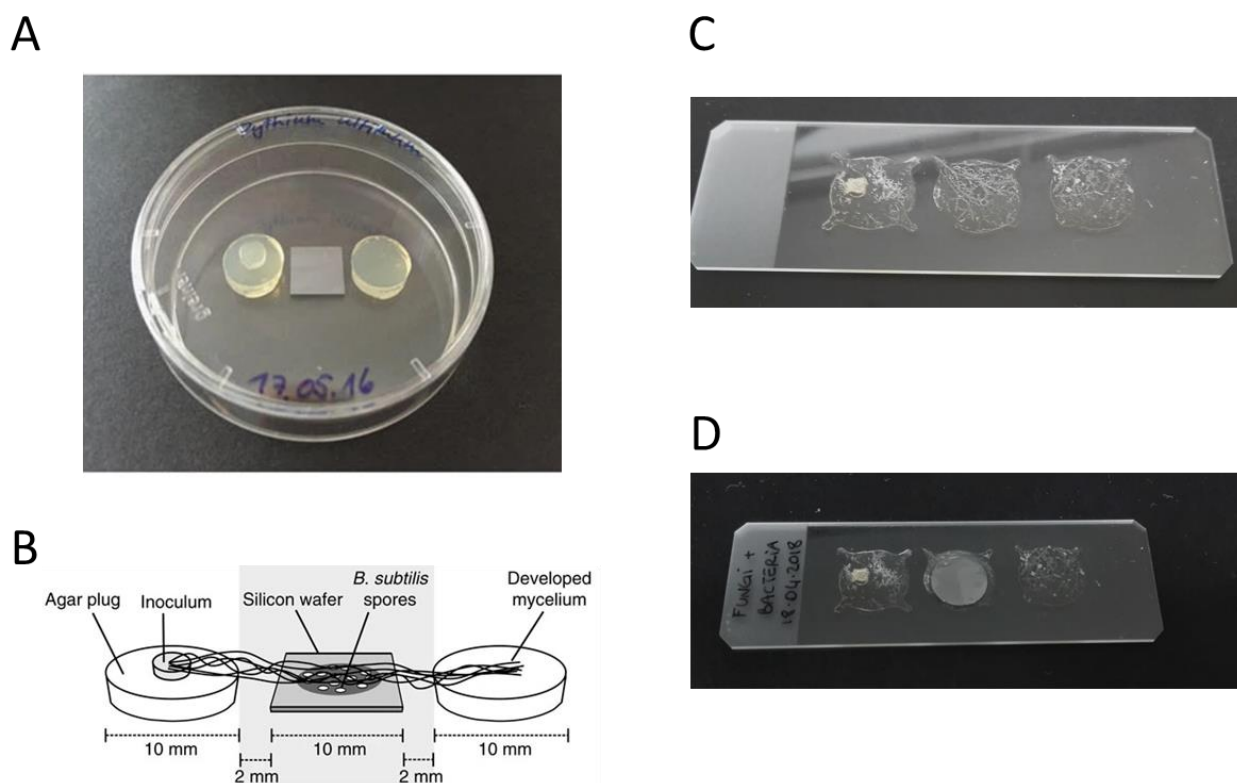
Figure 36. First try of the set-up based on the approach used by [117]. **A)** Set-up with two agar plugs and a Si-wafer in the middle and **B)** schematic illustration of hyphal growth on top of the Si-wafer in the middle used by [117]. **C)** Approach used in my project with thin layers of agar, using the same principle as **B)** but replacing the Si-wafer with a third agar well. **D)** Addition of a piece of Au/Pd-coated filter on top of the middle agar well for growing hyphae-bacteria co-cultures on a conductive support.

Agar could not be avoided due to the fact that bacteria needed a thin liquid film to disperse along hyphae and make HGT [230]. When using 1.8% agar (Bacto-Agar, Difco™, BD) in water w/v (hard agar), hyphae preferably grow above the agar surface; in turn bacteria cannot go through the thickness of the agar and will be "obliged" to run on top of the hyphae [230].

The Au/Pd coated filters (0.2 µm pores) are usually the preferred support for nanoSIMS analysis. We assumed that, if a piece of coated filter is placed on top of the middle agar well (Fig. 36-D), this should preserve the passage of nutrients and water through the pores while allowing the hyphae to grow undisturbed on top of it.
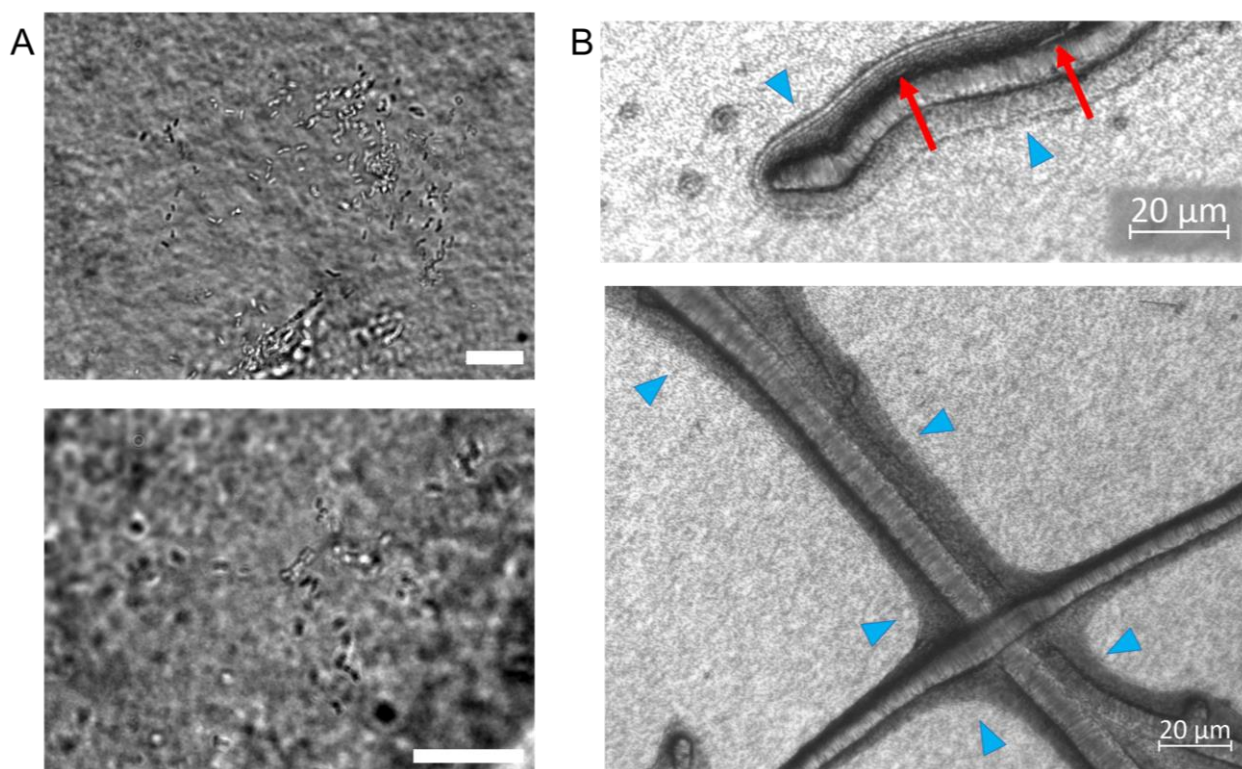
Figure 37. Microscopy observation with black field of the middle agar well. **A)** Agar well after fixation and air-drying; **B)** Pseudo-fungi and bacteria on the Au/Pd filter on top of the agar well. Red arrows indicate single bacterial cell migrating on the hyphae; light-blue arrow-heads indicate the water film around hyphae. Scale bar correspond 20 µm.
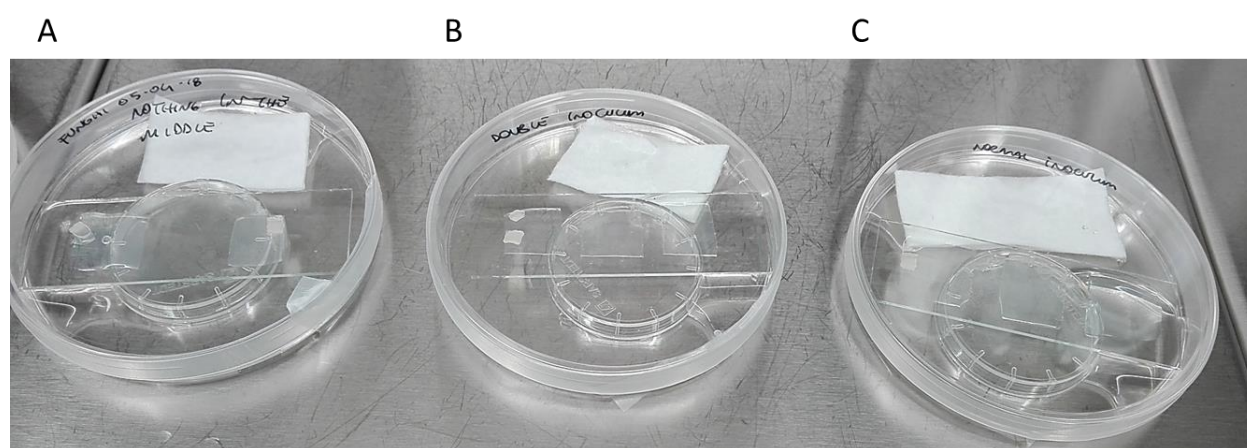
Figure 38. Growth of fungal hyphae on very thin agar plugs. **A)** Inoculum on both external agar plugs; **B)** double inoculum on the same plug; **C)** single inoculum on the first agar plug.

To be sure that the filter was hydrophilic, adhering to the agar and guarantying the formation of a thin layer of water, the UV cleaning system was used, developed for the removal of organic contaminants on top of the carriers used for microscopy and chemical imaging [181](see appendix). After treating with UV for

2 minutes, pieces of filters were placed directly on top of the middle agar well. Then, *P. ultimum* was inoculated in the first agar well and let to overgrow in a humid chamber (Sketch 4-A). Hyphae were not only able to grow on top of the Au/Pd filter but, most importantly, they could keep their surface properties and the water film which could allow bacteria to migrate and "take the highway" [179,230] (Fig. 37-B).

Study of the HGT

Under environmental conditions, bacteria are spread around the hyphae and they are not concentrated in few spots [231]. To simulate realistic conditions and understand the dynamics and the timing of the HGT events, the inoculum of the bacteria on top of the hyphae had to be considered. Three main factors were studied: i) the time, ii) the position and iii) the quantity of inoculum, i.e. amount of bacteria (optical density (OD)). First, I used the set-up as in Fig. 36-C.

If bacteria were inoculated at the same time as *P. ultimum*, yet not at the same location, after 24 h they formed a colony (Fig. 39-A) and when hyphae reached that area, they were physically hindered and instead they grew below the colony; thus bacteria did not migrate (Fig. 39-B). When fungal hyphae were allowed to overgrow first and then bacteria were inoculated, bacteria were able to migrate on top of them immediately after the inoculum (Fig. 40). For such reason, all the following experiments were performed in this way, letting hyphae growing on top of the filter for about 50-62 h and then inoculate bacteria.
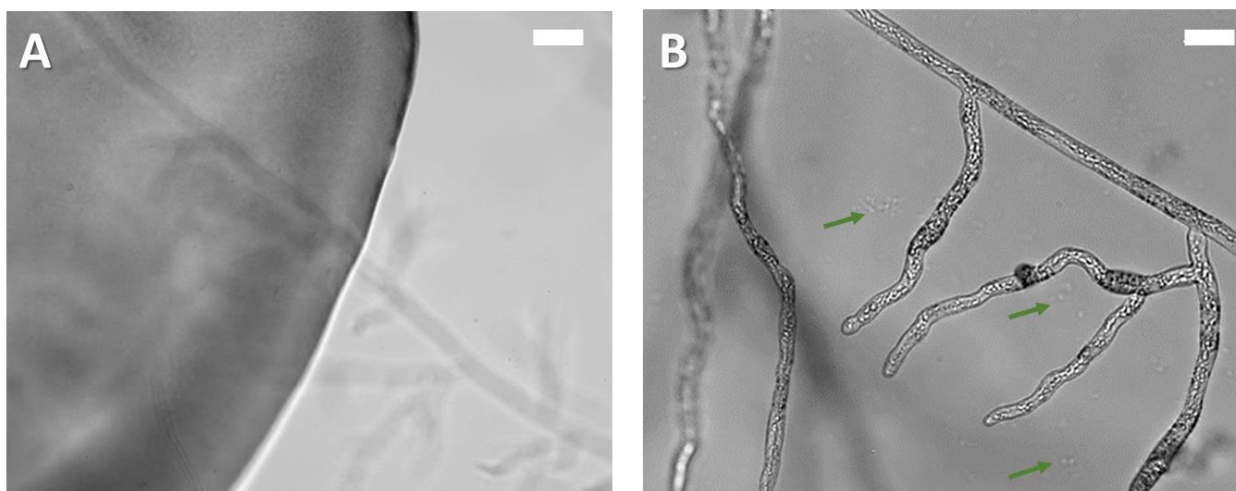
Figure 39. Inoculum of bacteria and pseudo-fungi at the same time on the same agar well. **A)** Bacteria after 24 h formed a colony. **B)** No bacteria migrated on top of the hyphae as a result, because of the slower growth of hyphae. Some bacteria remained stuck on the agar (green arrows). Scale bars correspond to 1mm.

In [230], HGT was studied inoculating separately the plasmid-donors and -recipients on the opposite sides of the agar plug. Using the same configuration with my set-up (Fig. 41-A), transconjugation events were monitored for 24, 36 and 48 h after co-incubation by fluorescence microscopy. Even after 48 h, no transconsjugants were visible, probably because it was difficult for bacteria to get in contact to each other with this set-up (Fig. 41-A). As alternative, the two bacterial types were inoculated together (Fig. 41-B),

with the assumption that they were "forced" to be closer and thus easily meet and transfer the plasmid upon migration. Plasmid-donor and -recipients were grown separately, mixed in a 1:1 v/v co-culture just before the inoculation, and immediately transferred on top of the middle agar well. After 72 h of incubation, many tranconjugation events took place as observed by fluorescence microscopy (Fig. 41-B).
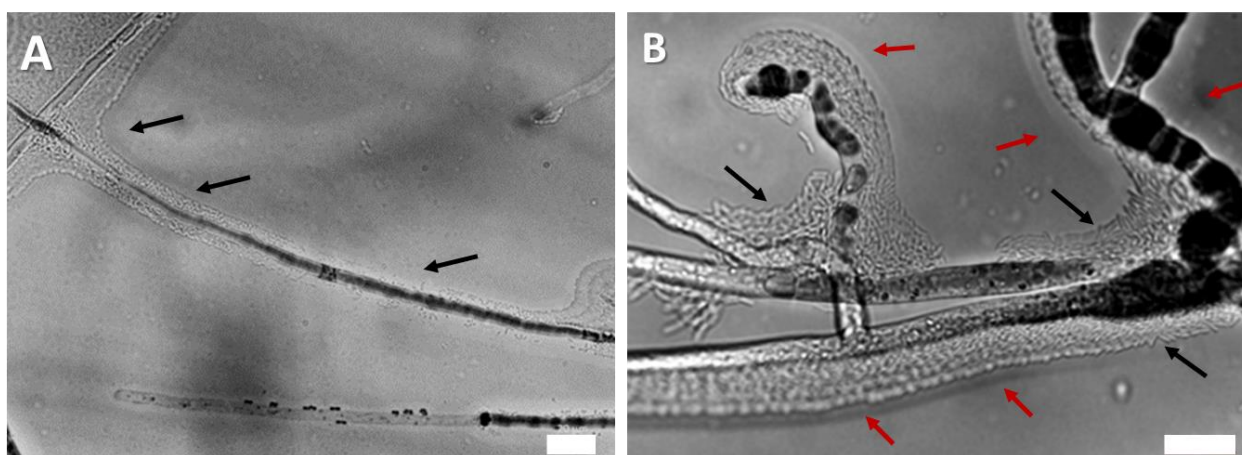
Figure 40. Inoculum bacteria after overgrowth of hyphae on the same agar well. **A)** Bacteria migrating along the hyphae after 12 h of co-incubation (black arrows). **B)** Many bacteria located in the intertwining points of hyphae. The water film responsible for the migration of bacteria (red arrows) is also visible. Scale bars correspond to 20 µm.

As bacterial concentration in the inoculum, I used the same procedure as in[230], i.e. an overnight bacterial culture with $OD_{600} = 3.8$, inoculating 1 µl of each suspension (plasmid- donors and recipients bacteria). However, the number of bacteria that migrated around the hyphae was high (Fig. 42-B) and bacterial concentration needed to be optimized for my set-up. Different dilutions of the abovementioned bacterial culture were tested.

The rationale was that I had to find a compromise in the cell number: too many bacteria tended to stack and eventually to form small colonies on the agar after 72 h (thus not migrating to perform HGT) but too few bacteria resulted in weak or no fluorescent signal (thus it would not be possible to observe and quantify the transconjugation events). Moreover, HGT events take about 4-5 min to occur [230], and a too long incubation would bring to an oversaturation of the fluorescence signal (as in Fig. 41-B). Dilutions of 1:10, 1:50 and 1:100 from the OD_{600} 3.8 cultures, still showed high bacterial numbers (Fig. 42), therefore a further dilution of 1:500 was tested (Fig. 43).
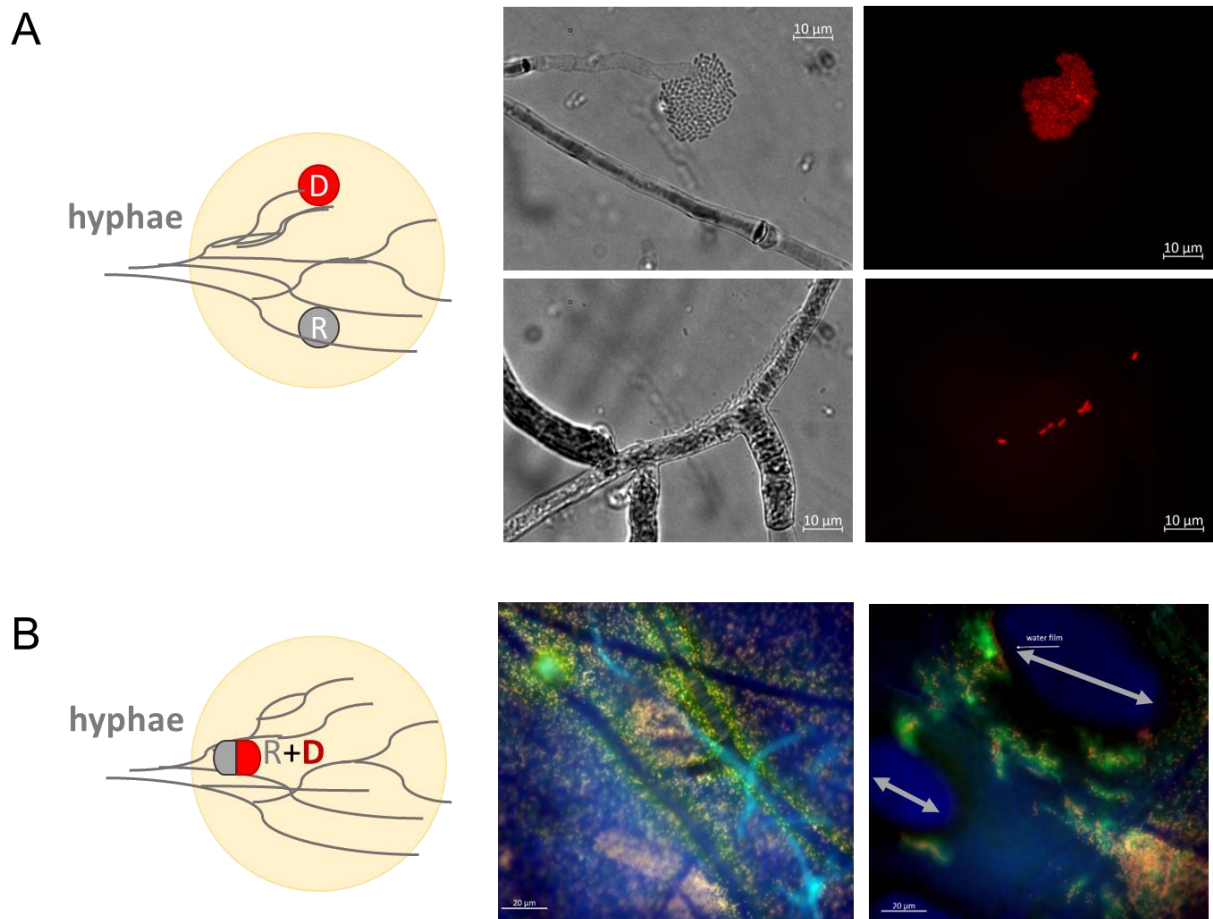
Figure 41. Position of the bacteria inoculum within the agar well. **A)** Plasmid-donor (D) and -recipients (R) are inoculated on the opposite sides resulting in no transconjugation event as shown by black field images with the corresponding areas observed with fluorescence microscopy; just red cells (plasmid-donor bacteria) are observed under this condition. **B)** Inoculation of (D) and (R) together, resulting in transconjugation events. Fluorescence pictures show bacteria migrating on the hyphae. Green color represents the tranconjugants bacteria, red color the plasmid-donor bacteria while hyphae either appear in dark color or emit auto-fluorescence (light blue color).Grey). Grey arrows indicate empty space in the agar-well where it is still possible to see the water film (grey double-headed arrows). Pictures were acquired after 72 h of co-incubation.
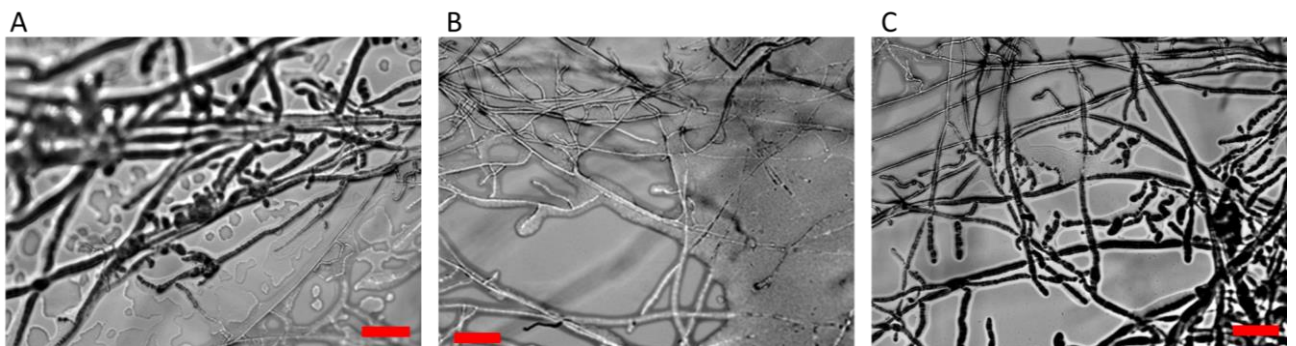
Figure 42. Trials with different concentrations of the bacterial inoculum. **A)** 1:10, **B)** 1:50, **C)** 1:100 dilution from OD_{600} 3.8 overnight culture (used in [230]). Bacteria formed ´carpets´ of cells on top and around hyphae. Scale bars correspond to 100 µm.

Both black field and fluorescence microscopy observations confirmed that after 8 h and 12 h of co-incubation bacteria were migrating without being stuck in the hyphal branches' nodes (Fig. 43-A, B); after 12 h the occurrence of the first transconjugation events were observed (Fig. 43-C). Thus, this incubation time, 8 to 12 h, seemed to be a good compromise for both fluorescence microscopy and nanoSIMS analysis.

Figure 43. Pseudo-fungi and bacteria co-cultures. Bacteria were diluted 1:500 (from OD_{600} 3.8 cultures[230]) and observed after **A)** 8 h, **B)** 12 h in black field and **C)** fluorescence microscopy. Green color represents the tranconjugants bacteria, red color the plasmid-donor bacteria.

Functional heterogeneity

One of the hypotheses to test was that bacteria would use nutrients, i.e. C and N, from fungi, especially under scarcity conditions and consequently the difference in HGT rates could depend on the different metabolic activity between the hyphosphere regions and the farther ones. Bacterial intra-population **MH** would be then different between bacteria close and far away from hyphae.

Transconjugations events took place mainly in the vicinity of the hyphae but not far away from them (Fig. 44) as observed with fluorescence microscope; instead without hyphae no transconjugation took place, although bacteria were motile by their own. This finding clearly revealed a **functional heterogeneity** occurring in this synthetic system; bacteria close to hyphae were possibly provided with a new function (TOL plasmid metabolic capability) while bacteria far from them did not benefit from it.

Transmissions of metabolic or functional information (HGT) such as new virulence or resistance genes, take place frequently in the hyphosphere [230,233,234]; plasmid transfers can occur in the presence of special spatial structures and nutrients conditions [235], or can require selection pressure [236]. However, there are not yet evidences on how HGT between bacteria is dependent on the metabolic and physiological status of the cells.

A previous study investigated the interactions between *Pseudomonas putida* and *Saccharomyces cerevisiae* to study the influence of fungal metabolism on the bacterial physiology [237]. It was shown that based on the available C-sources fungi can shape the pH of the environment allowing for the survival of bacteria, that otherwise would be killed by the high acidity in the medium [237]. However, studying the BFI

in liquid and solid medium, the spatial distribution and the correlation between physical and metabolic interactions were missing in this study. Fungal hyphae can act as dispersal networks for bacteria, facilitating biodegradation processes and the access to physically distant nutrients [179,226-228,231]. Using SIP-nanoSIMS approach, it was shown that spore-forming bacteria were able to resuscitate if they were in the vicinity of hyphae, due to the active transfer of water and nutrients; the germination of the spores did not happen if bacteria were not close to hyphae [117].
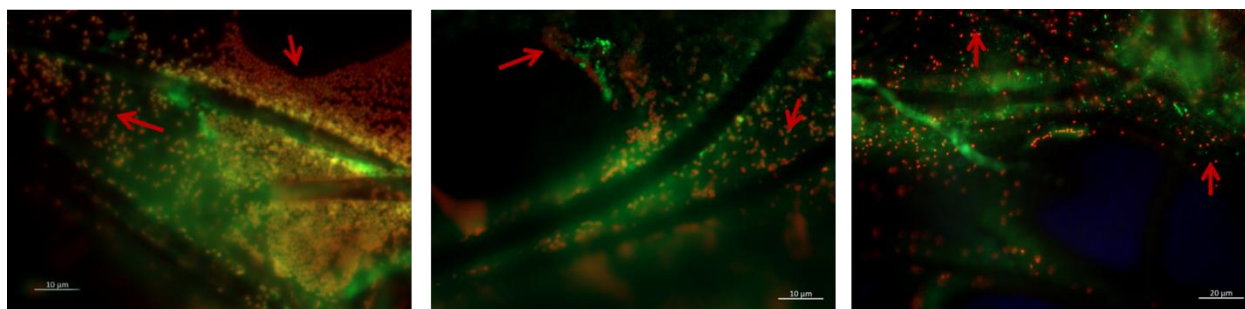
Figure 44. Transconjugation events taking place alongside hyphae after 24h of incubation. Transconjugants (green colored cells) were mainly distributed alongside the hyphae but not in the distant regions from hyphosphere. Red arrows indicate plasmid donors (red color) that stayed far from hyphae and were thus not able to transfer the plasmid anymore.

To correlate our findings on functional heterogeneity (HGT) with metabolic activities and consequently with **MH** at high lateral resolution, nanoSIMS experiments will be necessary. This will be the next and future step to perform, allowing to gain important insights on the BFI and how they shape and tune the functional (HGT) and in turn **MH** (C- and N-uptake). In the chapter 3.3, it was shown how **MH** was displayed by monoculture of *P. putida* (used as wild type strain in this set-up) under **non-limiting conditions**. It remains to investigate how and if bacterial **MH** will be different in co-cultures, due to the influence of the hyphosphere and the physiological status of the two species. These insights will shed more light on bacterial **MH** and its ecological consequences with a further level of interactions complexity.

3.5 *Metabolic heterogeneity and ecophysiology of natural microbial populations impacted by emerging contaminants*

Microorganisms play important ecological roles in their natural environments, being involved in biogeochemical cycles. For instance, inland water ecosystems, i.e. reservoirs, lakes and rivers, are active "hotspots" for the transformation of terrestrial Carbon (C), which is further remineralized by heterotrophic bacteria [238]. However, emerging water contaminants, including antibiotics, may affect microbial physiology and thus C-balance in the biosphere, due to their presence and persistence into the environment [239-241] [242].

Antibiotics are discharged in surface waters directly as aquacultures, surface runoffs, including those from livestock and agriculture, or indirectly as effluents from sewage treatment plants, receiving human, veterinary and drug manufacturers' wastes [243,244]. Wastewater treatment plants (WWTPs) are the main entry points of pharmaceuticals into the surface waters, because they are not built to retain and deactivate antibiotics [245-248]. Ciprofloxacin is the most frequently detected antibiotic in the rivers worldwide [249,250] while amoxicillin is the most frequently consumed antibiotic [251], however quite prone to hydrolysis and photo-degradation [252-254].

Antibiotics can undermine the equilibrium of natural ecosystems [255], impacting crucial functional features, such as community composition, species richness and metabolic capacity [256]. So far, studies assessing the impact of antibiotics on the aquatic microbial communities offered an overview by the use of either bulk tests [257-259] or model species [260,261], missing details on the impact on single cells or single phylotypes within natural communities. Bacterial model organisms exposed to antibiotics showed **phenotypic heterogeneity** [132,262].

Within isogenic bacterial populations, antibiotics exposure highlights preexisting **cell-to-cell differences** in growth rate. For instance, after ampicillin treatment *E. coli* population consisted of one normally growing subpopulation and two non-growing ones that become persisters; the latter were either dormant having a very long stationary phase (type I persisters) or continuously generated due to the slowing down of the growth (type II persisters) [132]. The nutrients gradient on a micrometer scale generated from growth on microfluidic chambers resulted in metabolic cross-feeding between *E. coli* subpopulations, one (glucose fermenting) at the opening of the channel and the other (acetate respiring) at the back of it. This metabolic specialization corresponded to different growth rates of the two subpopulations and in turn caused different response upon antibiotic exposure. The slow or non-growing subpopulations were indeed resistant to streptomycin exposure[74]. *Salmonella typhimurium* subpopulations, expressing the type three secretion system 1 (ttss-1) divided at very slow rate and increased the expression of virulence genes at the same time; such *phenotype* was able to survive ciprofloxacin and kanamycin exposure in contrast with fast-growing and avirulent *phenotype* that instead succumbed [95]. In all the above-mentioned studies, persistence to antibiotics was reversible after antibiotic removal and restoration of optimal growth conditions [74,95,132]. **Phenotypic heterogeneity** thus provided a chance for surviving in fluctuating and hostile environments. However, using microfluidic devices coupled with fluorescence time-lapse microscopy, these studies could

not provide quantitative information on the metabolic activity of the bacteria. SIP-nanoSIMS approach, instead, is the only tool that can provide quantitative information on the single-cell metabolic activity (measured as heavy-isotope uptake) and therefore can account for the contribution of microbial populations to specific biochemical processes [104]. Combining isotope labelling with the administration of ciprofloxacin and amoxicillin, I aimed to investigate i) the effect of these **emerging contaminants** on the metabolic activity of single cells, i.e. uptake of ^{13}C- and ^{15}N-labelled substrates, and on the ecophysiology of microorganisms inhabiting river waters and ii) the antibiotics influence on the **MH** of the most abundant microbial groups.

Sampling campaign and labelling experiments

The river Holtemme is located in the Hartz Mountain in Germany, where we carried our sampling campaign on the 8th of November 2018. Samples were collected at site 1, characterized by pristine (**Pr**) waters surrounded by forest and site 17, downstream water, close to a waste water treatment (**WWT**) plant in Halberstadt, Sachsen-Anhalt [263] (Sketch 5). Samples were collected *in situ* into 2 L pre-sterilized bottles and were immediately stored in the dark inside a thermic box, remaining in these conditions for approximately 5 h during transport in the laboratory. Immediately after arrival in the laboratory, the collected waters were further aliquoted in 1 L bottles, and samples were injected with 0.5 mM acetate, from which 25 – 38 at% of initial concentration was ^{13}C-labelled (Table 2, Sketch 5). For **Pr** samples, 1.7 mM ^{14}NH$_4$ from which 20 at% of ^{15}NH$_4$ was added as nitrogen source; for **WWT** samples just 0.425 mM ^{15}NH$_4$ (thus 99.9 at%) was added, since the natural ammonium concentration in this site was ca. 30 mg/L, that is ca. 1.7 mM (Table 2, Sketch 5). Together with isotope–labelled compounds, unlabeled Ciprofloxacin (**CIP**) and Amoxicillin (**AMO**) antibiotics were injected at two different concentrations: 1 µg/L and 1 mg/L (Table 2, Sketch 5). Samples were incubated for 24 h with a controlled temperature of 15 °C, in the dark to avoid photo-inactivation/photolysis of antibiotics. After this time, from each sample, three different aliquots were withdrawn for: community sequencing, fluorescence in situ hybridization (FISH and CARD-FISH) and cell counting, and single-cell nanoSIMS analysis (Sketch 5).

Community analysis

We investigated the diversity of both **Pr** and **WWT** communities before and after addition of antibiotics in order to identify changes in the community composition as well as in the abundance of bacterial phylotypes under each condition for further FISH-probe selection. An aliquot of 20 ml from each water sample was concentrated onto a polycarbonate filter and stored at -20°C. DNA extraction was performed with Macherey-Nagel Nucleospin® kit according to the manufacturer's instructions, using a beads-beater device (Power Lyzer TM, 24MoBIO). The DNA was concentrated in a final volume of 100 µl. The 16S rRNA gene in the DNA extracts was PCR-amplified using universal primers for Bacteria domain, GM3 forward (8-24; 5'-AGAGTTTGATCMTGGC-3') and GM4 reverse (1492–1507; 5'-TACCTTGTTACGACTT-3') [264] to verify quality and quantity of the extraction. Samples were sent to a genomic facility (LGC Genomics GmbH, Berlin) for sequencing with a MiSeq Illumina system (2 × 250

paired). Sequences were analyzed with the QIIME pipeline [265] for Operational Taxonomic Units (OTUs) clustering and taxonomic assignment. The OTUs accounting for more than 1% of total sequences were further selected for identification of the most abundant taxa in the communities under each of the studied conditions.

Diversity indices

To evaluate the impact of antibiotics on the species diversity in comparison with antibiotics-free samples (Ab−), we calculated alpha and beta diversity indices. Alpha index considers the quantitative diversity within each sample/condition and it was calculated as Chao1 index. The samples from **WWT** resulted much more diverse on average than **Pr** ones. The antibiotics treatments did not change the number of different taxa between the conditions in **WWT** samples, while in **Pr** the difference between Ab− and antibiotics-treated samples was more marked especially for **CIP** (Fig. 45-E). To assess how the communities changed after each treatment, we calculated Beta diversity index as 'weighted variant of UniFrac'. The Principal Coordinate Analysis Plot (PCoA) showed how far **Pr** resulted from **WWT** samples, highlighting a high dissimilarity between the two waters. Within each group (black ellipses, Fig. 45-E), further dissimilarities among the conditions were observed, suggesting a variation in the composition of the bacterial communities induced by different antibiotics exposure (Fig. 45-F).

Table2. Treatments applied for all tested conditions on Pr and WWT water samples. Ratio of $^{13}C/^{12}C$ and $^{15}N/^{14}N$ in the growth substrates (D_{gs}) are shown as well as the probes used for FISH and CARD-FISH protocols.

Conditions	Addition of ^{13}C-acetate at% in D_{gs}	Addition of ^{15}N-ammonium at% in D_{gs}	FISH probe	CARD-FISH probes
WTT (Ab−, Lab+)	0.369 ± 0.004	99.997 ± 0.001	ACA-652[266]	CTE-659[267], Eub338_I[268]–III[269]
WWT_AMO1 µg/L	0.367 ± 0.003	99.997 ± 0.001	ACA-652	CTE-659, Eub338_I -III
WWT_AMO 1 mg/L	0.373 ± 0.004	99.997 ± 0.001	ACA-652	CTE-659, Eub338_I -III
WWT_CIP1 µg/L	0.379 ± 0.004	99.997 ± 0.001	ACA-652	CTE-659, Eub338_I -III
WWT_CIP 1 mg/L	0.365 ± 0.003	99.997 ± 0.001	ACA-652	CTE-659, Eub338_I -III
Pr (Ab−, Lab+)	0.273 ± 0.006	0.211 ± 0.06		CTE-659, Eub338_I -III
Pr_AMO 1 µg/L	0.278 ± 0.005	0.211 ± 0.06		CTE-659, Eub338_I -III
Pr_AMO 1 mg/L	0.270 ± 0.003	0.211 ± 0.06		CTE-659, Eub338_I -III
Pr_CIP 1 µg/L	0.261 ± 0.013	0.211 ± 0.06		CTE-659, Eub338_I -III
Pr_CIP 1 mg/L	0.269 ± 0.006	0.211 ± 0.06		CTE-659, Eub338_I -III
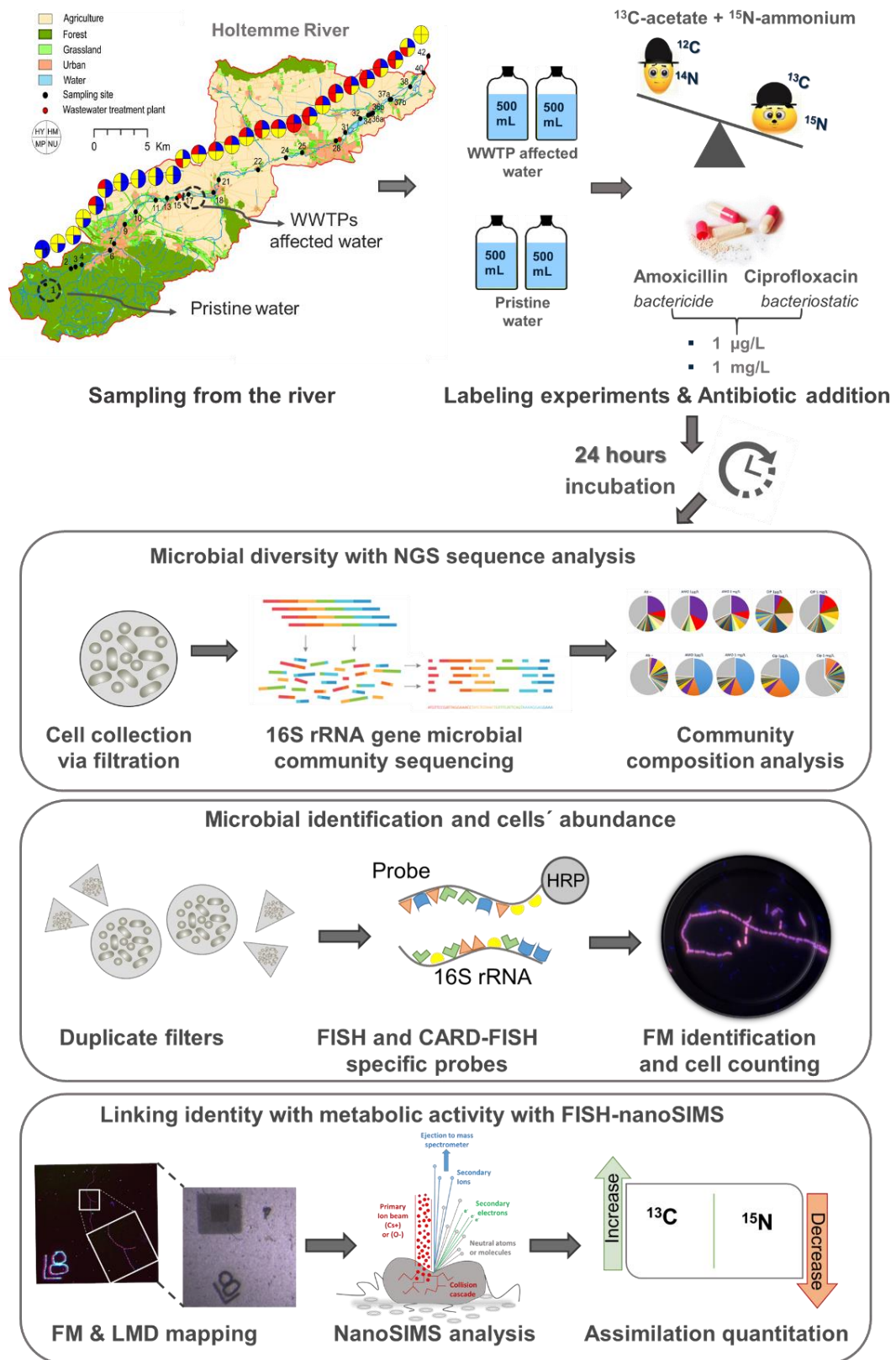
Sketch 5. Sampling and experimental set-up of river-water samples. Samples were collected from the Holtemme River and brought to the laboratory to start labelling experiments. ^{13}C-labelled acetate and ^{15}N-labelled ammonium (as markers of microbial activity) and two antibiotics (amoxicillin and Ciprofloxacin) at two different concentrations were injected. After 24h of incubation, samples underwent: 16S rRNA gene sequencing, FISH or CARD-FISH and nanoSIMS analysis. Prior to the nanoSIMS, specific areas (where FISH-probe-targeted cells were abundant) were visualized with fluorescence microscopy (FM) and mapped with Laser Microdissection (LMD) to be easily identified during nanoSIMS analysis.

Total cellular abundance

Total cell counts were performed to determine the natural microbial abundance and thus decide the amount of water volume to be withdrawn, from each site, for labelling and successive experiments.
The average cell counts at T0 (prior incubation) as quantified by DAPI staining was 5.0×10^5 cells·ml^{-1} for **Pr** and 1.5×10^6 cells·ml^{-1} for **WWT** sites, respectively. Thus, to achieve a sufficient number of cells for good cell abundance statistics during counting, a 5-times higher volume was filtered for **Pr** (10 ml) in comparison with **WWT** (2ml).

The initial total dissolved nitrogen (DNB) and dissolved organic carbon (DOC) were also measured at the two sites of sampling, corresponding to 1.76 mg/L and 3.75 mg/L in **Pr**, and 32.4 and 5.16 mg/L in **WWT** waters, respectively. Water samples were incubated with and without addition of labels and antibiotics for 24 h (Fig. 45-B, D). Ten to fifteen different FoVs were acquired under a fluorescent microscope for each condition and then averaged and converted in cell·ml^{-1}; standard deviations were also calculated from the counted FoVs for each condition. Total DAPI-cell counts increased under all conditions in comparison with T0, with the only exception of **CIP** 1 mg/L in **Pr** waters. The antibiotic-free samples (Ab−) showed an increase in cell numbers which was 1.4 time higher in **Pr** (7.0×10^5 cells·ml^{-1}) and 2.1 times higher (3.1×10^6 cells·ml^{-1}) in **WWT** water, possibly due to the addition of ^{13}C-labelled acetate and ^{15}N-ammonium as well as the available dissolved nitrogen and carbon sources in the two water samples (Fig. 45).

The addition, of the antibiotics induced distinct changes in the community composition also supported by changes in cell numbers. While **AMO** did not strongly changed the total cell numbers in comparison with antibiotic free treatment (Ab−) neither in **Pr** (**AMO** 1 µg/L was 7.7×10^5 cells·ml^{-1} and 1mg/L was 6.2×10^6 cells·ml^{-1}) nor in **WWT** (**AMO** 1 µg/L was 3.0×10^6 cells·ml^{-1} and 1mg/L was 2.9×10^6 cells·ml^{-1}), **CIP** treatment instead showed a clear dependence on the antibiotic concentration in comparison with Ab−. Thus, 1 mg/L brought to lower cell counts in both sites (4.5×10^5 cells·ml^{-1} in **Pr** and 2.3×10^6 cells·ml^{-1} in **WWT** samples) while CIP 1 µg/L caused a much higher cell number in **WWT** (4.0×10^6 cells·ml^{-1}) but a substantially lower number in **Pr** (5.8×10^5 cells·ml^{-1}).

The reason may lie in the different effects induced by the 2 antibiotics. **AMO** is a bactericide from the β-lactam class causing the disruption of the microbial cell walls and thus cell death, while **CIP** is a bacteriostatic from fluoroquinolone class acting on the DNA *gyrase*, inhibiting the DNA replication and hence the growth. Thus, their different spectrum of activity might be responsible for the different outcomes at the two sampling sites, where also the species composition was distinct as revealed by 16S rRNA gene sequencing (Fig. 45-A, C). Being affected from the effluent of a close WWTP, the **WWT** waters are already exposed to pharmaceuticals and other contaminants [270]. This suggested that the natural microbial communities may have developed different strategies for coping with antibiotics depending on the indigenous species and the class of pharmaceuticals.

Among the several detected OTUs, *Comamonadaceae, Oxalobacteriaceae, Lachnospiraceae* and *Ruminococcaceae* were mainly detected in **Pr** waters (Fig. 45-A) while *Acinetobacter, Arcobacter,*

Commamonadaceae and Flavobacter were detected in **WWT** samples (Fig. 45-C) as the most represented phylotypes after the addition of antibiotics. Hence, the strong increase in the total cell number with **CIP** 1 µg/L concentration in **WWT** can be due to the outgrowth of resistant or persistent bacteria, e.g. *Acinetobacter* and *Arcobacter* related species, largely abundant under this condition (Fig. 45-C).
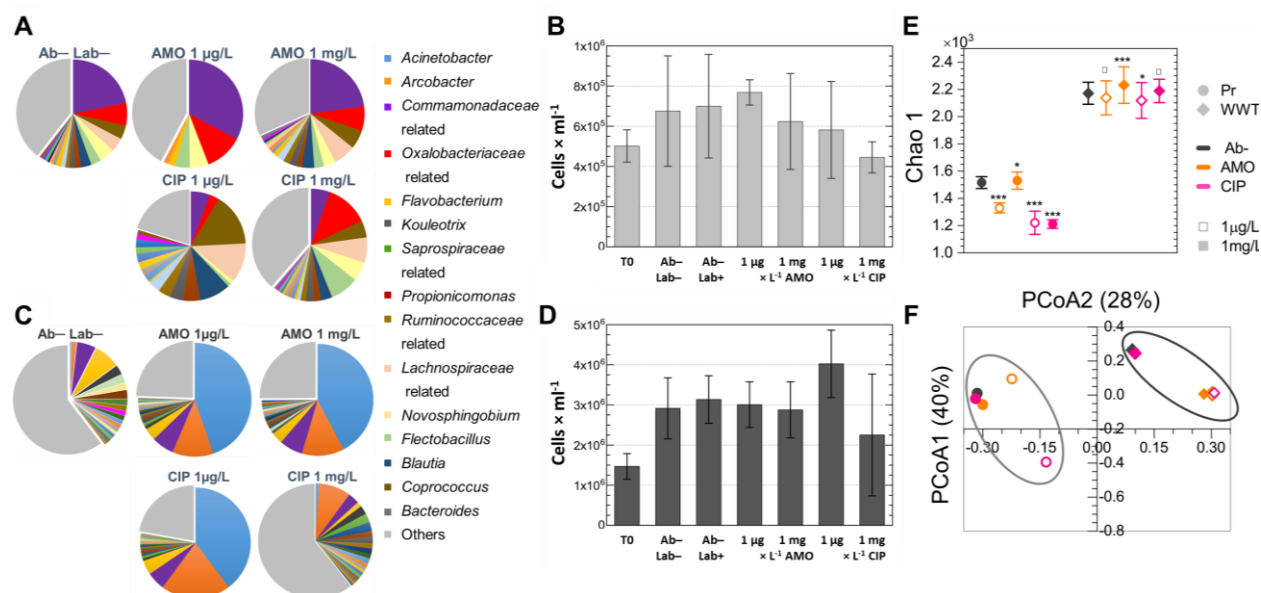
Figure 45. Microbial diversity and cell abundance in **Pr** (A and B) and **WWT** waters (C and D) after 24 h of incubation. Pies represent the community composition under different incubation conditions and colors depict different phylogenetic groups. Ab– indicates no antibiotics addition. **B)** and **D)** represent total cell counts calculated by DAPI staining for **Pr** and **WWT** waters, respectively. Each bar represents average cell abundances in cells·ml^{-1} (calculated from 10-15 different FoVs) and the corresponding standard deviation for each incubation condition. **E)** Alpha diversity measured with Chao1 index. **F)** Beta diversity calculated with UniFrac weighted method. Significance code for p values: □=Not Significant (> 0.05); * ≤0.05; ** ≤0.01; *** ≤0.001; **** ≤0.0001

Selection of Fluorescence In Situ Hybridization (FISH) probes

We aimed to apply FISH/CARD-FISH approaches in order to quantify the relative abundance of the most representative members in **Pr** and **WWT** communities. Thus, it was necessary at first to select suitable probes, which target the V3–V4 region of 16S rRNA genes (corresponding to the sequenced region by Illumina). Among the publicly available FISH probes, we could select 10 different ones. These probes were further aligned against all representative OTU sequences obtained from our water samples. This was to verify if the selected probes were indeed reverse complementary with the amplicons in our sequencing data (indirectly predicting the possibility to identify and target microorganisms present in our original samples). We could confirm just 2 out of 10 selected probes that meet such criteria: ACA-652 [266] specific for *Acinetobacter* genus and CTE-659 [267] for *Comamonadaceae* family.

Group-specific FISH and CARD-FISH analysis

Microbial identification and relative abundance

FISH and CARD-FISH with probes targeting *Acinetobacter* (ACA-652) and *Comamonadaceae* (CTE-659) related species (Table 2) were performed to quantify group-specific abundance in **Pr** and **WWT** samples. After overnight fixation (ca. 16 h) with 1% PFA, samples were filtered onto Au/Pd coated polycarbonate filters using a multi-chamber filtration system (Millipore 1225 Sampling Manifold, Merck). The hybridizations were performed following the standard FISH and CARD-FISH protocols [123,124]. All filters were counterstained with DAPI before fluorescence microscopy to calculate the relative abundance of the probe-targeted species in each sample as percentage of total DAPI-stained cells. For each treatment, ten different pictures (FoVs) were acquired and averaged, and then standard deviations were calculated for these FoVs.

FISH results showed the presence of *Acinetobacter* related species in the **WWT** samples (Fig. 46-E), that were almost absent after 24 h in the sample without labelled substrates and antibiotics (Ab−Lab−) and consisted of an average of 20.3±10.7 % of the total counts in the sample with labels but antibiotics free (Ab−Lab+), as also shown by OTU-based community analysis (Fig.45-A, C). In **WWT** waters, ACA-targeted cells were mostly affected by the **CIP** 1 mg/L concentration, which reduced their relative abundance down to 8.7±5.3%; **AMO** addition, instead, did not affect cell abundances much (**AMO** 1 µg/L was 26.2±10% and 1 mg/L was 21±20%) (Fig. 46-C). In **Pr** samples, this group was absent under all conditions tested (Figs. 45 and 46).

In most experimental conditions, the relative abundance of ACA-targeted-cells quantified with FISH (Fig. 46-C, E) was half than that calculated from 16S rRNA amplicon sequencing (Fig 45-C). While with the latter, all the OTU sequences found to be related to *Acinetobacter* genus were assigned to this group, we cannot rule out the possibility that the ACA-652 probe might not target all the phylotypes belonging to *Acinetobacter* genus present in our samples. Moreover, 16S rRNA sequencing is based on the PCR amplification and the consequent sequencing of specific regions of the 16S rRNA gene, thus being subjected to potential related bias, e.g. variation in copy numbers, chimaera formations and sequencing errors that may overestimate the relative proportion of some bacterial taxa in comparison with the original samples [271,272]. This could explain the differences detected between the OTU- and FISH-based abundance.

Comamonadaceae related species were present at both sampling sites. Using a similar FISH protocol for targeting *Comamonadaceae* related species by CTE-659 probe resulted in low fluorescence intensity or lack of signals in **Pr** samples. To overcome this issue CARD-FISH was performed instead, which resulted in high signal intensity (Fig. 46-B). To compare the relative abundance of this phylotype in **Pr** and **WWT** under the same experimental conditions, CARD-FISH approach was applied for both sampling sites (Fig. 46-B, D). After 24 h without addition of labels and antibiotics (Ab−Lab−), the relative abundance of CTE-659 targeted cells (Fig. 46) was higher in **Pr** (28.8±5.8%) than in **WWT** waters (17.0±6.3%), mirroring the results from OTU-based diversity (Fig. 45-A, C). The **AMO** addition did not have a negative impact on *Comamonadaceae* relative abundance not even at 1 mg/L concentration, which instead brought

to a slightly higher cell number; such trend was observed in both **Pr** (for 1 µg/L was on average 27.3±7.8% and 1 mg/L was 29.2±7.2%) and **WWT** samples (for 1 µg/L was on average 21.2±7.3% and 1 mg/L was 25.2±7.1%, respectively). In contrast, the addition of **CIP** had a strong influence on CTE-targeted cells in both sampling sites. In **Pr** samples, *Comamonadaceae* relative abundance decreased strongly from 29.3±6.6% in Ab− sample to 8.2±2.5% at **CIP** 1 µg/L and 6.3±1.8% at **CIP** 1 mg/L, respectively. A similar tendency was observed in **WWT** samples, with their relative abundance decreasing from 18.9±5.2% (Ab−) to 14.4±3.8% at **CIP** 1 µg/L and 11.7±3.9% at **CIP** 1 mg/L, respectively. Therefore, relative abundance results confirmed that these two phylotypes were numerically dominant in the natural water communities constituting up to ca. 30% of the whole communities even after antibiotics treatment.
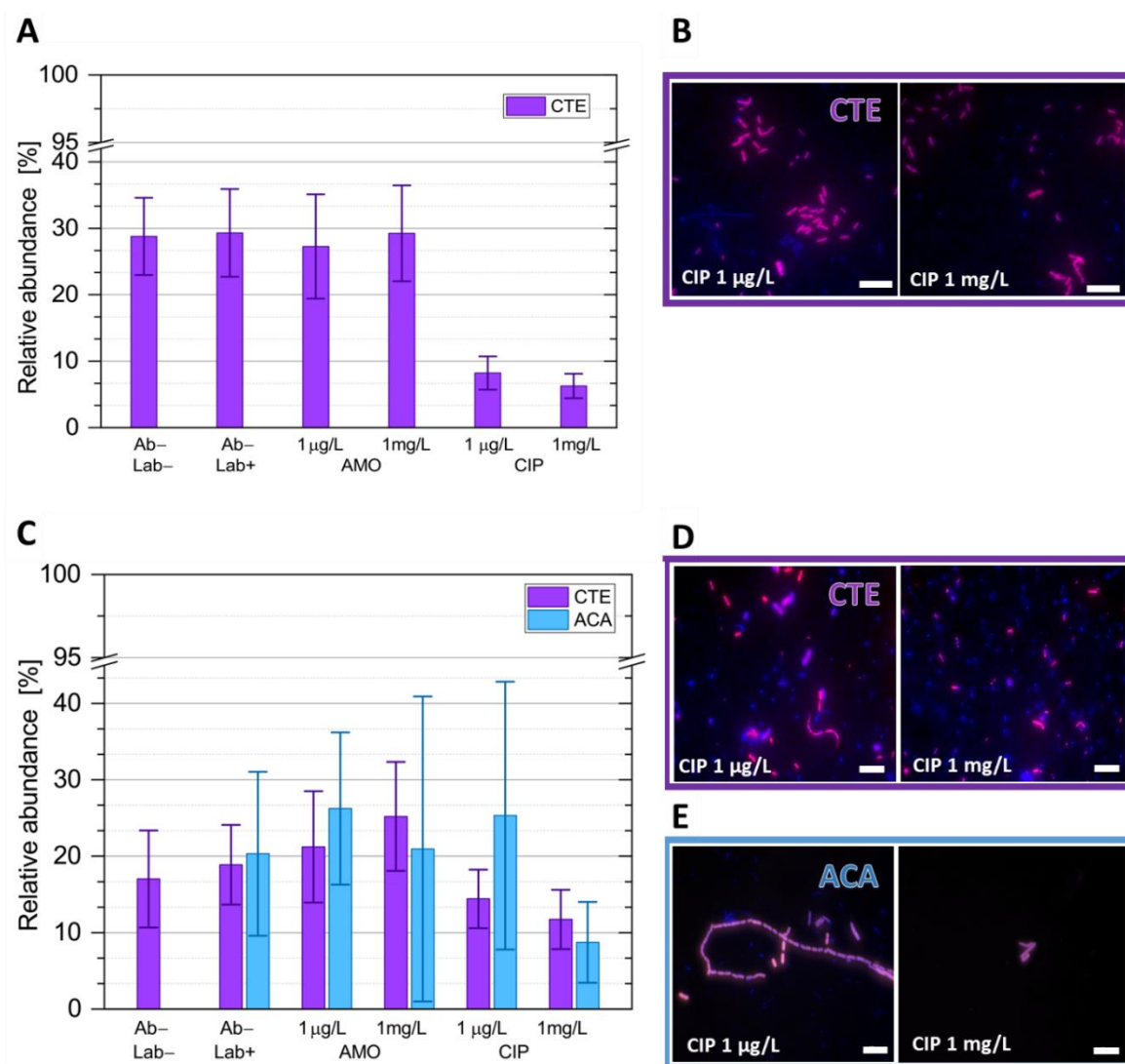
Figure 46. FISH and CARD-FISH using CTE-659 probe for targeting *Comamonadaceae* and ACA-652 probe *targeting Acinetobacter* related species, respectively in **Pr** (A-B) and **WWT** (C-E) samples exposed to different treatments upon 24h incubations. **A)** and **C)** show relative abundance of hybridized cells to total DAPI counts in % and its standard deviation. Antibiotics-free samples (Ab−) were treated with isotope-labelled compounds (Lab+) and without (Lab−). **B)** and **D)** depict representative fluorescence images after CARD-FISH with CTE659 probe (magenta) overlaid with DAPI staining (blue) at different Ciprofloxacin (**CIP**) concentrations. **E)** shows fluorescence pictures after mono-labelled-FISH with ACA-652 probe (magenta) overlaid with DAPI staining (blue).

Quantitation of metabolic activity

Anabolic activity of the whole community

In order to measure anabolic activity in the communities and potential changes induced by antibiotics addition, we added stable isotopes, ^{13}C-acetate and ^{15}N-ammonium into the samples and incubated for a time of 24 h. The first step was to compare the ^{13}C- and ^{15}N-enrichment into single cells measured by nanoSIMS with the uptake into the bulk biomass measured by Isotope Ratio Mass Spectrometry (IRMS). Before filtration, glass microfiber filters (GFF, 0.7 μm pores, Whatman) were baked at 450°C for 5h. Aliquots of 20 ml water samples were filtered onto each filter, followed by storage at –20°C. Prior to analysis, filters were dried at room temperature for 4 h, decalcified in a vapor atmosphere generated by 37% hydrochloric acid, dried for 2 h into a 55°C desiccator, trimmed in round 5mm diameter pieces and finally wrapped in small Tin cups (HEKA tech, Germany) for the combustion in IRMS (Thermo Fisher, Germany). NanoSIMS analysis was performed as described in the previous chapters using a raster area of 40 x 40 μm^2 (to include a higher number of cells per FoV) and adding the detection of the mass ^{12}C^{15}N−. Using different levels of resolution with IRMS and nanoSIMS, i.e. bulk vs. single-cell analysis, we measured heavy-isotope enrichment in unidentified microorganisms (no prior identification with FISH or CARD-FISH) (Fig. 47).

In general, microbial activity in both **Pr** and **WWT** communities was strongly affected by antibiotics exposure at higher concentrations. The 1 μg/L concentration of **AMO** and **CIP** did not change or resulted in slightly higher median values of isotope enrichment in comparison with Ab−; the addition of 1 mg/L **AMO** and **CIP** resulted instead in lower ^{13}C- and ^{15}N-enrichment median values in comparison with Ab−, as showed by both bulk and single-cell measurements. The median values at single-cell level showed that in **Pr** waters ^{13}C-enrichment was ca. 8 times lower for 1 mg/L of **AMO** and **CIP** treatments while ^{15}N-enrichment was drastically lower in comparison with Ab− samples, 27 times in **AMO** and 10 times in **CIP** treatments, respectively.

In **WWT** samples, ^{13}C-uptake decreased ca. 1.2 times in both **AMO** and **CIP** 1 mg/L treatments but ^{15}N-enrichment median values were lower, ca. 4 times in **AMO** and 11 times in **CIP** treatments than Ab− samples. The IRMS data of the same treatments mirrored the concentration dependency in C- and N-enrichment values, but could not quantify and discriminate the real variation between treatments (Fig 47-B, D). Moreover, with single-cell approach in **Pr** samples, ^{15}N-enrichment was always higher than ^{13}C-enrichment (except for **AMO** 1 mg/L), however the opposite trend was observed with IRMS method, which resulted in ^{15}N-enrichment values always lower than ^{13}C ones (Fig 47-A, B). In **WWT** samples, instead IRMS data were better mirroring the values obtained with nanoSIMS, i.e. higher median ^{15}N-enrichment values in comparison with ^{13}C (Fig 47-C, D).

Moreover, median values of the isotopic enrichment of single cells showed that in **Pr** waters ^{13}C-uptake was 6.2 times higher for Ab− (8.51 at% vs. 1.38 at%) and 3 times higher for **CIP** 1 μg/L addition (4.47 at% vs. 1.84 at%) than the corresponding treatments in **WWT**, and relatively similar for the rest of the conditions (Fig. 47- A, C). Instead, with IRMS the **WWT** values were more than 2 times higher in

comparison with **Pr** under all the tested conditions (Fig. 47-B, D). In general, however, both ^{13}C- and ^{15}N-enrichment median values were affected by the 1 mg/L concentration of **AMO** and **CIP** with a higher effect on the N-anabolic activity in comparison to C one, but differentially for the sampling sites: in **Pr** samples the values were mostly affected by **AMO**, while in **WWT** were mostly affected by **CIP**.
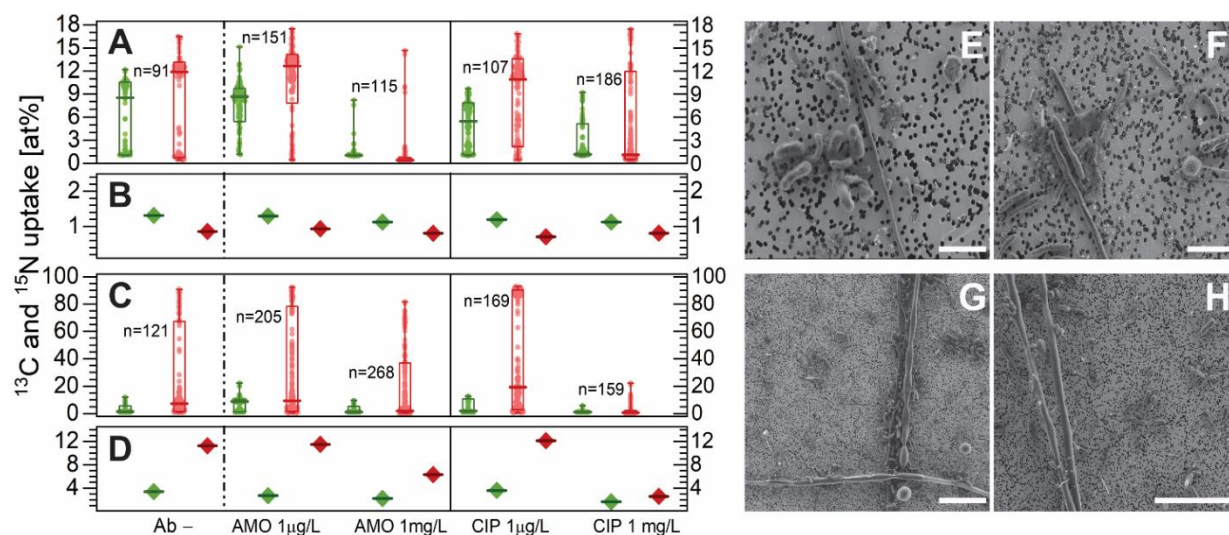
Figure 47. Community isotopic-ratio analysis by nanoSIMS and IRMS for **A) - B) Pr** and **C) - D) WWT** samples. Boxplots with green and red circles represent ^{13}C- and ^{15}N-uptake values respectively, for single cells (dots) calculated as atomic percent [at%] based on nanoSIMS data; thick horizontal lines represent median values, boxes comprise interpercentile range Q_{16}-Q_{84}, whiskers and min-max values are also shown. Green and red diamonds represent the ^{13}C- and ^{15}N-enrichment values calculated from the bulk IRMS measurements. SEM pictures corresponding to **E)** and **G)** antibiotic-free (Ab−) control samples; **F)** and **H)** samples after incubation with **AMO** 1μg/L (E and F show **Pr** samples, G and H **WWT** samples).

It is important to mention that in all the conditions, and especially in **Pr** samples, the distribution of single cells in the box plots was very scattered, suggesting a huge variability in cells activity among the different members of the communities. Indeed, a big variety of microorganisms were observed in both sampling sites with distinct morphology and size, prior and after antibiotics treatment, even though we found no clear evidences of particular morphotypes selection upon exposure as shown by the pictures acquired with SEM (Fig. 47-E to H). On the contrary, as observed with 16SrRNA gene sequencing, the community composition in both **Pr** and **WWT** shifted after antibiotics exposure, suggesting a selection of few phylotypes that outgrew and outcompeted the others (Fig. 45-A, C).

The anabolic activity measurement of the community proved that C- and N-assimilation were indeed influenced by the antibiotics´ concentration, and distinctively in respect with the two sampling sites (Fig. 47). However, we aimed to disentangle the antibiotics effect on the metabolic activity of the dominant microbial groups in comparison with non-targeted species and how this was translated in the functioning of the whole communities.

Anabolic activity of the FISH-targeted members of the microbial communities

To investigate the anabolic activity of the dominant microbial groups in both **Pr** and **WWT** waters, FISH/CARD-FISH using group-specific oligonucleotide probes coupled with nanoSIMS was performed: this was important to correlatively link their identity and relative abundance (Fig. 46) with their activity (Fig. 48). After FISH and CARD-FISH procedures, pieces of filters were marked with Laser Micro-Dissection microscope (LMD, Leica Germany) to map specific areas of interest in which probe-targeted microbial cells were highly abundant. In this way, it was possible to analyze the same observed cells with the nanoSIMS afterwards (Sketch 5).

NanoSIMS analysis was performed for all treatments specified in Table 2. For each defined single cell we first calculated the ^{13}C- and ^{15}N-enrichment in order to compare the data with the single-cell-community analysis (Fig. 47) and then we calculated the Fc (assimilation rate per single cell [187], Chapter 3.2), taking into account the dilution effect [185] on the isotopic enrichment introduced by the different FISH and CARD-FISH protocols prior to nanoSIMS [187]. We used biovolumes values previously published for *Acinetobacter* [273] and *Comamonadaceae* related specie [274] and converted the isotopic enrichment in uptake rates fg C/N·μm^{-3}, by following the equation used in [189] in order to obtain C and N density (ρ) values (ρ C=326×V$^{-0.35}$ and ρ N=78×V$^{-0.33}$) relative to these two phylotypes. The error of each single Fc median value was calculated as median absolute deviation (MAD).

The obtained results showed that the CTE-659 targeted cells were on average very active in comparison with most of non-targeted cells (Fig. 48). In general, *Comamonadaceae* related species were more active in N- than C-uptake in both **Pr** and **WWT** waters. Moreover, the median values of single-cell-^{13}C-enrichment showed that CTE-targeted cells activity was higher in **Pr** in comparison with **WWT** at all conditions, while their N-activity was showing the opposite (Fig. 48).

Due to the huge scatter in the distributions of single-cell values within each treatment, we based the comparison on the median values of ^{13}C- and ^{15}N-enrichment as well as on the single-cell distribution shapes between different incubation conditions. To do so, we performed the Mann Whitney U test, a parametric test which allows to evaluate if the differences between two populations (distributions) are statistically significant. The number of cells in each population and the p values obtained are shown in Table 3.

In **Pr** samples, the isotopic enrichment of the CTE-targeted cells remained almost unaltered between Ab− and samples treated with **AMO** at both concentrations. However, while ^{15}N-uptake and single-cells distribution was significantly (negatively) affected, no significant differences in the ^{13}C-uptake distribution of single cells were found. In contrast, by **CIP** exposure, both ^{13}C- and ^{15}N-single-cells distributions were changed in comparison with Ab− samples (Fig. 48-A, B). For both **AMO** and **CIP**, in general, the concentration of antibiotic did not seem to play a role in the activity of CTE-targeted cells neither in C-nor in N-activity (Fig. 48-A, B).

In **WWT** samples, the concentration of antibiotics impacted differently the activity of CTE-targeted cells for both C- and N-uptake (Fig. 48-C, D). The samples treated with 1 µg/L concentration of both **AMO** and **CIP** did not show significant differences in the median activity and the single-cells distributions in comparison with Ab−, while the 1 mg/L concentration of both antibiotics caused a strong decrease in C- and N-uptakes as well as in the single-cell enrichment-values distributions (Fig. 48 -C, D).
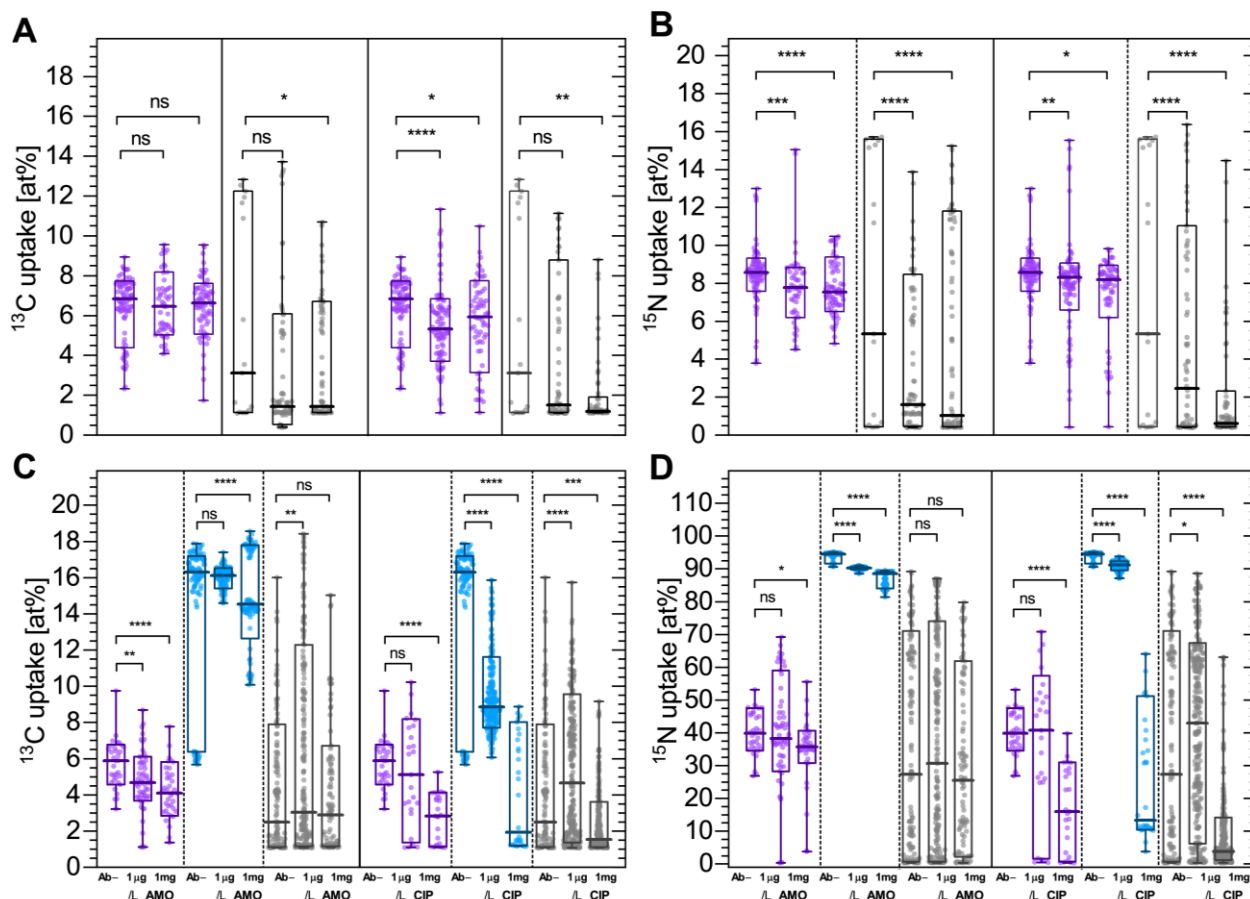
Figure 48. Carbon (C) and Nitrogen (N) uptake of single cells in **Pr** (**A-B**) and **WWT** waters (**C-D**). **A)** and **C)** show C-assimilation while **B)** and **D)** N-assimilation of single cells and their distribution in box plots for *Comamonadaceae* related species (CTE-659 targeted, purple circles) vs. non-targeted cells (grey circles). In **C)** and **D)** single cells belonging to *Acinetobacter* related species (ACA-652-targeted) are represented in light blue. Each condition is compared with antibiotics-free samples (Ab−). All boxes comprise interpercentile range Q_{16}-Q_{84}; horizontal lines within each box plot represents the median value for that particular group of cells, whiskers and Min-Max values are also represented. The number of cells analyzed and p values per each specific treatment can be found in Table 3. Significance code for p values: ns=not significant (> 0.05); * ≤0.05; ** ≤0.01; *** ≤0.001; **** ≤0.0001.

In general, **CIP** exposure had a stronger effect than **AMO** on both C- and N-activity of *Comamonadaceae* related species. In comparison with CTE-targeted cells, the activity of the non-targeted cells was always lower on average for both C- and N-uptake, at both sampling sites. In **Pr**, antibiotics exposure with **AMO** and **CIP** brought to lower median ^{13}C- and ^{15}N-enrichment values as compared with Ab− samples at both, higher and lower, concentrations (Fig. 48-A, B). In **WWT** samples, instead, the C-

and N-activity of the non-targeted cells were almost the same between Ab− and antibiotics-treated samples. The only exception was **CIP** 1mg/L condition, which resulted in significantly lower ^{13}C- and ^{15}N-enrichment median values and different single-cells distribution (Fig. 48-C, D).

ACA-targeted cell activity was higher than CTE-targeted cells for both C- and N-uptake in **WWT** samples. The antibiotics addition strongly decreased the ^{13}C- and ^{15}N-enrichment median values in comparison with Ab− samples, with the only exception of ^{13}C values of **AMO** 1 µg/L (Fig. 48-C, D). *Acinetobacter* related species activity was strongly dependent on both **AMO** and **CIP** concentration: in general, 1 mg/L concentration reduced more heavily than 1 µg/L the ^{13}C- and ^{15}N-median enrichment values. However, the impact of **CIP** at both concentrations was stronger than that of **AMO** (Fig. 48-C, D).

To conclude, the single-cell analysis, supported by the bulk data, showed that both C- and N-assimilation values were generally lower in antibiotic-treated samples in comparison with Ab− samples after 24 h of incubation in both **Pr** and **WWT** samples. The assimilation of C and N into the cell biomass depended on i) the concentration of antibiotics and ii) the antibiotic class, with the strongest effect played by **CIP** (Fig. 48).

Table 3. Single cells analyzed with nanoSIMS and p values obtained from the Mann Whitney U test. Numbers (n) of single cells per condition analyzed belonging to CTE-targeted, ACA-targeted or non-targeted (others) groups. P values (p) obtained from the single-cell-values distribution, comparison between antibiotics free sample (Ab−) vs. each of the conditions with antibiotics addition are provided for both Carbon (C) and Nitrogen (N) activity.

Conditions	CTE-targeted cells (n)	p of CTE in C	p of CTE in N	ACA-targeted cells (n)	p of ACA in C	p of ACA in N	Others (n)	p others in C	p others in N
WTT (Ab−)	33			107			140		
WWT_AMO 1 µg/L	55	5.41E-03	8.92E-01	128	9.96E-02	0.00E+00	219	2.88E-03	5.57E-01
WWT_AMO 1 mg/L	37	1.77E-05	1.29E-02	100	2.61E-12	6.70E-48	101	7.60E-01	5.28E-01
WWT_CIP 1 µg/L	25	5.30E-01	9.50E-01	245	0.00E+00	0.00E+00	279	8.91E-05	1.88E-02
WWT_CIP 1 mg/L	25	4.51E-11	2.62E-11	30	4.71E-17	1.30E-30	319	1.14E-04	9.77E-12
Pr (Ab−)	91						37		
Pr_AMO 1 µg/L	53	5.05E-01	2.23E-04				76	1.37E-01	1.82E-06
Pr_AMO 1 mg/L	73	4.95E-01	9.26E-05				83	2.95E-02	1.37E-05
Pr_CIP 1 µg/L	93	1.84E-06	5.70E-03				68	1.59E-01	1.10E-04
Pr_CIP 1 mg/L	63	1.14E-02	1.35E-03				76	4.25E-03	2.88E-05

While single-cell community analysis showed a strong influence on the anabolic microbial activity of the higher antibiotics' concentration in both **Pr** and **WWT**, the investigation on the anabolic activity of *Comamonadaceae* and *Acinetobacter* related species allowed us to discriminate how these specific phylotypes are impacted by antibiotics exposure within the communities.

For instance, anabolic activity of CTE-targeted species was affected more by the antibiotic class than the variations in concentration in **Pr** samples; instead, in **WWT** water their activity was strongly influenced by the concentration of both antibiotics. Similarly, ACA-targeted cells activity in **WWT** strongly depended on the **AMO** and **CIP** concentration. Moreover, cells belonging to the targeted species were on average more active in comparison with the non-targeted cells, suggesting that the dominance of these phylotypes was not only quantitative (as confirmed by 16S rRNA gene sequencing and FISH-based-relative abundance) but also qualitative (concerning their anabolic activity).

Interestingly, ^{13}C-enrichment median values of CTE-targeted cells were higher in **Pr** than **WWT** waters while ^{15}N-median values showed the opposite; this can be due to the diverse community composition at the two sampling sites and the amount of species that compete and thrive in the same environment for the same resources. In fact, in **WWT** waters *Acinetobacter* related species were much more active than *Comamonadaceae* in both C- and N-assimilation, reflecting not only the greater relative abundance of these two groups, but also the greater ability of *Acinetobacter* to outgrow and become dominant over the other species upon antibiotics exposure (Fig. 45-C).

Assimilation rates

To more precisely account for the impact of antibiotics exposure on the water communities we calculated and compared the C- and N-assimilation rates of *Acinetobacter* and *Comamonadaceae* vs. non-targeted cells (Fig. 49). We calculated the Fc values, i.e. fg of C and N assimilated per hour by each single cell, and then the median with its error (MAD) for each condition. Fc considers the initial C/N density of each single cell and the final one (amount of C/N assimilated during the time of incubation) and, considering each singe cell volume (as defined by manual RoI definition, see chapter 3.2.1), precisely estimates the single-cell-assimilation rate under the specific tested conditions [187].

CTE-targeted cells showed a very similar trend in their assimilation rates in both **Pr** and **WWT**. **AMO** exposure induced an increase in anabolic activity in comparison with Ab− samples: 1 μ/L concentration showed not only higher rates but also big MAD values (10.6 ± 6.0 fg C·cell^{-1}·h^{-1} and 4.3 ± 1.9 fg N·cell^{-1}·h^{-1} in **Pr** and 9.4 ± 6.8 fg C·cell^{-1}·h^{-1} and 7.2 ± 5.1 fg N·cell^{-1}·h^{-1} in **WWT**) in comparison with 1 mg/L concentration (7.6 ± 4.4 fg C·cell^{-1}·h^{-1} and 2.8 ± 1.4 fg N·cell^{-1}·h^{-1} in **Pr** and 4.2 ± 2.5 fg C·cell^{-1}·h^{-1} and 3.6 ± 2.3 fg N·cell^{-1}·h^{-1} in **WWT)** (Fig. 49-A to D). **CIP** treatment caused lower C- and N-assimilation rates in comparison with Ab− samples at both concentrations (Fig. 49-A to D). Specifically, **CIP** 1 μg/L lowered the rate to 4.8 ± 3.4 fg C·cell^{-1}·h^{-1} and 2.4 ± 1.3 fg N·cell^{-1}·h^{-1} in **Pr** and to 2.1 ± 2.0 fg C·cell^{-1}·h^{-1} and 1.3 ± 1.3 fg N·cell^{-1}·h^{-1} in **WWT**; rates at **CIP** 1 mg/L concentration were 5.8 ± 3.4 fg C·cell^{-1}·h^{-1} and 2.7 ± 1.1 fg N·cell^{-1}·h^{-1} in **Pr** and 1.6 ± 1.6 fg C·cell^{-1}·h^{-1} and 1.0 ± 0.9 fg N·cell^{-1}·h^{-1} in **WWT**.
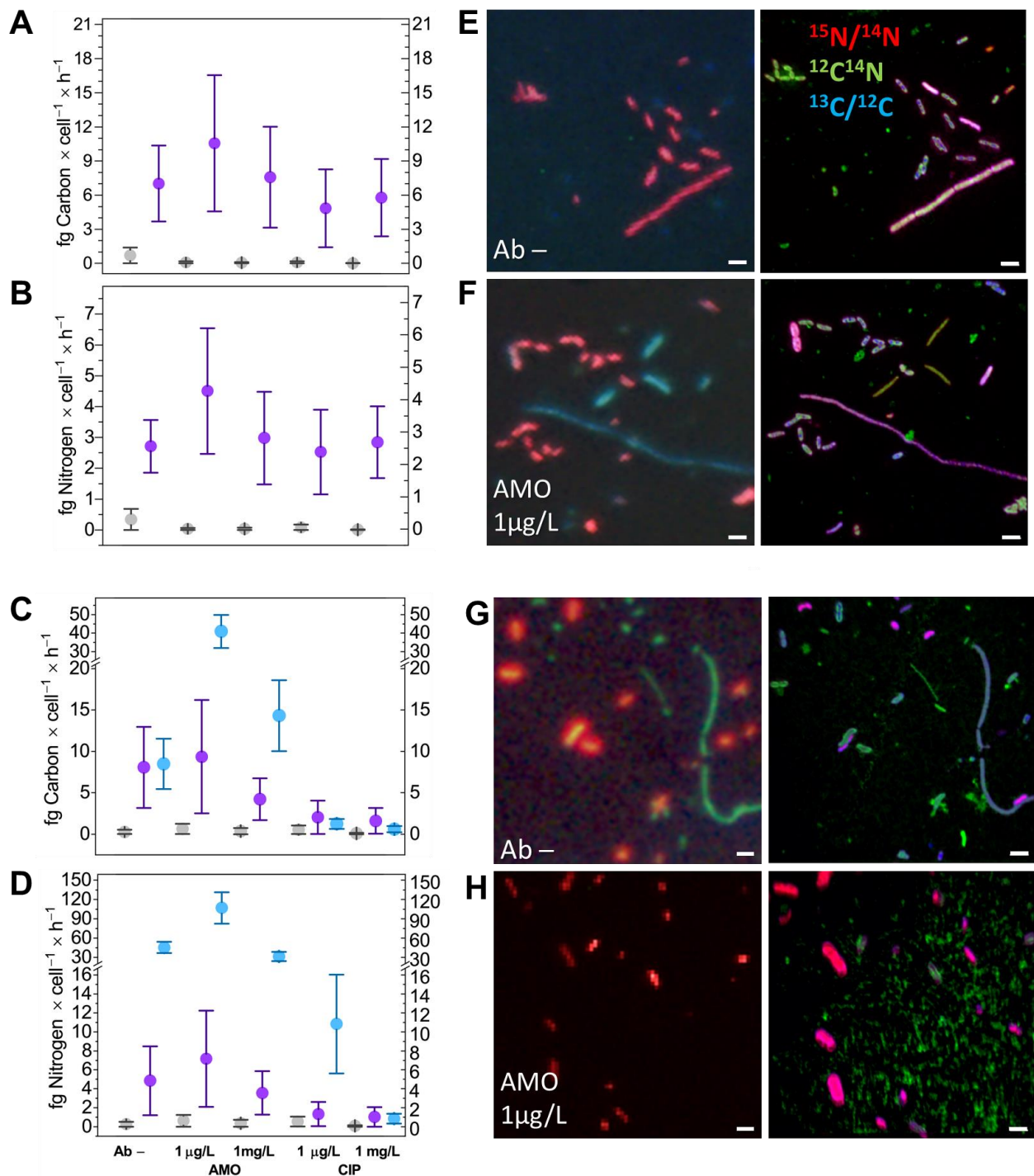
Figure 49. Carbon and Nitrogen assimilation rates in **Pr** (**A-B**) and **WWT** waters (**C-D**) after SIP-FISH/CARD-FISH nanoSIMS analysis. **A)** and **C)** represent the median values of fg C·cell^{-1}·hour^{-1}, while **B)** and **D)** median values of fg N·cell^{-1}·hour^{-1}; their errors are expressed as Median Absolute Deviation (MAD). Two FoVs from **Pr E)** and **F)** and from **WWT** samples **G)** and **H)** showing fluorescence micrographs after CARD-FISH (left panels) and the corresponding FoV analyzed with nanoSIMS (right panels) for the antibiotics free sample (Ab─) and **AMO** 1 μg/L, which corresponded to the condition where cells were most active. Left panels show microbial cells identified with CTE-659 probe (magenta) after CARD-FISH with close unidentified cells (blue, DAPI stained) that were not hybridized; right panels show nanoSIMS ions-maps represented as RGB (Red: $^{12}C^{15}N^-$/$^{12}C^{14}N^-$; Green: $^{12}C^{14}N^-$; Blue: $^{13}C^{14}N^-$/$^{12}C^{14}N^-$).

The assimilation rates of *Acinetobacter* related species confirmed that this phylotype was more active than *Comamonadaceae* in **WWT** samples. However, they showed a relatively similar behavior upon antibiotics exposure, with **AMO** (upon 1 µg/L rates were 40.9±9.0 fg C·cell^{-1}·h^{-1} and 106.9±24.4 fg N·cell^{-1}·h^{-1} while upon 1 mg/L were 14.3±4.3 fg C·cell^{-1}·h^{-1} and 31.3±7.1 fg N·cell^{-1}·h^{-1}) inducing much higher C- and N-assimilation rates than Ab− (8.5±3.0 fg C·cell^{-1}·h^{-1} and 45.3±8.7 fg N·cell^{-1}·h^{-1}). In contrast, **CIP** exposure resulted in much lower rates of 1.2±0.6 fg C·cell^{-1}·h^{-1} and 10.8±5.2 fg N·cell^{-1}·h^{-1} at 1 µg/L concentration while upon 1 mg/L, values were 0.6±0.4 fg C·cell^{-1}·h^{-1} and 0.8±0.5 fg N·cell^{-1}·h^{-1}, for C and N, respectively. The difference between **AMO** and **CIP** though was more marked for ACA-targeted species especially for N-assimilation, for which also the antibiotics' concentration played a big role (Fig. 49-D).

At all conditions the rates of targeted cells were much higher than those calculated for non-targeted cells, further confirming that the ACA-652 and CTE-659 targeted groups were metabolically dominant in the communities upon antibiotics exposure, driving the C- and N-anabolic activity at the expenses of the other phylotypes. Pictures acquired with LMD after CARD-FISH procedure were combined with ion maps showing the corresponding area analyzed with nanoSIMS: they nicely depicted the higher isotopic enrichment (^{13}C and ^{15}N) of the targeted cells in comparison with non-targeted cells (Fig. 49-E to H). Moreover, in the combined ion maps as pictures (RGB, Fig. 49-E to H) it was possible to appreciate the heterogeneous assimilation of heavy isotopes into the cell biomass among the CTE-targeted cells in both **Pr** and **WWT** waters (Fig. 49-E to H). This observation together with the huge scatter of the single-cell values distribution in ^{13}C- and ^{15}N-uptake (Fig. 48), as well as the big error values (MAD) relative to the assimilation rates (Fc), highlighted different extent of heterogeneity in the cellular anabolic activity within each treatment. For this reason, we aimed to understand the influence of antibiotics exposure on the **Anabolic Heterogeneity** (**AH)** of cells belonging to ACA-652 and CTE-659 targeted groups.

Anabolic Heterogeneity (AH) in natural microbial populations

To understand the magnitude of the antibiotics effect on the anabolic activity measured with nanoSIMS in the water communities we q**uantitated AH**, comparing the same phylogenetic groups (i.e. genus or family) under all tested conditions. Therefore, we calculated the **HC$_{corr}$** and its error ΔHC$_{corr}$ [201] for the *Acinetobacter* and *Comamonadaceae* related species in both C- and N-activity (Fig. 50). In **Pr** samples, after the addition of antibiotics, CTE-targeted cells increased their **AH** in comparison with Ab− in a concentration dependent manner: the higher the antibiotic concentration applied, the higher the **AH** in both C- and N-assimilation (Fig. 50).

In **WWT** samples, the **AH** of CTE-targeted cells in C- and N-assimilation strongly increased with **CIP** in comparison with **AMO** (Fig. 50); with **CIP** the **AH** was very similar between the two tested concentrations while with **AMO** the **AH** was higher at the 1 µg/L than 1 mg/L concentration. In general, for *Comamonadaceae* related species a higher **AH** value in N activity corresponded to a higher value in C anabolic activity in both **Pr** and **WWT** samples (Fig. 50).

ACA-targeted cells showed lower **AH** values in both C- and N-assimilation in comparison with CTE-targeted cells (Fig. 50). The **HC$_{corr}$** values for **AMO** were low and relatively similar at both tested concentrations in C- and N-assimilation, while **CIP** treatment influenced **AH** in a concentration dependent manner, with higher **HC$_{corr}$** values at 1 mg/L concentration (Fig. 50). Interestingly, the **AH** in C-activity for this specific group was much higher than **AH** in N-activity.
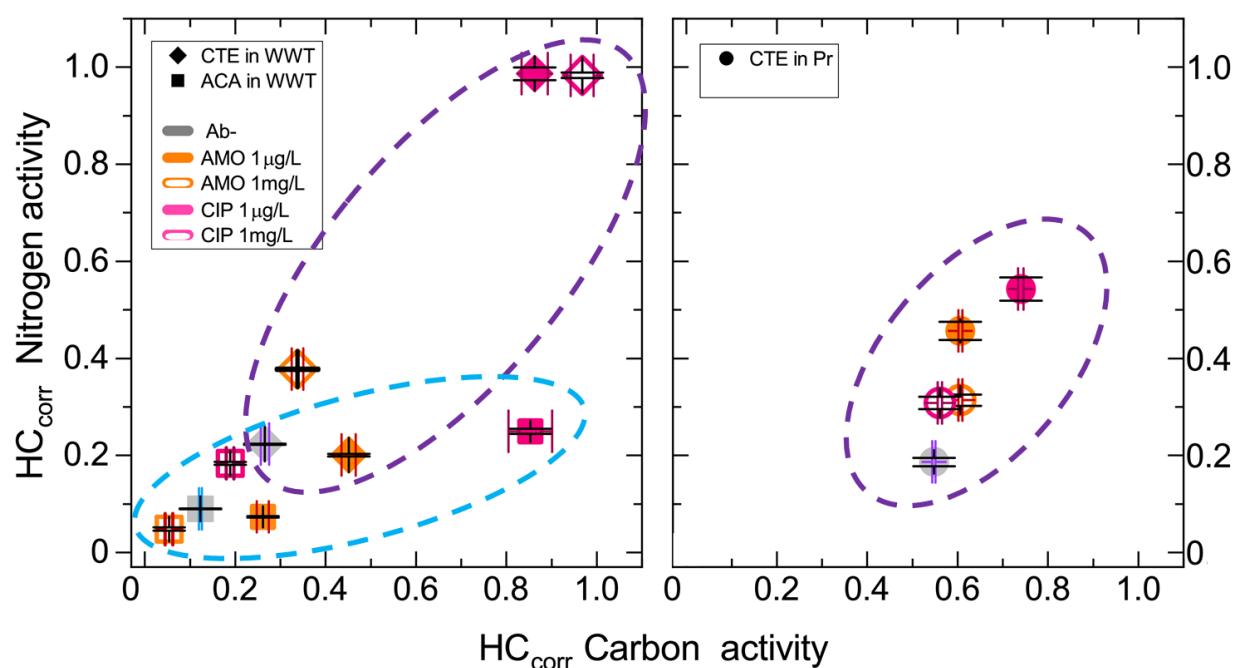
Figure 50. Corrected **Heterogeneity Coefficient (HC$_{corr}$)** values for all the tested conditions. Anabolic heterogeneity measured as **HC$_{corr}$** in C- and N-anabolic activity from CTE-659-targeted cells (purple dotted lines) and ACA-652-targeted cells (light blue dotted line) in **Pr** and **WWT** samples. Gray symbols indicate the antibiotic-free sample (Ab─), filled symbols represent the highest concentration of antibiotic and hollow ones the lowest concentration. **AMO** is in orange while **CIP** is in magenta. Errors values (ΔHC$_{corr}$) are depicted in black for C-activity and in colors for N-activity.

Studies with model organisms have shown that antibiotics exposure boosts **phenotypic heterogeneity**, allowing bacteria to increase their chance of survival after the antibiotic was removed from the culture and the conditions became favorable again [74,132]. Phytoplankton communities exposed to pharmaceutical mixture reduced their *phenotypic* diversity, namely morphology and Chlorophyll-a content, in a concentration dependent manner and changed their assemblage pattern along the water depth, thus potentially affecting the whole ecosystem functioning [275].

So far, no studies have shown **MH** or **AH** with single-cell approach upon antibiotic exposure in natural microbial communities. Neither they have quantified the **AH**. In our study, we investigated the effect of **AMO** and **CIP** on the anabolic activities of two different water samples, **Pr** and **WWT**, with special focus on specific phylotypes dominant in these communities after antibiotics treatment.

The same group, CTE-targeted present in both **Pr** and **WWT**, displayed different extent of **AH** in the two sampling sites, probably as result of different levels of competition with other species or previous exposure to other stressors into the water. CTE-targeted cells in fact were more heterogeneous in **WWT** than in **Pr**. The **AH** of both ACA-652 and CTE-659 targeted cells was affected much more by the highest concentration of antibiotics rather than the lowest, suggesting that the increase of heterogeneity might be a strategy to cope with high level of contaminants in the environment. In fact, although single-cell values were strongly differentiating from each other (in most case greatly scattering from the median values) the two phylotypes were always metabolically active upon **AMO** and **CIP** exposure. However, **CIP** impacted both anabolic activity and the **AH** much more than **AMO** overall, indicating the role of antibiotic class in shaping distinctively the heterogeneity of microbial populations.

Bacteria belonging to the genus *Acinetobacter* have gained increasing attention in recent years, due to their resistance to a wide variety of antimicrobials [276-279], in turn responsible for severe nosocomial infections [280,281]. Many representatives of this genus isolated from aquatic samples have shown to have resistance to **AMO** and **CIP** [279,281-283] and this can explain their dominance in abundance into the **WWT** waters as well as their higher metabolic rates upon antibiotics exposure in our experiments. Antibiotics-resistant representatives of *Comamonadaceae* family, as well as *Arcobater* genus (that could not be targeted in our study due to the lack of a suitable probe) have been also found in river waters and WWTP effluents [283-287]. The resistance to antibiotics could explain the ability of *Comamonadaceae* related species to thrive upon **AMO** and **CIP** treatments, maintaining high C- and N-assimilation rates and a great abundance into both sampling sites.

Interestingly, **AH** of ACA-652 and CTE-659 related species was higher in C activity than N activity. Heterotrophs in the aquatic ecosystem play a critical role in the global C-cycle. Rivers in particular not only transport huge quantity of C from the land to the ocean but actively take parts in the C-cycle thanks to respiration and sequestration processes [288,289]. In our study, antibiotics exposure brought to a very high metabolic activity on the one side, e.g. *Acinetobacter* under **AMO** treatment, or a strong suppression in metabolic activity on the other, e.g. both *Comamonadaceae* and *Acinetobacter* related species with **CIP**. These alterations may have important consequences on the community equilibrium and can be even at the expenses of other species. There is still a limited knowledge on how pollutants and other emerging contaminants, such as antibiotics, impact the C-cycle in freshwater ecosystems and more generally how they contribute to the total C-budget [290]. Our study showed that antibiotics may strongly affect the C-respiration/remineralization, thus undermining the equilibrium of the C-fluxes and -cycle in the rivers. **AH** could play a big role in the adaptation to stressing conditions and help the species to thrive even at high concentration of contaminants. Single-cell approach revealed that different species apply different strategies to cope and were not equally affected by antibiotics. These findings suggest that we need a deeper understanding on the impact of emerging contaminants on natural community and on how these effects can be translated to a wider scale.

Further studies are necessary to disentangle the mechanisms responsible for **AH** upon antibiotics exposure. As future perspective, it will be interesting to understand how **AH** shapes the community adaptation upon longer-term exposure and eventually when more than one contaminant is present in the environment, a phenomenon more commonly found due to the increasing human activity [244,291]. This poses a serious challenge in the understanding of the effects and the risks of these pharmaceuticals for the biogeochemical cycles in aquatic microbial communities.

Ecological significance of AH on natural communities

Many studies have focused on the effects of antibiotics in biogeochemical processes mainly in soil [292-297]. Despite the importance of aquatic ecosystems in biogeochemical cycles and the well-documented occurrence of antibiotics in water bodies [239,240,298], very little is known on the effects of antibiotics in aquatic natural communities, especially for individual cells. Antibiotics may have direct and indirect effects on the microbial communities [255]. Direct effects usually refer to the changes in the community composition, since antibiotics can act against both targeted (depending on the class of antibiotics) and non-targeted species, having direct effects on their inhibition or viability [255]. The reduction in microbial diversity can strongly affect the equilibrium of the ecosystem and alter the microbial-mediated processes [255,299,300]. Indirect effects comprise the *phenotypic variability*, modification of important ecological functions, e.g. while killing microorganisms engaged in single step of larger processes, or selection of antibiotics-resistant species [255]. Moreover, the effects of antibiotics may hugely vary depending on the phase of bacterial growth [301], in many cases strongly dependent on the trophic levels in the environment.

Few studies have investigated the impacts of antibiotics exposure in aquatic microbial populations. For instance, amoxicillin with clavulanic acid at 1 mg/L, but not ciprofloxacin at the same concentration, impaired denitrification processes performed by microbial communities from surface waters, sampled downstream from a sewage discharge [258]. Ciprofloxacin instead strongly decreased the microbial ability to degrade pyrene in marine/sediment communities [259] and modified the microbial composition selectively favoring Gram negative populations in detriment of Gram positive in salt marshes [257]. Ciprofloxacin induced bacterial mortality and reduced the extracellular enzymatic activity, mainly when combined with other antibiotics in biofilm from Llobregat river in Spain [302]; but instead it increased the activity of protease and dehydrogenase as well as the production of Exopolysaccharides and proteins in the biofilm of simulated drinking-water-distribution systems, especially in combination with sulfadiazine [261]. Being based on bulk measurements, these experimental works investigating the antibiotics effects may sometimes arrive to different conclusions and thus be ambiguous about the impact and the effects on the ecosystem function. In fact, with bulk approaches it is not possible to appreciate the differential sensitivity of single members of natural communities, since functions of some microbial groups may be substituted by functionally redundant microorganisms [258,259,303]. Single-cell analysis allowed to discriminate such differences, that most of the time are not detected.

In our work, following the incorporation into the biomass of C and N at single-cell level, and combining the phylogenetic identification with their activity with FISH/CARD-FISH-nanoSIMS approach, we were able to demonstrate that different phylogenetic groups in the natural communities can respond distinctively to stressors such as antibiotics, depending on the nature of the samples, the class of antibiotics and their concentrations. Interestingly, C- and N-activity are differently affected by the same treatments, thus highlighting different impacts on metabolic activities within the community. To the best of our knowledge, this was the first study focused on the activity of microorganisms withdrawn from their natural environments. Providing qualitative (who) and quantitative (how much) information on the anabolic activity (quantified as assimilation rates) allowed to evaluate the direct effect/s of these emerging contaminants on the environment on one side, and to disentangle these effects on particular community groups and their potential impact on the ecosystem functioning on the other.

In our study, C- and N-assimilation were strongly influenced by **CIP**, especially at the highest concentration. This finding has a strong relevance for two reasons: i) **CIP** is one of the widely used antibiotics for treating human and veterinary infections [304,305] and is (consequently) the most detected pharmaceutical in the river waters worldwide[249,306]. Additionally, **CIP** is more persistent in the environment in comparison with **AMO**, the latter being much more subjected to hydrolysis and photo-degradation in natural environments [252-254]. ii) The assimilation rates after **CIP** 1mg/L treatment were up to 50 times lower than our control without antibiotic (Ab−) for *Acinetobacter*. Thus, the presence and persistence into the aquatic environment of this antibiotic poses a serious risk, undermining C- and N-cycles, and pushing toward a reduced microbial diversity.

Antibiotics represent a threat for the environment and it is thus important to fully understand their effects on biogeochemical cycles for keeping a stable and heathy ecosystem functioning [300]. Knowing their direct and indirect effects will help us to understand the consequences of antibiotics in the aquatic environments and establish regulatory measures to limit their discharge and use worldwide.

4. <u>Conclusions</u>

The implementation of **single-cell techniques** made possible to shed light on the concept of *individuality*, overlooked so far by bulk approaches that hid the contribution of the individual cells within complex microbial populations. Overall, in my PhD work I was able to advance the field of single-cell microbiology, by providing:

i)   Optimized **sample-preparation** protocols for future studies on metabolic activity and heterogeneity with **SIP-nanoSIMS approach**. The same protocols can be used to visualize bacteria with SEM or HIM as well as other techniques where preservation of morphological and chemical integrity is required.
Adaptations of the protocol for co-cultured microbial species, especially when preservation of the spatial context is a desired component.

ii) Two new indices for the **quantitation of MH** in microbial populations. These indices are universal and can be applied to study different model strains and more complex environmental samples; importantly, they can be applied to other techniques such as flow cytometry and microscopy.

iii) Insights on the role played by **abiotic** and **biotic factors** on the **cell-to-cell variability** of different microbial populations and evidences about the occurrence of increased **MH** even under **non-limiting conditions**.

iv) New insights about the impact of **emerging contaminants** on the **MH** of natural microbial communities thriving in surface waters, **quantitatively** and qualitatively accounting for the effects on C- and N-assimilation upon antibiotics exposure.

5. <u>Outlook</u>

Phenotypic and **MH** are recently gaining a lot of interest in many fields, especially in medical and environmental microbiology and biotechnology. Understanding the mechanisms and the driving forces of heterogeneity can help to identify, for instance, *phenotypes* able to resist virus infections or antibiotic treatments on one side, or the factors that may decrease heterogeneity and thus leading to a better yield in bioreactors on the other side. Since **MH** affects the metabolism and the physiology of single cells, this raises the question about the contribution of heterogeneity on the ecosystem functioning and its stability. How interactions among different organisms shape the **MH** of the species and how this can translate in fluctuations of important biological processes, such as biodegradation or remineralization in the environment, is still poorly understood. The **MH** of one species involved in a certain metabolic pathway, in fact, may affect the entire function of the community, especially if that pathway becomes crucial in their environment. While co-culturing hyphal-forming species and bacteria in the synthetic set-up developed during my work, I was able to combine functional and spatial information. So far, this is still very challenging to achieve mainly due to methodological difficulties. Nonetheless, the field of 'spatial microbial ecology' is advancing, aiming to provide understanding on the mechanisms of complex interactions within microbial communities maintaining the spatial context [307].

The future perspective of my work is to link the spatial complexity of co-cultures with the metabolic interactions, and understand if they play a role in bacterial **MH** in such context. This approach could be then further implemented, for instance, increasing the complexity of the systems (more species) or studying the effect of stressors and limitations in such spatial constraints. In natural microbial communities, in fact, several species coexist and function as key players of biogeochemical cycles. Having methods to quantify assimilation of various isotope-labelled compounds, e.g. ^{13}C- or ^{15}N-labelled growth substrates, will help to scale-up from model organisms to complex microbial communities and as such to study the effects on the ecophysiology and **MH** upon exposure to emerging contaminants, e.g. antibiotics. I foresee that these types of studies will ultimately lead to a sort of automation of the *in situ*-processes **quantitation,** thus enlarging our view on the *in situ* functioning, which will be a valuable addition in the context of environmental changes that we are facing nowadays.

One of the remaining challenges is the integration of qualitative and quantitative data coming from different **single-cell techniques** to have a comprehensive and reproducible overview on the single-cells functions in their natural environments. Performing a multi-parameters analysis would be a breakthrough in microbial ecology, since it would make possible to combine gene-expression and -translation with other physiological and metabolic aspects at single-cell level. Nowadays, we are assisting at the growing development of **single-cell techniques** and technologies, which will allow us to understand fundamental and mechanistic insights into cellular processes, cellular heterogeneity and its importance and implication in broader environmental processes.

Bibliography

1   Monod, J. Diauxie et Respiration au cours de la croissance des cultures de *E. Coli* (1978)

2   Monod, J. THE GROWTH OF BACTERIAL CULTURES. *Annual Review of Microbiology* **3**, 371-394, doi:10.1146/annurev.mi.03.100149.002103 (1949).

3   Wilson, G. S. & Miles, A. A. Topley and Wilson's Principles of Bacteriology and Immunity. *Academic Medicine* **21**, 318 (1946).

4   Johannsen, W. The genotype conception of heredity. 1911. *Int J Epidemiol* **43**, 989-1000, doi:10.1093/ije/dyu063 (2014).

5   Benzer, S. Induced synthesis of enzymes in bacteria analyzed at the cellular level. *Biochimica et Biophysica Acta* **11**, 383-395, doi:https://doi.org/10.1016/0006-3002(53)90057-2 (1953).

6   Novick, A. & Weiner, M. ENZYME INDUCTION AS AN ALL-OR-NONE PHENOMENON. *Proceedings of the National Academy of Sciences of the United States of America* **43**, 553-566, doi:10.1073/pnas.43.7.553 (1957).

7   Cohn, M. & Horibata, K. Analysis of the differentiation and of the heterogeneity within a population of Escherichia coli undergoing induced beta-galactosidase synthesis. *Journal of bacteriology* **78**, 613-623 (1959).

8   Spiegelman, S., DeLorenzo, W. F. & Campbell, A. M. A Single-Cell Analysis of the Transmission of Enzyme-Forming Capacity in Yeast. *Proceedings of the National Academy of Sciences* **37**, 513-524, doi:10.1073/pnas.37.8.513 (1951).

9   Nester, E. W. & Stocker, B. A. BIOSYNTHETIC LATENCY IN EARLY STAGES OF DEOXYRIBONUCLEIC ACIDTRANSFORMATION IN BACILLUS SUBTILIS. *Journal of bacteriology* **86**, 785-796, (1963).

10   Hadden, C. & Nester, E. W. Purification of competent cells in the Bacillus subtilis transformation system. *Journal of bacteriology* **95**, 876-885, doi:10.1128/JB.95.3.876-885.1968 (1968).

11   Riggs, A. D. *et al.* Synthesis, cloning, and expression of hormone genes in Escherichia coli. *Recent Prog Horm Res* **36**, 261-276, doi:10.1016/b978-0-12-571136-4.50014-0 (1980).

12   McAdams, H. H. & Arkin, A. It's a noisy business! Genetic regulation at the nanomolar scale. *Trends in Genetics* **15**, 65-69, doi:https://doi.org/10.1016/S0168-9525(98)01659-X (1999).

13   Fedoroff, N. & Fontana, W. Genetic networks. Small numbers of big molecules. *Science* **297**, 1129-1131, (2002).

14   Swain, P. S., Elowitz, M. B. & Siggia, E. D. Intrinsic and extrinsic contributions to stochasticity in gene expression. *Proceedings of the National Academy of Sciences* **99**, 12795-12800, doi:10.1073/pnas.162041399 (2002).

15   Kærn, M., Elston, T. C., Blake, W. J. & Collins, J. J. Stochasticity in gene expression: from theories to phenotypes. *Nature Reviews Genetics* **6**, 451-464, doi:10.1038/nrg1615 (2005).

16   Maheshri, N. & O'Shea, E. K. Living with Noisy Genes: How Cells Function Reliably with Inherent Variability in Gene Expression. *Annual Review of Biophysics and Biomolecular Structure* **36**, 413-434, (2007).

17   Elowitz, M. B., Levine, A. J., Siggia, E. D. & Swain, P. S. Stochastic Gene Expression in a Single Cell. *Science* **297**, 1183-1186, doi:10.1126/science.1070919 (2002).

18   Ozbudak, E. M., Thattai, M., Kurtser, I., Grossman, A. D. & van Oudenaarden, A. Regulation of noise in the expression of a single gene. *Nature Genetics* **31**, 69-73, doi:10.1038/ng869 (2002).

19   Thattai, M. & van Oudenaarden, A. Intrinsic noise in gene regulatory networks. *Proceedings of the National Academy of Sciences of the United States of America* **98**, 8614-8619, doi:10.1073/pnas.151588598 (2001).

20   Chapon, C. Expression of malT, the regulator gene of the maltose region in Escherichia coli, is limited both at transcription and translation. *The EMBO Journal* **1**, 369-374, doi:10.1002/j.1460-2075.1982.tb01176.x (1982).

21   Rao, C. V., Wolf, D. M. & Arkin, A. P. Control, exploitation and tolerance of intracellular noise. *Nature* **420**, 231-237, doi:10.1038/nature01258 (2002).

22   Becskei, A. & Serrano, L. Engineering stability in gene networks by autoregulation. *Nature* **405**, 590-593, (2000).

23   Williams, J. W., Cui, X., Levchenko, A. & Stevens, A. M. Robust and sensitive control of a quorum-sensing circuit by two interlocked feedback loops. *Mol Syst Biol* **4**, 234, doi:10.1038/msb.2008.70 (2008).

24   Pérez, P. D., Weiss, J. T. & Hagen, S. J. Noise and crosstalk in two quorum-sensing inputs of Vibrio fischeri. *BMC Syst Biol* **5**, 153, doi:10.1186/1752-0509-5-153 (2011).

25   Teng, S. W. *et al.* Active regulation of receptor ratios controls integration of quorum-sensing signals in Vibrio harveyi. *Mol Syst Biol* **7**, 491, doi:10.1038/msb.2011.30 (2011).

26   Smits, W. K., Kuipers, O. P. & Veening, J. W. Phenotypic variation in bacteria: the role of feedback regulation. *Nat Rev Microbiol* **4**, 259-271, doi:10.1038/nrmicro1381 (2006).

27   Bury-Moné, S. & Sclavi, B. Stochasticity of gene expression as a motor of epigenetics in bacteria: from individual to collective behaviors. *Research in Microbiology* **168**, 503-514, doi:https://doi.org/10.1016/j.resmic.2017.03.009 (2017).

28   Samoilov, M. S., Price, G. & Arkin, A. P. From Fluctuations to Phenotypes: The Physiology of Noise. *Science's STKE* **2006**, re17-re17, doi:10.1126/stke.3662006re17 (2006).

29   Raj, A. & van Oudenaarden, A. Nature, nurture, or chance: stochastic gene expression and its consequences. *Cell* **135**, 216-226, doi:10.1016/j.cell.2008.09.050 (2008).

30   Ozbudak, E. M., Thattai, M., Lim, H. N., Shraiman, B. I. & Van Oudenaarden, A. Multistability in the lactose utilization network of Escherichia coli. *Nature* **427**, 737-740, doi:10.1038/nature02298 (2004).

31   Fraser, D. & Kærn, M. A chance at survival: gene expression noise and phenotypic diversification strategies. *Molecular Microbiology* **71**, 1333-1340, doi:10.1111/j.1365-2958.2009.06605.x (2009).

32   Veening, J. W., Smits, W. K. & Kuipers, O. P. Bistability, epigenetics, and bet-hedging in bacteria. *Annu Rev Microbiol* **62**, 193-210, doi:10.1146/annurev.micro.62.081307.163002 (2008).

33   Ferrell, J. E. Self-perpetuating states in signal transduction: positive feedback, double-negative feedback and bistability. *Current Opinion in Cell Biology* **14**, 140-148, doi:https://doi.org/10.1016/S0955-0674(02)00314-9 (2002).

34   Dubnau, D. & Losick, R. Bistability in bacteria. *Mol Microbiol* **61**, 564-572, (2006).

35   Avery, S. V. Cell individuality: the bistability of competence development. *Trends Microbiol* **13**, 459-462, (2005).

36   Angeli, D., Ferrell, J. E. & Sontag, E. D. Detection of multistability, bifurcations, and hysteresis in a large class of biological positive-feedback systems. *Proceedings of the National Academy of Sciences* **101**, 1822-1827, (2004).

37   Guantes, R. & Poyatos, J. F. Multistable decision switches for flexible control of epigenetic differentiation. *PLoS computational biology* **4**, e1000235-e1000235, doi:10.1371/journal.pcbi.1000235 (2008).

38   Gardner, T. S., Cantor, C. R. & Collins, J. J. Construction of a genetic toggle switch in Escherichia coli. *Nature* **403**, 339-342, doi:10.1038/35002131 (2000).

39   Pardee, A. B., Jacob, F. & Monod, J. The genetic control and cytoplasmic expression of "Inducibility" in the synthesis of β-galactosidase by E. coli. *Journal of Molecular Biology* **1**, 165-178, (1959).

40   Maamar, H. & Dubnau, D. Bistability in the Bacillus subtilis K-state (competence) system requires a positive feedback loop. *Molecular Microbiology* **56**, 615-624, doi:10.1111/j.1365-2958.2005.04592.x (2005).

41   Smits, W. K. *et al.* Stripping Bacillus: ComK auto-stimulation is responsible for the bistable response in competence development. *Mol Microbiol* **56**, 604-614, doi:10.1111/j.1365-2958.2005.04488.x (2005).

42   Maamar, H., Raj, A. & Dubnau, D. Noise in gene expression determines cell fate in Bacillus subtilis. *Science* **317**, 526-529, doi:10.1126/science.1140818 (2007).

43   Leisner, M., Stingl, K., Rädler, J. O. & Maier, B. Basal expression rate of comK sets a 'switching-window' into the K-state of Bacillus subtilis. *Mol Microbiol* **63**, 1806-1816, doi:10.1111/j.1365-2958.2007.05628.x (2007).

44   González-Pastor, J. E., Hobbs, E. C. & Losick, R. Cannibalism by sporulating bacteria. *Science* **301**, 510-513, (2003).

45   Mirel, D. B. & Chamberlin, M. J. The Bacillus subtilis flagellin gene (hag) is transcribed by the sigma 28 form of RNA polymerase. *Journal of bacteriology* **171**, 3095-3101, doi:10.1128/jb.171.6.3095-3101.1989 (1989).

46   Mirel, D. B. *et al.* Environmental regulation of Bacillus subtilis sigma(D)-dependent gene expression. *J Bacteriol* **182**, 3055-3062, doi:10.1128/jb.182.11.3055-3062.2000 (2000).

47   Diethmaier, C. *et al.* A Novel Factor Controlling Bistability in Bacillus subtilis: the YmdB Protein Affects Flagellin Expression and Biofilm Formation. *Journal of Bacteriology* **193**, 5997-6007, doi:10.1128/jb.05360-11 (2011).

48   Jablonka, E. *et al.* The adaptive advantage of phenotypic memory in changing environments. *Philos Trans R Soc Lond B Biol Sci* **350**, 133-141, doi:10.1098/rstb.1995.0147 (1995).

49   Elf, J., Li, G.-W. & Xie, X. S. Probing Transcription Factor Dynamics at the Single-Molecule Level in a Living Cell. *Science* **316**, 1191-1194, doi:10.1126/science.1141967 (2007).

50   Lambert, G. & Kussell, E. Memory and Fitness Optimization of Bacteria under Fluctuating Environments. *PLOS Genetics* **10**, e1004556, doi:10.1371/journal.pgen.1004556 (2014).

51   Casadesús, J. & Low, D. Epigenetic gene regulation in the bacterial world. *Microbiol Mol Biol Rev* **70**, 830-856, doi:10.1128/MMBR.00016-06 (2006).

52   Satory, D., Gordon, A. J., Halliday, J. A. & Herman, C. Epigenetic switches: can infidelity govern fate in microbes? *Curr Opin Microbiol* **14**, 212-217, doi:10.1016/j.mib.2010.12.004 (2011).

53   Wong Ng, J., Chatenay, D., Robert, J. & Poirier, M. G. Plasmid copy number noise in monoclonal populations of bacteria. *Physical Review E* **81**, 011909, doi:10.1103/PhysRevE.81.011909 (2010).

54   Casadesús, J. Bacterial DNA Methylation and Methylomes. *Adv Exp Med Biol* **945**, 35-61, (2016).

55   Mohapatra, S. S. & Biondi, E. G. in *Cellular Ecophysiology of Microbe*s (ed Tino Krell) 1-21 (Springer International Publishing, 2017).

56   Braaten, B. A., Nou, X., Kaltenbach, L. S. & Low, D. A. Methylation patterns in pap regulatory DNA control pyelonephritis-associated pili phase variation in E. coli. *Cell* **76**, 577-588, (1994).

57   Hernday, A. D., Braaten, B. A. & Low, D. A. The mechanism by which DNA adenine methylase and PapI activate the pap epigenetic switch. *Mol Cell* **12**, 947-957, doi:10.1016/s1097-2765(03)00383-6 (2003).

58   Hernday, A., Krabbe, M., Braaten, B. & Low, D. Self-perpetuating epigenetic pili switches in bacteria. *Proceedings of the National Academy of Sciences of the United States of America* **99 Suppl 4**, 16470-16476, (2002).

59   Hatfield, G. W. & Benham, C. J. DNA topology-mediated control of global gene expression in Escherichia coli. *Annu Rev Genet* **36**, 175-203, doi:10.1146/annurev.genet.36.032902.111815 (2002).

60   Mutlu, A. *et al.* e in Bacillus subtilis links dormancy entry and exit by a spore quantity-quality tradeoff. *Nature Communications* **9**, 69, doi:10.1038/s41467-017-02477-1 (2018).

61   Levin, B. R. & Rozen, D. E. Non-inherited antibiotic resistance. *Nature Reviews Microbiology* **4**, 556-562, (2006).

62   Bull, J. J., Vegge, C. S., Schmerer, M., Chaudhry, W. N. & Levin, B. R. Phenotypic resistance and the dynamics of bacterial escape from phage control. *PLoS One* **9**, e94690, doi:10.1371/journal.pone.0094690 (2014).

63   Gangwe Nana, G. Y. *et al.* Division-Based, Growth Rate Diversity in Bacteria. **9**, doi:10.3389/fmicb.2018.00849 (2018).

64   Kotte, O., Volkmer, B., Radzikowski, J. L. & Heinemann, M. Phenotypic bistability in Escherichia coli's central carbon metabolism. *Molecular Systems Biology* **10**, 736, doi:10.15252/msb.20135022 (2014).

65   Acar, M., Mettetal, J. T. & van Oudenaarden, A. Stochastic switching as a survival strategy in fluctuating environments. *Nature Genetics* **40**, 471-475, doi:10.1038/ng.110 (2008).

66   Takhaveev, V. & Heinemann, M. Metabolic heterogeneity in clonal microbial populations. *Current Opinion in Microbiology* **45**, 30-38, doi:https://doi.org/10.1016/j.mib.2018.02.004 (2018).

67   Schreiber, F. & Ackermann, M. Environmental drivers of metabolic heterogeneity in clonal microbial populations. *Current Opinion in Biotechnology* **62**, 202-211, doi:https://doi.org/10.1016/j.copbio.2019.11.018 (2020).

68   Soltani, M., Vargas-Garcia, C. A., Antunes, D. & Singh, A. Intercellular Variability in Protein Levels from Stochastic Expression and Noisy Cell Cycle Processes. *PLOS Computational Biology* **12**, e1004972, (2016).

69   Schreiber, F. *et al.* Phenotypic heterogeneity driven by nutrient limitation promotes growth in fluctuating environments. *Nature Microbiology* **1**, 16055, doi:10.1038/nmicrobiol.2016.55 (2016).

70   Zimmermann, M. *et al.* Phenotypic heterogeneity in metabolic traits among single cells of a rare bacterial species in its natural environment quantified with a combination of flow cell sorting and NanoSIMS. *Frontiers in Microbiology* **6**, 243, doi:10.3389/fmicb.2015.00243 (2015).

71   Zimmermann, M. *et al.* Substrate and electron donor limitation induce phenotypic heterogeneity in different metabolic activities in a green sulphur bacterium. *Environmental Microbiology Reports* **10**, 179-183, (2018).

72   Şimşek, E. & Kim, M. Power-law tail in lag time distribution underlies bacterial persistence. *Proc Natl Acad Sci U S A* **116**, 17635-17640, doi:10.1073/pnas.1903836116 (2019).

73   Dal Co, A., Ackermann, M. & van Vliet, S. Metabolic activity affects the response of single cells to a nutrient switch in structured populations. *J R Soc Interface* **16**, 20190182, doi:10.1098/rsif.2019.0182 (2019).

74   Dal Co, A., van Vliet, S. & Ackermann, M. Emergent microscale gradients give rise to metabolic cross-feeding and antibiotic tolerance in clonal bacterial populations. *Philos Trans R Soc Lond B Biol Sci* **374**, 20190080, 0 (2019).

75   Stewart, P. S. & Franklin, M. J. Physiological heterogeneity in biofilms. *Nature Reviews Microbiology* **6**, 199-210, doi:10.1038/nrmicro1838 (2008).

76   Liu, J. *et al.* Metabolic co-dependence gives rise to collective oscillations within biofilms. *Nature* **523**, 550-554, (2015).

77   Ackermann, M. A functional perspective on phenotypic heterogeneity in microorganisms. *Nature Rev. Microbiology* **13**, 497, doi:10.1038/nrmicro3491 (2015).

78   Grimbergen, A. J., Siebring, J., Solopova, A. & Kuipers, O. P. Microbial bet-hedging: the power of being different. *Curr Opin Microbiol* **25**, 67-72, doi:10.1016/j.mib.2015.04.008 (2015).

79   Momeni, B. Division of Labor: How Microbes Split Their Responsibility. *Current Biology* **28**, R697-R699, d (2018).

80   Avery, S. V. Microbial cell individuality and the underlying sources of heterogeneity. *Nature Reviews Microbiology* **4**, 577, doi:10.1038/nrmicro1460 (2006).

81   Cooper, G. A. & West, S. A. Division of labour and the evolution of extreme specialization. *Nature Ecology & Evolution* **2**, 1161-1167, doi:10.1038/s41559-018-0564-9 (2018).

82   Kussell, E. & Leibler, S. Phenotypic Diversity, Population Growth, and Information in Fluctuating Environments. *Science* **309**, 2075-2078, doi:10.1126/science.1114383 (2005).

83   Beaumont, H. J., Gallie, J., Kost, C., Ferguson, G. C. & Rainey, P. B. Experimental evolution of bet hedging. *Nature* **462**, 90-93, doi:10.1038/nature08504 (2009).

84   Levy, S. F., Ziv, N. & Siegal, M. L. Bet Hedging in Yeast by Heterogeneous, Age-Correlated Expression of a Stress Protectant. *PLOS Biology* **10**, e1001325, doi:10.1371/journal.pbio.1001325 (2012).

85   Veening, J.-W. *et al.* Bet-hedging and epigenetic inheritance in bacterial cell development. *Proceedings of the National Academy of Sciences* **105**, 4393-4398, doi:10.1073/pnas.0700463105 (2008).

86   Solopova, A. *et al.* Bet-hedging during bacterial diauxic shift. *Proc Natl Acad Sci U S A* **111**, 7427-7432, (2014).

87   Sheik, A. R. *et al.* In situ phenotypic heterogeneity among single cells of the filamentous bacterium Candidatus Microthrix parvicella. *The Isme Journal* **10**, 1274, doi:10.1038/ismej.2015.181(2015).

88   Rosenthal, A. Z. *et al.* Metabolic interactions between dynamic bacterial subpopulations. *Elife* **7**, e33099, (2018).

89   Eiteman, M. A. & Altman, E. Overcoming acetate in Escherichia coli recombinant protein fermentations. *Trends Biotechnol* **24**, 530-536, doi:https://doi.org/10.1016/j.tibtech.2006.09.001 (2006).

90   Franklin, F. C., Bagdasarian, M., Bagdasarian, M. M. & Timmis, K. N. Molecular and functional analysis of the TOL plasmid pWW0 from Pseudomonas putida and cloning of genes for the entire regulated aromatic ring meta cleavage pathway. *Proc Natl Acad Sci U S A* **78**, 7458-7462, doi:10.1073/pnas.78.12.7458 (1981).

91   Silva-Rocha, R. & de Lorenzo, V. Stochasticity of TOL plasmid catabolic promoters sets a bimodal expression regime in Pseudomonas putida mt-2 exposed to m-xylene. *Mol Microbiol* **86**, 199-211, x (2012).

92   Silva-Rocha, R., Pérez-Pantoja, D. & de Lorenzo, V. Decoding the genetic networks of environmental bacteria: regulatory moonlighting of the TOL system of Pseudomonas putida mt-2. *Isme j* **7**, 229-232, (2013).

93   Nikel, P. I., Silva-Rocha, R., Benedetti, I. & de Lorenzo, V. The private life of environmental bacteria: pollutant biodegradation at the single cell level. *Environmental Microbiology* **16**, 628-642, doi:10.1111/1462-2920.12360 (2014).

94   Almendro, V., Marusyk, A. & Polyak, K. Cellular Heterogeneity and Molecular Evolution in Cancer. *Annual Review of Pathology: Mechanisms of Disease $V 8*, 277-302 (2013).

95   Arnoldini, M. *et al.* Bistable expression of virulence genes in salmonella leads to the formation of an antibiotic-tolerant subpopulation. *PLoS biology* **12**, e1001928-e1001928, doi:10.1371/journal.pbio.1001928 (2014).

96   Delvigne, F., Zune, Q., Lara, A. R., Al-Soud, W. & Sørensen, S. J. Metabolic variability in bioprocessing: implications of microbial phenotypic heterogeneity. *Trends in Biotechnology $V 32*, 608-616 (2014).

97   Dhar, N., McKinney, J. & Manina, G. Phenotypic Heterogeneity in Mycobacterium tuberculosis. *Microbiology Spectrum* **4**, doi:doi:10.1128/microbiolspec.TBTB2-0021-2016 (2016).

98   Müller, S., Harms, H. & Bley, T. Origin and analysis of microbial population heterogeneity in bioprocesses. *Curr Opin Biotechnol* **21**, 100-113, doi:10.1016/j.copbio.2010.01.002 (2010).

99   Sadiq, F. A. *et al.* Phenotypic and genetic heterogeneity within biofilms with particular emphasis on persistence and antimicrobial tolerance. *Future Microbiology* **12**, 1087-1107, doi:10.2217/fmb-2017-0042 (2017).

100   Brehm-Stecher, B. F. & Johnson, E. A. Single-Cell Microbiology: Tools, Technologies, and Applications. *Microbiology and Molecular Biology Reviews* **68**, 538-559, doi:10.1128/mmbr.68.3.538-559.2004 (2004).

101   Ma, Z. *et al.* Applications of single-cell technology on bacterial analysis. *Quantitative Biology* **7**, (2019).

102   Altschuler, S. J. & Wu, L. F. Cellular heterogeneity: do differences make a difference? *Cell* **141**, 559-563, (2010).

103   Lidstrom, M. E. & Konopka, M. C. The role of physiological heterogeneity in microbial population behavior. *Nature Chemical Biology* **6**, 705-712, doi:10.1038/nchembio.436 (2010).

104   Musat, N., Musat, F., Weber, P. K. & Pett-Ridge, J. Tracking microbial interactions with NanoSIMS. *Current Opinion in Biotechnology* **41**, 114-121, doi:https://doi.org/10.1016/j.copbio.2016.06.007 (2016).

105   Richards, T. A., Massana, R., Pagliara, S. & Hall, N. Single cell ecology. *Philos Trans R Soc Lond B Biol Sci* **374**, 20190076-20190076, doi:10.1098/rstb.2019.0076 (2019).

106   Weaver, W. M. *et al.* Advances in high-throughput single-cell microtechnologies. *Current opinion in biotechnology* **25**, 114-123, doi:10.1016/j.copbio.2013.09.005 (2014).

107   Watrous, J. D. & Dorrestein, P. C. Imaging mass spectrometry in microbiology. *Nature Reviews Microbiology* **9**, 683-694, doi:10.1038/nrmicro2634 (2011).

108   Hillion, F., Daigne, B., Girard, F. & Slodzian, G. A new high performance SIMS instrument: The Cameca "nanosims 50". *Secondary Ion Mass Spectrometry SIMSIX*, 254-257 (1993).

109   G. Slodzian, B. D., F. Girard, and F. Hillion, Ion Optics for a High Resolution Scanning Ion Microscope and Spectrometer: Transmission Evaluations, Secondary Ion Mass Spectrometry in *Secondary Ion Mass Spectrometry (SIMS IX)* 294-297 (Yokohama, Japan, 1993.).

110   Slodzian, G., Daigne, B., Girard, F., Boust, F. & Hillion, F. Scanning secondary ion analytical microscopy with parallel detection. *Biol Cell* **74**, 43-50, doi:10.1016/0248-4900(92)90007-n (1992).

111   McMahon, G., Glassner, B. J. & Lechene, C. P. Quantitative imaging of cells with multi-isotope imaging mass spectrometry (MIMS)—Nanoautography with stable isotope tracers. *Applied Surface Science* **252**, 6895-6906, (2006).

112   Polerecky, L. *et al.* Look@NanoSIMS – a tool for the analysis of nanoSIMS data in environmental microbiology. *Environmental Microbiology* **14**, 1009-1023, doi:10.1111/j.1462-2920.2011.02681.x (2012).

113   Nuñez, J., Renslow, R., Cliff, J. & Anderton, C. NanoSIMS for biological applications: Current practices and analyses. *Biointerphases* **13**, 03B301, doi:10.1116/1.4993628 (2018).

114   Lechene, C. *et al.* High-resolution quantitative imaging of mammalian and bacterial cells using stable isotope mass spectrometry. *Journal of biology* **5**, 20, doi:10.1186/jbiol42 (2006).

115   Decelle, J. *et al.* Subcellular Chemical Imaging: New Avenues in Cell Biology. *Trends in Cell Biology* **30**, 173-188, doi:https://doi.org/10.1016/j.tcb.2019.12.007 (2020).

116   Decelle, J. *et al.* Visualization of the Ionome in Planktonic Symbioses. *Microscopy and Microanalysis* **25**, 1074-1075, doi:10.1017/S143192761900610X (2019).

117   Worrich, A. *et al.* Mycelium-mediated transfer of water and nutrients stimulates bacterial activity in dry and oligotrophic environments. *Nature Communications* **8**, 15472, doi:10.1038/ncomms15472 (2017).

118   Kopf Sebastian, H. *et al.* Heavy water and 15N labelling with NanoSIMS analysis reveals growth rate-dependent metabolic heterogeneity in chemostats. *Environmental Microbiology* **17**, 2542-2556, (2015).

119   Nikolic, N. *et al.* Cell-to-cell variation and specialization in sugar metabolism in clonal bacterial populations. *PLoS Genetics* **13**, e1007122, doi:10.1371/journal.pgen.1007122 (2017).

120   Musat, N. *et al.* A single-cell view on the ecophysiology of anaerobic phototrophic bacteria. *Proceedings of the National Academy of Sciences of the United States of America* **105**, 17861-17866, doi:10.1073/pnas.0809329105 (2008).

121   Gao, D., Huang, X. & Tao, Y. A critical review of NanoSIMS in analysis of microbial metabolic activities at single-cell level. *Critical Reviews in Biotechnology* **36**, 884-890, doi:10.3109/07388551.2015.1057550 (2016).

122 Jiang, H., Kilburn, M. R., Decelle, J. & Musat, N. NanoSIMS chemical imaging combined with correlative microscopy for biological sample analysis. *Current Opinion in Biotechnology* **41**, 130-135, (2016).

123 Amann, R. (Kluwer Academic Publishers, The Netherlands, 1995).

124 Pernthaler, A., Pernthaler, J. & Amann, R. Fluorescence In Situ Hybridization and Catalyzed Reporter Deposition for the Identification of Marine Bacteria. *Applied and Environmental Microbiology* **68**, 3094-3101, (2002).

125 Kubota, K. CARD-FISH for environmental microorganisms: technical advancement and future applications. *Microbes and environments* **28**, 3-12, doi:10.1264/jsme2.me12107 (2013).

126 Musat, N. *et al.* A single-cell view on the ecophysiology of anaerobic phototrophic bacteria. *Proceedings of the National Academy of Sciences* **105**, 17861-17866, doi:10.1073/pnas.0809329105 (2008).

127 Arandia-Gorostidi, N. *et al.* Warming the phycosphere: Differential effect of temperature on the use of diatom-derived carbon by two copiotrophic bacterial taxa. *Environmental Microbiology* **22**, 1381-1396, (2020).

128 Chen, S.-C. *et al.* Anaerobic oxidation of ethane by archaea from a marine hydrocarbon seep. *Nature* **568**, 108-111, doi:10.1038/s41586-019-1063-0 (2019).

129 Rotaru, A.-E. *et al.* Conductive Particles Enable Syntrophic Acetate Oxidation between Geobacter and Methanosarcina from Coastal Sediments. *mBio* **9**, e00226-00218, doi:10.1128/mBio.00226-18 (2018).

130 Guo, M. T., Rotem, A., Heyman, J. A. & Weitz, D. A. Droplet microfluidics for high-throughput biological assays. *Lab on a Chip* **12**, 2146-2155, doi:10.1039/C2LC21147E (2012).

131 Dhar, N. & Manina, G. Single-cell analysis of mycobacteria using microfluidics and time-lapse microscopy. *Methods Mol Biol* **1285**, 241-256, doi:10.1007/978-1-4939-2450-9_14 (2015).

132 Balaban, N. Q., Merrin, J., Chait, R., Kowalik, L. & Leibler, S. Bacterial Persistence as a Phenotypic Switch. *Science* **305**, 1622-1625, doi:10.1126/science.1099390 (2004).

133 Rosenthal, K., Oehling, V., Dusny, C. & Schmid, A. Beyond the bulk: disclosing the life of single microbial cells. *FEMS Microbiology Reviews* **41**, 751-780, doi:10.1093/femsre/fux044 (2017).

134 Akanny, E., Bonhommé, A., Bessueille, F., Bourgeois, S. & Bordes, C. Surface enhanced Raman spectroscopy for bacteria analysis: a review. *Applied Spectroscopy Reviews*, 1-43, doi:10.1080/05704928.2020.1796698 (2020).

135 Dietzek, B., Cialla, D., Schmitt, M. & Popp, J. in *Confocal Raman Microscopy* (eds Thomas Dieing, Olaf Hollricher, & Jan Toporski) 21-42 (Springer Berlin Heidelberg, 2011).

136 Xie, C. *et al.* Identification of Single Bacterial Cells in Aqueous Solution Using Confocal Laser Tweezers Raman Spectroscopy. *Analytical Chemistry* **77**, 4390-4397, doi:10.1021/ac0504971 (2005).

137 Navas-Moreno, M. & Chan, J. W. Laser Tweezers Raman Microspectroscopy of Single Cells and Biological Particles. *Methods Mol Biol* **1745**, 219-257, doi:10.1007/978-1-4939-7680-5_13 (2018).

138 Keloth, A., Anderson, O., Risbridger, D. & Paterson, L. Single Cell Isolation Using Optical Tweezers. *Micromachines (Basel)* **9**, 434, doi:10.3390/mi9090434 (2018).

139 Eberhardt, K., Stiebing, C., Matthäus, C., Schmitt, M. & Popp, J. Advantages and limitations of Raman spectroscopy for molecular diagnostics: an update. *Expert Review of Molecular Diagnostics* **15**, 773-787, (2015).

140 Wang, Y., Huang, W. E., Cui, L. & Wagner, M. Single cell stable isotope probing in microbiology using Raman microspectroscopy. *Current Opinion in Biotechnology* **41**, 34-42, (2016).

141 Huang, W. E., Griffiths, R. I., Thompson, I. P., Bailey, M. J. & Whiteley, A. S. Raman Microscopic Analysis of Single Microbial Cells. *Analytical Chemistry* **76**, 4452-4458, doi:10.1021/ac049753k (2004).

142 Everall, N. J. Confocal Raman Microscopy: Performance, Pitfalls, and Best Practice:Invited Lecture at the Symposium "50 Years of SAS: Looking to the Future with Vibrational Spectroscopy" at Pittcon 2008, New Orleans, Louisiana. *Applied Spectroscopy* **63**, 245A-262A, doi:10.1366/000370209789379196 (2009).

143 Dieing, T., Hollricher, O. & Toporski, J. *Confocal raman microscopy*. Vol. 158 (Springer, 2011).

144 Shapiro, H. M. Fluorescent dyes for differential counts by flow cytometry: does histochemistry tell us much more than cell geometry? *J Histochem Cytochem* **25**, 976-989, doi:10.1177/25.8.894012 (1977).

145 Radcliff, G. & Jaroszeski, M. J. Basics of flow cytometry. *Methods Mol Biol* **91**, 1-24, (1998).

146 Bergquist, P. L., Hardiman, E. M., Ferrari, B. C. & Winsley, T. Applications of flow cytometry in environmental microbiology and biotechnology. *Extremophiles* **13**, 389-401, doi:10.1007/s00792-009-0236-4 (2009).

147 Davey, H. M. & Kell, D. B. Flow cytometry and cell sorting of heterogeneous microbial populations: the importance of single-cell analyses. *Microbiol Rev* **60**, 641-696 (1996).

148 Shapiro, H. M. Microbial analysis at the single-cell level: tasks and techniques. *Journal of Microbiological Methods* **42**, 3-16, doi:https://doi.org/10.1016/S0167-7012(00)00167-6 (2000).

149 Lieder, S. *et al.* Subpopulation-proteomics reveal growth rate, but not cell cycling, as a major impact on protein composition in Pseudomonas putida KT2440. *AMB Express* **4**, 71-71, doi:10.1186/s13568-014-0071-6 (2014).

150 Shapiro, H. M. *Practical flow cytometry*. (John Wiley & Sons, 2005).

151 Ishoey, T., Woyke, T., Stepanauskas, R., Novotny, M. & Lasken, R. S. Genomic sequencing of single microbial cells from environmental samples. *Curr Opin Microbiol* **11**, 198-204, doi:10.1016/j.mib.2008.05.006 (2008).

152 Fierer, N. *et al.* Metagenomic and small-subunit rRNA analyses reveal the genetic diversity of bacteria, archaea, fungi, and viruses in soil. *Applied and environmental microbiology* **73**, 7059-7066, doi:10.1128/AEM.00358-07 (2007).

153 Creecy, J. P. & Conway, T. Quantitative bacterial transcriptomics with RNA-seq. *Current Opinion in Microbiology* **23**, 133-140, doi:https://doi.org/10.1016/j.mib.2014.11.011 (2015).

154 Raghunathan, A. *et al.* Genomic DNA amplification from a single bacterium. *Applied and environmental microbiology* **71**, 3342-3347, doi:10.1128/AEM.71.6.3342-3347.2005 (2005).

155 Zenobi, R. Single-cell metabolomics: analytical and biological perspectives. *Science* **342**, 1243259, (2013).

156 Wang, D. & Bodovitz, S. Single cell analysis: the new frontier in 'omics'. *Trends Biotechnol* **28**, 281-290, doi:10.1016/j.tibtech.2010.03.002 (2010).

157 Thomen, A., Robert, F. & Remusat, L. Determination of the nitrogen abundance in organic materials by NanoSIMS quantitative imaging. *Journal of Analytical Atomic Spectrometry* **29**, 512-519, doi:10.1039/C3JA50313E (2014).

158 Hoppe, P., Cohen, S. & Meibom, A. NanoSIMS: Technical Aspects and Applications in Cosmochemistry and Biological Geochemistry. *Geostandards and Geoanalytical Research* **37**, 111-154, doi:10.1111/j.1751-908X.2013.00239.x (2013).

159 Pett-Ridge, J. & Weber, P. K. NanoSIP: NanoSIMS applications for microbial biology. *Methods Mol Biol* **881**, 375-408, doi:10.1007/978-1-61779-827-6_13 (2012).

160 Fischer, E. R., Hansen, B. T., Nair, V., Hoyt, F. H. & Dorward, D. W. Scanning electron microscopy. *Curr Protoc Microbiol* **Chapter 2**, Unit2B.2-2B.2., doi:10.1002/9780471729259.mc02b02s25 (2012).

161 Glauert, A. M. & Lewis, P. R. *Biological Specimen Preparation for Transmission Electron Microscopy*. (Princeton University Press, 1998).

162   Kalab, M., Yang, A.-F. & Chabot, D. Conventional Scanning Electron Microscopy of Bacteria. *infocus Magazine* **2008**, 42-61, doi:10.22443/rms.inf.1.33 (2008).

163   Sabatini, D. D., Bensch, K. & Barrnett, R. J. Cytochemistry and electron microscopy. The preservation of cellular ultrastructure and enzymatic activity by aldehyde fixation. *J Cell Biol* **17**, 19-58, doi:10.1083/jcb.17.1.19 (1963).

164   Singh, H. *et al.* Fixation and Fixatives: Roles and Functions—A Short Review. *Dental Journal of Advance Studies* **07**, 051-055, doi:10.1055/s-0039-1693098 (2019).

165   Mercer, E. H. Fixation of Bacteria for Electron Microscopy. *Nature* **181**, 1550-1551, doi:10.1038/1811550a0 (1958).

166   Glauert, A. M. & Lewis, P. R. in *Biological Specimen Preparation for Transmission Electron Microscopy*   77-128 (Princeton University Press, 1998).

167   Jones, C. G. in *Forensic Microscopy for Skeletal Tissues: Methods and Protocols* (ed Lynne S. Bell) 1-20 (Humana Press, 2012).

168   ANDERSON, T. F. TECHNIQUES FOR THE PRESERVAATION OF THREE-DIMENSIONAL STRUCTURE IN PREPARING SPECIMENS FOR THE ELECTRON MICROSCOPE*. *Transactions of the New York Academy of Sciences* **13**, 130-134, doi:https://doi.org/10.1111/j.2164-0947.1951.tb01007.x (1951).

169   Bozzola, J. J. & Russell, L. D. *Electron Microscopy: Principles and Techniques for Biologists*.(Jones and Bartlett Publishers, 1992).

170   Golding, C. G., Lamboo, L. L., Beniac, D. R. & Booth, T. F. The scanning electron microscope in microbiology and diagnosis of infectious disease. *Scientific Reports* **6**, 26516, doi:10.1038/srep26516 (2016).

171   Au - Koon, M. A. *et al.* Preparation of Prokaryotic and Eukaryotic Organisms Using Chemical Drying for Morphological Analysis in Scanning Electron Microscopy (SEM). *JoVE*, e58761, doi:doi:10.3791/58761 (2019).

172   Shively, S. & Miller, W. R. The use of HMDS (hexamethyldisilazane) to Replace Critical Point Drying (CPD) in the Preparation of Tardigrades for SEM (Scanning Electron Microscope) Imaging. *Transactions of the Kansas Academy of Science* **112**, 198-200, 193 (2009).

173   Said, N., Chatzinotas, A. & Schmidt, M. Have an Ion on It: The Life-Cycle of Bdellovibrio bacteriovorus Viewed by Helium-Ion Microscopy. *Advanced Biosystems* **3**, 1800250, doi:10.1002/adbi.201800250 (2019).

174   Kuchenbrod, M. T., Schubert, U. S., Heintzmann, R. & Hoeppener, S. Revisiting staining of biological samples for electron microscopy: perspectives for recent research. *Materials Horizons*, doi:10.1039/D0MH01579B (2021).

175   Roeser, J., Bischoff, R., Bruins, A. P. & Permentier, H. P. Oxidative protein labeling in mass-spectrometry-based proteomics. *Analytical and Bioanalytical Chemistry* **397**, 3441-3455, doi:10.1007/s00216-010-3471-8 (2010).

176   Fratesi, S., Lynch, F., Kirkland, B. & Brown, L. Effects of SEM Preparation Techniques on the Appearance of Bacteria and Biofilms in the Carter Sandstone. *Journal of Sedimentary Research* **74**, doi:10.1306/042604740858 (2004).

177   Liu, B. Y., Zhang, G. M., Li, X. L. & Chen, H. Effect of glutaraldehyde fixation on bacterial cells observed by atomic force microscopy. *Scanning* **34**, 6-11, doi:10.1002/sca.20269 (2012).

178   Strukul, G. *Catalytic oxidations with hydrogen peroxide as oxidant*. Vol. 9 (Springer Science & Business Media, 2013).

179   Kohlmeier, S. *et al.* Taking the Fungal Highway: Mobilization of Pollutant-Degrading Bacteria by Fungi. *Environmental Science & Technology* **39**, 4640-4646, doi:10.1021/es047979z (2005).

180   Thompson, A. W. *et al.* Unicellular Cyanobacterium Symbiotic with a Single-Celled Eukaryotic Alga. *Science* **337**, 1546-1550, doi:10.1126/science.1222700 (2012).

181   Benettoni, P. *et al.* Surface cleaning and sample carrier for complementary high-resolution imaging techniques. *Biointerphases* **15**, 021005 (2020).

182   Goldstein, J. I. *et al.* in *Scanning Electron Microscopy and X-Ray Microanalysis: A Text for Biologists, Materials Scientists, and Geologists*   671-740 (Springer US, 1992).

183   Zaoli, S. *et al.* Generalized size scaling of metabolic rates based on single-cell measurements with freshwater phytoplankton. *Proceedings of the National Academy of Sciences* **116**, 17323-17329, (2019).

184   Redmond, M. C. & Valentine, D. L. in *Encyclopedia of Microbiology (Third Edition)*   (ed Moselio Schaechter) 281-285 (Academic Press, 2009).

185   Musat, N. *et al.* The effect of FISH and CARD-FISH on the isotopic composition of (13)C- and (15)N-labeled Pseudomonas putida cells measured by nanoSIMS. *Syst Appl Microbiol* **37**, 267-276, (2014).

186   Meyer, N. R., Fortney, J. L. & Dekas, A. E. NanoSIMS sample preparation decreases isotope enrichment: magnitude, variability and implications for single-cell rates of microbial activity. *Environmental Microbiology* (2020),

187   Stryhanyuk, H. *et al.* Calculation of Single Cell Assimilation Rates From SIP-NanoSIMS-Derived Isotope Ratios: A Comprehensive Approach. *Frontiers in Microbiology* **9**, doi:10.3389/fmicb.2018.02342 (2018).

188   Kendall, C. & Caldwell, E. A. in *Isotope tracers in catchment hydrology*   51-86 (Elsevier, 1998).

189   Khachikyan, A. *et al.* Direct Cell Mass Measurements Expand the Role of Small Microorganisms in Nature. *Applied and Environmental Microbiology* **85**, e00493-00419, doi:10.1128/aem.00493-19 (2019).

190   Tourna, M. *et al.* Nitrososphaera viennensis, an ammonia oxidizing archaeon from soil. *Proceedings of the National Academy of Sciences* **108**, 8420-8425, doi:10.1073/pnas.1013488108 (2011).

191   Dekas, A. E., Poretsky, R. S. & Orphan, V. J. Deep-Sea Archaea Fix and Share Nitrogen in Methane-Consuming Microbial Consortia. *Science* **326**, 422-426, doi:10.1126/science.1178223 (2009).

192   Fike, D. A., Gammon, C. L., Ziebis, W. & Orphan, V. J. Micron-scale mapping of sulfur cycling across the oxycline of a cyanobacterial mat: a paired nanoSIMS and CARD-FISH approach. *The ISME Journal* **2**, 749-759, (2008).

193   Morono, Y. *et al.* Carbon and nitrogen assimilation in deep subseafloor microbial cells. *Proceedings of the National Academy of Sciences* **108**, 18295, doi:10.1073/pnas.1107763108 (2011).

194   Woebken, D. *et al.* Identification of a novel cyanobacterial group as active diazotrophs in a coastal microbial mat using NanoSIMS analysis. *The ISME Journal* **6**, 1427-1439, doi:10.1038/ismej.2011.200 (2012).

195   Lee, J. *et al.* Fermentation couples Chloroflexi and sulfate-reducing bacteria to Cyanobacteria in hypersaline microbial mats. *Frontiers in Microbiology* **5**, doi:10.3389/fmicb.2014.00061 (2014).

196   Großkopf, T. *et al.* Doubling of marine dinitrogen-fixation rates based on direct measurements. *Nature* **488**, 361-364, doi:10.1038/nature11338 (2012).

197   Halm, H. *et al.* Co-occurrence of denitrification and nitrogen fixation in a meromictic lake, Lake Cadagno (Switzerland). *Environmental Microbiology* **11**, 1945-1958, doi:https://doi.org/10.1111/j.1462-2920.2009.01917.x (2009).

198   Krupke, A. *et al.* In situ identification and N2 and C fixation rates of uncultivated cyanobacteria populations. *Systematic and applied microbiology* **36**, 259-271 (2013).

199   Popa, R. *et al.* Carbon and nitrogen fixation and metabolite exchange in and between individual cells of Anabaena oscillarioides. *The ISME Journal* **1**, 354-360, doi:10.1038/ismej.2007.44 (2007).

200   Kopf, S. H. *et al.* Trace incorporation of heavy water reveals slow and heterogeneous pathogen growth rates in cystic fibrosis sputum. *Proceedings of the National Academy of Sciences of the United States of America* **113**, E110-E116, doi:10.1073/pnas.1512057112 (2016).

201 Calabrese, F. *et al.* Quantitation and Comparison of Phenotypic Heterogeneity Among Single Cells of Monoclonal Microbial Populations. *Frontiers in Microbiology* **10**, doi:10.3389/fmicb.2019.02814 (2019).

202 van Boxtel, C., van Heerden, J. H., Nordholt, N., Schmidt, P. & Bruggeman, F. J. Taking chances and making mistakes: non-genetic phenotypic heterogeneity and its consequences for surviving in dynamic environments. *J R Soc Interface* **14**, 20170141, doi:10.1098/rsif.2017.0141 (2017).

203 Grover, N. B. & Woldringh, C. L. Dimensional regulation of cell-cycle events in Escherichia coli during steady-state growth. *Microbiology* **147**, 171-181, doi:https://doi.org/10.1099/00221287-147-1-171 (2001).

204 Zipf, G. *The Psychobiology of Language: An Introduction to Dynamic Philology*. (M.I.T. Press, 1935).

205 Voloshynovska, I. A. Characteristic Features of Rank-Probability Word Distribution in Scientific and Belletristic Literature. *Journal of Quantitative Linguistics* **18**, 274-289, doi:10.1080/09296174.2011.583405 (2011).

206 Heins, A.-L. *et al.* Quantitative Flow Cytometry to Understand Population Heterogeneity in Response to Changes in Substrate Availability in Escherichia coli and Saccharomyces cerevisiae Chemostats. *Frontiers in Bioengineering and Biotechnology* **7**, doi:10.3389/fbioe.2019.00187 (2019).

207 Sassi, H. *et al.* Segregostat: a novel concept to control phenotypic diversification dynamics on the example of Gram-negative bacteria. *Microb Biotechnol* **12**, 1064-1075, doi:10.1111/1751-7915.13442 (2019).

208 Berthelot, H. *et al.* NanoSIMS single cell analyses reveal the contrasting nitrogen sources for small phytoplankton. *The ISME Journal* **13**, 651-662, doi:10.1038/s41396-018-0285-8 (2019).

209 Müller, S. Modes of cytometric bacterial DNA pattern: a tool for pursuing growth. *Cell Proliferation* **40**, 621-639, doi:10.1111/j.1365-2184.2007.00465.x (2007).

210 Tschech, A. & Fuchs, G. Anaerobic degradation of phenol by pure cultures of newly isolated denitrifying pseudomonads. *Archives of Microbiology* **148**, 213-217, doi:10.1007/BF00414814 (1987).

211 Laso-Pérez, R., Krukenberg, V., Musat, F. & Wegener, G. Establishing anaerobic hydrocarbon-degrading enrichment cultures of microorganisms under strictly anoxic conditions. *Nature Protocols* **13**, 1310-1330, (2018).

212 Kiviet, D. J. *et al.* Stochasticity of metabolism and growth at the single-cell level. *Nature* **514**, 376, doi:10.1038/nature13582, (2014).

213 Sudarsan, S. *et al.* Dynamics of benzoate metabolism in Pseudomonas putida KT2440. *Metabolic Engineering Communications* **3**, 97-110, doi:https://doi.org/10.1016/j.meteno.2016.03.005 (2016).

214 Bremer, H. & Dennis, P. Modulation of Chemical Composition and Other Parameters of the Cell at Different Exponential Growth Rates. *EcoSal Plus*, doi:doi:10.1128/ecosal.5.2.3 (2008).

215 Cowles, C. E., Nichols, N. N. & Harwood, C. S. BenR, a XylS Homologue, Regulates Three Different Pathways of Aromatic Acid Degradation in Pseudomonas putida. *J Bacteriol* **182**, 6339-6346, doi:10.1128/jb.182.22.6339-6346.2000 (2000).

216 Musat, N., Foster, R., Vagner, T., Adam, B. & Kuypers, M. M. M. Detecting metabolic activities in single cells, with emphasis on nanoSIMS. *FEMS Microbiology Reviews* **36**, 486-511, doi:10.1111/j.1574-6976.2011.00303.x (2012).

217 Orphan, V. J., Turk, K. A., Green, A. M. & House, C. H. Patterns of 15N assimilation and growth of methanotrophic ANME-2 archaea and sulfate-reducing bacteria within structured syntrophic consortia revealed by FISH-SIMS. *Environ Microbiol* **11**, 1777-1791, doi:10.1111/j.1462-2920.2009.01903.x (2009).

218 Fleming, E. J. *et al.* Insights into the Fundamental Physiology of the Uncultured Fe-Oxidizing Bacterium Leptothrix ochracea. *Applied and Environmental Microbiology* **84**, e02239-02217, doi:10.1128/aem.02239-17 (2018).

219 Ploug, H. *et al.* Carbon and nitrogen fluxes associated with the cyanobacterium Aphanizomenon sp. in the Baltic Sea. *The ISME Journal* **4**, 1215-1223, doi:10.1038/ismej.2010.53 (2010).

220 Berry, D. *et al.* Host-compound foraging by intestinal microbiota revealed by single-cell stable isotope probing. *Proceedings of the National Academy of Sciences* **110**, 4720-4725, doi:10.1073/pnas.1219247110 (2013).

221 Jaekel, U. *et al.* Anaerobic degradation of propane and butane by sulfate-reducing bacteria enriched from marine hydrocarbon cold seeps. *The ISME Journal* **7**, 885-895, doi:10.1038/ismej.2012.159 (2013).

222 Boer, W. d., Folman, L. B., Summerbell, R. C. & Boddy, L. Living in a fungal world: impact of fungi on soil bacterial niche development⋆. *FEMS Microbiology Reviews* **29**, 795-811, doi:10.1016/j.femsre.2004.11.005 (2005).

223 Deveau, A. *et al.* Bacterial-fungal interactions: ecology, mechanisms and challenges. *FEMS Microbiol Rev* **42**, 335-352, doi:10.1093/femsre/fuy008 (2018).

224 Malik, A. A. *et al.* Soil Fungal:Bacterial Ratios Are Linked to Altered Carbon Cycling. *Frontiers in Microbiology* **7**, doi:10.3389/fmicb.2016.01247 (2016).

225 Zhang, L. *et al.* Carbon and phosphorus exchange may enable cooperation between an arbuscular mycorrhizal fungus and a phosphate-solubilizing bacterium. *New Phytologist* **210**, 1022-1032, d (2016).

226 Banitz, T. *et al.* Dispersal networks for enhancing bacterial degradation in heterogeneous environments. *Environ Pollut* **159**, 2781-2788, doi:10.1016/j.envpol.2011.05.008 (2011).

227 Wick, L. Y. *et al.* Effect of Fungal Hyphae on the Access of Bacteria to Phenanthrene in Soil. *Environmental Science & Technology* **41**, 500-505, doi:10.1021/es061407s (2007).

228 Worrich, A. *et al.* Mycelium-Like Networks Increase Bacterial Dispersal, Growth, and Biodegradation in a Model Ecosystem at Various Water Potentials. *Applied and Environmental Microbiology* **82**, 2902-2908, (2016).

229 Worrich, A., Wick, L. Y. & Banitz, T. in *Advances in Applied Microbiology* Vol. 104 (eds Geoffrey Michael Gadd & Sima Sariaslani) 93-133 (Academic Press, 2018).

230 Berthold, T. *et al.* Mycelia as a focal point for horizontal gene transfer among soil bacteria. *Scientific Reports* **6**, 36390, doi:10.1038/srep36390 (2016).

231 Simon, A. *et al.* Exploiting the fungal highway: development of a novel tool for the in situ isolation of bacteria migrating along fungal mycelium. *FEMS Microbiol Ecol* **91**, doi:10.1093/femsec/fiv116 (2015).

232 Murray, S. in *Methods in Cell Biology* Vol. 88 3-17 (Academic Press, 2008).

233 Nazir, R., Shen, J.-P., Wang, J.-T., Hu, H.-W. & He, J.-Z. Fungal networks serve as novel ecological routes for enrichment and dissemination of antibiotic resistance genes as exhibited by microcosm experiments. *Scientific reports* **7**, 15457-15457, doi:10.1038/s41598-017-15660-7 (2017).

234 Ochman, H., Lawrence, J. G. & Groisman, E. A. Lateral gene transfer and the nature of bacterial innovation. *Nature* **405**, 299-304, doi:10.1038/35012500 (2000).

235 Fox, R. E., Zhong, X., Krone, S. M. & Top, E. M. Spatial structure and nutrients promote invasion of IncP-1 plasmids in bacterial populations. *The ISME journal* **2**, 1024-1039, doi:10.1038/ismej.2008.53 (2008).

236 Haagensen, J. A., Hansen, S. K., Johansen, T. & Molin, S. In situ detection of horizontal transfer of mobile genetic elements. *FEMS Microbiol Ecol* **42**, 261-268, doi:10.1111/j.1574-6941.2002.tb01016.x (2002).

237 Romano, J. D. & Kolter, R. Pseudomonas-Saccharomyces interactions: influence of fungal metabolism on bacterial physiology and survival. *J Bacteriol* **187**, 940-948, doi:10.1128/JB.187.3.940-948.2005 (2005).

238 Giorgio, P. & Williams, P. Vol. 267-316 267-303 (2005).

239   aus der Beek, T. *et al.* Pharmaceuticals in the environment—Global occurrences and perspectives. *Environmental Toxicology and Chemistry* **35**, 823-835, doi:https://doi.org/10.1002/etc.3339 (2016).

240   Cycoń, M., Mrozik, A. & Piotrowska-Seget, Z. Antibiotics in the Soil Environment-Degradation and Their Impact on Microbial Activity and Diversity. *Frontiers in microbiology* **10**, 338-338, doi:10.3389/fmicb.2019.00338 (2019).

241   Patrolecco, L. *et al.* Persistence of the antibiotic sulfamethoxazole in river water alone or in the co-presence of ciprofloxacin. *Science of The Total Environment* **640-641**, doi:10.1016/j.scitotenv.2018.06.025 (2018).

242   Felis, E. *et al.* Antimicrobial pharmaceuticals in the aquatic environment - occurrence and environmental implications. *European Journal of Pharmacology* **866**, doi:10.1016/j.ejphar.2019.172813 (2020).

243   Larsson, D. G. J., de Pedro, C. & Paxeus, N. Effluent from drug manufactures contains extremely high levels of pharmaceuticals. *Journal of Hazardous Materials* **148**, 751-755, (2007).

244   Kümmerer, K. Antibiotics in the aquatic environment – A review – Part I. *Chemosphere* **75**, 417-434, (2009).

245   Krzeminski, P. *et al.* Performance of secondary wastewater treatment methods for the removal of contaminants of emerging concern implicated in crop uptake and antibiotic resistance spread: A review. *Science of The Total Environment* **648**, 1052-1081, doi:https://doi.org/10.1016/j.scitotenv.2018.08.130 (2019).

246   Rizzo, L. *et al.* Urban wastewater treatment plants as hotspots for antibiotic resistant bacteria and genes spread into the environment: A review. *Science of The Total Environment* **447**, 345-360, (2013).

247   Tran, N. H., Chen, H., Reinhard, M., Mao, F. & Gin, K. Y.-H. Occurrence and removal of multiple classes of antibiotics and antimicrobial agents in biological wastewater treatment processes. *Water Research* **104**, 461-472, (2016).

248   Wang, J., Chu, L., Wojnárovits, L. & Takács, E. Occurrence and fate of antibiotics, antibiotic resistant genes (ARGs) and antibiotic resistant bacteria (ARB) in municipal wastewater treatment plant: An overview. *Science of The Total Environment* **744**, 140997, doi:https://doi.org/10.1016/j.scitotenv.2020.140997 (2020).

249   Wilkinson, J. in *SETAC Europe 29th Annual Meeting - Abstract Book* 73 (SETAC, Helsinki, 2019).

250   Wilkinson, J. L. & Hooda, P. S. Special Issue on the Environmental Fate of Emerging Organic Micro-Contaminants. *Applied Sciences* **9**, doi:doi:10.3390/app9152997 (2019).

251   WHO. *https://www.who.int/medicines/areas/rational_use/oms-amr-amc-report-2016-2018-media-note/en*, 2018).

252   Arsand, J. B. *et al.* Transformation products of amoxicillin and ampicillin after photolysis in aqueous matrices: Identification and kinetics. *Science of The Total Environment* **642**, 954-967, (2018).

253   Gozlan, I., Rotstein, A. & Avisar, D. Amoxicillin-degradation products formed under controlled environmental conditions: Identification and determination in the aquatic environment. *Chemosphere* **91**, 985-992, d (2013).

254   Hirte, K., Seiwert, B., Schüürmann, G. & Reemtsma, T. New hydrolysis products of the beta-lactam antibiotic amoxicillin, their pH-dependent formation and search in municipal wastewater. *Water Research* **88**, 880-888, (2016).

255   Grenni, P., Ancona, V. & Barra Caracciolo, A. Ecological effects of antibiotics on natural ecosystems: A review. *Microchemical Journal* **136**, 25-39, doi:https://doi.org/10.1016/j.microc.2017.02.006 (2018).

256   Danner, M.-C., Robertson, A., Behrends, V. & Reiss, J. Antibiotic pollution in surface fresh waters: Occurrence and effects. *Science of The Total Environment* **664**, 793-804, doi:https://doi.org/10.1016/j.scitotenv.2019.01.406 (2019).

257   Córdova-Kreylos, A. L. & Scow, K. M. Effects of ciprofloxacin on salt marsh sediment microbial communities. *The ISME Journal* **1**, 585-595, doi:10.1038/ismej.2007.71 (2007).

258   Costanzo, S. D., Murby, J. & Bates, J. Ecosystem response to antibiotics entering the aquatic environment. *Mar Pollut Bull* **51**, 218-223, doi:10.1016/j.marpolbul.2004.10.038 (2005).

259   Näslund, J., Hedman, J. E. & Agestrand, C. Effects of the antibiotic ciprofloxacin on the bacterial community structure and degradation of pyrene in marine sediment. *Aquat Toxicol* **90**, 223-227, doi:10.1016/j.aquatox.2008.09.002 (2008).

260   Ebert, I. *et al.* Toxicity of the fluoroquinolone antibiotics enrofloxacin and ciprofloxacin to photoautotrophic aquatic organisms. *Environ Toxicol Chem* **30**, 2786-2792, doi:10.1002/etc.678 (2011).

261   Wang, H. *et al.* Response of microorganisms in biofilm to sulfadiazine and ciprofloxacin in drinking water distribution systems. *Chemosphere* **218**, 197-204, doi:https://doi.org/10.1016/j.chemosphere.2018.11.106 (2019).

262   Co, A. D., Vliet, S. v. & Ackermann, M. Emergent microscale gradients give rise to metabolic cross-feeding and antibiotic tolerance in clonal bacterial populations. *Philosophical Transactions of the Royal Society B: Biological Sciences* **374**, 20190080, doi:doi:10.1098/rstb.2019.0080 (2019).

263   Kamjunke, N. *et al.* Molecular change of dissolved organic matter and patterns of bacterial activity in a stream along a land-use gradient. *Water Research* **164**, 114919, doi:https://doi.org/10.1016/j.watres.2019.114919 (2019).

264   Muyzer, G., Teske, A., Wirsen, C. O. & Jannasch, H. W. Phylogenetic relationships ofThiomicrospira species and their identification in deep-sea hydrothermal vent samples by denaturing gradient gel electrophoresis of 16S rDNA fragments. *Archives of Microbiology* **164**, 165-172, doi:10.1007/BF02529967 (1995).

265   Caporaso, J. G. *et al.* QIIME allows analysis of high-throughput community sequencing data. *Nat Methods* **7**, 335-336, doi:10.1038/nmeth.f.303 (2010).

266   Wagner, M. *et al.* Development of an rRNA-targeted oligonucleotide probe specific for the genus Acinetobacter and its application for in situ monitoring in activated sludge. *Appl Environ Microbiol* **60**, 792-800, (1994).

267   Schleifer, K. *et al.* Pseudomonas: molecular biology and biotechnology. *American Society for Microbiology, Washington DC, USA* (1992).

268   Amann, R. I. *et al.* Combination of 16S rRNA-targeted oligonucleotide probes with flow cytometry for analyzing mixed microbial populations. *Appl Environ Microbiol* **56**, 1919-1925, doi:10.1128/aem.56.6.1919-1925.1990 (1990).

269   Daims, H., Brühl, A., Amann, R., Schleifer, K. H. & Wagner, M. The domain-specific probe EUB338 is insufficient for the detection of all Bacteria: development and evaluation of a more comprehensive probe set. *Syst Appl Microbiol* **22**, 434-444, doi:10.1016/s0723-2020(99)80053-8 (1999).

270   Beckers, L.-M., Busch, W., Krauss, M., Schulze, T. & Brack, W. Characterization and risk assessment of seasonal and weather dynamics in organic pollutant mixtures from discharge of a separate sewer system. *Water Research* **135**, 122-133, doi:https://doi.org/10.1016/j.watres.2018.02.002 (2018).

271   Edgar, R. *UNBIAS: An attempt to correct abundance bias in 16S sequencing, with limited success.* (2017).

272   Aird, D. *et al.* Analyzing and minimizing PCR amplification bias in Illumina sequencing libraries. *Genome Biology* **12**, R18, doi:10.1186/gb-2011-12-2-r18 (2011).

273   Özel Duygan, B. D., Hadadi, N., Babu, A. F., Seyfried, M. & van der Meer, J. R. Rapid detection of microbiota cell type diversity using machine-learned classification of flow cytometry data. *Commun Biol* **3**, 379, (2020).

274   Kasalický, V., Jezbera, J., Hahn, M. W. & Šimek, K. The diversity of the Limnohabitans genus, an important group of freshwater bacterioplankton, by characterization of 35 isolated strains. *PLoS One* **8**, e58209-e58209, (2013).

275   Pomati, F., Orlandi, C., Clerici, M., Luciani, F. & Zuccato, E. Effects and Interactions in an Environmentally Relevant Mixture of Pharmaceuticals. *Toxicological Sciences* **102**, 129-137, doi:10.1093/toxsci/kfm291 (2007).

276   Doughari, H. J., Ndakidemi, P. A., Human, I. S. & Benade, S. The Ecology, Biology and Pathogenesis of *Acinetobacter* spp.: An Overview. *Microbes and Environments* **26**, 101-112, (2011).

277   Higgins, P. G., Hrenovic, J., Seifert, H. & Dekic, S. Characterization of Acinetobacter baumannii from water and sludge line of secondary wastewater treatment plant. *Water Research* **140**, 261-267, (2018).

278   Akbulut, S., Yilmaz, F. & Icgen, B. Surface water isolates of hemolytic and non-hemolytic Acinetobacter with multiple drug and heavy metal resistance ability. *Journal of Water and Health* **12**, 1-12, doi:10.2166/wh.2013.304 (2013).

279   Narciso-da-Rocha, C., Vaz-Moreira, I., Svensson-Stadler, L., Moore, E. R. B. & Manaia, C. M. Diversity and antibiotic resistance of Acinetobacter spp. in water from the source to the tap. *Applied Microbiology and Biotechnology* **97**, 329-340, doi:10.1007/s00253-012-4190-1 (2013).

280   Boral, B. *et al.* A prospective multicenter study on the evaluation of antimicrobial resistance and molecular epidemiology of multidrug-resistant Acinetobacter baumannii infections in intensive care units with clinical and environmental features. *Annals of Clinical Microbiology and Antimicrobials* **18**, 19, doi:10.1186/s12941-019-0319-8 (2019).

281   Peleg, A. Y., Seifert, H. & Paterson, D. L. Acinetobacter baumannii: emergence of a successful pathogen. *Clin Microbiol Rev* **21**, 538-582, doi:10.1128/CMR.00058-07 (2008).

282   Zhang, Y., Marrs, C. F., Simon, C. & Xi, C. Wastewater treatment contributes to selective increase of antibiotic resistance among Acinetobacter spp. *Science of The Total Environment* **407**, 3702-3706, (2009).

283   Marti, E. *et al.* Characterization of ciprofloxacin-resistant isolates from a wastewater treatment plant and its receiving river. *Water Research* **61**, 67-76, doi:https://doi.org/10.1016/j.watres.2014.05.006 (2014).

284   Jia, S. *et al.* Fate of antibiotic resistance genes and their associations with bacterial community in livestock breeding wastewater and its receiving river water. *Water Research* **124**, 259-268, (2017).

285   Novo, A., André, S., Viana, P., Nunes, O. C. & Manaia, C. M. Antibiotic resistance, antimicrobial residues and bacterial community composition in urban wastewater. *Water Research* **47**, 1875-1887, (2013).

286   Zhou, Z.-C. *et al.* Antibiotic resistance genes in an urban river as impacted by bacterial community and physicochemical parameters. *Environmental Science and Pollution Research* **24**, 23753-23762, doi:10.1007/s11356-017-0032-0 (2017).

287   Hayward, C., Ross, K. E., Brown, M. H. & Whiley, H. Water as a Source of Antimicrobial Resistance and Healthcare-Associated Infections. *Pathogens* **9**, 667, doi:10.3390/pathogens9080667 (2020).

288   Cole, J. J. *et al.* Plumbing the Global Carbon Cycle: Integrating Inland Waters into the Terrestrial Carbon Budget. *Ecosystems* **10**, 172-185, doi:10.1007/s10021-006-9013-8 (2007).

289   Tranvik, L. J. *et al.* Lakes and reservoirs as regulators of carbon cycling and climate. *Limnology and Oceanography* **54**, 2298-2314, doi:https://doi.org/10.4319/lo.2009.54.6_part_2.2298 (2009).

290   Regnier, P. *et al.* Anthropogenic perturbation of the carbon fluxes from land to ocean. *Nature Geoscience* **6**, 597-607, doi:10.1038/ngeo1830 (2013).

291   Carvalho, I. T. & Santos, L. Antibiotics in the aquatic environments: A review of the European scenario. *Environment International* **94**, 736-757, doi:https://doi.org/10.1016/j.envint.2016.06.025 (2016).

292   Conkle, J. & White, J. An initial screening of antibiotic effects on microbial respiration in wetland soils. *Journal of Environmental Science and Health Part A* **47**, doi:10.1080/10934529.2012.672315 (2012).

293   Toth, J. D., Feng, Y. & Dou, Z. Veterinary antibiotics at environmentally relevant concentrations inhibit soil iron reduction and nitrification. *Soil Biology and Biochemistry* **43**, 2470-2472, (2011).

294   Rosendahl, I. *et al.* Persistence of the Fluoroquinolone Antibiotic Difloxacin in Soil and Lacking Effects on Nitrogen Turnover. *Journal of environmental quality* **41**, 1275-1283, doi:10.2134/jeq2011.0459 (2012).

295   Liu, F., Wu, J., Ying, G.-G., Luo, Z. & Feng, H. Changes in functional diversity of soil microbial community with addition of antibiotics sulfamethoxazole and chlortetracycline. *Applied Microbiology and Biotechnology* **95**, 1615-1623, doi:10.1007/s00253-011-3831-0 (2012).

296   Ma, J. *et al.* Soil microbial systems respond differentially to tetracycline, sulfamonomethoxine, and ciprofloxacin entering soil under pot experimental conditions alone and in combination. *Environ Sci Pollut Res Int* **21**, 7436-7448, doi:10.1007/s11356-014-2685-2 (2014).

297   Guo, T. *et al.* Increased occurrence of heavy metals, antibiotics and resistance genes in surface soil after long-term application of manure. *Science of The Total Environment* **635**, 995-1003, (2018).

298   Watkinson, A. J., Murby, E. J., Kolpin, D. W. & Costanzo, S. D. The occurrence of antibiotics in an urban watershed: From wastewater to drinking water. *Science of The Total Environment* **407**, 2711-2723, (2009).

299   Schmidt, M. L. *et al.* Microhabitats are associated with diversity–productivity relationships in freshwater bacterial communities. *FEMS Microbiology Ecology* **96**, doi:10.1093/femsec/fiaa029 (2020).

300   Roose-Amsaleg, C. & Laverman, A. M. Do antibiotics have environmental side-effects? Impact of synthetic antibiotics on biogeochemical processes. *Environmental Science and Pollution Research* **23**, 4000-4012, (2016).

301   Singla, S., Harjai, K. & Chhibber, S. Susceptibility of different phases of biofilm of Klebsiella pneumoniae to three different antibiotics. *J Antibiot (Tokyo)* **66**, 61-66, doi:10.1038/ja.2012.101 (2013).

302   Santos, L. H. M. L. M. *et al.* Contribution of hospital effluents to the load of pharmaceuticals in urban wastewaters: Identification of ecologically relevant pharmaceuticals. *Science of The Total Environment* **461-462**, 302-316, (2013).

303   Wunder, D. B., Tan, D. T., LaPara, T. M. & Hozalski, R. M. The effects of antibiotic cocktails at environmentally relevant concentrations on the community composition and acetate biodegradation kinetics of bacterial biofilms. *Chemosphere* **90**, 2261-2266, doi:https://doi.org/10.1016/j.chemosphere.2012.10.031 (2013).

304   Janecko, N., Pokludova, L., Blahova, J., Svobodova, Z. & Literak, I. Implications of fluoroquinolone contamination for the aquatic environment—A review. *Environmental Toxicology and Chemistry* **35**, 2647-2656, (2016).

305   Zarb, P. *et al.* The European Centre for Disease Prevention and Control (ECDC) pilot point prevalence survey of healthcare-associated infections and antimicrobial use. *Euro Surveill* **17**, doi:10.2807/ese.17.46.20316-en (2012).

306   Wilkinson, J., Boxall, A. & Kolpin, D. A Novel Method to Characterise Levels of Pharmaceutical Pollution in Large-Scale Aquatic Monitoring Campaigns. *Applied Sciences* **9**, 1368, doi:10.3390/app9071368 (2019).

307   Worrich, A., Musat, N. & Harms, H. Associational effects in the microbial neighborhood. *The ISME Journal* **13**, 2143-2149, doi:10.1038/s41396-019-0444-6 (2019).

Appendix

First author publications

- **Calabrese F**., Voloshynovska I., Musat F., Thullner M., Schlömann M., Richnow H.H., Wick Y.L., Musat N., Stryhanyuk H., *"Quantitation and comparison of phenotypic heterogeneity among single cells of monoclonal microbial populations",* (2019), Frontiers Micr., 10, 2814, published in **Frontiers in Microbiology Journal**

- **Calabrese F**., Stryhanyuk H., Moraru C., Schlömann M., Wick Y.L., Richnow H.H., Musat F., Musat N. *Metabolic heterogeneity is an intrinsic feature of monoclonal microbial populations*, submitted to **Environmental Microbiology Journal** at the time of the thesis submission.

  A modified version has recently been **accepted** for publication in **Environmental Microbiology Journal** with the title *"Metabolic history and metabolic fitness as drivers of anabolic heterogeneity in isogenic microbial populations"*

- **Calabrese F**., Stryhanyuk H., Chen S., Brauns M., Akay C. Kümmel S., Richnow H.H., Musat F., Musat N.; *Antibiotics impact on the metabolic activity of single cells from natural microbial communities*
  Article in preparation. Planned submission to **Nature Communications**

- Said N.*, **Calabrese F.***, Stryhanyuk H., Richnow H.H., Musat N., Schmidt M.; *To each its own protocol: preparation of different microbial strains for scanning electron and ion microscopy (*equal contribution)*
  Article in preparation. Planned submission to **Journal of Microscopy**

Other contributions

- Stryhanyuk H., **Calabrese F**., Kümmel S., Musat, F., Richnow H.-H., Musat N.; (2018); *Calculation of single cell assimilation rates from SIP-nanoSIMS-derived isotope ratios: a comprehensive approach*, **Frontiers Microbiology** 9, 2342.

- Rotaru A. E., **Calabrese F**., Stryhanyuk H., Musat F., Shrestha P.M., Weber H.S., Snoeyenbos-West O.L.O., Hal, P.O.J., Richnow H.H., Musat N., Thamdrup B.; (2018), *Conductive particles enable syntrophic acetate oxidation between Geobacter and Methanosarcina from coastal sediments*, ***mBio*** 9 (3), e00226-18.

- Chen S., Musat N., Lechtenfeld O.J., Paschke H., Schmidt M., Said N., Popp D., **Calabrese F**., Stryhanyuk H., Jaekel U., Zhu Y.G., Joye S.B., Richnow H.-H., Widdel F., Musat F.; (2019), *Anaerobic oxidation of ethane by archaea from a marine hydrocarbon seep*, ***Nature*** 568 (7750).

- Benettoni P., Ye J.-Y., Holbrook T.R., **Calabrese F.**, Wagner S., Zarejousheghani M., Griebel J.,.Ullrich M.K., Musat N., Schmidt M., Flyunt R., Reemtsma T., Richnow H.H., Stryhanyuk H.; (2020), *Surface cleaning and sample carrier for complementary high-resolution imaging techniques*; ***Biointerphases*** 15, 021005

- Davoudpour Y., Schmidt M., **Calabrese F**., Richnow H.H., Musat N.; (2020), High resolution microscopy to evaluate the efficiency of surface sterilization of Zea Mays seeds; PLOS One 15 (11), e024224

Acknowledgements

I have many people to thank and I hope not to forget anyone.

The first big thanks go to Dr. Niculina Musat who gave me the opportunity to start my PhD project in her group and supported me over these years, always giving support, valuable advices and encouraging me with enthusiasm. She was more than just my supervisor and I will never forget what she did for me.

Special thanks go to Dr. Hryhoriy Stryhanyuk who dedicated a lot of patience and effort to teach me how to use nanoSIMS and a lot of time for discussions and explanations, not to mention the help in solving many troubles in the lab. I would like to express my gratitude to Dr Lukas Wick that was co-supervising part of my work and with whom I have always had fruitful and stimulating discussions. A particular thanks to Dr. Florin Musat who taught me so many things in the lab and was always available for discussions, questions answering and explanations. Many thanks to Dr. Hans H. Richnow for his support and his encouragement during these years.

My great gratitude to Prof. Dr. Michael Schlömann for giving me the opportunity to submit and defend my thesis within the Institute of Bioscience at the TU Bergakademie Freiberg and his availability for discussion, questions and valuable advices.

I would like to acknowledge all people from ProVIS at the UFZ Leipzig, and especially Matthias Schmidt for his help with SEM and HIM and the stimulating discussions about my work, and all the other colleagues from Isotope Biogeochemistry department at the UFZ who make part or most of the PhD journey with me.

A special thanks to Katja Nerlich who took care of the lab during these years and often supported me during my experiments, being there whenever I needed her help. A warm thank to Dr. Yalda Davoudpour for creating a nice and friendly environment in our working routine and for her comforting presence in my down moments.

Of course I would not be who I am and where I am without the love and the support of my parents and my lovely sisters, my boyfriend, my family and my friends, who have always believed in me and have been my pushing force to keep going **always**.

Marveling at everything is the first step of the reason towards discovery
(***Louis Pasteur***)

Curriculum Vitae

Calabrese Federica

federica.calabrese@ufz.de
calabresefederica@hotmail.it
https://orcid.org/0000-0002-4660-1405

Education

May 2021/ currently	**Postdoctoral scientist** *Applied Vascular Research Group* Helmholtz Institute for Metabolic, Obesity and Vascular Research (HI-MAG) *ProVIS-Centre for chemical microscopy* Helmholtz Centre for Environmental Research (UFZ) *University of Leipzig Medical Center*
September 2016/ September 2021	**PhD candidate** *Department of Isotope Biogeochemistry* *ProVIS-Centre* Helmholtz Centre for Environmental Research (UFZ) Leipzig *Environmental Microbiology group* (Institute of Bioscience) TU-Bergakademie Freiberg University
16th October 2013	**Master's degree in Biology** (Curriculum of Biotechnology and Applied Microbiology), Messina, Italy Final grade: 110/110 cum laude
20th March 2012	**Bachelor's degree in Biological Science**, Messina, Italy Final grade: 110/110 cum laude

Further Educational certificates

11th-15th August 2014	**24th Summer School of Jyväskylä, Finland** *"Nano machinery & Imaging towards personalized* *medicine" Course* (3 ECTS)
11th May - 10th July 2011	**Undergraduate Traineeship** *"Diagnostics of virological, microbiological,* *parasitological diagnosis and genetic disease"* Clinical Institute "Prof. Dr. De Blasi R." in Reggio Calabria, Italy"
1st October – 23rd December 2006	**"Risk and safety in Science labs" Course** at the University of Messina, Italy

Research experience

January - June 2015	**Post-Graduate Internship** at Eli Lilly and Company Ltd (Windlesham, UK)
July - December 2014	**Research Fellowship** "Phage Display Technology for recognition of bacteria involved in sepsis"
November 2013 - June 2014	**Research Assistant** at the Micro & Nano biotechnology laboratory, University of Messina "Phage display for biosensor applications".

Technical Skills

- Nano-scale Secondary Ion mass Spectrometry (nanoSIMS) for analysis of biological samples, instrument manipulation.
- Fluorescence in situ based techniques (mono-labeled-FISH and CARD-FISH) for bacteria visualization in mixed cultures and complex microbial communities
- Sample preparation for nanoSIMS and electron microscopy
- Nucleic acid extraction and purification from laboratory cultures and environmental (i.e. water, soil) samples
- Stable isotope labeling and cultivation of microorganisms under aerobic and anaerobic conditions.
- Molecular biology techniques (PCR, colony PCR, agarose gel electrophoresis)
- SDS-PAGE, Native electrophoresis, Western blot, ELISA
- Confocal Microscopy, Fluorescence microscopy, Laser microdissection (LMD), High Content Imaging (96-well plate), Immunofluorescence techniques
- Basics of Raman spectroscopy
- Phage Display Technology, phage-ELISA and all related techniques
- Coating for functionalization of flat surfaces and beads with bacteriophage, antibodies and peptides
- Filed collection of microbial samples, cell filtration and separation, sample preparation prior to microscopy and single-cell analyses

Language Skills

- Mother tongue: Italian
- English: B2
- German: B2
- French: B2

Personal Skills

- High motivation and good communication
- Problem solving; good organization and independence in planning experiments
- Determined, details-focused, dynamic and precise
- Ability to work in team and in an interdisciplinary environment

Conferences participation

7th – 9th July 2021	**Poster presentation** EMBL Symposium: New Approaches and Concepts in Microbiology
08th – 11th March 2020	**Oral presentation** 6th Joint Conference of the German Society for Hygiene and Microbiology (**DGHM**) & the Association for General and Applied Microbiology (**VAAM**) Leipzig, Germany
7-11th July 2019	**Poster pitch (oral) presentation** 8th Congress of European microbiologist (**FEMS19**) Glasgow, Scotland
20th-22nd August 2018	**Oral presentation** 8th International **NanoSIMS user meeting** conference Bremen, Germany
12th -17th August 2018	**Poster presentation** 17th International Symposium on Microbial Ecology (**ISME17**) Leipzig, Germany
8th August 2017	**Invited talk** Chance for Science Workshop 2017(Universität Leipzig) Leipzig, Germany
22nd-24th August 2017	**Poster presentation** 7th International **NanoSIMS user meeting** conference Leipzig, Germany

Other contributions

- Lecturer and guide for lab-tours in the ProVIS center at the UFZ (2016-2020)

- Video recordings and advertisements on the advantages and applications of nanoSIMS instrument in environmental research

  (https://www.youtube.com/watch?v=BevXJDLatX4; https://www.ufz.de/index.php?en=36243).

- Chair of "The Night of Microbes" within the context of ISME17, the International Symposium on Microbial Ecology which was held in Leipzig on 2018

  (https://www.youtube.com/watch?v=6CHExPQ2oNs).

- Trainer within the Workshop "Chance for Science" dedicated to refugees scientists (2017)

  Support for poster design and presentation in the scientific conference "Akademiker auf der Flucht" held at the University of Leipzig on 15th September 2017.

List of publications

Peer-reviewed papers

Calabrese, F., Stryhanyuk H., Moraru C., Schlömann M., Wick L.Y., Richnow H.H., Musat F., Musat N., (2021) *Metabolic history and metabolic fitness as drivers of anabolic heterogeneity in isogenic microbial populations;* **Environmental Microbiology**

Chen S., Budhraja R., Adrian L., **Calabrese F**., et al., (2021) *Novel clades of soil biphenyl degraders revealed by integrating isotope probing, multi-omics, and single-cell analyses;* **ISME Journal**

Davoudpour Y., Schmidt M., **Calabrese F**., Richnow H.H., Musat N., (2020) *High resolution microscopy to evaluate the efficiency of surface sterilization of Zea Mays seeds; **PLOS One*** 15 (11), e024224

P. Benettoni, J-Y Ye, T. R. Holbrook, **F. Calabrese**, S. Wagner, et al.; (2020) *Surface cleaning and sample carrier for complementary high-resolution imaging techniques*; **Biointerphases** 15, 021005.

Calabrese F., Voloshynovska I., Musat F., Thullner M., Schlömann M., et al*.,* (2019) *Quantitation and comparison of phenotypic heterogeneity among single cells of monoclonal microbial populations;* **Frontiers Microbiology** 10, 2814.

Chen S., Musat N., Lechtenfeld O.J., Paschke H., Schmidt M., Said N., Popp D., **Calabrese F**., Stryhanyuk H., et al., (2019) *Anaerobic oxidation of ethane by archaea from a marine hydrocarbon seep*, **Nature** 568 (7750), 108 – 11.

Rotaru A. E., **Calabrese F**., Stryhanyuk H., Musat F., et al., (2018) *Conductive particles enable syntrophic acetate oxidation between Geobacter and Methanosarcina from coastal sediments*, **mBio** 9 (3), e00226-18.

Stryhanyuk H., **Calabrese F**., Kümmel S., Musat, F., Richnow H.-H., Musat N.; (2018); *Calculation of single cell assimilation rates from SIP-nanoSIMS-derived isotope ratios: a comprehensive approach*, **Frontiers Microbiology** 9, 2342.

G. Lentini, E. Fazio, **F. Calabrese**, L.M. De Plano, M. Puliafico, et al, (2015) *Phage-AgNPs complex as sers probe for U937 cell identification*; **Biosensors and Bioelectronics**, 74, 398–40.

Conference papers

Calabrese F., Carnazza S., De Plano L.M., Lentini G., Franco D., Guglielmino S.P.P., P*hage-coated paramagnetic beads as selective and specific capture system for biosensor applications*; (2015), **IEEE** Publisher, Conference Paper, Proceedings of the AISEM Annual Conference, XVIII Ed., Vol., no., pp.1,4. https://doi.org/10.1109/aisem.2015.7066851.

De Plano L.M., **Calabrese F**., Lentini G., Nicolò M., Franco D., Fazio E., Trusso S., Allegra A., Neri F., Guglielmino S.P.P., (2014) *Phage display as a tool for rapid in vitro cell characterization by fluorescence imaging and Raman spectroscopy***,** Conference paper, **New Biotechnology**, Vol. 31, Page S107. https://doi.org/10.1016/j.nbt.2014.05.1870